From theory to practice: Phasor-based insights into FRET-sensing

Quinten COUCKE

January 2024

Supervisor:
Prof. Johan HOFKENS

Co-Supervisor:
Prof. Susana ROCHA

Members of the Examination Committee:
Prof. Jelle HENDRIX (assessor)
Prof. Wim ANNAERT (assessor)
Prof. Winnok DE VOS (jury)
Dr. Mar CONDOR (jury)

Chair:
Prof. Daniel Escudero Masa

Dissertation presented in partial fulfilment of the requirements for the degree of Doctor of Science: Biochemistry & Biotechnology

© 2024 KULeuven, Science, Engineering and Technology, Arenberg Doctoral School, Celestijnenlaan 200, B-3001, Heverlee Belgium.

Alle rechten voorbehouden. Niets uit deze uitgave mag worden vermenigvuldigd en/of openbaar gemaakt worden door middel van druk, fotokopie, microfilm, elektronisch of op welke andere wijze ook zonder voorafgaandelijke schriftelijke toestemming van de uitgever.

All rights reserved. No part of the publication may be reproduced in any form by print, photoprint, microfilm, electronic or any other means without written permission from the publisher.

“ An expert is someone who knows some of the worst mistakes that can be made in his subject, and how to avoid them. ”

— Werner Heisenberg

Acknowledgements

This work, my PhD thesis, is the result of a very long, complex and tedious scientific and social experience. When starting it, I could have never estimated the amount of skills I would learn, the life lessons I would experience and the marvellous people I would meet. In this section of my thesis I want to take my time in giving credit where credit is due. Unsurprisingly, it involves a long list of people that have marked my journey. It was wonderful to work for so many years with so many young and ambitious people, scientists and bright minds. It was a unique experience working in the resulting mishmash of scientific topics. Here I will take some pages to accredit those people. However, it is dangerous to forget someone. Therefore, I'd like to start with a general 'thank you' to everyone I have crossed roads with during the last years at university. I consider myself lucky and prejudiced to have met you.

First of all, my sincerest thank you to **Johan**, my promotor. I remember our first encounter in the Willem de Croylaan 46 where I had my face-to-face examination with you for *Advanced Fluorescence*. Although my interest and commitment to the course was solid, neither of us knew at that point we would be connected for many more years to come. First, as a master student working on the PIE-FLIM with Guillermo, my entanglement in the group started slowly as a FRET-novice and before finishing my master you proposed me to stay. I took my chances, said yes, and believed I could contribute in your lab, which is and was filled with countless of skilled people which you managed to get together in your group. When covid-19 hit, I will not easily forget how you reached out to stay connected, thank you. Believing in someone, and ultimately giving a student a chance to prove themselves in a PhD is with times a difficult job. I hope you will recall my contribution to the team with a smile. I know I will. Johan, thank you for supporting me, and for stopping me in the corridor, just to check why I was looking concerned or for asking "Hey, everything going ok?". It makes a difference.

Lucky for Johan, and even more so for me, the task of supervising was not only burdened upon him. As co-supervisor, **Susana** adopted me into the Rocha Lab. I was there when she became professor, and witnessed the Rocha lab being born. It was a privilege to be part of the group, to support those in need, and be supported myself. I can tell you in honesty that the best professional thing you have accomplished is the group you managed to pull together. You balance listening with managing and asking with giving. I have been thinking the longest to write this section since there are so many experiences I owe to you. I thank you for the Picanha barbecues and teambuilding activities (cops and robbers in the city, or Friday drinks ft. Johan). The coffee sessions discussing life and science with all lows and highs included, were a pillar in my past years. Susana, never change. You are rightly proud of your group and your group is more than proud of their PI.

Jelle, I'm still not sure if we produced more versions of the phasor paper than we rode kilometres on the bike, but we'll agree both were worth it, and plentiful. During my master you were the one responsible for drawing me into the homebuilt microscopy world and the eventual phasor rabbit hole. You always remain true to yourself, even though it sometimes means crashing bumper to bumper. Thank you for all on- and off-topic conversations and for being as accessible. Your approach to science is detailed, sharp and complex-less. Thank you for co-spending hours in dark rooms with the sound of some cooling fans and stubborn laser/mirror/pinhole alignment. Without your hands-on knowledge, I'm sure this thesis wouldn't have happened.

Prof. Annaert, thank you for your devotion in reading and evaluating my work. Having someone outside of microscopy was crucial for me to not lose the biology out of sight. Thank you for the interim comments and tips, even though I sometimes let too much time in between. The role of an assessor is not always easy, but I would like to stress my appreciation.

Prof. De Vos, when I was researching you in advance of a conference where you gave a talk, I encountered a picture of you on a bike. In my mind this made a connection. When the end of my PhD approached and I was looking for an external jury member I immediately thought of 'That cyclist and microscopy guru from UA!'. Thank you for accepting my invitation. I hope you have no regrets and, who knows, can see this as a kickstart for future collaborations or (phasor) microscopy endeavours.

Last jury member, but not the least: I was lucky to meet **Mar** during my PhD. *Esque*, how can one not be smiling when they meet you. Your true passion for climbing, friends, life, ... and especialy research was contagious. I'm glad you found your place (and an amazing one) at IMEC. I'm even happier that you picked up cycling and that you are absorbing the West-Flemish culture and found happiness surrounding you. We are set to keep in touch, share passions, life and science. You made a mark on me as a person, thank you for everything.

I have to talk about **Michiel** next. Since you became my co- inhabitant in our dorm in Kortrijk (#blok4), you have become one of my best friends. As destiny had it written out for us you studied chemistry, which meant we were set to share many interests, classes and some though exams. For some years now, we also became colleagues. As things turned out we are a successful duo (or a hilarious combo at least). Our partnership is strong, and we knew that when academia wouldn't work out we could switch to our other services: decorations, Christmas tree planting, party preparations & catering, logistical services, webmasters, social media consultants, professional naggers, pest liquidations, coffee sommelier, gardening, and much more. Thank you for the 1000+ coffees shared and the accompanying conversations, I'm sure they saved me plenty hours of professional therapy. I wish you the best in reaching the finish line yourself and hope we never stop our adventures together.

Charlotte, you came to the group of Susana as a godsent gift. While the Rocha lab was just setting in you were often there to keep it on the tracks (more than you

realise). Thank you for showing us (and forcing others) such high level of organisation and control. While at first some found it funny, I'm sure many now hope to be a bit more 'Charlotteke', since you simply rock your science. Additionally, I'd like to give you the advice to buy a racing bike. Or to at least keep cycling. You are as much a naturally gifted cyclist as you are a scientist, never give it up. Even when work is pushing you away from spending time on the bike, prioritize your rides. (and please never cook banana's)

Johannes, 'Mister Business', PDG of the life science consulting industry NV. You seemed like my older brother during this PhD. We felt a solid connection, supplied each other with questions and tried coming up with many answers. Sailing rough seas is easier in the wake of the boat ahead. Thank you for all the amazing adventures and 'connerie' (with our 'top' endeavour: driving towards Bédoin, climbing Mont Ventoux by bike, and driving back in only four days with Michiel). We know for sure not a single one will play the first of April better on Susana than we did (for readers that wonder, ask Susana).

Miss Van Zundert, **Indra**. Thank you for showing me your lifestyle, in which you seemingly glide through the toughest of obstacles. I'm sure it helped me in my PhD when I paraphrased you in my mind at difficult times: "How would Indra have dealt with this?". This often led me to the most efficient approach. Each from a far end of Flanders we found ourselves alike. I wish you the absolute best in your future career path and wish you, Martin and Marco a great future together.

Guillermo. Your almost auto-reply "aaah, it's fine" when you again did something for someone else is a true inspiration. Not often have I come across someone with your energy and passion for research. From being my mentor during the master up until today, I'd recon you truly know me. Thank you for everything I could learn from you, the tapas in Madrid and the beers we shared in the last years. Thank you as well for you input on many aspects of this thesis.

Dear **Sam**, darling, when I say "You will drive this PhD home". I'm counting on your research, not your driving skills. The flurry of energy you brought into the office caught me by surprise, but was inspiring. After I 'guided' you when you just arrived, you soon picked up you own interests and got your teeth in the challenges presented. While I still think a little less keto wouldn't hurt no one, I wouldn't want you to change at all. Thank you for the help, the countless hours of cloning, and for the laughter all year round. You were my first teammate in 'doing phasor', which was a huge help. Much of Chapter 4, I owe to you.

Almost nearing the finish line of her PhD, **Elizabete** deserves credit. Sharing an office is not just saying 'hi' in the morning, that we understood. We shared life, with big ups and deep or sometimes long lows. I'm confident you got through the lows because of your strong mentality and willpower. Never forget to enjoy every day and every once in a while take a bird's-eye view on things. Best of luck, you will reach the end!

Meme machine from the 'Kempe', **Sarah**, you were a great master student and I'm confident you will continue on that positive trend in your PhD. You have an

open visor for science, a contagious laugh and healthy motivation. Thank you for all the support. It is a pity we didn't start the PhD together as we only shared a couple of years, because I think we make a great team. Please keep updating me on the chronicles of the first year bachelor practical course we teach(ed)!

To my dearest colleagues of the Rocha Lab: **Boris**, thank you for always being at the ready for a coding question; **Maria** when I close my eyes I will never get rid of your contagious (loud) laughter; **Hongbo** thank you for your calm and composed contributions, I wish you the best with your amazing family; **Samantha**/Mantha, thank you for teaching me that an Aussie sparkie carries his brekky in his esky, has heaps of maccas for lunch and always wears his sunnies. Please, stay upright on the bike. **Haoxiang**, keep growing peppers, and thanks for the office conversations. Additionally**, Bea, Sandra, Silke and Pierre** best of luck in your research and thanks for everything. All of these wonderful lab colleagues helped me out when I reached out, thank you for having joined me in this amazing part of my life. These experiences are never forgotten!

A special mention goes to **Prof. Dr. Emeritus Frans Deschryver**. I still find it unbelievable with which perseverance and dedication you keep in touch with the latest developments in the lab and that you follow the important literature to share your thoughts with us. The best moment of any MIP meeting is for sure your sharp, precise and supportive remarks and questions. I think any researcher could learn from you, I'm sure I did. Thank you for the small chats now and then, thank you for your support. 'Never stop learning and always be critical' is the message you gave me.

Rik, more than being colleagues, we were teammates. Every once in a while we were fighting together for a world in which microscopes are not abused. I will miss our talks on our most rare wildlife finds on waarnemingen.be. Inevitable, also **Carine** and **An** deserve a highlighted message of appreciation. Always at the ready for everyone, you are an infinite source advice or guidance. I'm confident that your work is crucial for the science conducted in our lab, a massive thank you. **Débora**, thank you for all the pointers in cell culture and the order you bring to meetings and lab logistics, your friendliness was overwhelming.

Steven, I hope the Rocha lab will soon forget your nickname of 'the new Quinten', because you really are a super enjoyable personality of your own. I enjoyed being your mentor, but enjoy most of all the thought you will be a great scientist to take control of our precious hardware. You start your PhD when I finish but you know where to find me whenever you have questions. I'm confident you will further deepen your scientific mind. Above all, keep cycling.

During my PhD I was lucky to never walk this path alone. My best friend since elementary school, co-houser, ultra trailrun partner, and now also excellent dad, was my sounding board. **Robin,** thank you for your steady and calm mind which I could occasionally pick. Since the PhD more than ever, the long runs together were a welcome relief to share and nag about our experiences. In full analogy with the PhD: I was lucky you were running ahead as I can trust you blind to pick the right trails. Our friendship will last forever, I'm sure.

A special mention goes to my good friends of **#blok4**, my student housing friends from Kortrijk. Together with partners, we have an amazing group and I'm thankful for all the conversations and weekends in the Ardennes we yearly arrange. I consider myself extremely lucky to be part of this. Finding myself among you guys has had a tremendous positive impact on my life.

To my lovely aunt and godmother **Nele**. Your encouragement and positive energy has been incredibly valuable throughout my life. With some hard setbacks and the immensely difficult news of the cancer diagnosis, your happy and determined attitude served, and will always serve, as true inspiration. I much appreciated the following-up on my scientific endeavours. Thank you, and Salvatore, for everything, and cheers to many more adventures together.

Being raised in a warm and supportive home is another privilege I could always rely on. To my **parents** and my **brother**, thank you for being there along every step the way. I praise you for understanding my occupation the last few years and showing interest. I believe I'm a result of this positive environment which you all cultivated. I'm proud of the way we can stick together, and openly talk about anything.

Finally, last but not least, to my love, **Margot**, keppe. While being together for such long time already, having a partner doing a PhD takes some flexibility. With me being that partner, your patience got tested past what people will believe. Your natural support during the most difficult times writing this thesis, publishing my paper or failing experiments was crucial. I can barely put into words what your unconditional love has meant to me. It will take me plenty of good dinners to ever equal the balance, but I'm determined to do so. I'm convinced we are on the right track towards a warm family, in a warm home. I can't wait to hold our future in our hands.

Summary

Fluorescent molecules have historically always been used as a reporter, such as the fluorescein staining in the early 1900s. With more advanced microscopy came more complex and detailed usage of fluorophores: labelling specific tissues, cells, and subcellular organelles. With the use of fluorescent proteins (FPs) that could easily be expressed by the cell itself, new options opened on what could be reported using fluorescence. In modern cellular biology and biochemistry research Förster resonance energy transfer (FRET) has become indispensable tool to study biomolecules at the nanometre scale. Using FRET, the basal usage of fluorescence emission is surpassed an can now report on the nanometre relation of two fluorescent proteins. This is exactly within the scale of protein interactions and dynamics. Many factors influence FRET, and a plethora of FRET measuring approaches exist.

Therefore, **Chapter 1** broadly introduces the FRET principle and discusses the main two measuring classifications: intensity based measurements and fluorescent lifetime measurements. We discuss to what degree these methods can correctly reflect the true FRET efficiency and what experimental implications these methods have regarding control samples. Special attention is paid to the phasor analysis for fluorescence lifetime imaging microscopy (FLIM) data, as visual tool to decipher FRET. This fluorophore concentration independent graphical analysis methodology is heavily promising but is currently underused in bio-oriented research, partly due to the seeming analysis complexity. Here we provide the overview of FRET methodologies to understand how phasor separates itself from the alternative approaches.

After this introduction to FRET measuring, the aims and objectives of this thesis are stated in **Chapter 2**. Focussed on FRET biosensing with the phasor approach, we present two cases in this dissertation: intermolecular FRET and intramolecular FRET.

Firstly, in **Chapter 3**, we demonstrate a case of intermolecular FRET by investigating protein-protein interactions involved in HIV-1 integrase multimerization within assembled viral particles. The multimeric state of integrase is reported to be crucial for the protein function in integrating viral DNA into the host genome, but the exact multimeric states are difficult to track down. While currently lacking in current literature, this chapter contains a solid theoretical breakdown of the phasor approach to time correlated single photon counting (TCSPC)-FLIM with several explanatory figures. Afterwards, the principles are applied in the context of integrase multimerization. Several FPs were evaluated attached to integrase inside viral particles to investigate the effect of the local environment inside a viral particle on the lifetime signature. Our analysis was tested on simulated photon data, a labelled DNA FRET control and viral particles labelled for FRET. A detailed analysis of the integrase multimers using the FRET trajectory is supplied and broadly discussed. The importance of the fraction of

donors involved in FRET is highlighted and our findings proving multimerization past dimer formation are presented.

Secondly, we aimed at applying phasor-FLIM to intramolecular sensors. Therefore, we continued in **Chapter 4** by connecting to the field of mechanobiology. More specifically, the performance of molecular tension sensors incorporated inside vinculin, a load-bearing protein in the mechanotransduction pathway, was evaluated. Using the graphical phasor plot analysis, we demonstrated the generation of FRET efficiency images and revealed heterogeneities within focal adhesions and among mouse embryonic fibroblasts (MEF). While not only showing how transferrable the modus operandi of the phasor analysis is between Chapter 3 and 4, it highlights the straight forward generation of a FRET image from the created phasor plot.

Chapter 5 concludes this dissertation with a broad discussion on the future of the presented phasor approach to FLIM and evaluates why it is an important tool for any FLIM microscopist toolbox. The future possibilities in succession of the presented findings for integrase multimerization and genetically encoded molecular tension sensors are proposed and discussed.

For added information directed at future phasor adventurers and home-built microscopists, addendum II serves as protocol legacy. The protocols involved with measuring on the confocal and time resolved microscope that is responsible for all data presented in this thesis are explained and extra information is added for phasor analysis. It marks and explains key protocols for validation, referencing and alignment of the microscope and in doing so delivers valuable tools.

Samenvatting

Fluorescerende moleculen zijn historisch gezien al lange tijd gebruikt als indicator voor het maken van biologische beelden. Met meer geavanceerde microscopie kwam een meer complex en gedetailleerd gebruik van fluoroforen: het labelen van weefsels, cellen en subcellulaire organellen. door het gebruik van fluorescerende eiwitten die gemakkelijk door de cel zelf konden worden aangemaakt, openden zich nieuwe mogelijkheden voor wat met fluorescentie kon worden gerapporteerd. In het huidige cellulair biologisch en biochemisch onderzoek is Förster-resonantie-energieoverdracht (FRET) een onmisbaar instrument geworden om biomoleculen op nanometerschaal te bestuderen. Met behulp van FRET wordt het basale gebruik van fluorescentie-emissie overtroffen door informatie te rapporteren over de nanometerrelatie tussen twee aparte eiwitten. Deze metingen op de schaal van nanometers vallen precies binnen de schaal van eiwitinteracties en -dynamiek. Veel factoren beïnvloeden FRET, en er bestaan talloze meetmethoden voor FRET.

Daarom introduceert **Hoofdstuk 1** uitgebreid het FRET-principe en bespreekt de twee belangrijkste meetclassificaties: op intensiteit gebaseerde metingen en metingen van de fluorescentieleeftijd. We bespreken in hoeverre deze methoden de ware FRET-efficiëntie correct kunnen weergeven en welke experimentele implicaties deze methoden hebben met betrekking tot controlestalen en gebruiksmethode. Er wordt speciale aandacht besteed aan de fasoranalyse voor op fluorescentieleeftijd gebaseerde microscopie (FLIM) als visuele methode om FRET te ontcijferen. Deze grafische analysemethode, onafhankelijke van de concentratie van de fluoroforen, is veelbelovend maar wordt momenteel onderbenut in het biologisch onderzoek, mede vanwege de schijnbare analysecomplexiteit. Hier bieden we het overzicht van FRET-methodologieën om te begrijpen hoe de fasortechniek zich onderscheidt van alternatieve benaderingen voor FRET bepaling.

Na deze introductie over FRET-metingen worden in **Hoofdstuk 2** de doelstellingen van dit proefschrift uiteengezet. Gericht op FRET-biosensing met de fasorbenadering presenteren we twee gevallen in deze dissertatie: intermoleculaire FRET en intramoleculaire FRET.

Ten eerste demonstreren we in **Hoofdstuk 3** een geval van intermoleculaire FRET door het onderzoeken van eiwit-eiwit interacties betrokken bij de multimerisatie van HIV-1 integrase in geassembleerde virale deeltjes. De multimerische toestand van integrase is cruciaal voor de eiwitfunctie bij het integreren van viraal DNA in het gastheergenoom, maar de exacte multimerische toestanden zijn moeilijk te bepalen. Door het ontbreken van een complete en genuanceerde theoretische beschrijving in de huidige literatuur over de fasoranalyse voor FLIM metingen in het tijdsdomein bevat dit hoofdstuk een

solide theoretische uiteenzetting met verschillende verklarende figuren. Vervolgens worden de principes toegepast in de context van integrase-multimerisatie. Verschillende fluorescente proteïnen werden geëvalueerd in de context van integraselabels binnen virale deeltjes om het effect van de lokale omgeving in een viraal partikel op de fluorescentieleeftijd te onderzoeken. Onze analyse werd getest op gesimuleerde fotonengegevens, een gelabeld DNA-FRET-controle en in FRET-gelabeld HIV-1 virussen. Een gedetailleerde analyse van de integrase-multimeren met behulp van de fasoranalyse werd gepresenteerd en breed besproken. De nadruk werd gelegd op het belang van het percentage donoren betrokken bij FRET. Daarnaast worded onze bevindingen besproken die hogere multimerisatie dan dimeren aantonen.

Ten tweede streefden we ernaar om de fasor-FLIM techniek toe te passen op intramoleculaire sensoren. Daarom gingen we verder in **Hoofdstuk 4** door aan te sluiten in het veld van mechanobiologie. Meer specifiek werd de prestatie van moleculaire FRET-spanningssensoren ingebracht in vinculine, een cruciaal eiwit in het mechanotransductiepad, geëvalueerd. Met behulp van de grafische fasoranalyse hebben we de aanmaak van FRET-efficiëntiebeelden gedemonstreerd en heterogeniteiten binnen focale adhesies in muis embryonale fibroblasten (MEF) aangetoond. Hiermee wordt niet alleen bewezen hoe overdraagbaar de modus operandi van de fasoranalyse is tussen Hoofdstuk 3 en 4, maar het benadrukt ook de eenvoudige generatie van een FRET-beeld uit de eenvoudig bekomen fasorgrafiek.

Hoofdstuk 5 besluit dit proefschrift met een brede discussie over de toekomst van de gepresenteerde fasorbenadering voor FLIM en evalueert waarom het een belangrijk instrument is voor elke FLIM-microscopist. De toekomstmogelijkheden in opvolging van de gepresenteerde bevindingen voor integrase-multimerisatie en genetisch gecodeerde moleculaire spanningsensoren worden voorgesteld en besproken.

Voor aanvullende informatie gericht op toekomstige gebruikers van de fasortechniek en wetenschappers die werken met zelfgebouwde microscopen, dient bijlage II als protocolbron. De protocollen die betrokken zijn bij metingen op de confocale en tijdsgeresolveerde microscoop, verantwoordelijk voor alle data in dit proefschrift, worden uitgelegd en extra informatie wordt toegevoegd voor het bekomen van een correcte fasoranalyse. Het legt belangrijke protocollen uit voor o.a. validatie, referentie en afregelen van de microscoop en levert zo waardevolle hulpmiddelen.

List of Abbreviations

A	Acceptor
AFM	Atomic force microscopy
APD	Avalanche photodiode
ATP	Adenosine triphosphate
BG	Background
BHQ	Black hole quencher
BP	Band pass
D	Donor
DFD	Digital frequency domain
DFM	Dichroic filter mount
DM	Dichroic mirror
DMEM	Dulbecco's modified eagle medium
DNA	Desoxyribonucleic acid
DO	Donor-only
E_FRET	FRET efficiency
ECM	Extracellular matrix
EMT	Epithelial-mesenchymal transition
F_C	Fluorophore concentration
F_int	Fluorophore intensity
FA	Focal adhesion
FAK	Focal adhesion kinase
FBS	Fetal bovine serum
FCS	Fluorescence correlation spectroscopy
FEM	Finite element method
FFT	Fast Fourier transform
FLIM	Fluorescence lifetime imaging microscopy
FP	Fluorescence protein
FRET	Förster resonance energy transfer
FWHM	Full width at half maximum
HIV	Human immunodeficiency virus
hPMT	Hybrid photomultiplier tube
I	Intensity
IN	Integrase
INM	Inner nuclear membrane
IRF	Instrument response function
KI	Potassium iodide

LDH	Laser diode head
LINC	Linker of nucleoskeleton and cytoskeleton
LLPS	Liquid-liquid phase separated
LP	Long pass
MEF	Mouse embryonic fibroblast
MLV	Meurine leukemia virus
NADH	Nicotinamide-adenine-denucleotide
OF	Optical fibre
ONM	Outer nuclear membrane
PAA	Polyacrylamide
PAINT	Point accumulation in nanoscale toppography
PAM	PIE analysis with MATLAB
PBS	Phosphate buffered saline
PBS	Polarizing beam splitter
PCR	Polymerase chain reaction
PDA	Photon distribution analysis
PDL	Picosecond diode laser
PDMS	Polydimethylsiloxane
PEG	Polyethylene glycol
PIC	Polyisocyanide
PIE	Pulsed Interleaved Excitation
PLL	Poly L-lysin
PMT	Photomultiplier tube
RICS	Raster image correlation spectroscopy
ROCK	Rho-associated protein kinase
SDS	Sodium dodecyl sulfate
smFRET	Single molecule FRET
SP	Short pass
TAZ	Transcriptional coactivator with PDZ-binding motif
TCSPC	Time-correlated single photon counting
TL	Tube lens
TR	Time range
YAP	Yes-associated protein

Health, Safety and Environment (HSE)

All experiments mentioned in this thesis were performed in agreement with the HSE regulations as prescribed by KU Leuven. This means all personal protective equipment such as lab coats, safety glasses and gloves were worn for every action in a lab environment. Before execution of every experiment a risk assessment (RA) was made which i) describes in great detail the lab equipment, chemicals, lab hazard levels and waste streams used in experiments ii) contains an explanation of all lab activities included in the RA iii) identifies the required preventive actions. This ensures a smooth workflow in the lab for all those included in the RA and focuses on preventing incidents. In the case of an incident, clear guidelines in the RA describe the needed actions.

All biological waste of was collected in the assigned boxes for hazardous biological waste. In disposing of materials caution was taken to avoid sharp items or liquids that could leak. Extra attention was given to the correct labelling of all vessels.

An organized laser safety seminar was followed to ensure proper handling of powerful and potentially dangerous light sources within our spectroscopy labs. Around microscopes and in labs dedicated protective glasses were worn at all times when a light visible outside and inside indicated that a light source is turned on in the lab. Access to these labs was restricted to all lab members prior to following the necessary training by an experienced lab employee.

All guidelines that were followed can be found online:
https://admin.kuleuven.be/sab/vgm/kuleuven/en/riskactivities/riskassessment

https://admin.kuleuven.be/sab/vgm/kuleuven/en/environment-sustainability/waste/associatienet/

https://admin.kuleuven.be/sab/vgm/algemeen/en/procedures

Table of content

Acknowledgements v
Summary xi
Samenvatting xiii
List of abbreviations xv
Health, Safety and Environment xvii

Introduction

Chapter 1: Introduction to FRET imaging 1
1.1 Introduction 2
1.1.1 The FRET phenomenon in short 2
1.1.2 The application diversity of FRET 5
1.1.3 Absolute vs apparent FRET 6
1.1.4 The two telltale signs of FRET 9
1.2 Intensity-based FRET 11
1.2.1 Acceptor Photobleaching 11
1.2.2 Sensitized emission (SE-FRET) 14
1.2.3 Additional intensity-based FRET methods 17
1.3 Fluorescence lifetime imaging microscopy (FLIM) for FRET 18
1.3.1 Decay fitting to calculate FRET from the donor lifetime 19
1.3.2 Non-fitting approaches for FRET-FLIM 21
1.3.3 Direct FRET efficiency from phasor-FLIM 22
1.4 From single to multiplexed FRET imaging 30
1.4.1 Large Stokes shift fluorescent proteins 31
1.4.2 Dark fluorescent proteins 32
1.5 Practical considerations for FRET imaging 35
1.5.1 Sample fixation and photobleaching 35
1.5.2 How many control measurements? 35
1.5.3 FRET imaging artifacts to keep in mind 36
1.6 References 38

Chapter 2: Problem statement and thesis objectives: 49

Results

Chapter 3: Particle-based phasor-FLIM-FRET resolves protein-protein interactions inside single viral particles 53
3.1 Abstract 54
3.2 Introduction 55
3.3 Theory 57
3.3.1 Phasor approach to FLIM 57
3.3.2 Phasor-FLIM using TCSPC 58
3.3.3 Resolving mixtures of pure species 60
3.3.4 Phasors in the presence of background signal 60

3.3.5 Quenching trajectory of FRET species 60
3.4 Materials and Methods 62
3.4.1 Analysis software 62
3.4.2 Phasor cloud center 63
3.4.3 Background and passive donor fraction 63
3.4.4 FRET histograms 63
3.4.5 DNA strand hybridization 63
3.4.6 DNA experiments 64
3.4.7 Microscope 65
3.4.8 Fluorescent HIV-1 particles 67
3.4.9 Glass coating and viral particle plating 67
3.4.10 Photobleaching of viral particles 68
3.5 Results 69
3.5.1 Particle-detection-based pixel binning improves phasor-FLIM of dim particles 69
3.5.2 Particle-based phasor-FLIM resolves individual DNA molecule lifetimes 70
3.5.3 Performance comparison of single FP labeled integrase 72
3.5.4 Graphical phasor analysis reveals integrase multimers in HIV-1 viral particles 74
3.6 Discussion 77
3.7 Conclusion 81
3.8 Supporting material 82
3.9 Acknowledgements 83
3.10 References 84

Chapter 4: FRET tension sensing in vinculin using the phasor approach to time domain FLIM 89
4.1 Abstract 90
4.2 Introduction 91
4.2.1 ECM-cell interactions 91
4.2.2 Transduction towards the nucleus 92
4.2.3 The toolbox for investigating cellular forces 95
4.2.4 FLIM for tension measuring 98
4.3 Materials and Methods 99
4.3.1 Cell culture 99
4.3.2 Transient transfection of MEF cells 99
4.3.3 Fluorescence lifetime imaging microscopy 100
4.3.4 FRET analysis with the phasor approach 101
4.3.5 ROCK-inhibitor and blebbistatin 102
4.4 Results 103
4.4.1 FRET Trajectory 103
4.4.2 Measuring molecular tension across vinculin molecules 104
4.4.3 Evaluating the effect of tension inhibitors 111
4.5 Discussion and conclusion 115
4.6 References 119

Chapter 5: Discussion and future outlook 125
5.1 Phasor for intermolecular FRET 126
5.2 Phasor for FRET-based molecular tension sensors 127
5.3 The future of phasor application in FLIM microscopy 130
5.4 Popularizing home-built microscopes for biology research labs 132
5.5 References 134

Addendum I: Supplemental information Chapter 3 137

Addendum II: Protocols for a home-built confocal time-resolved fluorescence microscope 159
1 Intro to addendum 160
2 The PIE-FLIM microscope 161
3 Alignment 162
3.1 Alignment of excitation light to the objective 163
3.2 Collar ring adjustments 163
3.3 Evaluation of alignment through FCS 164
3.4 Choice of single-photon detectors 165
3.5 Pinhole alignment 166
3.6 Pixel size determination 167
4 Instrument Response Function 169
4.1 Reflection measurements 169
4.2 Potassium Iodide quenching of a dye for IRF measurements 169
4.3 Relation IRF-Pulse power 170
4.4 IRF correction for phasor analysis 171
5 References 173

Addendum III: CV 175

Chapter 1

Navigating FRET Imaging Techniques for Biological Applications

Quinten Coucke, Samet Aytekin, Sarah Vorsselmans, Steven Huysecom, Johan Hofkens & Susana Rocha

Part of this chapter is included in a manuscript in preparation for *Methods and Applications in Fluorescence* as a tutorial paper. Large study contributions were made by Q. Coucke (FLIM-FRET), S. Vorsselmans (intensity-based FRET) and S. Aytekin (multiplexing of FRET). Q. Coucke wrote the first version of the article and made the illustrations. Literature review contributions were provided by S. Vorsselmans, S. Aytekin and S. Huysecom. Prof. Rocha and Prof. Hofkens supervised the work and provided feedback.

1.1 Introduction

1.1.1 The FRET phenomenon in short

FRET is a process which occurs when two molecules, referred to as the donor and acceptor, are able to transfer excited state energy from one to another. During normal fluorescence, the electron in the excited state returns to a lower stable energy state (ground state), emitting a photon in the process. During FRET however, energy is transferred from the excited state of the donor molecule to the acceptor molecule without emission of a photon. This energy transfer occurs through a dipole-dipole resonance event on quantum scale (1). Specifically, the oscillating electric dipole of the emission transition dipole of the donor interacts with absorption transmission dipole of the acceptor, resulting in the transfer of energy. As a consequence, the donor's excited state becomes depopulated while a nearby acceptor is excited, see also Fig. 1.1 *A*. The efficiency of energy transfer, also referred to as FRET efficiency (E_{FRET}), represents the probability of energy transfer from the donor to the acceptor. The FRET efficiency is defined as

$$E_{FRET} = \frac{k_{FRET}}{k_f + k_{FRET} + \sum k_i} \quad , \qquad \text{Eq. 1}$$

where k_{FRET} is the rate constant of the additional de-excitation pathway and where the denominator is the sum of all rate constants of de-excitation pathways such as FRET, fluorescence (k_f) or any other non-radiative pathway (intersystem crossing, internal conversion, … represented as $\sum k_i$).

As mentioned above, for energy transfer to occur, the two fluorophores need to be in proximity. This implies that FRET is a highly distance dependent phenomenon. E_{FRET} relates to the inversed sixth power of the variable distance separating donor and acceptor (r) as following (1, 2):

$$E_{FRET} = \frac{{R_0}^6}{r^6 + {R_0}^6} \, , \qquad \text{Eq. 2}$$

where R_0 is the Förster radius, a characteristic distance parameter that represents the interchromophore distance at which the FRET efficiency is 50% (Fig. 1.1 *C*). It defines the operational and sensitive range of the FRET system and can be calculated as

$$R_0 = 0.211(\kappa^2 * n^{-4} * Q_D^0 * J(\lambda)^{\frac{1}{6}} \quad \text{(in Å)}. \qquad \text{Eq. 3}$$

where Q_D^0 is the quantum yield of the donor fluorophore in absence of the acceptor, n is the refractive index of the medium and κ^2 is the orientation factor. $J(\lambda)$ is the spectral overlap between the donor's emission and acceptor excitation spectra (Fig. 1.1 *D*). It is defined as

$$J(\lambda) = \int_0^\infty F_D(\lambda) * \varepsilon_A(\lambda) * \lambda^4 d\lambda \ , \qquad \text{Eq. 4}$$

with $F_D(\lambda)$ being the normalized fluorescence emission of the donor at a given wavelength λ and $\varepsilon_A(\lambda)$ the extinction coefficient at wavelength λ. $F_D(\lambda)$ is dimensionless. When the wavelength is expressed in nm, and the extinction coefficient $\varepsilon_A(\lambda)$ in $M^{-1}cm^{-1}$, then $J(\lambda)$ is defined in units of $M^{-1}cm^{-1}nm^4$. For most conventional FRET-pairs, these parameters result in an R_0-value of approximately 5-6 nm (3, 4) establishing a typical sensitive range of 1-10 nm. When selecting FRET labels to use in a biological application, multiple considerations must be taken into account to achieve measurable FRET for a chosen FRET pair. Spectral overlap, the donor-acceptor orientation, the donor quantum yield and the refractive index at the fluorophores will determine the R_0, and as such the sensitive range of the FRET pair.

Calculating FRET efficiency in biological samples can be challenging due to the difficulty in accurately determining these parameters. This can result in either leaving out these parameters or treating them as constant averages, which in turn makes it impossible to obtain true distance data. One of these parameters is the orientation factor κ^2, which defines the relative orientation between the fluorophores. κ^2 can range from 0 to 4. In a head-to-tail parallel configuration, $\kappa^2 = 4$. Considering side-to-side parallel dipole orientations, $\kappa^2 = 1$. At 90° opposite, the κ^2 factor is 0 and, according to Eq. 3, now reduces R_0 to zero. The value of κ^2 can be calculated as

$$\kappa^2 = (\cos\theta_{DA} - 3\cos\theta_D \cos\theta_A)^2 \ , \qquad \text{Eq. 5}$$

using the angles as illustrated in Fig. 1.1 *B*. In most experiments, κ^2 is unknown and an averaged value equal to 2/3 is used (5, 6). The Förster distance R_0 and refractive index n are often approximated from an experimental dataset and carried over as global parameters to other experiments while in practice these parameters vary throughout the sample depending on local influences (7, 8). The Förster distance of commonly used fluorescent protein FRET pairs can be found in (9).

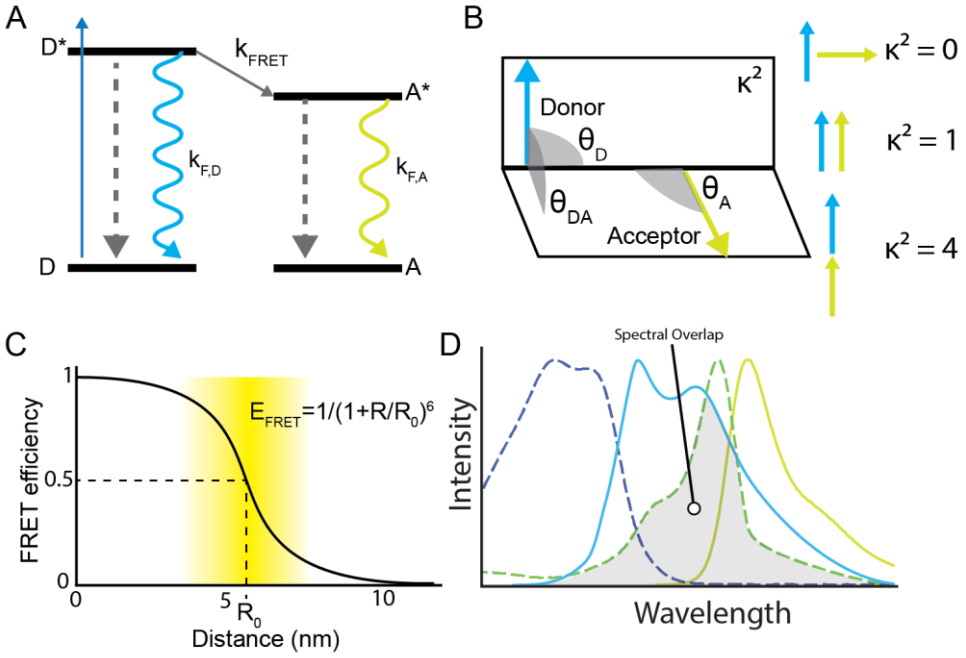


Figure 1.1: Schematics of important factors regarding Förster Resonance Energy Transfer (FRET) (A) The simplified Jablonski diagram for FRET illustrating the energy transfer of an excited state of the donor to the acceptor. When no energy is transferred, the donor can fluoresce, when energy is transferred, the acceptor can fluoresce. The rate constant of energy transfer k_{FRET} determines the process. (B) The orientation factor of the donor and acceptor transition dipoles determine whether energy can be transferred or not. Three angles (θ_{DA}, θ_D, θ_A) determine the kappa squared. (C) Plot depicting the dependency of the FRET efficiency to the distance, illustrating R_0 (D) Spectral overlap between the emission of the donor and excitation spectrum of the acceptor is required for FRET and determines, along with other factors, the R_0.

The key takeaway from the FRET theory is the following: for a given donor-acceptor pair, E_{FRET} is influenced by many parameters. Firstly, the distance between the fluorophores and secondly, the Förster radius of the FRET pair determined by κ^2, n, $J(\lambda)$ and Q_D^0. As a result, using experimentally measured E_{FRET} to precisely determine the inter-label distance poses significant challenges. However, FRET proves to be a valuable tool for investigating events where changes in the distance between the donor and acceptor, and/or their relative changes, play a crucial role.

1.1.2 The application diversity of FRET

The four primary applications of FRET are probing protein-protein interactions, assessing intramolecular FRET (FRET-based biosensors, protein dynamics,…), characterizing protein structure and assessing protein kinetics (10). This is illustrated in Fig. 1.2.

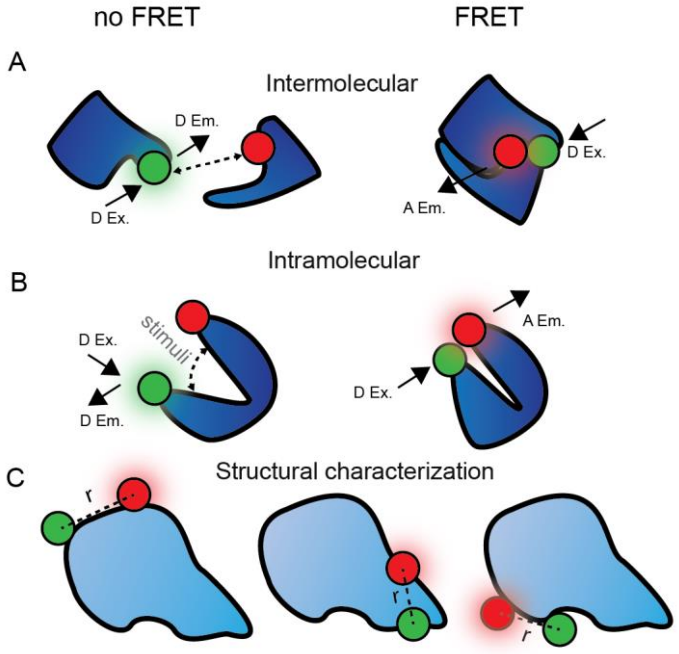


Figure 1.2: Schematic illustration of usages of FRET in modern sciences. (A) Intermolecular FRET is FRET between two separate molecules that can interact. (B) Intramolecular sensors are double labeled molecules that change conformation based on a stimuli, thereby engaging in FRET. (C) FRET for structural characterization uses extensive research to label specific sites of a protein, and determine the absolute FRET to retrieve exact donor-acceptor distance information.

Firstly, in the realm of studying interactions, FRET enables the detection of changes in fluorophore distance when the two proteins interact by labeling each interaction partner with a donor or acceptor (11–15). This type of interaction is intermolecular FRET (Fig. 1.2 *A*). Secondly, many of the FRET-based biosensors used in biology rely on intramolecular FRET, as depicted in Fig. 1.2 *B*. These biosensors undergo conformational changes (i.e. swapping open and closed protein conformations) in response to specific events, resulting in alterations in the distance and/or relative orientation between the acceptor and donor.

The most known example are Ca^{2+} biosensors (16, 17). These single chain Ca^{2+} sensors contain a calmodulin domain that changes its conformation upon the binding of calcium ions. As a bonus, the FRET efficiency can therefore be correlated to the concentration of Ca^{2+}. Other sensors can monitor pH (18) or protein phosphorylation (19), to give some examples. Another emerging branch of intramolecular FRET-based sensors with increasing application are protein or DNA tension-based biosensors (20–22). These intramolecular FRET biosensors contain a spring-like genetically encoded module or a tension-dependent unfolding DNA-hairpin between the donor and acceptor. In the case of genetically encoded molecular tension sensors, the FRET-spring is often placed within a mechano-sensitive protein inside the cell such as vinculin, talin or cadherin while DNA-based tension sensors can be applied on the outside or inside of a cell. In these cases, the tension applied along the sensor results in a changed distance between the donor and the acceptor (23–25).
As third type, FRET serves as a powerful tool for revealing structural information with nanometer accuracy (Fig. 1.2 *C*). By precisely localizing the fluorescent probes by measuring absolute FRET efficiencies, researchers can gain insights into the conformation of a given protein. This type of FRET experiments is often referred to as single molecule FRET (smFRET) and requires a quantitative analysis of the data acquired (as recently reviewed in (26)).
Apart from the usage of FRET in conformational studies, and inter- and intramolecular biosensors, FRET is also heavily used in enzyme (kinetic) studies exploring the dynamics of a system. Often, the enzyme is labeled with a donor and acceptor in active site or regulatory domain. Enzymatic activity will in many cases alter the protein conformation and as such report on the activity using the altered FRET signature. This tool can be used to evaluate the enzyme kinetics but also the enzyme-substrate or inhibitor interactions, even in real time and in living cells. For these types of FRET measurements, burst-wise single molecule FRET evaluation is commonly used. For additional reading on the diverse applications of FRET sensing we kindly refer to some extensive reviews (27, 28).
In the continuation of this introductory chapter, we will explore the tools available for these FRET applications, focusing primarily on biosensor applications while acknowledging the potential relevance of some methods in other biological applications.

1.1.3 Absolute vs apparent FRET

Calculating the efficiency of energy transfer experimentally can be a complex task due to various challenges and uncertainties. One of the primary difficulties arises from the presence of bleed-through (emission in unwanted detection channels) and crosstalk (excitation of the unwanted fluorophore) between fluorophores (Fig. 1.3 *A*). These photophysical phenomena can compromise FRET measurements,

rendering it challenging to accurately determine the actual FRET efficiency from the four measurable images (Fig. 1.3 *B*). Careful selection of fluorophores with well-separated spectral profiles can partially mitigate these effects, but it should be remembered that different overlap integrals ($J(\lambda)$) will affects the Förster distance of the FRET pair. Moreover, the measured FRET value is influenced by the ratio of active and passive FRET donors in the sample. As such, the measured donor fluorescence consists of contributions from both active FRET donors, which interact with an acceptor fluorophore causing partial donor quenching, and passive FRET donors, which exhibit unquenched fluorescence. The relative proportion of these donors contributes to the observed FRET signal, leading to challenges in achieving a straightforward and accurate quantification of the FRET efficiency for the FRET-active population. In short, an increase in measured FRET can originate from a changed stoichiometry of donor types or an actual increase in FRET efficiency (E_{FRET}) of individual FRET pairs.

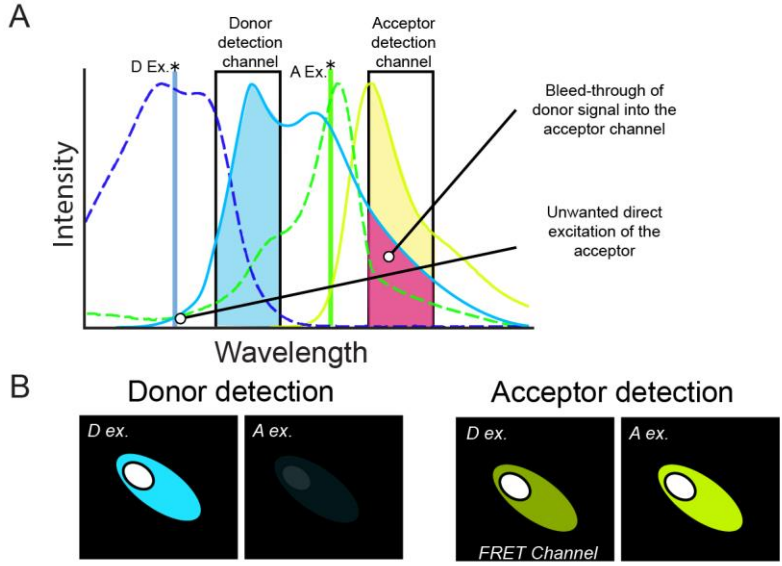


Figure 1.3: Spectrum of a CFP-YFP FRET pair in the view of intensity-based FRET measurements. (A) Visualization of excitation lines, detection windows for donor and acceptor. Marked acceptor excitation by crosstalk and donor bleed-through to the acceptor detection channel (purple) illustrate that both excitation and detection is not pure. (B) Schematic illustration of the four images that can be obtained from the FRET sample. The image obtained from acceptor excitation with donor detection will practically never contain information using a single FRET pair, and is not used in the calculation of E_{FRET}.

To overcome some of these complexities, researchers can use different methods or approaches to estimate the FRET efficiency, selecting the most appropriate technique based on the specific requirements and accuracy needed for the given

application. In general, FRET measurements can be categorized into two groups: apparent FRET sensing methods, which provide a FRET index reflecting changes in transfer efficiency, and absolute FRET methods, aiming to accurately determine the energy transfer efficiency to retrieve absolute distances between the fluorophores.

Relative FRET sensing methods are useful for detecting whether FRET is occurring and to monitor changes in FRET efficiency over time or upon changed experimental conditions. They rely on the measurement of a FRET index or apparent FRET efficiency. A wide variety of correction factors used and the exact experimental conditions often make it challenging to compare results across different research groups.

On the other hand, absolute FRET sensing methods aim for a more quantitative approach in determining the energy transfer efficiency, seeking to reflect absolute E_{FRET} and therefore retrieve accurate distances between fluorophores. However, achieving accurate measurements can be challenging, as numerous parameters are involved, some of which will need to be assumed rather than experimentally determined (29, 30). Additionally, absolute FRET is often assessed at a single-molecule level in an often strictly controlled environment (e.g. burst measurements in solution). Here, it is crucial to assess and estimate the required parameters as best as possible. Illustrating the power of absolute FRET measuring, a large-scale multi-lab benchmark study was published by Hellenkamp et al. to assess the accuracy of independent labs all set to determine the label distance of the same FRET labeled DNA sample (31). This study showed the great accuracy absolute FRET measurements can establish, despite being very complex to achieve.

Because of the difficulties involved with absolute FRET, the evaluation of FRET biosensors strongly relies on determination of an apparent FRET efficiency. The aim of these sensors is comparative and not aimed at determining exact donor-acceptor distances. Especially in a cellular context, many parameters necessary to describe absolute FRET (i.e. no accurate Förster radius because of missing information on the refractive index, kappa-factor, unknown donor-acceptor stoichiometry for an ensemble measurement). As such, FRET is most often used as a reporter, rather than an exact ruler.

This introductory chapter is focused on measuring of FRET as a relative parameter, in which we do not focus on retrieving the absolute donor-acceptor distance, but aim at evaluating FRET changes. This implies that when we deal with the FRET efficiency of a biosensor, we actually describe the apparent FRET efficiency (7). When the sample displays partial interaction of donor and acceptor labels, an apparent FRET efficiency can be calculated. As will be clear, different methods of FRET measuring will provide different levels on the scale of relative to absolute FRET efficiency determination (32).

1.1.4 The two telltale signs of FRET

As previously mentioned, the transfer efficiency (E_{FRET}) defines what fraction of the donor's excitation energy is transferred to the acceptor. Experimentally, it can be calculated by evaluation of the donor and acceptor intensity and/or the donor lifetime. Both methodologies report on the E_{FRET} since they are directly influenced by the energy transfer (Fig. 1.4 *A, B*). In the first case, FRET leads to a measurable fluorescence emission shift of the FRET pair: a higher E_{FRET} causes a drop in the donor's emission intensity as it transfers its excitation energy to the acceptor, resulting in an increase in the acceptor's emission (Fig. 1.4 *A*). For the donor, FRET offers an extra de-excitation pathway which draws energy away and reduces its energy available for fluorescence. This reduced fluorescence quantum yield offers an observable change in intensity. Monitoring these fluorescence intensity changes allows a fast, 'low-tech' measurement of apparent E_{FRET} which can be directly calculated as

$$E_{FRET} = 1 - \frac{I_{FRET\ Quenched\ Donor}}{I_{Unquenched\ Donor}}. \qquad \text{Eq. 6}$$

Here $I_{FRET\ Quenched\ Donor}$ is the donor emission in the presence of the acceptor, and $I_{Unquenched\ Donor}$ is the donor emission in the absence of the acceptor. Alternatively, FRET efficiency can also be measured by a decrease in fluorescence lifetime of the donor (1, 33, 34)(Fig. 1.4 *B*). The fluorescence lifetime is defined as the time an electron resides in the excited state (D* in Fig. 1.1 *A*) before its relaxation to the ground state via fluorescence. The added de-excitation pathway through energy transfer results in a lower average time a donor fluorophore spends in the excited state, and hence a reduced fluorescence lifetime. In other words, a long lasting excited state has an increased chance of transferring its energy and not fluoresce. Therefore the probability increases that a photon is emitted shortly after the excitation of the fluorophore. The FRET efficiency (E_{FRET}) is extracted from lifetime measurements as follows (1):

$$E_{FRET} = 1 - \frac{\tau_{FRET\ Quenched\ Donor}}{\tau_{Unquenched\ Donor}}. \qquad \text{Eq. 7}$$

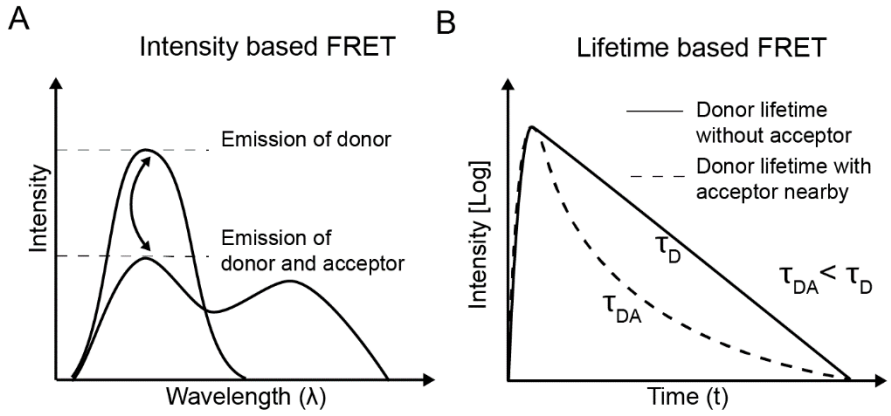


Figure 1.4: Simplified illustration of the main FRET methods. (A) Intensity based FRET compares the fluorescence of the sample with and without acceptor nearby. Full simplified emission spectrum is shown for both samples. (B) Lifetime based methods evaluate donor lifetimes in the absence (τ_D) and presence (τ_{DA}) of an acceptor. Illustration depicts time-domain FLIM.

Focus Box 1

When referring to an intensity parameter with a certain excitation, detection channel and measurement sample the notation $I^{Sample}_{Excitation\ Detection}$ is used. Donor excitation with donor detection channel (DD), acceptor excitation with acceptor detection channel (AA) and donor excitation with acceptor detection channel (DA) are possible. The superscript is used to highlight when it refers to a donor or acceptor only sample; when it refers to the FRET sample this field is empty.

Here $\tau_{FRET\ Quenched\ Donor}$ and $\tau_{Unquenched\ donor}$ are the lifetimes of the quenched and unquenched donor, respectively. Deeper insight into the principles of the FRET phenomena and measuring techniques can be retrieved from the excellent review paper of Piston et al. (35) or the more extensive literature provided by Lakowicz (1). In this chapter we will introduce the current approaches for calculating FRET efficiency experimentally, using either fluorescence intensity or the fluorescence lifetime, and highlight key concepts and common pitfalls. While we recognize the availability of methodologies that evaluate FRET through assessing purely the acceptor fluorescence or by using anisotropy (in case of HOMO-FRET), these are not included given their more niche application.

1.2 Intensity-based FRET

From the two main approaches to measure FRET efficiently, the intensity-based ones are the most popular, largely due to lower technical requirements of the user setup. As was briefly introduced before, FRET occurs when energy from an excited donor is transferred to a nearby acceptor, quenching the donor's fluorescence in the process. Hence, the efficiency of energy transfer, or FRET efficiency E_{FRET}, can be estimated using the measured donor and/or acceptor fluorescence intensity. The measurements of intensity-based FRET can be performed on any conventional fluorescence microscope that provides quantifiable signal intensities. In its most basic form, intensity-based FRET does not require any advanced hardware. However, more photon sensitive detectors will contribute to accurate FRET measurements in dim samples. To achieve a reliable intensity-based analysis, a variety of control experiments are needed (36), depending on the level of accuracy aimed at by the user. This renders it a tedious procedure.

Eq. 6 showed us how FRET can be calculated from the donor fluorescence. However, it is important to realize I_D and I_{DA} cannot be extracted simultaneously from the FRET sample. Therefore, several methods are developed to calculate intensity-based FRET, each approaching the quantification of energy transfer in a different way. Here, we will introduce acceptor photobleaching FRET (AP-FRET), sensitized emission FRET (SE-FRET) and derivatives thereof.

1.2.1 Acceptor photobleaching (AP-FRET)

A straightforward approach to calculate E_{FRET} is via acceptor photobleaching FRET (AP-FRET) (1, 37–39). In AP-FRET, donor specific fluorescence is imaged once in presence of its functional acceptor and once in absence. To achieve this, AP-FRET offers a very logical solution: the photodestruction of the acceptor, as a means to eliminate its donor-quenching properties. In doing so, E_{FRET} is calculated in the form of fluorescence emission recovery of the donor after acceptor photobleaching. To perform AP-FRET three steps need to be followed. Firstly, the sample is excited with a donor specific wavelength and the donor's emission is measured. If FRET is occurring, the measured fluorescence is partially quenched by the acceptor. Secondly the acceptor molecules are bleached without recording any emission. The photobleaching process uses a wavelength outside of the excitation spectrum of the donor to avoid donor bleaching, but within the excitation spectrum of the acceptor, to ensure precise and irreversible photodestruction of the acceptor. Lastly, the fluorescence of the donor is measured once more, using donor specific excitation, in a manner similar to the initial measurement, but the acceptor has been

photobleached. The apparent E_{FRET} is calculated using Eq. 8. This equation calculates E_{FRET} by dividing the recovered donor signal by the total donor signal post-bleaching.

$$E_{FRET} = \frac{I_{DD,post} - I_{DD,pre}}{I_{DD,post}} \left(= 1 - \frac{I_{DD,pre}}{I_{DD,post}} = Eq.6 \right) \qquad \text{Eq. 8}$$

In this formula $I_{DD,pre}$ and $I_{DD,post}$ indicate the donor fluorescence after donor excitation pre and post acceptor photobleaching, respectively.

Given the irreversible photobleaching of the acceptor in AP-FRET, this method can't be applied to a time-lapsed study or real time FRET study. Samples for AP-FRET prefer fixation protocols to avoid diffusion of the labeled proteins which can partially replenish the photobleached region of interest (ROI) in between two measurements. Even for samples in which the FRET probes don't have a diffuse character, fixation is advised to avoid any movement of the labeled structures in between images resulting in skewed FRET calculations.

Focus Box 2

It is often extremely difficult to ensure a 1:1 ratio of donor to acceptor. A measurement may contain donors which are not engaged in FRET while others are, or could contain non matured fluorophores disrupting the intended donor-acceptor ratio. This means that the calculated FRET efficiency E_{FRET} based on donor fluorescence will be influenced by the presence of unpaired donor molecules. For example, imagine 100 donor molecules in an imaged pixel and only 10 of them are in FRET range with an acceptor. When these 10 molecules have a 50% FRET efficiency state, the calculation using Eq. 8 after performing AP-FRET will result in an E_{FRET} of 5%, being the averaged value (5% of total donor fluorescence is recovered). However, the active donor-acceptor pairs that are involved in FRET actually display a 50% efficiency. This issue applies to all FRET methodologies, with exception of single molecule applications where presence of one donor and one acceptor can be measured. Therefore, it is essential for every FRET researcher to be cautious and recognize that a measured FRET signal is not a direct measure of only those FRET pairs that are interacting. See Algar et al. for more experimental caveats involved with FRET imaging (40).

Additionally, since complete photobleaching is required, low intensity excitation lamp sources found in some wide-field microscopes are often not suited, rendering a laser widefield or a scanning confocal microscope advised. The imaging-bleaching-imaging sequence can be performed manually, however some systems offer dedicated software controls for sequenced imaging and photobleaching. It is important to note that this method is sensitive to incomplete bleaching and

nonuniform bleaching. When not all of the acceptor is photodestructed, the recovered donor fluorescence will be underestimated, leading to a lower E_{FRET} measured.

Similar to other FRET measurement techniques, intensities should be background corrected per channel. For AP-FRET this means both $I_{DD,pre}$ and $I_{DD,post}$ need to be corrected for background, taken from a ROI outside of the imaged cell, for example. One benefit of AP-FRET is the fact that the sample itself serves as its own negative control, since the $I_{DD,post}$ measurement is a no-FRET sample. When the donor detection is free from acceptor emission, highly accurate E_{FRET} can be calculated without other corrections. However, it remains advised to measure additional control experiments to build confidence around the AP-FRET measurement: i) a sample only containing donor fluorophore is imaged in the full three step process, as such sample should not have an increased or decreased $I_{DD,post}$, where decreased would hint at accidental donor photobleaching, ii) a sample with co-expression of both donor and acceptor freely diffusing (where no donor recovery should be measured) or iii) a sample with a donor-acceptor tandem (fused D-A in a high FRET state, showing clear donor recovery). Here *i* and *ii* are negative controls and iii a positive control (41, 42). The donor-acceptor tandem should also be evaluated closely to ensure that the photobleached acceptor is no longer serving as FRET acceptor.

The main drawback of using AP-FRET is the single-shot type measurement, due to the photodestruction of the acceptor. To circumvent this, photoswitching FRET (psFRET) was developed as a mean to have non-destructive or reversible acceptor inactivation by photoswitching allowing to probe the donor in presence and absence of the acceptor (43). In the original paper by Subach et al., the red acceptor (rsTagRFP) can be photoswitched ON and OFF using cyan and yellow light respectively, allowing for repeated measurements of the same sample and using low intensity light to photoswitch off the acceptor, heavily reducing phototoxicity. While highly promising for live cell imaging, this method hasn't been widely adopted and remains to be further improved at the time of writing (44).

In conclusion, AP-FRET is a fast and accessible method to assess FRET that has been successfully applied, for instance in HIV-1 integrase multimerization (45). However, it has a limited range of applications since it is single-shot bound and accuracy heavily depends on full photobleaching of the acceptor. Finding the correct time required for full photobleaching is often determined using trial and error. As such, exposure time, optimal acceptor photobleaching power and wavelength can be cumbersome to pinpoint.

1.2.2 Sensitized emission (SE-FRET)

Another approach to determine FRET is the assessment of the sensitized emission of the acceptor upon donor excitation, which results from energy transfer. Sensitized emission FRET (SE-FRET) uses the difference in spectral emission profile of the FRET-pair upon donor (and acceptor) excitation to calculate a FRET ratio using two detection channels (46, 47). Many papers have been published using this method and it was perfected by adding more reference experiments to calculate additional correction factors (7, 47). To measure donor and acceptor emission profiles simultaneously, non-overlapping optical filters are used in combination with two detectors. Alternatively, the two signals can be recorded in a single detector, sequentially, swapping the filters during image acquisition. To understand the complexity of SE-FRET it is essential to be aware that the measured emission channels rarely exclusively present pure donor or acceptor signal. Bleed-through of donor emission in the selected acceptor channel and unintended excitation of the acceptor by donor excitation are often unavoidable and should be corrected. In general, in addition to the FRET sample itself, three controls are commonly used: a sample with donor only, a sample with only acceptor and a no-FRET sample with both donor and acceptor present but not interacting. Depending on whether the sample is an intermolecular or intramolecular sensor, several control samples are possible. For intramolecular sensors one could devise a mutated/blocked interaction site and for intramolecular sensors distant labeling on the protein that can never reach is a viable approach for a no-FRET sample.

To illustrate the most used approaches of SE-FRET, we consider a detection system in which the detectable spectrum is divided in two: donor detection and acceptor detection.

We first explain SE-FRET calculations used for FRET-based color coding of the image. These values reflect FRET, but are not necessarily scaled between 0 and 1, and are therefore not a FRET efficiency. In the most rudimentary form of SE-FRET, no correction factors are used. By simply dividing the intensity of acceptor channel with the intensity of the donor channel, both with donor excitation, a ratio is found only using the FRET sample, as shown in Eq. 9.

$$FRET\ ratio\ = \frac{I_{DA}}{I_{DD}} \qquad \text{Eq. 9}$$

This ratio provides a very powerful, yet simplified ‘probing’ of FRET in your sample but is widely popular as ‘quick and dirty’ FRET measurement. Evaluation over time of this ratio can report on shifts of the apparent FRET efficiency, but depends

heavily on the measurement parameters and is therefore not directly comparable with other labs/setups.

In a more robust calculation, Wouters et al. uses two extra samples to calculate an apparent FRET efficiency: a sample with donor only (I^D_{XX}) and acceptor only (I^A_{XX}) (see Fig. 1.5 *A, B*, correction factors *β* and *γ*). The equation is described as:

$$apparent\ FRET = \frac{I_{DA} - I_{DD}\cdot\beta - I_{AA}\cdot\gamma}{I_{AA}}. \qquad \text{Eq. 10}$$

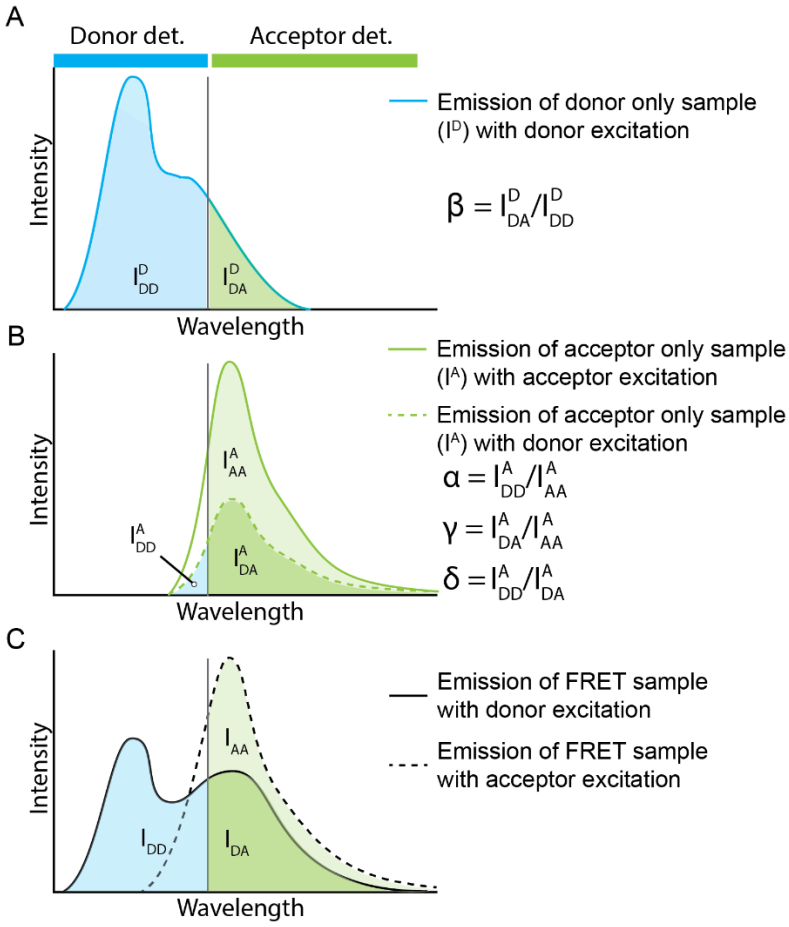


Figure 1.5: Overview of measurements required to calculate an apparent FRET value from SE-FRET, based on the Leica 2006 *Confocal Application Notes.* (A,B) Measurement of samples containing only the donor or acceptor allow the calculation of 4 different correction factors. (C) The FRET sample (containing both donor and acceptor) can be imaged with both donor and acceptor excitation.

In this equation, β corrects for donor bleed-through, and is derived from a donor only sample. And γ corrects the acceptor intensity upon unwanted direct excitation with the donor excitation laser. An even more refined calculation was proposed by van Rheenen et al. (48). They introduced two more correction factors (α and δ) derived from the acceptor only sample further improving the FRET calculation as described in Eq. 10:

$$apparent\ FRET\ = \frac{I_{DA}-I_{DD}\cdot\beta-I_{AA}\cdot(\gamma-\alpha\cdot\beta)}{I_{AA}(1-\beta\cdot\delta)}. \qquad \text{Eq. 11}$$

Importantly, in contrast to β and δ, γ and α are dependent on the relative laser line intensities to obtain the apparent FRET. Fig. 1.5 illustrates the correction factors for the presented calculations by Van Rheenen et al. and Wouters et al. (48, 49).

More recently, Coullomb et al. published QuanTI-FRET. This method allows the calculation of a more quantitative SE-FRET (50). It name stems from Quantitative Three-Image FRET and uses, as indicated, three images of the FRET sample for its calculation. The basis of the calculation is highly similar to Eq. 10 and 11. E_{FRET} is now calculated as

$$E_{FRET} = \frac{I_{DA}-I_{DD}\alpha^{BT}-I_{AA}\delta^{DE}}{I_{DA}-\alpha^{BT}I_{DD}-\delta^{DE}I_{AA}+\gamma^{M}I_{DD}} = \frac{I_{DA}^{corr}}{\gamma^{M}I_{DD}+I_{DA}^{corr}}\ . \qquad \text{Eq. 12}$$

Here α^{BT} and δ^{DE}, although named differently compared to Eq. 10, represent the correction factors for donor bleed-through and unwanted direct excitation of the acceptor. γ^{M} represents the correction factor for the different detection efficiencies in both donor and acceptor detection channels. The equation is simplified by grouping the corrected sensitized emission (FRET channel) as I_{DA}^{corr}. The correction factors are calculated from additional donor-only or acceptor-only samples as follows:

$$\alpha^{BT} = \frac{I_{DA}^{D}}{I_{DD}^{D}}\ , \qquad \delta^{DE} = \frac{I_{DA}^{A}}{I_{AA}^{A}} \qquad \text{Eq. 13}$$

The correction factor γ^{M} and β^{X} (β^{X} is required for FRET stoichiometry analysis and corrects for different energy absorption in the detection channels) cannot be determined from the donor-only or acceptor-only samples. Instead, they are retrieved from a fitting algorithm where the experimental data ($I_{DD}, I_{DA}^{corr}, I_{AA}$) is fitted to a 3D plane. When the donor-acceptor stoichiometry is unknown, an additional experiment is needed with known stoichiometry (S) to calibrate the fitting. The equation of the plane is described by

$$\beta^X \gamma^M I_{DD} + \beta^X I_{DA}^{corr} = \frac{S}{1-S} I_{AA} \quad \text{Eq. 14}$$

Note that other research groups have proposed further alternative calculations involving up to nine images to correct the calculated sensitized emission FRET values (36). Advised additional literature on advanced SE-FRET approaches can be found in Kaminski et al. and Broussard et al. (41, 51) and papers covering the 'three-cube method' approach to FRET (52–54).

Clearly, SE-FRET offers a wide toolbox for quantification of FRET, ranging from crude to more refined. While the quantitative possibilities and its applicability in confocal and widefield microscopes are direct advantages, the required measuring of (at least) three samples is a complication.

1.2.3 Additional intensity-based FRET methods

Another intensity-based FRET approach is spectral FRET (sFRET) (55). With sFRET, a FRET system can be probed using the measured spectra (per pixel) using , for example, a single detector that scans the sample per wavelength using donor specific excitation (as opposed to dividing emissions into a two channel measurements for classical SE-FRET). This approach, similar to SE-FRET, determines a ratio of both donor and acceptor emission. Importantly, in sFRET this ratio is quantified by the amplitude of the donor and acceptor emission peak in the measured spectra. With the added input of control sample spectra, unmixing of the FRET spectrum leads to a FRET quantification. The main challenge of sFRET involves correcting the signal bleed-through (SBT). While the donor SBT can be determined by linear unmixing, acceptor SBT is very challenging as the direct but unwanted excitation of the acceptor by the donor laser can't easily be differentiated from FRET related acceptor excitation. To further resolve such problems computational algorithms have been developed (56). In 2008, Wlodarczck et al. presented a new methodology called lux-FRET (57). This method seeks to decompose the measured total spectrum into a sum of previously measured spectra of donor and acceptor also determining the fractions of incomplete labeling for donor or acceptor and the effect of unpaired donor and acceptor labels onto the calculated FRET efficiency. Additionally, SensorFRET improves on classical sFRET and lux-FRET methods by presenting an intensity independent methodology which does not require single fluorophore standards to be measured. This results in an improved imaging speed and allows illumination levels to be tuned to FRET labels present (think about the heterogeneous levels of FRET biosensor expression seen in in-vivo experiments)(58).

1.3 Fluorescence Lifetime Imaging Microscopy (FLIM) for FRET

As previously mentioned FRET leads to a decrease of the fluorescence quantum yield of the donor. Due to the added de-excitation pathway via energy transfer, the excited state of the donor depopulates at a higher rate. This reduces the time an electron spends in the excited state and results in a reduced fluorescence lifetime of the donor.

The fluorescence lifetime is a characteristic property of a fluorescent molecule. In contrast to fluorescence intensity, the lifetime of a molecule does not depend on the local concentration of the fluorophore or on the intensity of the excitation light. Additionally, the fluorophore concentration independence makes the fluorescent lifetime largely robust against photobleaching artifacts. For a homogeneous FRET sample, the determination of the fluorescence lifetime of the donor allows for the direct quantification of E_{FRET}, but requires advanced microscopy equipment such as a pulsed or modulated light source and a gain-modulated detector or a time correlated single photon counting device (TCSPC). The time-dependant detection of fluorescence in a sample is called fluorescent lifetime imaging microscopy (FLIM) and can generally be executed in either frequency domain (FD-FLIM) or in time domain (TD-FLIM). Generally, in frequency domain a modulated excitation light source is used giving rise to a fluorescence signal yielding a phase shift and demodulation. These characteristics are subsequently converted to a lifetime (34, 59, 60). In TD-FLIM an excitation laser is pulsed at a high frequency and emission photons are timed and registered by single-photon detectors. A time correlated single photon counting (TCSPC) device is used to synchronize signals from both laser driver and photon detector and can accurately time-tag every incoming photon. The assembly of all time-tagged photons is used to create a photon arrival histogram, also called the fluorescence decay. Although historically frequency domain was more popular due to the lower technical requirements (a modulated light source and detector), currently, time-domain (pulsed laser with single photon detectors) has become equally widespread. For the experiments that are more time dependent (i.e. live cell FLIM imaging with high sample dynamics), often (wide-field) FD-FLIM is used with a fast camera detector (61–63). While TD-FLIM measurements are more used in confocal systems to achieving higher spatial resolution. It is important to note that both TD-FLIM and FD-FLIM need to be calibrated for their instrument response function (IRF), which is a contributor in any time-dependent measurement and reflects the total instrument response time of a processed detection event.

The fluorescence lifetime calculated for a donor signal can be used, as shown in Eq. 6, to calculate the FRET efficiency. While the fluorescence lifetime of the donor

can be a direct readout for the amount of energy transferred (64), it is often obscured by other measuring factors. In general, the fluorescence lifetime can be influenced by other, non-FRET factors in the immediate vicinity of the fluorophore: temperature, pH or other nearby quenchers can severely affect the lifetime readout. Therefore, in parallel to controls for intensity-based FRET, it is also advised to always determine the donor lifetime without a nearby acceptor. In the following sections we focus on TD-FLIM strategies to determine lifetimes, and thus FRET. In TD-FLIM, the lifetime of the fluorophore is retrieved from the fluorescence decay, using exponential curve fitting or non-fitting approaches.

Due to its growing popularity, we will place the non-fitting phasor approach to FLIM and FRET in the spotlight. For readers interested in the frequency-domain approaches, the book chapter published by Clegg et al. on real time fluorescence lifetime imaging for FRET applications is recommended (65).

1.3.1 Decay fitting to calculate FRET from the donor fluorescence lifetime

As previously mentioned, time-tagged photon information from TD-FLIM forms the arrival time histogram, a.k.a. the fluorescence decay (1). The fluorescence decay visualizes the probability of a photon emission event at a certain time after the excitation pulse. This decay can be fitted with one or more exponential functions depending on the number and characteristics of the emitters contributing photons to the decay. The y-axis of the exponential fluorescence decay is often displayed using a logarithmic scale, rather than a linear scale. In this representation, a single exponential is visualized as a straight line and its slope ($-1/\tau$) directly reveals the lifetime (Fig. 1.6 *A*).

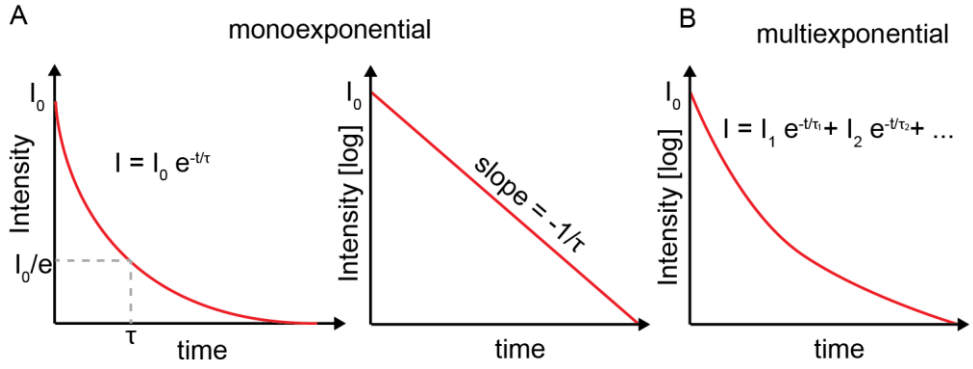


Figure 1.6: graphical representation of a mono- and multiexponential fluorescence decay. (A) A monoexponential decay can be viewed in a linear or logarithmic representation (B) a multiexponential decay can be presented as the sum of its parts.

For measurements with more than one contributing exponential, a multiexponential fitting model is used that determines the optimal fit for the recorded curve attributing a percentual contribution to every exponential (Fig. 6 *B*). For FRET experiments, each pixel can contain a mixture of donors participating in FRET, and donors not engaged in FRET. This means that the fluorescence decay will always have at least two components and, consequently, a multi-exponential fitting model is used (61, 66). More complex cases can occur when a FRET sensor can take any state in between low and high FRET (more than two states are possible). Importantly, when more fluorescent contributors (or FRET states) need to be disentangled, more photons are needed to realize such analysis. To obtain a successful fit, the instrument response function needs to be measured separately, so it can be used in the fit model. Additional samples next to the FRET sample itself are a sample with only donor (negative control delivering τ_D in Eq. 6), and optionally, a positive control with maximum FRET (like a tandem construct).

Generally, fitting approaches can be subdivided in non-linear least-squares (NLS) fitting and maximum likelihood estimation (MLE). Within NLS methods the two main methods are pixel-level fitting and global analysis. The most adopted fitting approach for FLIM-FRET is pixel-level fitting. This method assumes the presence of a mixture of both FRET active (quenched form) and FRET passive (not partaking in FRET) donors per pixel. As such, a bi-exponential fitting model is used to reveal the component lifetime and each of their fractional amplitudes. Importantly, this is only a correct approach when the donor exhibits a monoexponential decay, which is not always the case (e.g. CFP). Pixel-per-pixel nonlinear approaches to FLIM analysis are commonly slower since the image analysis is dependent on the number of pixels that need fitting. Secondly, aiming at fast analysis, the global analysis approaches to FLIM globalizes the fit using a model that assumes a constant lifetime for donor molecules that take part in FRET (active donors) and those that are not (passive donors) across the whole image (61). This bi-exponential model with only pixel-to-pixel fractional amplitude variations is often an oversimplification but can provide fast analysis results. For both the NLS approaches, the minimization problem of the chi-squared surface can be a troublesome computational challenge which can get stuck in a local minimum. However, improvements have been offered to decrease computational time by using the image morphology to pre-inform the fitting algorithm (67) or optimizing the required computing power (68). For FRET-based (bio)sensors the usage of global fitting doesn't allow heterogeneous imaging of the FRET efficiencies but will rather supply (non-quantitative) information a fraction of donors in FRET. This can still be useful if the biosensor has a well characterized on-or-off state (68).

The second type of decay fitting approaches utilizes a maximum likelihood estimation (MLE). This approach estimates the fluorescence lifetime of a sample by maximizing a likelihood function to determine the lifetime parameters most

consistent with the measured time-tagged photons. In short, the lifetime is extracted by comparison of the probability distribution function, evaluating the number of photons registered in each TCSPC bin. While a dedicated approach is developed using intensity-based FRET with MLE (69), the application of MLE strategies to FLIM data are also well studied (70). NLS (pixel-wise and global analysis) will assume gaussian noise with fixed variance across pixels. Contrary, MLE will estimate Poisson-distributed noise (71) and use intensity integration across several time windows to retrieve lifetime estimates. This approach is capable of resolving true lifetimes with $1/5^{th}$ of the photons compared to NLS in analysis with limited photons (61, 72, 73).

1.3.2 Non-fitting approaches for FLIM-FRET

Non-fitting approaches for FLIM-FRET allow for direct evaluation of the lifetime components and/or their fractions in a sample. These direct approaches allow faster acquisition and open up possibilities for further in-vivo research or FRET experiments. Firstly, Rapid lifetime determination (RLD) (74) integrates the fluorescence signal two or four several time gates, for a mono or bi-exponential analysis respectively. By largely under sampling the decay, this fast methodology, based on time-gated FLIM, is not suited for multiexponential decays. Secondly, the minimal fraction of interacting donor (mf_D) approach (61, 74–76) is used to retrieve information on the minimal percentage of donors involved in FRET. As such it provides a tool to monitor changes in e.g. protein-protein interactions. Importantly, this methods relies on a narrow distribution of the FRET efficiency which is not always the case. Lastly, the phasor analysis offers a direct interpretation of lifetime information as lifetime species are sorted in a 2D phasor plot, allowing for graphical interaction with the lifetime data. Fractional analysis and FRET-trajectories can be applied on the plot to learn about the sample heterogeneity (74). In the next section we will broadly introduce the phasor approach for FLIM-FRET.

1.3.3 Direct FRET efficiency from phasor-FLIM

In this thesis I have explored the phasor analysis to quantify FRET. This method has proven to be versatile for general FLIM imaging and can deliver a fast FRET quantification in a relative or absolute manner as well as provide cues on the fractions of involved species. We will first introduce the phasor approach to FLIM and thereafter discuss the extraction of FRET efficiency information.

1.3.3.1 Phasor approach for FLIM

Phasor, a blend of ‘phase’ and ‘vector’, was originally developed for frequency domain FLIM (FD-FLIM) data. For FD-FLIM, a modulated light source and modulated detector are used to measure the emission which yields the same frequency as the excitation light. During the analysis of FD-FLIM data, the recorded fluorescence signal is analyzed in comparison to the modulated excitation light. In doing so, the phase-shift and demodulation of the fluorescence retrieves lifetime information of all contributing frequency components (34, 65, 77–84). Generally lower spatial resolutions are obtained with a camera-based FD-FLIM setup. Therefore, it is a popular approach for highly dynamic FLIM samples, often expressed in living cells (i.e. FLIM measurements of EPAC sensor (85)).

Focus Box 3

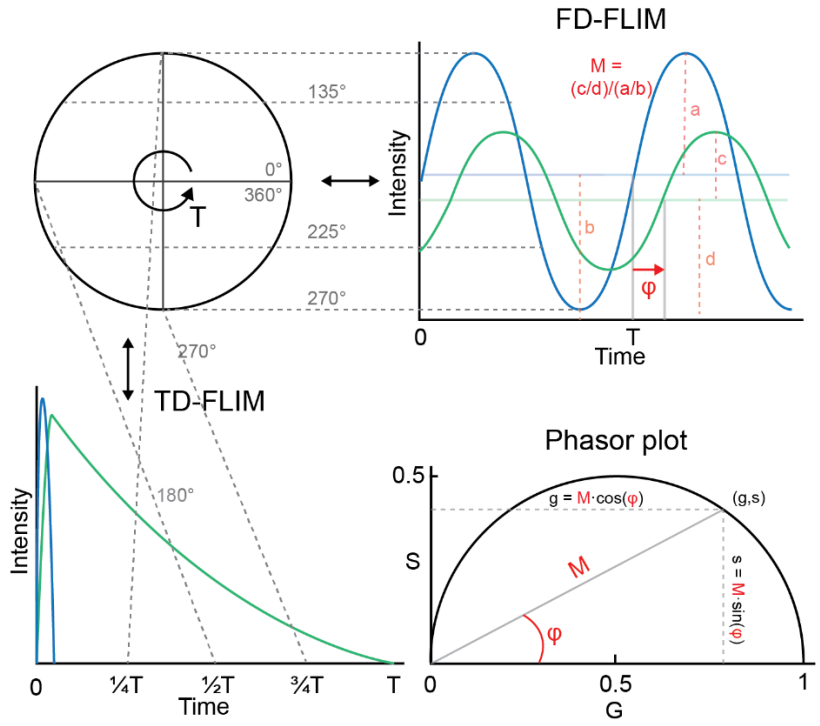


Figure 1.7: Schematic of TD-FLIM and FD-FLIM and their relation to a periodic signal and the phasor plot. Blue depicts the excitation light, green the sample emission.

A rotating vector can be used to illustrate the FLIM approach to phasor using the time period T. For TD-FLIM, the time period T is the laser pulse window, for FD-FLIM, the period T is one period of the excitation sinusoidal. From FD-FLIM, a **phase-shift** (φ) and **demodulation** (M) are calculated to directly determine a phasor point (g,s) in the phasor space representing the lifetime of the measured signal. TD-FLIM signals are equally repeating signals and can also be transformed to the phasor space. While the FD-FLIM is readily transformed to the phasor space using φ and M, the TD-FLIM fluorescence decay is transformed into the Fourier sine (s) and Fourier cosine transform (g).

TD-FLIM, based on TCSPC measurements, has the advantage of being suited for dim measurements, owing to its single photon detection. A high signal to noise ratio, and a high temporal resolution (1-20 ps) contribute to the accurate lifetime determination of short (1/2 ns) to long (+10 ns) lifetimes. However, the slow accumulation of sufficient photons and the limited count rate due to pile-up are persistent drawbacks. On the other hand, FD-FLIM is a lower-cost, fast lifetime imaging tool with no intrinsic count rate limit (not regarding camera saturation). The main limitations of FD-FLIM are the lower spatial resolution (using camera based systems) and the smaller applicable lifetime range.

The group of Digman et al. have re-popularized the phasor plot representation for FLIM in 2008 (86). While originally developed for frequency domain data (84, 87), time-domain data can be analogously used for phasor analysis (88). Instead of a modulated excitation source and detection scheme, a periodically pulsing laser is used in combination with TCSPC/time-tagging. The phasor for time domain is a transformation of photon arrival times to frequency space. A visual trick to understand the phasor representation for TD-FLIM is to think of the universal circle (radius 1 and centered at (0, 0)) as the full period of the laser repetition (Fig. 1.8 *A*). Assuming every photon is assigned a single phasor, we now visualize a rotating phasor which covers all TCSPC bins (N bins) in a full rotation of the universal circle, or 2π. This means that the universal circle contains N points, each separated by 2π/N radians. When every photon in a phasor is allocated a point on the universal circle, the pixel-phasor is the averaged location.

The decay (for TD-FLIM) or phase and demodulation parameters (for FD-FLIM) of every pixel is transformed into a single point in the phasor plot practically sorting the pixels based on lifetime information in a 2D histogram, see also Focus Box 3. In the phasor plot, the x and y-axis represent the sine and cosine Fourier transforms of the fluorescence signal, also named s and g. The phasor semicircle is the half circle with middle point (0.5, 0) and radius 0.5, spanning from (0, 0) to (1, 0), see also Fig. 1.8 *A*. A decay with a monoexponential lifetime has a unique location on the semicircle line itself. Here, all mono-exponentials are sorted on the semicircle with the infinite lifetime at (0, 0) and the 'zero' lifetime at (1, 0). Thinking of TD-FLIM, an infinitely long lifetime will result in a near-equal amount of photons in all bins on the universal circle, leading to an average position that is indeed (0,0).

When a pixel contains two exponentials, the resulting phasor location of the two contributors, which would each lie on the semicircle, is found on the line connecting both. From the location of the phasor on this line, the photon intensity fraction (f_n) of each monoexponential can be retrieved (Fig 1.8 *B*). Analyzed pixels with three or more exponential signals are similarly linear combinations of the semicircle locations weighted for their photon fraction (Fig. 1.8 *B*). However, from the moment a signal contains more than one exponential, the resulting phasor is no longer unique but can be the result of many different combinations. Therefore, knowledge of the contributing exponentials is imperative to unmixing. With pure monoexponential species having their unique location on the semicircle, and multiexponential combinations of those pure species occupying the inside of the semicircle, the outside of the semicircle is reserved for non-exponential contributions (i.e. a reflection peak in the detection path). Such non-exponential contribution within the measured signal can therefor throw off the analysis and should always be avoided or taken into account as it can misplace the phasor location of a targeted species.

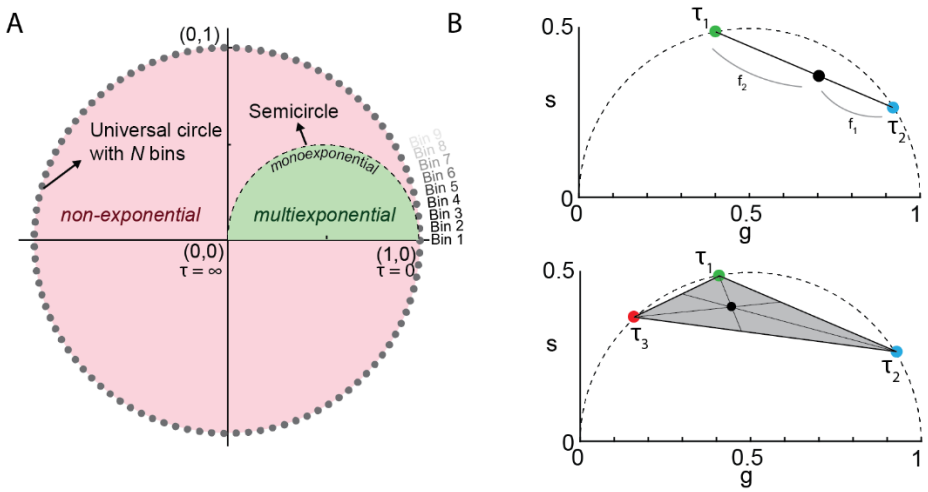


Figure 1.8: (A) The universal circle from the viewpoint of TD-FLIM. (B) Illustration showing how a bi-exponential and tri-exponential relate to their pure monoexponential contributors.

Further explanation of phasor theory for TD and FD FLIM can be found in the ISS phasor tech note (89), in a paper on three-probe multiplexed lifetime phasor by Rahim et al. (90), an extensive *nature protocols* paper by Ranjit et al. (91) and our own work on particle-based phasor analysis which includes a broad theoretical explanation and is included in this dissertation in Chapter 3 (11). The phasor method is interesting as it allows the 'sorting' of FLIM pixels rather than applying a strenuous fitting algorithm. The true power of using phasor analysis is to visually sort the lifetime signatures of pixels allowing graphical unmixing and identification clusters of similar apparent lifetimes which can be directly related back to pixels in the image.

1.3.3.2 Evaluating FRET in the phasor plot

Interestingly, FRET efficiencies can be estimated from the phasor plot without the need of deriving absolute lifetimes. In any case, a phasor analysis does not require more photons than conventional NLS fitting. Therefore it can be applied to experiments with relative high FRET dynamics or dim fluorescent samples such as FRET biosensors with fluorescent proteins (1, 11, 92).

In phasor analysis of a FRET sample in which we know there is only an on-or-off state, analyzed pixels will all contain a mixture of unquenched donor and quenched

donor (all quenched to the same degree) resulting in a bi-exponential decay. The resulting phasor position will be found on the line connecting both single-exponential positions from the unquenched donor and the quenched donor on the semi-circle as illustrated in Fig. 1.8 *B*. Here fractions of the active and passive FRET donors can be retrieved using the fraction line. While in many analysis cases, the analysis is steered towards a FRET and no-FRET biexponential interpretation, FRET biosensors can often accommodate many intermediate FRET states. Hence a continuous approach, such as offered by phasor analysis is highly interesting.

Acquiring the lifetime of the unquenched donor (Fig. 1.9 *A*) is the starting point of any FRET analysis to fix the no-FRET value. In a perfect case where all donor molecules with a certain lifetime τ_D would exhibit perfect quenching (i.e. homogeneous quenching of all donors without background signal), the resulting phasor would be found on the semicircle (τ_{DA}) further shifted towards the position with a 'zero' lifetime (1, 0). The accumulation of all possible FRET states of τ_{DA} in perfect quenching is represented by the FRET trajectory (Fig. 1.9 *B*). In this perfect case, all possible phasor points resulting from the full 0 % to 100 % E_{FRET} range are located on the semicircle. Since the phasor points are located on the semicircle, a lifetime can be calculated (see Eq. 6) or, E_{FRET} is readily obtained from the FRET trajectory. In reality, the signal is convoluted with the autofluorescence signal of the sample and/or background. For cellular imaging, such autofluorescence needs to be taken into consideration when calculating the FRET efficiency using phasor. The contribution of autofluorescence makes the measured donor-only phasor position slightly inward of the semicircle (linear combination of a point on the semicircle and the multiexponential autofluorescence signature inside the semicircle, Fig. 1.9 *C*).

As depicted in Fig. 1.9 *D*, the background signal (BG) also affects the FRET trajectory. When a donor has a near fully quenched state, its fluorescence output/quantum yield is equally decreased. Therefore, photons from BG become a larger fraction of the signal with increased E_{FRET}. Hence, the FRET trajectory curves back onto the location of BG for high FRET (Fig. 1.9 *D*). Now, the FRET trajectory is the calculated result of many fraction lines: all possible combinations of BG (with a fixed phasor location) and the a quenched donor τ_{DA} (with a varying location depending on the lifetime). Additionally, there might be donors present in the pixel which are not actively participating in energy transfer (passive donors, Fig. 1.9 *E*). The FRET trajectory is influenced because now the remaining donor signal (and BG) persist when all active donors are increasingly quenched. Contrary to Fig. 1.9 *B*, the FRET trajectory is not on the semicircle anymore, making it impossible to determine a single lifetime for a point on the trajectory. However, the trajectory itself remains a direct ruler to determine E_{FRET}. This is possible, because we can graphically unmix the measured signal (red dot in Fig. 1.9 *F*) in a combination of FRET donors with lifetime τ_{DA} and the combination of BG and the passive donors. When the autofluorescence is known, the fraction line can be drawn through BG

and the measured phasor (red dot) to reveal τ_{DA}.The distribution of FRET efficiencies on the FRET trajectory does not display a linear spreading since the relative BG contribution increases rapidly with increasing FRET due to its lowered donor fluorescence quantum yield resulting in big jumps on the trajectory for higher end FRET efficiency changes.

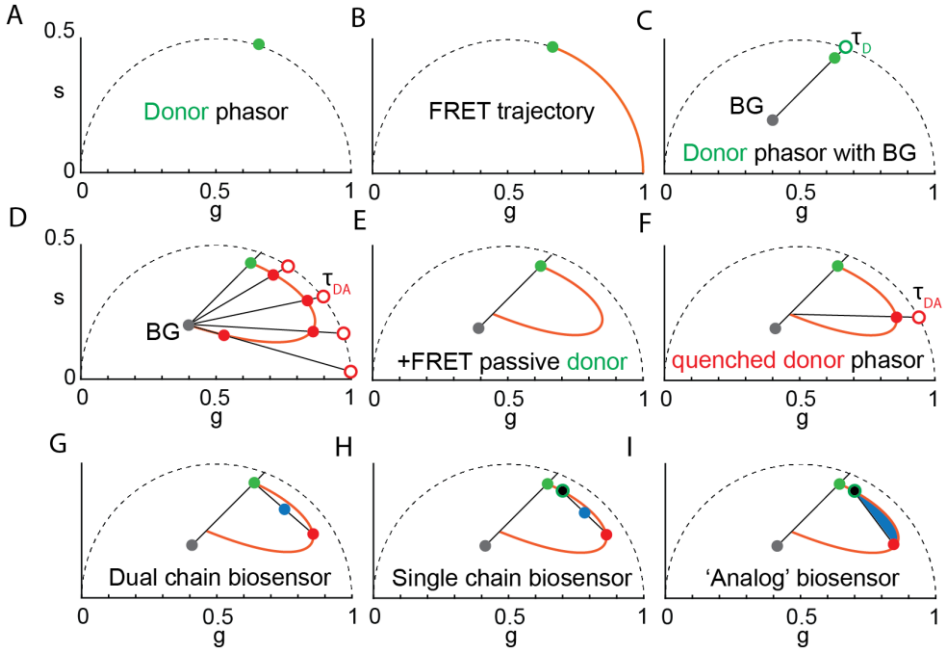


Figure 1.9: Overview of FRET trajectory construction in the phasor plot. (A-F) Iterations to construct the FRET trajectory in the phasor plot. Dotted line: phasor semicircle; orange line: FRET trajectory; green dot: donor only phasor; black line: fraction line ; gray dot: autofluorescence and background location (BG); red dot: phasor a (homogeneous) FRET state; red hollow dot: pure FRET state lifetime (G) FRET trajectory for Dual chain FRET sensors. Blue dot: phasor of a measurement containing a mixture of FRET sensor states (H) FRET trajectory for single chain FRET biosensors. Green/black dot: minimal FRET state of the FRET sensor (I) FRET trajectory for 'analog' FRET biosensors which have a continuous range of possible FRET states. Blue region: area that will include all possible phasors for a pixel containing various FRET states.

To unlock the full potential of FRET analysis using the FRET trajectory, it is important to distinguish 3 main types of FRET sensors: i) dual chain sensors, which have a 1-on-1 on/off FRET state where donor and acceptor are labelled upon the complementary proteins. (e.g. studying protein-protein interactions(13)), ii) single chain sensors with only an open or closed state/conformation (e.g. cAMP FRET sensors to detect calcium ions (93, 94)), and iii) single chain sensors with multiple FRET states (e.g. tension sensors (95)). In case of dual chain FRET biosensors

the free or bound state of the sensor makes the measurement of a heterogeneous pixel a linear combination of the donor only and the FRET-state (green and red dot in Fig. 1.9 *G,* respectively), which are measured in control samples separately. Using a fraction line (black line) the photon fractions of the measured phasor (blue dot) can be retrieved. For single chain biosensors, even in the non-active state, the donor and acceptor might be in close proximity, allowing a degree of FRET. This means that the longest lifetime measured is still shorter than that of free donor. Hence, the fraction line should start in the phasor determined by a control that does not 'close' the single chain biosensor conformation (green/black dot in Fig. 1.9 *H*). Fig. 1.9 G and H present a digital view of FRET, since only two possible states, high and no/low FRET are expected. Lastly, when such single chain biosensor can be in many different FRET states ('analog'), the expected phasor of such measurement falls within the region defined by the FRET trajectory and the fraction line (blue region in Fig. 1.9 *I*). The FRET efficiency of a phasor is now estimated by looking at the nearest point of the FRET trajectory to obtain an averaged view on the pixels' FRET heterogeneity. Importantly, this approach needs to be well considered. In case of tension sensors, while the sensor may display FRET heterogeneity throughout the image, within a pixel this is not expected. This effectively reduces the possible phasor region. Additionally, for many sensors the FRET activity if often assumed to be affecting all sensors in the pixel (no passive donors), simplifying the analysis, but reducing quantitative information. This is largely due to the inability to quantify the fraction of passive donors and makes any FRET efficiency obtained with the phasor plot is a measure of apparent FRET, not absolute FRET reflecting true donor-acceptor distances. However, the phasor approach is an excellent and visual tool to interpret changes and evaluate FRET using the FRET trajectory.

1.3.3.3 Extensions on the Phasor approach

For completeness, several adaptations have been proposed for phasor-FLIM and FRET. 3D multispectral phasor analysis and Phasor-S-FLIM have been proposed to analyze multi-labeled FLIM or FRET samples by considering the emission wavelengths as third dimension in the phasor analysis (96). Both show improved unmixing capabilities leading to more accurate determination of FRET, also for FRET biosensor analysis (97). Another phasor derived improvement for FLIM-FRET is the rapid multi-beam confocal FLIM which allows for fast imaging of biochemical dynamics (98). Phasor-based global analysis can be widely implemented in research studies such as cell arrays, maximizing the spatial characteristics of phasor (99). The global analysis originally developed for frequency domain FLIM data has also been applied to TCSPC exploiting the usage

of the phasor plot in combination with a bi-exponential model for FRET-FLIM experiments in intact cells (100).

1.3.3.4 Decay fitting vs Phasor for FLIM

A thorough evaluation between fitting and non-fitting (phasor) analysis strategies has been published by Leray et. al. (60). Clearly, both strategies are viable in the absence of background. However, once some background photons are present, think about autofluorescence of the cell, the phasor approach proves more reliable as it allows to take these factors into account when constructing the trajectory. For a fluorescence decay fitting algorithm, fixing the background as a contributing parameter or fraction requires the marking of this contribution with its lifetime. This is a highly difficult task, as autofluorescence is often low intensity and almost always highly multiexponential. For FRET applications, phasor analysis provides the additional advantage over decay fitting of not requiring the computation of absolute lifetimes. However, phasor is not capable of solving all measurement issues: i) the autofluorescence is estimated from other measurements and is treated as a constant across the analysis of all pixels, and ii) the graphical analysis still implies a 'model' of the measured signal. A summary of available software for FLIM-FRET analysis, limitations and advantages and more is provided in Table 1.

Table 1: Brief FLIM-FRET overview

Technique	Advantages	Limitations	FRET Calc	software
Fitting-based algorithms	Fast crude calculations	Advanced calculations are slow, Global fitting is crude 'forced' fitting	Most often bi-exponential fit leading to a single 'FRET' lifetime.	• Lasx/symphotime64/… • FAST (https://www.edinst.com/products/fast-software-advanced-lifetime-analysis/) • DecayFit (www.fluortools.com/software/decayfit) • FLIMFIT (https://flimfit.org/) • PAM (101) • SPCImage (102)
Phasor approach	Relative fast and flexible, no need to pinpoint 'a lifetime' for FRET	Advanced setups / high cost	Multiple analysis possible, relative FRET efficiency estimates can be obtained without the need of determining FRET lifetimes.	• GLOBALS (https://www.lfd.uci.edu/globals/) • Lasx/symphotime64/… • SPCImage (102) • ImageJ/Fiji plugin by Farzad Fereidouni • PAM (101) • FLUTE (103)

1.4 From single to multiplexed FRET imaging

Since their development, FRET (bio)sensors led to a deeper understanding of a vast variety of biological phenomena at the nanometer scale. However, most biological processes do not operate secluded but instead through interactions within the complex network of biochemical and biophysical pathways. Being able to measure multiple phenomena at once is therefore an active research field. However, the simultaneous use of multiple biosensors was technically hard to achieve. Due to the recent advances in imaging technologies and the development of new probes, multiparameter imaging with multiple FRET systems has become possible.

Regardless of the chosen FRET measuring methodology, measuring pure donor or acceptor emission is often crucial. More fluorophores will crowd the useable spectrum and will create challenges to maintain pure fluorophore emission signals. Using more than one traditional FRET pair results in the significant spectral overlap between the pairs that gives rise to crosstalk and bleed-through, resulting in unwanted spectral overlap. For this reason, initial research aimed at increasing the number of usable fluorophores within the working spectrum by development of new fluorescent proteins to fill the gap between yellow and red FPs (e.g., mOrange (104)) or to utilize the unconventional regions of the visible spectrum such as the violet region (e.g., TagBFP (105)) and far-red range (e.g., mPlum (106)). However, such approaches came with further complications such as: i) the spectral overlap of orange fluorescent proteins with the commonly used CFP/YFP and GFP/RFP pairs, ii) increased autofluorescence and phototoxicity by using blue/violet excitation wavelengths and iii) the lower quantum yield, low folding efficiency and long maturation time of far-red proteins. While some of these proteins and their derivatives have been used for dual-FRET purposes (107, 108), this multiplexing approach suffers from the bleed-through of the first acceptor into the emission channel of the second donor. Additionally, multiple excitation wavelengths can require sequential imaging in case of intensity-based FRET imaging, making the application slower and less compatible with live cell imaging. For FLIM, it is possible to explore pulsed interleaved excitation (PIE) to efficiently excite both donors (109).

Another early attempt to reach multiplexed systems for FRET-pairs was to combine multispectral imaging with a computational approach to decompose the detected signal into the different fluorescent emitters. Using linear unmixing, the measured signal is modeled as a linear combination of the individual florescence signals (110). Similar to the approach in spectral FRET, the spectral profile of each molecule in each detection channel is obtained individually. Linear unmixing can be performed in two ways: a single excitation wavelength is applied to each fluorophore and the emission is collected at multiple detection channels

(simultaneous detection) or multiple excitation wavelengths are applied to collect the emission in a single detection channel (sequential detection). The latter is ideal for set-ups that allow fast switching of the excitation light (111). However, linear unmixing requires a highly accurate spectral fingerprint for each fluorescent molecule in the actual measuring sample environment and any error in this reference data can lead to inaccurate decomposition. And lastly, linear unmixing is a highly noise-sensitive method; the error in the processed image increases with the increasing number of detectors due to higher percentage of noise in the final readout. Regardless, this method had been successfully applied to separate two or more FRET-sensors in a single sample and remains to be a valuable addition to multiplexed FRET measurements (112–114).

1.4.1 Large Stokes Shift Fluorescent Proteins

A more elegant approach came with the development of Large Stoke Shift (LSS) fluorescent proteins (LSSFPs). The use of these proteins reduces unwanted spectral overlap by pushing the excitation and emission spectra further away from each other. This increase of the Stokes shift occurs when the phenol (protonated) form of the fluorescent protein is lost due to the hydrogen-bond stabilized deprotonation of the chromophore in the excited state (115). This leads to excited state proton transfer (ESPT) and red-shifted (lower energy) emission from the phenolate form**.** Due to the large separation between their excitation and emission spectra, LSS proteins can be used as donors to transfer energy to fluorescent proteins located further in the visible spectra. LSS proteins in FRET pairs offer several advantages such as i) reduced donor crosstalk and acceptor bleed-through, ii) possibility of combining multiple donor molecules with similar excitation but distinct emission spectra by equipping one pair with a LSSFP and iii) possibility of detecting FPs with similar emission but distinct excitation spectra. The first LSSFP to be used in FRET was mAmetrine, a yellow LSSFP modified form of T-Sapphire (116). The FRET application of mAmetrine was demonstrated in a proof-of-concept study for dual FRET-biosensor measurements (117). By combining mAmetrine-tdTomato with mTFP1-mCitrine, Ai et al. were able to detect two FRET events separately and detect the delay between the onset of caspase-3 activity in nucleus and in the cytoplasm during apoptosis. However, both FRET sensors were localizes in different parts of the cell (nucleus and cytoplasm) and a crude ratiometric intensity-based analysis was used to measure the changes in donor over acceptor emission. Later, another cascade-3 sensor was developed using LSSmOrange and mKate2. This sensor was combined with the calcium sensor YC3.6, using ECFP and cpVenus proteins (see Fig. 1.10)(118). This combination allowed the evaluation of two biological processes that were present together in the same region. In this case, one excitation line was used to excite both donors, while the LSS properties allowed separate acceptor emission detection.

Despite the development of a wide range of LSS fluorescent proteins covering the spectrum (green (116, 119), yellow (117), orange (118), red (120–122) and far-red (123, 124)), the use of LSSFPs in FRET-biosensors had remained limited so far. Less efficient photon detection of the blue-shifted and far-red light in most detectors, lower brightness and longer maturation times remain some of the main disadvantages. However, in recent years, an impressive number of LSSFPs was introduced improving the number of possible combinations with existing FPs.

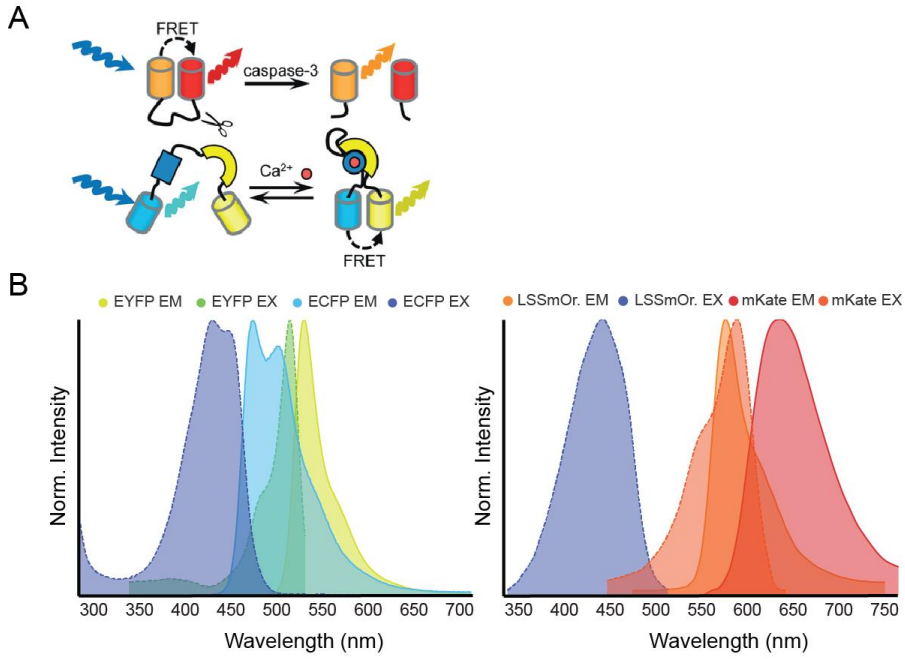


Figure 1.10: Illustration of single excitation wavelength for combined FRET sensors. (A) LSSmOrange- mKate2 (caspase-3 sensor) and CFP-YFP for calcium sensor (adopted from (118)). (B) Normalized spectra of both FRET pairs showing the single excitation dual detection possibilities.

1.4.2 Dark Fluorescent Proteins

Eliminating one of the emitters is an alternative method to increase the number of channels for multiplexed FRET sensing. In FLIM-based FRET analysis, the acceptor signal is usually left aside. This characteristic of the FLIM approach offers the chance to design a FRET pair incorporating a low quantum yield acceptor (<0.1) (125). These acceptors, which have low emission but can be efficiently excited, are referred to as dark FRET acceptors. By freeing up a significant portion of the visible

spectra, dark acceptors allow the distribution of available wavelengths among multiple donor molecules. This, in turn, allows for the simultaneous use of additional FRET biosensors.

Dark acceptors initially emerged in the form of organic dark quenchers (e.g., DABCYL, BHQs, BBQs). Since their commercialization, more than a hundred versions of dark quenchers have been developed (125). However, research on intracellular phenomena often relies on genetically encoded FRET biosensors. The development of non-fluorogenic proteins with low quantum yield is only possible through directed evolution and genetic modification rendering the generation of dark fluorescent proteins challenging, and their availability scarce. However, it is possible to find dark protein acceptors that can be combined with commonly used FRET donor FPs.

With the use of a dark acceptor, the bleed-through of acceptor emission into donor channel is reduced. Additionally, the use of dark FP acceptors allows the detection of the full emission spectrum of the donor. This can increase the signal-to-noise ratio (SNR) when compared to narrow spectral detection regions in traditional FRET-pairs. The expanded detection range increases the photon count, which decreases the imaging time and improves the fluorescence lifetime determination. Increased photon acquisition efficiency allows the use of lower excitation powers, minimizing photobleaching and phototoxicity in live cells (9). In FRET, the acceptor lifetime limits the rate of the energy transfer when an already excited acceptor cannot accept further energy from the donor (126). This occurs when the donor lifetime is shorter than the acceptor. The extremely short lifetime (<0.2 ns) of dark proteins overcomes this limitation by providing a fast FRET energy transfer cycle. Having a short lifetime also minimizes the acceptor photobleaching as the electrons of the acceptor spend significantly less time in the excited state. Both advantages can be profoundly useful in scenarios with high excitation probabilities as is the case for high laserpower confocal laser scanning microscopy, multiphoton microscopy and high-frequency FLIM.

Among the first dark acceptors developed was the Resonance Energy Accepting Chromoprotein (REACh), an altered form of the enhanced yellow fluorescent protein (eYFP), with a significantly reduced quantum yield (127). Further improvements led to the creation of superREACh (sREACh), which shows improved folding efficiency when attached to eGFP compared to REACh (128). Subsequent mutagenesis of REACh mutants led to the development of ShadowY (129). In parallel, a blue-shifted dark acceptor named ShadowG was engineered, with a quantum yield of only 0.005. Imaging of a ShadowG-eGFP FRET pair while measuring mCherry labelled ERK showcased its potential for multicolor FLIM-FRET (130). Recently, more red-region dark fluorescent proteins were introduced, including: Ultramarine, ShadowR and Dark Cherry (131–133), maximizing the

potential of using a dark fluorophore in FRET experiments. A comprehensive overview is provided in Table 3.

Table 3: Overview of dark fluorescent proteins

	Ex	Em	EC	QY	Lifetime	FRET Couple	Multiplexed with	Ref.
REACh	510	538	ND	0.100	0.32 ns	eGFP	mRFP	(127)
sREACh	517	531	115000	0.070	0.45 ns	eGFP	mCherry	(128)
ShadowY	519	531	136000	0.010	0.17 ns	eGFP and Clover* mTurquoise2**	NA	(129)
ShadowG	486	510	89000	0.005	0.16 ns	eGFP* mTurquoise2** msfGFP***	mCherry	(130)
Ultramarine	586	626	64000	0.001	1.6 ns	Sapphire	NA	(131)
ShadowR	585	ND	97100	ND	ND	mRuby2 and mScarlet	NA	(132)
Dark mCherry	590	620	32000	0.020	0.45 ns	mRuby2	GFP	(133)

ND = non disclosed NA = not applicable

In a recent study, researchers brought together dark acceptors and LSSFPs for the first time (134). Accordingly, ShadowG served as acceptor to mTFP1 while LSSmOrange served as donor to mKate2. The overlap between the absorption spectra of mTFP1 and LSSmOrange allowed the use of single laser to excite both donors at the same time, while the donor emission is spectrally separated by the LSS properties of the second donor. Additionally, ShadowG barely emits and mKate2 undergoes sensitized emission separately from LSSmOrange. By taking advantage of these two novel proteins, the authors were able to simultaneously track PKA and ERK1/2 kinase activities using dual color FLIM-FRET.

Dark chromoproteins are an exciting avenue for multiplexed FRET-biosensor measurements. Although currently limited to dual-parameter experiments, there is theoretical potential for dark acceptors to enable a higher degree of multiplexing. However, since this will rely on FLIM measurements, the sparse availability of such setups is likely withholding faster research implementation.

1.5 Practical Considerations for FRET imaging

1.5.1 Sample fixation and photobleaching

FRET imaging requires a clear rationale regarding the sample preparation and imaging setup. First, when studying dynamic cellular processes with biosensors over time, live-cell imaging methods are the logical choice. In contrast, chemical fixation of the samples (e.g. with 4% paraformaldehyde) provide an irreversible stationary snapshot of the cellular processes at a single timepoint and therefore provide no dynamic data. Careful consideration for measuring fixed samples is advised, since control experiments are needed to verify whether the biosensor readout is actually fixed in the process. Fixed samples, however, still hold value where the biosensor readout only requires one timepoint evaluation. Even more, acceptor photobleaching can't be used on live cells given the sequential imaging principle that requires an unchanged- sample, together with the permanent fluorophore inactivation.

Furthermore, using high intensity or prolonged illumination in FRET imaging approaches generates photobleaching and phototoxicity artifacts, mostly in samples using fluorescent proteins, not organic dyes. Photobleaching of a donor protein leads to the inability to fluoresce by itself or transfer energy to an acceptor nearby. Therefore, it doesn't affect the donor to acceptor signal ratio in the FRET channel but it will lower the overall signal to noise ratio. For FLIM approaches, photobleaching effects will not lead to a changed donor lifetime signature, but will lead to lower photon budgets, similarly lowering the lifetime determination quality of any fit or fit-free analysis approach.

1.5.2 How many control measurements?

The design of good control samples are paramount to reliable and comparable FRET measurements. As we have mentioned before throughout this chapter, aside from imaging of donor (and acceptor emissions for intensity-based FRET) following donor excitation, many FRET imaging methods of a biosensor require separate measurements such as measuring the donor only lifetime for FLIM-FRET and donor or acceptor-only measurements in SE-FRET.

Intensity-based FRET approaches carry the most extensive measurement controls. While data from acceptor emission due to direct acceptor excitation is often acquired within a full FRET sensor with donor and acceptor, separate cells

expressing donor-only and/or acceptor-only constructs (or purified protein samples of know concentration for spectral FRET) are often advised. This is mainly due to the spectral overlap of donor and acceptor, these controls are necessary to estimate the contribution of donor and acceptor bleed-through and crossover (see the correction factors involved with SE-FRET). Importantly, because the intensity is used to calculate FRET, it is crucial to measure all these controls on the same microscopy setup with the same laser, laser power, detector and at the same detection range as the measured samples. Moreover, it is essential to repeat these measurements regularly since small changes in the setup can occur over time leading to a changed photon detection efficiency during measurements. Using a control with donor-only and acceptor-only as single-label reference samples, it presumes a linear relationship between the single (D/A)- and double (D&A)-labeled samples when measured under equal conditions to correct for SBT. While this relationship is rarely linear due to differences in sample type, excitation power or imaged intensity levels, the obtained values are still transferred to the FRET measurement and are often adequate.

Similarly, for FLIM-FRET the lifetime of the donor without FRET needs to be determined. Additionally, modified FRET sensors with minimum/maximum sensor FRET are preferably measured in a similar sample type to obtain information of the expected FRET range. In FLIM-FRET approaches, the acceptor fluorescence is not evaluated and therefore doesn't need SBT correction. It remains important however to keep the donor detection range outside of the acceptor emission spectrum and to use an excitation wavelength that minimizes direct acceptor excitation which would block the acceptor from partaking in FRET.

1.5.3 FRET imaging artifacts to keep in mind:

Regarding intensity-based FRET, the variations in fluorophore expression level (FEL) within biological samples cannot be forgotten since the exact concentration of fluorescent molecules within cells is most often unknown. This is especially true when intensity variations are not detected perfectly linear. These variations can be neutralized by performing a basic FRET ratio imaging when assuming equal donor and acceptor quantities (I_A/I_D), but this metric is not equivalent to a FRET efficiency (9). Next to that, FP maturation has a substantial effect on the FRET efficiency of genetically encoded FRET sensors, but is a frequently overlooked quality of FRET pairs. Fast maturation rates reduce the likelihood of incompletely folded FPs during imaging (135). Moreover, differences in maturation of donor and acceptor can impact a FRET determination. For FLIM-FRET specifically, a faster maturing acceptor is recommended since a sensor with an unfolded donor but folded

acceptor will be invisible. Inversely, having sensors with folded donors, but unfolded acceptors will disturb the FRET signal by lowering the apparent FRET (9, 136).

Pointing to further prevalent imaging artifacts, (137–139) detector saturation poses a problem for both TD-FLIM and intensity-based measurements. Once saturated, there is no longer a linearly proportional relationship between the emitted fluorescence and excitation photon influx (140). Also the donor/acceptor fluorescence emission ratio will be skewed towards an artificially larger contribution of the non-saturated species, since the saturated species fluorescence contribution can't rise further. For TD-FLIM, the count rate has another implication. Upon time-tagging of a single photon by TCSPC, the detector has a 'dead time' during which it is unable to detect another photon. Therefore, a traditional TCPSC device can only register a single photon per pulse. When a photon arrives during the dead time or a second photon arrives in a single pulse window, the pile-up effect will deform the true lifetime signature and lead to a measurement of a lower, incorrect, lifetime, since it is biased towards the first arriving photon. In the context of FRET, this would lead to an overestimation of the FRET value. Most often, the advised photons per pulse ratio is 1-3 photons per 100 pulses. Newer TD-FLIM systems such as the FALCON module of Leica utilize a bitstream-TCPSC, multiple detector FLIM with severely reduced dead time which push towards a 1:1 photon per pulse ratio, drastically improving FLIM recordings.

For a spatial analysis method such as FLIM-phasor, the frequency at which the data is gathered is crucial to obtain spatial separation in the phasor plot. Choosing the best frequency to display your pixel data points is an important part in setting up your experiment and can be calculated by

(87) $$\omega_{optimal} = \frac{1+\sqrt{3}}{2\tau^2} = f_{optimal} 2\pi \ . \qquad \text{Eq. 11}$$

Computationally, the real improvement for TD-FLIM is the time-resolution at which the measurement can be performed. However, the photon budget needs to be in balance with the amount of time-bins utilized to record the fluorescence decay for fitting approached.

For time dependent methods, such as FD-FLIM and TD-FLIM, an important measurement is the determination of the instrument response function (IRF) since it is convoluted with the measured fluorescence decay or modulated emission. For TD-FLIM, the IRF needs to be incorporated into the fitting procedure for optimal results. Generally, measuring a reflection in water or measuring a quenched saturated dye solution with KI gives a good IRF approximation. For the phasor approach to FLIM, referencing is performed to incorporate the IRF and the delayed registration of the fluorescence decay. Such referencing requires an easily obtained measurement of a dye with a well-known monoexponential lifetime, which will yield

the IRF in its measurement. More details on referencing for successful application of the phasor can be found in Ranjit et al. (141), Michalet et al. (142) and Coucke et al. (11).

1.6 References

1. Lakowicz, J.R. 2006. Principles of fluorescence spectroscopy. .
2. Förster, T. 1965. Delocalized excitation and excitation transfer. *Acad. Press Inc., New-York*. Vol. 3.:93–137.
3. Patterson, G.H., D.W. Piston, and B.G. Barisas. 2000. Forster distances between green fluorescent protein pairs. *Anal. Biochem.* 284:438–440.
4. Wu, P.G., and L. Brand. 1994. Resonance Energy Transfer: Methods and Applications. *Anal. Biochem.* 218:1–13.
5. Andrews, D.L. 2009. Resonance energy transfer: theoretical foundations and developing applications. .
6. Dos Remedios, C.G., and P.D.J. Moens. 1995. Fluorescence resonance energy transfer spectroscopy is a reliable "ruler" for measuring structural changes in proteins. Dispelling the problem of the unknown orientation factor. *J. Struct. Biol.* 115:175–185.
7. Zeug, A., A. Woehler, E. Neher, and E.G. Ponimaskin. 2012. Quantitative Intensity-Based FRET Approaches—A Comparative Snapshot. *Biophys. J.* 103:1821–1827.
8. Jares-Erijman, E.A., and T.M. Jovin. 2003. FRET imaging. *Nat. Biotechnol.* 21:1387–1395.
9. Bajar, B.T., E.S. Wang, S. Zhang, M.Z. Lin, and J. Chu. 2016. A guide to fluorescent protein FRET pairs. *Sensors (Switzerland)*. 16:1–24.
10. Lerner, E., A. Barth, J. Hendrix, B. Ambrose, V. Birkedal, S.C. Blanchard, R. Börner, H.S. Chung, T. Cordes, T.D. Craggs, A.A. Deniz, J. Diao, J. Fei, R.L. Gonzalez, I. V. Gopich, T. Ha, C.A. Hanke, G. Haran, N.S. Hatzakis, S. Hohng, S.C. Hong, T. Hugel, A. Ingargiola, C. Joo, A.N. Kapanidis, H.D. Kim, T. Laurence, N.K. Lee, T.H. Lee, E.A. Lemke, E. Margeat, J. Michaelis, X. Michalet, S. Myong, D. Nettels, T.O. Peulen, E. Ploetz, Y. Razvag, N.C. Robb, B. Schuler, H. Soleimaninejad, C. Tang, R. Vafabakhsh, D.C. Lamb, C.A.M. Seidel, S. Weiss, and O. Boudker. 2021. FRET-based dynamic structural biology: Challenges, perspectives and an appeal for open-science practices. *Elife*. 10:1–69.
11. Coucke, Q., N. Parveen, G.S. Fernández, C. Qian, J. Hofkens, Z. Debyser, and J. Hendrix. 2023. Particle-based phasor-FLIM-FRET resolves protein-protein interactions inside single viral particles. *Biophys. Reports*. 3.
12. Borrenberghs, D., W. Thys, S. Rocha, J. Demeulemeester, C. Weydert, P. Dedecker, J. Hofkens, Z. Debyser, and J. Hendrix. 2014. HIV virions as nanoscopic test tubes for probing oligomerization of the integrase enzyme. *ACS Nano*. 8:3531–3545.
13. Margineanu, A., J.J. Chan, D.J. Kelly, S.C. Warren, D. Flatters, S. Kumar, M. Katan, C.W. Dunsby, and P.M.W. French. 2016. Screening for protein-protein interactions using Förster resonance energy transfer (FRET) and fluorescence lifetime imaging microscopy (FLIM). *Sci. Rep.* 6.

14. Kraynov, V.S., C. Chamberlain, G.M. Bokoch, M.A. Schwartz, S. Slabaugh, and K.M. Hahn. 2000. Localized Rac activation dynamics visualized in living cells. *Science (80-.).* 290:333–337.
15. Chen, Y., J.D. Mills, and A. Periasamy. 2003. Protein localization in living cells and tissues using FRET and FLIM. *Differentiation*. 71:528–541.
16. Yoon, S., Y. Pan, K. Shung, and Y. Wang. 2020. FRET-Based Ca2+ Biosensor Single Cell Imaging Interrogated by High-Frequency Ultrasound. .
17. Miyawaki, A., J. Llopis, R. Heim, J. Michael McCaffery, J.A. Adams, M. Ikura, and R.Y. Tsien. 1997. Fluorescent indicators for Ca2+based on green fluorescent proteins and calmodulin. *Nat. 1997 3886645*. 388:882–887.
18. Esposito, A., M. Gralle, M.A.C. Dani, D. Lange, and F.S. Wouters. 2008. pHlameleons: A family of FRET-based protein sensors for quantitative pH imaging. *Biochemistry*. 47:13115–13126.
19. Green, H.M., and J. Alberola-Ila. 2005. Development of ERK Activity Sensor, an in vitro, FRET-based sensor of extracellular regulated kinase activity. *BMC Chem. Biol.* 5:1–8.
20. Jayachandran, C., A. Ghosh, M. Prabhune, J. Bath, A.J. Turberfield, L. Hauke, J. Enderlein, F. Rehfeldt, and C.F. Schmidt. 2021. A DNA-based optical force sensor for live-cell applications. *bioRxiv*. 2021.12.21.473677.
21. Glazier, R., J.M. Brockman, E. Bartle, A.L. Mattheyses, O. Destaing, and K. Salaita. 2019. DNA mechanotechnology reveals that integrin receptors apply pN forces in podosomes on fluid substrates. *Nat. Commun.* 10:4507.
22. Grashoff, C., B.D. Hoffman, M.D. Brenner, R. Zhou, M. Parsons, M.T. Yang, M.A. McLean, S.G. Sligar, C.S. Chen, T. Ha, and M.A. Schwartz. 2010. Measuring mechanical tension across vinculin reveals regulation of focal adhesion dynamics. *Nature*. 466:263–266.
23. Rothenberg, K.E., D.W. Scott, N. Christoforou, and B.D. Hoffman. 2018. Vinculin Force-Sensitive Dynamics at Focal Adhesions Enable Effective Directed Cell Migration. *Biophys. J.* 114:1680–1694.
24. Arsenovic, P.T., I. Ramachandran, K. Bathula, R. Zhu, J.D. Narang, N.A. Noll, C.A. Lemmon, G.G. Gundersen, and D.E. Conway. 2016. Nesprin-2G , a Component of the Nuclear LINC Complex , Is Subject to Myosin-Dependent Tension. *Biophysj*. 110:34–43.
25. Lacroix, A.S., A.D. Lynch, M.E. Berginski, and B.D. Hoffman. 2018. Tunable molecular tension sensors reveal extension-based control of vinculin loading. 1–36.
26. Agam, G., C. Gebhardt, M. Popara, R. Mächtel, J. Folz, B. Ambrose, N. Chamachi, S.Y. Chung, T.D. Craggs, M. de Boer, D. Grohmann, T. Ha, A. Hartmann, J. Hendrix, V. Hirschfeld, C.G. Hübner, T. Hugel, D. Kammerer, H.S. Kang, A.N. Kapanidis, G. Krainer, K. Kramm, E.A. Lemke, E. Lerner, E. Margeat, K. Martens, J. Michaelis, J. Mitra, G.G. Moya Muñoz, R.B. Quast, N.C. Robb, M. Sattler, M. Schlierf, J. Schneider, T. Schröder, A. Sefer, P.S. Tan, J. Thurn, P. Tinnefeld, J. van Noort, S. Weiss, N. Wendler, N. Zijlstra, A. Barth, C.A.M. Seidel, D.C. Lamb, and T. Cordes. 2023. Reliability and accuracy of single-molecule FRET studies for characterization of structural dynamics and distances in proteins. *Nat. Methods 2023 204*. 20:523–535.

27. Verma, A.K., A. Noumani, A.K. Yadav, and P.R. Solanki. 2023. FRET Based Biosensor: Principle Applications Recent Advances and Challenges. *Diagnostics*. 13.
28. Fang, C., Y. Huang, and Y. Zhao. 2023. Review Article Review of FRET biosensing and its application in biomolecular detection. *Am J Transl Res*. 15:694–709.
29. Jares-Erijman, E.A., and T.M. Jovin. 2003. FRET imaging. *Nat. Biotechnol.* 21:1387–1395.
30. Andrews, D.L., and J. Rodríguez. 2007. Resonance energy transfer: Spectral overlap, efficiency, and direction. *J. Chem. Phys.* 127.
31. Hellenkamp, B., S. Schmid, O. Doroshenko, O. Opanasyuk, R. Kühnemuth, S. Rezaei Adariani, B. Ambrose, M. Aznauryan, A. Barth, V. Birkedal, M.E. Bowen, H. Chen, T. Cordes, T. Eilert, C. Fijen, C. Gebhardt, M. Götz, G. Gouridis, E. Gratton, T. Ha, P. Hao, C.A. Hanke, A. Hartmann, J. Hendrix, L.L. Hildebrandt, V. Hirschfeld, J. Hohlbein, B. Hua, C.G. Hübner, E. Kallis, A.N. Kapanidis, J.Y. Kim, G. Krainer, D.C. Lamb, N.K. Lee, E.A. Lemke, B. Levesque, M. Levitus, J.J. McCann, N. Naredi-Rainer, D. Nettels, T. Ngo, R. Qiu, N.C. Robb, C. Röcker, H. Sanabria, M. Schlierf, T. Schröder, B. Schuler, H. Seidel, L. Streit, J. Thurn, P. Tinnefeld, S. Tyagi, N. Vandenberk, A.M. Vera, K.R. Weninger, B. Wünsch, I.S. Yanez-Orozco, J. Michaelis, C.A.M. Seidel, T.D. Craggs, and T. Hugel. 2018. Precision and accuracy of single-molecule FRET measurements—a multi-laboratory benchmark study. *Nat. Methods*. 15:669–676.
32. Berney, C., and G. Danuser. 2003. FRET or no FRET: A quantitative comparison. *Biophys. J.* 84:3992–4010.
33. Dewey, T.G., and G.G. Hammes. 1980. Calculation on fluorescence resonance energy transfer on surfaces. *Biophys. J.* 32:1023–1035.
34. Gadella, T.W.J., T.M. Jovin, and R.M. Clegg. 1993. Fluorescence lifetime imaging microscopy (FLIM): Spatial resolution of microstructures on the nanosecond time scale. *Biophys. Chem.* 48:221–239.
35. Piston, D.W., and G.J. Kremers. 2007. Fluorescent protein FRET: the good, the bad and the ugly. *Trends Biochem. Sci.* 32:407–414.
36. Pietraszewska-Bogiel, A., and T.W.J. Gadella. 2011. FRET microscopy: from principle to routine technology in cell biology. *J. Microsc.* 241:111–118.
37. Jovin, T.M., and D.J. Arndt-Jovin. 1989. Luminescence Digital Imaging Microscopy. *Annu. Rev. Biophys. Biophys. Chem.* 18:271–308.
38. Szabà, G., P.S. Pine, J.L. Weaver, M. Kasari, and A. Aszalos. 1992. Epitope mapping by photobleaching fluorescence resonance energy transfer measurements using a laser scanning microscope system. *Biophys. J.* 61:661–670.
39. De Los Santos, C., C.W. Chang, M.A. Mycek, and R.A. Cardullo. 2015. FRAP, FLIM, and FRET: Detection and analysis of cellular dynamics on a molecular scale using fluorescence microscopy. *Mol. Reprod. Dev.* 82:587–604.
40. Algar, W.R., N. Hildebrandt, S.S. Vogel, and I.L. Medintz. 2019. FRET as a biomolecular research tool — understanding its potential while avoiding pitfalls. *Nat. Methods 2019 169*. 16:815–829.
41. Broussard, J., R. B, W. DJ, and B. CM. 2013. Fluorescence resonance energy transfer microscopy of the serine/threonine kinase Akt. *Nat. Protoc.* 8:265–281.
42. Ishikawa-Ankerhold, H.C., R. Ankerhold, and G.P.C. Drummen. 2012. Advanced

Fluorescence Microscopy Techniques—FRAP, FLIP, FLAP, FRET and FLIM. *Molecules*. 17:4047.
43. Subach, F. V., L. Zhang, T.W.J. Gadella, N.G. Gurskaya, K.A. Lukyanov, and V. V. Verkhusha. 2010. Red fluorescent protein with reversibly photoswitchable absorbance for photochromic FRET. *Chem. Biol.* 17:745.
44. Rainey, K.H., and G.H. Patterson. 2019. Photoswitching FRET to monitor protein-protein interactions. *Proc. Natl. Acad. Sci. U. S. A.* 116:864–873.
45. Borrenberghs, D., L. Dirix, F. De Wit, S. Rocha, J. Blokken, S. De Houwer, R. Gijsbers, F. Christ, J. Hofkens, J. Hendrix, and Z. Debyser. 2016. Dynamic Oligomerization of Integrase Orchestrates HIV Nuclear Entry. *Sci. Rep.* 6:1–14.
46. Qian, J., B. Yao, C. Wu, and C. Wu. 2014. Fluorescence resonance energy transfer detection methods: Sensitized emission and acceptor bleaching. *Exp. Ther. Med.* 8:1375–1380.
47. Sudhaharan, T., and S. Ahmed. 2016. Fluorescence Sensitized Emission FRET (SE-FRET). *Prat. Man. Fluoresc. Microsc. Tech.*
48. Van Rheenen, J., M. Langeslag, and K. Jalink. 2004. Correcting Confocal Acquisition to Optimize Imaging of Fluorescence Resonance Energy Transfer by Sensitized Emission. *Biophys. J.* 86:2517.
49. Wouters, F.S., P.J. Verveer, and P.I.H. Bastiaens. 2001. Imaging biochemistry inside cells. *Trends Cell Biol.* 11:203–211.
50. Coullomb, A., C.M. Bidan, C. Qian, F. Wehnekamp, C. Oddou, C. Albigès-Rizo, D.C. Lamb, and A. Dupont. 2020. QuanTI-FRET: a framework for quantitative FRET measurements in living cells. *Sci. Reports 2020 101*. 10:1–11.
51. Kaminski, C.F., E.J. Rees, and G.S.K. Schierle. 2014. A quantitative protocol for intensity-based live cell FRET imaging. *Methods Mol. Biol.* 1076:445–454.
52. Zhang, C., Y. Liu, H. Sun, F. Lin, Y. Ma, W. Qu, and T. Chen. 2019. Automated E-FRET microscope for dynamical live-cell FRET imaging. *J. Microsc.* 274:45–54.
53. Chen, H., H.L. Puhl, S. V. Koushik, S.S. Vogel, and S.R. Ikeda. 2006. Measurement of FRET Efficiency and Ratio of Donor to Acceptor Concentration in Living Cells. *Biophys. J.* 91:L39–L41.
54. Zal, T., and N.R.J. Gascoigne. 2004. Photobleaching-corrected FRET efficiency imaging of live cells. *Biophys. J.* 86:3923–3939.
55. Leavesley, S.J., A.L. Britain, L.K. Cichon, V.O. Nikolaev, and T.C. Rich. 2013. Assessing FRET using Spectral Techniques. *Cytometry. A.* 83:898.
56. Chen, Y., J.P. Mauldin, R.N. Day, and A. Periasamy. 2007. Characterization of spectral FRET imaging microscopy for monitoring nuclear protein interactions. *J. Microsc.* 228:139.
57. Wlodarczyk, J., A. Woehler, F. Kobe, E. Ponimaskin, A. Zeug, and E. Neher. 2008. Analysis of FRET signals in the presence of free donors and acceptors. *Biophys. J.* 94:986–1000.
58. Arsenovic, P.T., C.R. Mayer, and D.E. Conway. 2017. SensorFRET: A Standardless Approach to Measuring Pixel-based Spectral Bleed-through and FRET Efficiency using Spectral Imaging. *Sci. Reports 2017 71*. 7:1–15.
59. Jares-Erijman, E.A., and T.M. Jovin. 2003. FRET imaging. *Nat. Biotechnol.* 21:1387–

1395.
60. Leray, A., C. Spriet, D. Trinel, R. Blossey, Y. Usson, and L. Héliot. 2011. Quantitative comparison of polar approach versus fitting method in time domain FLIM image analysis. *Cytometry. A*. 79:149–158.
61. Rajoria, S., L. Zhao, X. Intes, and M. Barroso. 2014. FLIM-FRET for Cancer Applications. *Curr. Mol. Imaging*. 3:144.
62. Sumetsky, D., J.Y. Jiang, M.A. Ayad, T. Mahon, A. Menaesse, M.M. Cararo-Lopes, M. V. Patel, B.L. Firestein, and N.N. Boustany. 2021. Linear Behavior of the Phase Lifetime in Frequency-Domain Fluorescence Lifetime Imaging of FRET Constructs. *Front. Phys.* 9:648016.
63. Collier, B.B., and M.J. McShane. 2013. Time-resolved measurements of luminescence. *J. Lumin.* 144:180–190.
64. Clegg, R.M. 1995. Fluorescence resonance energy transfer. *Curr. Opin. Biotechnol.* 6:103–110.
65. Redford, G., and R.M. Clegg. 2005. Real-Time Fluorescence Lifetime Imaging and FRET Using Fast-Gated Image Intensifiers. *Mol. Imaging FRET Microsc. Spectrosc.* 193–226.
66. Elangovan, M., R.N. Day, and A. Periasamy. 2002. Nanosecond fluorescence resonance energy transfer-fluorescence lifetime imaging microscopy to localize the protein interactions in a single living cell. *J. Microsc.* 205:3–14.
67. Pelet, S., M.J.R. Previte, L.H. Laiho, and P.T.C. So. 2004. A Fast Global Fitting Algorithm for Fluorescence Lifetime Imaging Microscopy Based on Image Segmentation. *Biophys. J.* 87:2807–2817.
68. Warren, S.C., A. Margineanu, D. Alibhai, D.J. Kelly, C. Talbot, Y. Alexandrov, I. Munro, M. Katan, C. Dunsby, and P.M.W. French. 2013. Rapid Global Fitting of Large Fluorescence Lifetime Imaging Microscopy Datasets. *PLoS One*. 8:70687.
69. Nagy, P., Á. Szabó, T. Váradi, T. Kovács, G. Batta, and J. Szöllosi. 2014. Maximum likelihood estimation of FRET efficiency and its implications for distortions in pixelwise calculation of FRET in microscopy. *Cytom. Part A*. 85:942–952.
70. A. Chessel, F. Waharte, J. Salamero, K.C. A Maximum Likelihood method for lifetime estimation in photon counting-based Fluorescence Lifetime Imaging Microscopy. In: EUSIPCO (conference paper). EURASIP.
71. Bajzer, Ž., T.M. Therneau, J.C. Sharp, and F.G. Prendergast. 1991. Maximum likelihood method for the analysis of time-resolved fluorescence decay curves. *Eur. Biophys. J.* 20:247–262.
72. Maus, M., M. Cotlet, J. Hofkens, T. Gensch, F.C. De Schryver, J. Schaffer, and C.A.M. Seidel. 2001. An experimental comparison of the maximum likelihood estimation and nonlinear least-squares fluorescence lifetime analysis of single molecules. *Anal. Chem.* 73:2078–2086.
73. Santra, K., J. Zhan, X. Song, E.A. Smith, N. Vaswani, and J.W. Petrich. 2016. What Is the Best Method to Fit Time-Resolved Data? A Comparison of the Residual Minimization and the Maximum Likelihood Techniques As Applied to Experimental Time-Correlated, Single-Photon Counting Data. *J. Phys. Chem. B*. 120:2484–2490.
74. Padilla-Parra, S., N. Auduge, M. Coppey-Moisan, and M. Tramier. 2011. Non fitting

based FRET–FLIM analysis approaches applied to quantify protein–protein interactions in live cells. *Biophys. Rev.* 3:63.
75. Padilla-Parra, S., N. Audugé, H. Lalucque, J.C. Mevel, M. Coppey-Moisan, and M. Tramier. 2009. Quantitative Comparison of Different Fluorescent Protein Couples for Fast FRET-FLIM Acquisition. *Biophys. J.* 97:2368.
76. Padilla-Parra, S., N. Audugé, M. Coppey-Moisan, and M. Tramier. 2008. Quantitative FRET analysis by fast acquisition time domain FLIM at high spatial resolution in living cells. *Biophys. J.* 95:2976–2988.
77. Spencer, R.D., and G. Weber. 1969. MEASUREMENTS OF SUBNANOSECOND FLUORESCENCE LIFETIMES WITH A CROSS-CORRELATION PHASE FLUOROMETER*. *Ann. N. Y. Acad. Sci.* 158:361–376.
78. Clayton, A.H.A., Q.S. Hanley, and P.J. Verveer. 2004. Graphical representation and multicomponent analysis of single-frequency fluorescence lifetime imaging microscopy data. *J. Microsc.* 213:1–5.
79. Bastiaens, P.I.H., and A. Squire. 1999. Fluorescence lifetime imaging microscopy: spatial resolution of biochemical processes in the cell. *Trends Cell Biol.* 9:48–52.
80. J Gadella, T.W., R.M. Clegg, and T.M. Jovint. 1994. Fluorescence lifetime imaging microscopy: pixel-by-pixel analysis of phase-modulation data. *Bioimaging*. 2:139–159.
81. Booth, M.J., and T. Wilson. 2004. Low-cost, frequency-domain, fluorescence lifetime confocal microscopy. *J. Microsc.* 214:36–42.
82. Squire, A., P.J. Verveer, and P.I.H. Bastiaens. 2000. Multiple frequency fluorescence lifetime imaging microscopy. *J. Microsc.* 197:136–149.
83. Holub, O., M.J. Seufferheld, C. Gohlke, Govindjee, and R.M. Clegg. 2000. Fluorescence Lifetime Imaging (FLI) in Real-Time - a New Technique in Photosynthesis Research. *http://ps.ueb.cas.cz/doi/10.1023/A:1012465508465.html*. 38:581–599.
84. Clegg, R.M., O. Holub, and C. Gohlke. 2003. Fluorescence lifetime-resolved imaging: Measuring lifetimes in an image. *Methods Enzymol.* 360:509–542.
85. Klarenbeek, J., J. Goedhart, A. Van Batenburg, D. Groenewald, and K. Jalink. 2015. Fourth-Generation Epac-Based FRET Sensors for cAMP Feature Exceptional Brightness, Photostability and Dynamic Range: Characterization of Dedicated Sensors for FLIM, for Ratiometry and with High Affinity. *PLoS One*. 10.
86. Digman, M.A., V.R. Caiolfa, M. Zamai, and E. Gratton. 2008. The phasor approach to fluorescence lifetime imaging analysis. *Biophys. J.* 94:L14–L16.
87. Redford, G.I., and R.M. Clegg. 2005. Polar plot representation for frequency-domain analysis of fluorescence lifetimes. *J. Fluoresc.* 15:805–815.
88. Martelo, L., A. Fedorov, and M.N. Berberan-Santos. 2015. Fluorescence Phasor Plots Using Time Domain Data: Effect of the Instrument Response Function. *J. Phys. Chem. B*. 119:10267–10274.
89. Liao, S., Y. Sun, and U. Coskun. 2014. FLIM Analysis using the Phasor Plots. *ISS Tech. Note*. 1–13.
90. Rahim, M.K., J. Zhao, H. V. Patel, H.A. Lagouros, R. Kota, I. Fernandez, E. Gratton, and J.B. Haun. 2022. Phasor Analysis of Fluorescence Lifetime Enables Quantitative Multiplexed Molecular Imaging of Three Probes. *Anal. Chem.* 94:14185–14194.

91. Ranjit, S., L. Malacrida, D.M. Jameson, and E. Gratton. 2018. Fit-free analysis of fluorescence lifetime imaging data using the phasor approach. *Nat. Protoc.* 13:1979–2004.
92. Tramier, M., M. Zahid, J.C. Mevel, M.J. Masse, and M. Coppey-Moisan. 2006. Sensitivity of CFP/YFP and GFP/mCherry pairs to donor photobleaching on FRET determination by fluorescence lifetime imaging microscopy in living cells. *Microsc. Res. Tech.* 69:933–939.
93. Kim, N., S. Shin, and S.W. Bae. 2021. cAMP Biosensors Based on Genetically Encoded Fluorescent/Luminescent Proteins. *Biosens. 2021, Vol. 11, Page 39*. 11:39.
94. Hinde, E., M.A. Digman, C. Welch, and K.M. Hahn. 2012. Biosensor FRET detection by the phasor approach to fluorescence lifetime imaging microscopy (FLIM). *Microsc. Res. Tech. Author Manuscr.* 75:271–281.
95. Grashoff, C., B.D. Hoffman, M.D. Brenner, R. Zhou, M. Parsons, M.T. Yang, M.A. McLean, S.G. Sligar, C.S. Chen, T. Ha, and M.A. Schwartz. 2010. Measuring mechanical tension across vinculin reveals regulation of focal adhesion dynamics. *Nature*. 466:263–266.
96. Campos-Delgado, D.U., O. Gutiérrez Navarro, E.R. Arce-Santana, J.A. Jo, L. Marcu, P. French, D. Elson, S. Shrestha, B. Applegate, J. Park, X. Xiao, P. Pande, J. Jo, N. Galletly, J. McGinty, C. Dunsby, F. Teixeira, J. Requejo-Isidro, I. Munro, D. Elson, M. Neil, A. Chu, P. French, B.H. Malik, R. Cuenca, J.A. Jo, J. Wright, Y.L. Cheng, K.C. Maitland, I. Gimenez-Conti, J. Brandon, F. Clubb, and B.E. Applegate. 2015. Extended output phasor representation of multi-spectral fluorescence lifetime imaging microscopy. *Biomed. Opt. Express, Vol. 6, Issue 6, pp. 2088-2105*. 6:2088–2105.
97. Scipioni, L., A. Rossetta, G. Tedeschi, and E. Gratton. 2021. Phasor S-FLIM: a new paradigm for fast and robust spectral fluorescence lifetime imaging. *Nat. Methods*. 18:542–550.
98. Levitt, J.A., S.P. Poland, N. Krstajic, K. Pfisterer, A. Erdogan, P.R. Barber, M. Parsons, R.K. Henderson, and S.M. Ameer-Beg. 2020. Quantitative real-time imaging of intracellular FRET biosensor dynamics using rapid multi-beam confocal FLIM. *Sci. Rep.* 10:1–9.
99. Grecco, H.E., P. Roda-Navarro, A. Girod, J. Hou, T. Frahm, D.C. Truxius, R. Pepperkok, A. Squire, and P.I.H. Bastiaens. 2010. In situ analysis of tyrosine phosphorylation networks by FLIM on cell arrays. *Nat. Methods*. 7:467–472.
100. Grecco, H.E., P. Roda-Navarro, and P.J. Verveer. 2009. Global analysis of time correlated single photon counting FRET-FLIM data. *Opt. Express*. 17:6493.
101. Schrimpf, W., A. Barth, J. Hendrix, and D.C. Lamb. 2018. PAM: A Framework for Integrated Analysis of Imaging, Single-Molecule, and Ensemble Fluorescence Data. *Biophys. J.* 114:1518–1528.
102. Wolfgang Becker, A.B. New SPCImage Version Combines Time-Domain Analysis with Phasor Plot. .
103. Gottlieb, D., B. Asadipour, T.P.L. Ung, and C. Stringari. 2023. FLUTE: a Python GUI for interactive phasor analysis of FLIM data. *bioRxiv*. 2023.03.31.534529.
104. Shaner, N.C., R.E. Campbell, P.A. Steinbach, B.N.G. Giepmans, A.E. Palmer, and R.Y. Tsien. 2004. Improved monomeric red, orange and yellow fluorescent proteins

derived from Discosoma sp. red fluorescent protein. *Nat. Biotechnol. 2004 2212*. 22:1567–1572.
105. Subach, O.M., I.S. Gundorov, M. Yoshimura, F. V. Subach, J. Zhang, D. Grüenwald, E.A. Souslova, D.M. Chudakov, and V. V. Verkhusha. 2008. Conversion of red fluorescent protein into a bright blue probe. *Chem. Biol.* 15:1116–1124.
106. Wang, L., W.C. Jackson, P.A. Steinbach, and R.Y. Tsien. 2004. Evolution of new nonantibody proteins via iterative somatic hypermutation. *Proc. Natl. Acad. Sci. U. S. A.* 101:16745–16749.
107. Piljic, A., and C. Schultz. 2008. Simultaneous recording of multiple cellular events by FRET. *ACS Chem. Biol.* 3:156–160.
108. Grant, D.M., W. Zhang, E.J. McGhee, T.D. Bunney, C.B. Talbot, S. Kumar, I. Munro, C. Dunsby, M.A.A. Neil, M. Katan, and P.M.W. French. 2008. Multiplexed FRET to image multiple signaling events in live cells. *Biophys. J.* 95.
109. Hendrix, J., and D.C. Lamb. 2013. Pulsed interleaved excitation: Principles and applications. 1st ed. Elsevier Inc.
110. Dickinson, M.E., G. Bearman, S. Tille, R. Lansford, and S.E. Fraser. 2018. Multi-Spectral Imaging and Linear Unmixing Add a Whole New Dimension to Laser Scanning Fluorescence Microscopy. *https://doi.org/10.2144/01316bt01*. 31:1272–1278.
111. Zimmermann, T., J. Rietdorf, and R. Pepperkok. 2003. Spectral imaging and its applications in live cell microscopy. *FEBS Lett.* 546:87–92.
112. Sun, Y., H. Wallrabe, C.F. Booker, R.N. Day, and A. Periasamy. 2010. Three-color spectral FRET microscopy localizes three interacting proteins in living cells. *Biophys. J.* 99:1274–1283.
113. Woehler, A. 2013. Simultaneous Quantitative Live Cell Imaging of Multiple FRET-Based Biosensors. *PLoS One*. 8:e61096.
114. Elliott, A.D., N. Bedard, A. Ustione, M.A. Baird, M.W. Davidson, T. Tkaczyk, and D.W. Piston. 2017. Hyperspectral imaging for simultaneous measurements of two FRET biosensors in pancreatic β-cells. *PLoS One*. 12:e0188789.
115. Chattoraj, M., B.A. King, G.U. Bublitz, and S.G. Boxer. 1996. Ultra-fast excited state dynamics in green fluorescent protein: multiple states and proton transfer. *Proc. Natl. Acad. Sci.* 93:8362–8367.
116. Zapata-Hommer, O., and O. Griesbeck. 2003. Efficiently folding and circularly permuted variants of the Sapphire mutant of GFP. *BMC Biotechnol.* 3:1–6.
117. Ai, H.W., K.L. Hazelwood, M.W. Davidson, and R.E. Campbell. 2008. Fluorescent protein FRET pairs for ratiometric imaging of dual biosensors. *Nat. Methods*. 5:401–403.
118. Shcherbakova, D.M., M.A. Hink, L. Joosen, T.W.J. Gadella, and V. V. Verkhusha. 2012. An orange fluorescent protein with a large stokes shift for single-excitation multicolor FCCS and FRET imaging. *J. Am. Chem. Soc.* 134:7913–7923.
119. Campbell, B.C., M.G. Paez-Segala, L.L. Looger, G.A. Petsko, and C.F. Liu. 2022. Chemically stable fluorescent proteins for advanced microscopy. *Nat. Methods*. 19:1612–1621.
120. Piatkevich, K.D., J. Hulit, O.M. Subach, B. Wu, A. Abdulla, J.E. Segall, and V. V. Verkhusha. 2010. Monomeric red fluorescent proteins with a large Stokes shift. *Proc.*

Natl. Acad. Sci. U. S. A. 107:5369–5374.
121. Shen, Y., Y. Chen, J. Wu, N.C. Shaner, and R.E. Campbell. 2017. Engineering of mCherry variants with long Stokes shift, red-shifted fluorescence, and low cytotoxicity. *PLoS One*. 12:1–14.
122. Subach, O.M., A. V Vlaskina, Y.K. Agapova, P. V Dorovatovskii, A.Y. Nikolaeva, O.I. Ivashkina, V.O. Popov, K.D. Piatkevich, M.G. Khrenova, T.A. Smirnova, K.M. Boyko, and F. V Subach. 2021. LSSmScarlet, dCyRFP2s, dCyOFP2s and CRISPRed2s, Genetically Encoded Red Fluorescent Proteins with a Large Stokes Shift. *Int. J. Mol. Sci.* 22.
123. Yang, J., L. Wang, F. Yang, H. Luo, L. Xu, J. Lu, S. Zeng, and Z. Zhang. 2013. mBeRFP, an Improved Large Stokes Shift Red Fluorescent Protein. *PLoS One*. 8:1–6.
124. Kogure, T., S. Karasawa, T. Araki, K. Saito, M. Kinjo, and A. Miyawaki. 2006. A fluorescent variant of a protein from the stony coral Montipora facilitates dual-color single-laser fluorescence cross-correlation spectroscopy. *Nat. Biotechnol.* 24:577–581.
125. Fang, B., Y. Shen, B. Peng, H. Bai, L. Wang, J. Zhang, W. Hu, L. Fu, W. Zhang, L. Li, and W. Huang. 2022. Small-Molecule Quenchers for Förster Resonance Energy Transfer: Structure, Mechanism, and Applications. *Angew. Chemie - Int. Ed.* 61.
126. Hänninen, P.E., L. Lehtelä, and S.W. Hell. 1996. Two- and multiphoton excitation of conjugate-dyes using a continuous wave laser. *Opt. Commun.* 130:29–33.
127. Ganesan, S., S.M. Ameer-Beg, T.T.C. Ng, B. Vojnovic, and F.S. Wouters. 2006. A dark yellow fluorescent protein (YFP)-based Resonance Energy-Accepting Chromoprotein (REACh) for Förster resonance energy transfer with GFP. *Proc. Natl. Acad. Sci. U. S. A.* 103:4089–4094.
128. Murakoshi, H., S.J. Lee, and R. Yasuda. 2008. Highly sensitive and quantitative FRET-FLIM imaging in single dendritic spines using improved non-radiative YFP. *Brain Cell Biol.* 36:31–42.
129. Murakoshi, H., and A.C.E. Shibata. 2017. ShadowY: a dark yellow fluorescent protein for FLIM-based FRET measurement. *Sci. Reports 2017 71*. 7:1–10.
130. Murakoshi, H., A.C.E. Shibata, Y. Nakahata, and J. Nabekura. 2015. A dark green fluorescent protein as an acceptor for measurement of Förster resonance energy transfer. *Sci. Reports 2015 51*. 5:1–11.
131. Pettikiriarachchi, A., L. Gong, M.A. Perugini, R.J. Devenish, and M. Prescott. 2012. Ultramarine, a Chromoprotein Acceptor for Förster Resonance Energy Transfer. *PLoS One*. 7:e41028.
132. Murakoshi, H., H. Horiuchi, T. Kosugi, M. Onda, A. Sato, N. Koga, and J. Nabekura. 2019. ShadowR: a novel chromoprotein with reduced non-specific binding and improved expression in living cells. *Sci. Reports 2019 91*. 9:1–11.
133. Nakahata, Y., J. Nabekura, and H. Murakoshi. 2016. Dual observation of the ATP-evoked small GTPase activation and Ca2+ transient in astrocytes using a dark red fluorescent protein. *Sci. Reports 2016 61*. 6:1–10.
134. Demeautis, C., F. Sipieter, J. Roul, C. Chapuis, S. Padilla-Parra, F.B. Riquet, and M. Tramier. 2017. Multiplexing PKA and ERK1&2 kinases FRET biosensors in living cells using single excitation wavelength dual colour FLIM. *Sci. Reports 2017 71*. 7:1–14.
135. Nagai, T., K. Ibata, E.S. Park, M. Kubota, K. Mikoshiba, and A. Miyawaki. 2002. A variant

of yellow fluorescent protein with fast and efficient maturation for cell-biological applications. *Nat. Biotechnol.* 20:87–90.
136. Höfig, H., J. Otten, V. Steffen, M. Pohl, A.J. Boersma, and J. Fitter. 2018. Genetically Encoded Förster Resonance Energy Transfer-Based Biosensors Studied on the Single-Molecule Level. *ACS Sensors*. 3:1462–1470.
137. Spiering, D., J.J. Bravo-Cordero, Y. Moshfegh, V. Miskolci, and L. Hodgson. 2013. Quantitative ratiometric imaging of FRET-biosensors in living cells. *Methods Cell Biol.* 114:593–609.
138. Hodgson, L., F. Shen, and K. Hahn. 2010. Biosensors for characterizing the dynamics of rho family GTPases in living cells. *Curr. Protoc. cell Biol.* Chapter 14:14111–141126.
139. Waters, J.C. 2009. Accuracy and precision in quantitative fluorescence microscopy. *J. Cell Biol.* 185:1135–1148.
140. Szendi-Szatmári, T., Á. Szabó, J. Szöllösi, and P. Nagy. 2019. Reducing the Detrimental Effects of Saturation Phenomena in FRET Microscopy. *Anal. Chem.* 91:6378–6382.
141. Ranjit, S., L. Malacrida, and E. Gratton. 2018. Differences between FLIM phasor analyses for data collected with the Becker and Hickl SPC830 card and with the FLIMbox card. *Microsc. Res. Tech.* 81:980–989.
142. Michalet, X. 2021. Continuous and discrete phasor analysis of binned or time-gated periodic decays. *AIP Adv.* 11:35331.

Chapter 2

Problem statement and objectives

2.1 Contributing to accessible but correct usage of the phasor analysis for time-domain FLIM data

This dissertation is focused on the phasor approach to time domain fluorescence lifetime imaging microscopy (FLIM). The phasor approach, initially introduced for frequency domain FLIM, has regained popularity in the last 20 years. The phasor approach is especially interesting for lifetime-based image color-coding and the analysis of Förster resonance energy transfer (FRET) since there is no need to determine 'a fluorescence lifetime' to acquire FRET efficiency information. When the correct reference measurements are considered, a direct FRET efficiency read-out is available in the phasor plot. When properly understood and used, the current scientific field could benefit from using phasor based FLIM-FRET analysis giving the assumption free conversion of FLIM data to the phasor plot offering a methodology that is unifiable across labs.

As described in **Chapter 1**, where the diverse methodologies of measuring FRET are introduced, intensity-based approaches are by far most popular. While FLIM-based FRET present important advantages, such as less correction factors required and concentration independent values, the cost of the required system and the lack of clear guiding papers hinders the widespread use of FLIM-FRET. Phasor-FLIM, especially for time-domain FLIM, is still in the early phase of its adoption by non-expert groups. With this dissertation, across its chapters, I aim at providing a clear view on the considerations required for correct phasor analysis and display the potential of the phasor approach to measure both intermolecular (**Chapter 3**) and intramolecular (**Chapter 4**) FRET sensors. These two chapters are linked to the two main objectives in this thesis, addressing protein interaction in viral particles and reporting molecular tension within the cell. This double objective aims at providing rigorous handles for researchers to understand that FRET measurements and their interpretation are not always easy but should not be feared.

2.2 Intermolecular FRET sensing of HIV-1 integrase

To apply the phasor approach to the intermolecular FRET analysis, I connected to virology and investigated the multimerization of HIV-1 integrase (IN). This retroviral enzyme is responsible for the organized integration of the viral DNA in the host genome. However, it is unclear what the multimeric state of IN is during the infection cycle. Innovative studies aimed at gaining insights into the multimeric state of integrase are therefore an important pillar for future work. FRET is the ideal tool to investigate protein oligomerization and was previously for this goal using the intensity-based acceptor photobleaching to evaluate changed FRET during the

infection cycle. However, using this approach it was not possible to evaluate the multimer state of the enzyme. In this chapter I developed a convenient workflow for phasor-FLIM analysis of the heterogenous FRET in viral particles which have a low fluorescence signal. Being more assumption free compared to fitting-based FLIM analysis, phasor is very well suited for the investigation of these unknown multimers. Additionally, the double target of this chapter is investigating how the particles can be optimized for such study and how best to analyse them. Ultimately, the overhead goal of this work is the time-lapsed imaging of viral particles during infection. While not performed in this work, it would allow the relative lifetime-based evaluation of the multimeric integrase complexes indicating when multimerization increases or decreases by tracking the viral particle phasor over time. To achieve this, a photon efficient imaging technique is required together with an analysis that is free from fitting bias. To reach this, **Chapter 3** lays down a foundation for the FRET analysis using phasor. Given this is the first chapter in which we analyse FLIM data with phasor, I aim at providing a solid theoretical breakdown of the time-domain FLIM analysis with phasor to aid novice users to correctly implement phasor-FLIM as standard microscopy practice.

2.3 Resolving tension heterogeneities with FRET tension sensors

In the second application, I delve into the field of intramolecular FRET tension sensors. Here, in **Chapter 4,** I focus on the generation of FRET efficiency images through the graphical analysis of the constructed phasor plot. These sensors exhibit a variable FRET readout based on the tension driven elongation of the FRET module. While seemingly very different, the first goal within Chapter 4 is to demonstrate the practical similarities between the analysis of intermolecular and intramolecular FRET.

Within the field of mechanotransduction, several types of sensors and imaging techniques have been proposed to study the forces that cells apply and internally transduce. Genetically encoded tension sensors were the first type of molecular that could provide a tension reading within cells. Therefore, the second goal of Chapter 4 is the exploration of vinculin tension sensors with phasor-FLIM, which can supply a convincing framework to employ this methodology in other tension sensors. Vinculin was chosen as exemplary tension protein given its broad use in the leading scientific papers on the topic and its relative ease of imaging close to the imaging glass.

So far, the majority of scientific reports using these tension FRET sensors rely on intensity-based approaches such as sensitized emission (SE-FRET). This supplies another direct motivation to use phasor-FLIM in my work to investigate FRET

tension sensors. Especially given the later stage goal of a multiplexed FRET sensor readout, FLIM is the best option to mitigate the problems that arise when trying to combine multiple sensors using intensity-based FRET approaches since only donor fluorescence is evaluated.

In this dissertation, I explore the use of phasor-FLIM to directly evaluate the FRET efficiency of these sensors throughout the image, paying attention to the data interpretation. Aiming at an honest evaluation of the obtained FRET within single focal adhesions, the methodology is explained and illustrated for vinculin tension sensors. Additionally, FRET efficiencies were recorded upon admission of drugs that inhibit cellular tension.

2.4 Providing guidelines for the current and future users of home-built confocal TD-FLIM microscopes

All the experimental work reported in this dissertation was performed using a home-built PIE-FLIM (pulsed interleaved excitation fluorescence lifetime imaging microscopy) microscope. Due to the constant advancements in both hardware and software, home-built setups constantly evolving and require frequent modification to be kept up-to-date with the latest developments. While the setup is described in **Chapter 3**, more detailed technical and practical considerations of the setup are given in **Addendum II**. The analysis software used throughout this thesis was executed in an open-source software freely available called PIE analysis with MATLAB (PAM) or with custom MATLAB code, which can serve as inspiration for future research.

Chapter 3

Particle-based phasor-FLIM-FRET resolves protein-protein interactions inside single viral particles

Quinten Coucke, Nagma Parveen, Guillermo Solís Fernández, Chen Qian, Johan Hofkens, Zeger Debyser and Jelle Hendrix

Guillermo Solís Fernández, Jelle Hendrix and Quinten Coucke designed, built and aligned the microscope for this work. Quinten Coucke and Jelle Hendrix performed simulations. Nagma Parveen imaged the DNA. Irena Zurnic produced the viral particles. Nagma Parveen and Quinten Coucke imaged viral particles. Quinten Coucke, Chen Qian and Jelle Hendrix adapted the PAM software for the specific analyses. Nagma Parveen performed preliminary analyses. Quinten Coucke, Nagma Parveen and Jelle Hendrix performed all analyses. Quinten Coucke and Jelle Hendrix wrote the manuscript. All authors reviewed and edited the manuscript.

This chapter is published in Biophysical Reports on the 9th august 2023

https://doi.org/10.1016/j.bpr.2023.100122

3.1 Abstract

Fluorescence lifetime imaging microscopy (FLIM) is a popular modality to create additional contrast in fluorescence images. By carefully analyzing pixel-based nanosecond lifetime patterns, FLIM allows studying complex molecular populations. At the single molecule or single particle level, however, image series often suffer from low signal intensities per pixel, rendering it difficult to quantitatively disentangle different lifetime species, such as during FRET analysis in the presence of a significant donor-only fraction. In this manuscript we investigate whether an object localization strategy and the phasor approach to FLIM have beneficial effects when carrying out FRET analyses of single particles. Using simulations, we first showed that an average of ~300 photons, spread over the different pixels encompassing single fluorescing particles and without background, is enough to determine a correct phasor signature (standard deviation <5% for a 4 ns lifetime). For immobilized single- or double-labeled dsDNA molecules, we next validated that particle-based phasor-FLIM-FRET readily allows estimating fluorescence lifetimes and FRET from single molecules. Thirdly, we applied particle-based phasor-FLIM-FRET to investigate protein-protein interactions in sub diffraction HIV-1 viral particles. To do this, we first quantitatively compared the fluorescence brightness, lifetime and photostability of different popular fluorescent protein-based FRET probes when genetically fused to the HIV-1 integrase enzyme (IN) in viral particles, and conclude that eGFP, mTurquoise2 and mScarlet perform best. Finally, for viral particles co-expressing FRET-donor/acceptor labeled IN, we determined the absolute FRET efficiency of IN oligomers. Available in a convenient open-source graphical user interface, we believe that particle-based phasor-FLIM-FRET is a promising tool to provide detailed insights in samples suffering from low overall signal intensities.

3.2 Introduction

Fluorescence lifetime imaging microscopy (FLIM) exploits the excited state fluorescence lifetime of fluorophores to generate image contrast (1–3). For FLIM data recorded using pulsed lasers and photon counting (i.e., time-domain FLIM), pixel-based analysis is typically performed via (multi-component) fluorescence decay fitting (4, 5) or more recently, the phasor approach to FLIM (from here on referred to as phasor-FLIM) (6).

The mathematical concepts behind phasor-FLIM were first introduced by Weber et al. (7) and applied by Jameson et al. in analysis of heterogenous fluorescent samples (8). The polar (phasor) plot representation of frequency-domain fluorescence lifetime data was originally introduced by Clayton et al. (9). In the original phasor-FLIM paper by Digman et al. phasor analysis was carried out on lifetime data obtained via a classic time-domain FLIM microscope equipped with pulsed excitation and time-correlated single photon counting (TCSPC) (6). In the more recent digital frequency domain (DFD) FLIM, pulsed lasers are also employed, but the phase and modulation information needed for phasor representation are directly available in the resulting data (10).

Applications of phasor-FLIM vary widely from biosensors based on FRET (11–14), analyzing sample autofluorescence signatures (15–20) or investigating the nanoscale diversity of crystalline materials (21), to name just a few. Additionally, new techniques sprouted using phasor principles such as spectral phasor focused on unmixing (22), phasor S-FLIM focused on species photophysics (23), and several others (24–26).

The broad applicability of FLIM comes with some limitations, the most notable of which is heterogeneity in FLIM data. Lifetime heterogeneity in FLIM data between individual pixels, in general, is extracted and utilized by a per-pixel lifetime analysis. Heterogeneity within one pixel, on the other hand, presents a complication for quantitative FLIM regardless of whether decay-fitting or phasor-transformation based analysis is used. In these approaches, the unmixing of contributing species is executed in different manners, each with benefits and drawbacks. While global lifetime fitting can provide an analysis for the whole FLIM image, it requires critical user input such as the number of exponentials and the fitting boundaries (27, 28). The phasor approach to FLIM attempts the unmixing of contributing factors in a graphical way but equally requires user input such as the instrumental referencing (29), characterization of the autofluorescence contribution and correct location of pure species in the phasor plot (6, 19). Nonetheless, it is generally accepted that phasor-FLIM allows for an easy identification of data clusters and species assignment combined with convenient data representation using the image-phasor reciprocity (30). Indeed, one can select pixels from within the image and analyze

these in phasor space, or inversely, one can select a region-of-interest in phasor space, and false-color these in the image.

Despite the relative ease of use, the application of phasor-FLIM has primarily focused on bright dyes, abundant label-free autofluorescence (such as nicotinamide adenine dinucleotide, NADH) or overexpressed fluorescent protein systems (12, 19, 31, 32). Lower photon yields, sub-pixel species heterogeneity and other experimental complications (e.g., fluorophore maturation, photobleaching) present, however, quite common experimental situations that render quantitative phasor-FLIM analysis challenging (33, 34). For example, while fluorescent protein-based biosensors, generally offer high signal intensities due to strong subcellular expression (35–39), FLIM-based Förster resonance energy transfer (FRET) protein-protein interaction studies at physiological cellular concentrations, are conversely often carried out at much weaker overall fluorescence signals. Methodologies that facilitate quantitative analysis under such conditions of low photon budget and/or signal/noise, e.g., the recently developed particle-based phasor-FLIM approach, are therefore highly desirable (40).

As a specific low-signal example, we focus here on fluorescent protein-based FLIM-FRET of homo-interactions of human immunodeficiency virus 1(HIV-1) integrase (IN) enzymes inside single viral particles. The sub-resolution HIV-1 particles can incorporate only a limited number of fluorescent proteins/fluorescently-labelled IN molecules. As such, they present a challenge for quantitative FRET analysis because of the overall low signal intensities. We previously employed acceptor photobleaching intensity-based FRET studies on the HIV-1 and murine leukemia virus (MLV) IN enzyme to show that the multimerization state of IN functionally changes during nuclear entry or after drug treatment of infected cells (41–43). However, since the IN-labelled donor (D) and acceptor (A) could oligomerize in different combinations in the FRET system used, intensity-derived FRET values are significantly underestimated by the presence of D-D homodimers, which in turn limited the overall FRET dynamic range. Furthermore, the intensity-based FRET analyses used was completely blind to possible sub-particle species heterogeneity.

In this chapter we quantitatively explored the effect of grouping pixels from a single particle. In particular, we investigated at the advantages such grouping might present during the analysis of dim photon-limited samples that would render normal pixel-based phasor-FLIM analysis difficult. Additionally, we present phasor-FLIM analysis in conjunction with the phasor theory to clarify phasor-FLIM for novice users. In doing so we finally present a fair evaluation of FRET data on the oligomerization of HIV-1 integrase.

3.3 Theory

3.3.1 Phasor approach to FLIM

Frequency-domain FLIM utilizes a modulated excitation source at an angular frequency ω. The frequency-dependent demodulation M_ω and phase shift φ_ω are characteristics of the emitted fluorescence, and each quantity can be related to the fluorescence lifetime (44, 45):

$$\tau_M = \omega^{-1}\sqrt{M_\omega^{-2} - 1}, \text{ and} \quad \text{Eq. 1}$$

$$\tau_\varphi = \omega^{-1}\tan(\varphi_\omega), \quad \text{Eq. 2}$$

where the phase (τ_φ) and modulation (τ_M) lifetimes are equal for high-signal and pure-species data (see also Supplemental Figure S1A and S2). Next to this, every lifetime can also be represented in a polar plot as a vector with length equal to the demodulation M_ω and an angle with respect to the abscissa equal to φ_ω. This vector is called the phasor, a portmanteau of phase vector. The point determined by the phasor is described using the Cartesian coordinates g_ω and, s_ω which are the first cosine and sine Fourier coefficients, respectively, of the time-dependent fluorescence signal $I(t)$, normalized for the total intensity of the sample (Supplemental Figure S1A) (7):

$$g_\omega = M_\omega \cos(\varphi_\omega)\left[= \frac{\int_0^\infty I(t)\cos(\omega t)dt}{\int_0^\infty I(t)dt}\right] \text{ and} \quad \text{Eq. 3}$$

$$s_\omega = M_\omega \sin(\varphi_\omega)\left[= \frac{\int_0^\infty I(t)\sin(\omega t)dt}{\int_0^\infty I(t)dt}\right]. \quad \text{Eq. 4}$$

The parts between brackets, stemming from the time-domain, were added merely for comparative purposes. A direct relation between φ_ω and M_ω is found when investigating a mono-exponential decay, where Eqs. 1 and 2 result in the same lifetime:

$$M_\omega = (1 + \tan(\varphi_\omega)^2)^{-1/2}. \quad \text{Eq. 5}$$

M_ω and φ_ω can subsequently be written as:

$$M_\omega = \sqrt{g_\omega^2 + {s_\omega}^2} \text{ and} \quad \text{Eq. 6}$$

$$\varphi_\omega = tan^{-1}(s_\omega / g_\omega), \quad \text{Eq. 7}$$

which allows rewriting Eq. 5 in the Cartesian coordinates of the polar plot:

$${s_\omega}^2 + (g_\omega - \tfrac{1}{2})^2 = \tfrac{1}{4}. \quad \text{Eq. 8}$$

Eq. 8 describes the so-called semi-circle, on which all mono-exponential signals will be spread out, with the phasors for shorter lifetimes lying closer to the point (1,0), and larger lifetimes closer to (0,0) at the origin of the semi-circle (see also Supplemental Figure S1D). Combining Eq. 8 with Eqs. 3 and 4 subsequently allows calculating the g and s coordinates using the angular frequency and the monoexponential lifetime.

$$g_\omega = \frac{1}{1+\omega^2\tau^2} \qquad \text{Eq. 9}$$

$$s_\omega = \frac{\omega\tau}{1+\omega^2\tau^2} \qquad \text{Eq. 10}$$

All multi-exponentials, which are a sum of mono-exponentials, are linear vector combinations of the constituent phasors, and thus will be found inside the described semi-circle. For a combination of P species the resulting phasor coordinates are calculated by the sum of fractional (photon-weighted) contributions (f_i) of every pure species $(g_{\omega,i}, s_{\omega,i})$(see Supplemental Figure S1A and S1E):

$$g_\omega = \sum_{i=1}^{P}(f_i g_{\omega,i}) \text{ and} \qquad \text{Eq. 11}$$

$$s_\omega = \sum_{i=1}^{P}(f_i s_{\omega,i}). \qquad \text{Eq. 12}$$

3.3.2 Phasor-FLIM using TCSPC

When using pulsed excitation and time-correlated single photon counting (TCSPC) detection, as in time-domain FLIM, ω is no longer the modulation frequency but is rather determined by the TCSPC range (TR, in units of time), i.e., the total time period in which photons are timed. In this case, the angular frequency ω_{TR} used for phasor transformations is given by:

$$\omega_{TR} = 2\pi/\mathrm{TR}\,. \qquad \text{Eq. 13}$$

When calculating the phasor for a pixel, or by extension, an image, the idealized scenario where mono-exponential components are directly positioned on the semicircle does not hold true. Most importantly, the fluorescence decay and TCSPC range do not start at the same point relative to the TR, and even for a pure species, the mathematical mono-exponential decay determined by its lifetime, will be convoluted with the instrument response function (IRF) of the measuring device, both effects significantly throwing off any phasor determination. Therefore, a reference measurement is necessary of a stable, well-characterized and mono-exponentially decaying dye with a lifetime similar to the measured lifetime. The reader is referred to Ranjit et al. 2018 (46) and Michalet et al. 2021 (47) for more

information on referencing and phasor transformations, and data corrections to maintain transformations of mono-exponentially decaying phasor data on the semicircle. Alternatively, the pure IRF signal can be used, representing a lifetime of 0. The reference's known fluorescence lifetime τ_{ref} is first used to calculate (using Eqs. 6,7,9,10) the expected demodulation M_{ref} and phase shift φ_{ref} values for the reference (see Supplemental Figure S1B)

$$M_{ref} = \left(1 + (2\pi\tau_{ref}/TR)^2\right)^{-1/2} \text{ and} \qquad \text{Eq. 14}$$

$$\varphi_{ref} = \tan^{-1}(2\pi\tau_{ref}/TR). \qquad \text{Eq. 15}$$

These values are subsequently used to calculate the phasor values for the instrument:

$$g_{instr} = \sum_{n=1}^{N_{TR}} I_{ref}(n) M_{ref}^{-1} \cos\left(2\pi n/N_{TR} - \varphi_{ref}\right) \text{ and} \qquad \text{Eq. 16}$$
$$s_{instr} = \sum_{n=1}^{N_{TR}} I_{ref}(n) M_{ref}^{-1} \sin\left(2\pi n/N_{TR} - \varphi_{ref}\right), \qquad \text{Eq. 17}$$

where N_{TR} is the total number of time channels within the TCSPC range and $I_{ref}(n)$ the normalized intensity of the experimentally measured reference in time bin n. These instrumental phasor coordinates can subsequently be used to calculate the phase and demodulation of the instrument, φ_{inst} and M_{inst} via Eqs. 6 and 7. This finally allows to convert (instrument-dependent time-domain data from) the TCSPC range to (instrument-independent phasor data in) a polar plot:

$$g_{TR}(n) = M_{inst}^{-1} \cos(2\pi n/N_{TR} - \varphi_{inst}) \text{ and} \qquad \text{Eq. 18}$$
$$s_{TR}(n) = M_{inst}^{-1} \sin(2\pi n/N_{TR} - \varphi_{inst}). \qquad \text{Eq. 19}$$

Every photon is assigned such coordinates depending on its arrival time channel in the TCSPC range, and depending on the subsequent analysis, photon phasors were either averaged per pixel or per identified object. An overview figure of the phasor approach to FLIM illustrating pulse frequency impact and reference implementation is provided as Supplemental Figures S1B-D and Supplemental figure S3.

3.3.3 Resolving mixtures of pure species

Pixels containing photons that originate from a single type of pure (mono-exponentially decaying) fluorophore translate to phasor values that lie on the semicircle. Phasors from samples containing a mixture of two pure fluorescent species, with each having a different fluorescence lifetime, on the other hand, are located on a straight 'fraction line' connecting the two constituent pure phasors. The location of this phasor on this line is determined by the number of photons contributed by each species (Eqs. 11 and 12). Therefore, for a two-component mixture, the phasor (or fluorescence lifetime) of at least one species has to be known *a priori*. Finally, the concentration fraction f_C of each species is determined from the lifetimes and the intensity fraction f_{int} as follows:

$$f_{C,1} = \left(\frac{\tau_1}{\tau_2}\left(\frac{1}{f_{int,1}} - 1\right) + 1\right)^{-1}, \qquad \text{Eq. 20}$$

where $\boldsymbol{f_{int,1}}$ is the intensity fraction of species 1. For the derivation of this formula, a conceptual illustration and a proof-of-concept simulation, the reader is referred to Supplemental Note 1, Fig. S1E and Fig. S4, respectively. Practically, the fraction line is manually drawn, starting at the phasor value of one species (which can be a mixture itself) and through the center-of-mass of the mixture's phasor value. This then renders the fractions and the lifetime of all species.

3.3.4 Phasors in the presence of background signal

Background signals (autofluorescence from impurities, detector dark counts, Rayleigh or Raman scattering, laser reflections…) will cause the phasor value of a pure species to be shifted away from the semicircle. The average phasor location of the background (BG) needs to be determined in a separate experiment. In further experimental analyses, a fraction line can then be drawn through the background phasor and the measured sample phasor. The lifetime of the pure species is subsequently determined from the intersection of the fraction line and the semicircle. In this way, for FRET analyses, the location of the DO phasor within the semicircle was quantified via the BG fraction. This concept is illustrated in Fig. 3.2 *D* and Fig. S1G.

3.3.5 Quenching trajectory of FRET species

In the case of a pure fluorophore that is quenched by FRET, its phasor describes a trajectory starting from the DO species (no FRET) along the semicircle to

approximate a 0-ns lifetime (100% FRET) as described by the resulting mono-exponential lifetimes on the semi-circle by the formula:

$$\tau_{DA} = (1 - E) * \tau_D \qquad \text{Eq. 21}$$

(Fig. S1F). Here, τ_{DA} is the quenched lifetime upon FRET, τ_D is the pure donor lifetime and E is the FRET efficiency (i.e., the quantum yield of the Förster transfer process depopulating the fluorophore's excited state). In reality, however, background (BG) and a possible contribution from donor molecules with no nearby acceptor (passive donors) will cause this trajectory to deviate from the semicircle. For points resembling higher FRET states the fluorescence quantum yield of the involved species decreases leading to increased fluorescence contribution of passive donors and BG, which maintain a constant brightness (i.e. fluorescence quantum yield in the case of fluorescing species). Taking this into consideration, the quenching trajectory in a non-perfect condition folds back and the trajectory ends at the phasor determined by the remaining passive donors and BG (Fig. S1G). The quenching trajectory connecting all possible FRET efficiency E states for a given BG and passive donor pD can therefore be determined by fraction lines between all monoexponential points on the semicircle < τ_D and the BG & pD phasor. The g and s coordinates of the quenching line are given by:

$$g_{quenchline} = \frac{(((1 - f_{BG\&pD}) . (1 - E)) . g_{quenched\ D}) + ((f_{BG\&pD}) . g_{BG\&pD})}{(((1 - f_{BG\&pD}) . (1 - E)) + (f_{BG\&pD})} \qquad \text{Eq. 22}$$

$$s_{quenchline} = \frac{(((1 - f_{BG\&pD}) . (1 - E)) . s_{quenched\ D}) + ((f_{BG\&pD}) . s_{BG\&pD})}{(((1 - f_{BG\&pD}) . (1 - E)) + (f_{BG\&pD})} \qquad \text{Eq. 23}$$

in which $g_{quenched\ D}$ and $s_{quenched\ D}$, the coordinates of the pure quenched form on the semicircle, can be found using Eqs. 9 and 10 in which the lifetime of the quenched form is $\tau_D(1 - E)$. $g_{BG\&pD}$ and $s_{BG\&pD}$ are the location coordinates of the mixture of contributions by BG and pD. $f_{BG\&pD}$ is the summed fractional contribution of BG and pD at the starting point (no FRET). The term $(1 - E)$ scales the fractional contribution of the quenched species $(1 - f_{BG\&pD})$ given the fluorescence quantum yield drops with increasing E. From the formulation it is clear that with increasing FRET of the pure quenched state the fractional contribution of the BG & passive donor phasor becomes larger. Construction of the quenching line and its contributing factors are displayed in Supplemental Figure S1 F-I. A more in-depth explanation of Eqs. 22-23 can be found in Supplemental Note 2.

3.4 Materials and Methods

3.4.1 Analysis software

All analysis of imaging data (simulated or experimental .ptu files) was done in the open source Pulsed Interleaved Excitation (PIE) Analysis with MATLAB (PAM) software, a versatile software package offering a variety of analysis tools, including phasor analysis of FLIM data (48). The software is available as a source code, requiring MATLAB to run, or as compiled standalone software compatible with Windows or MacOS at http://www.cup.uni-muenchen.de/pc/lamb/software/pam.html or hosted in Git repositories under http://www.gitlab.com/PAM-PIE/PAM and http://www.gitlab.com/PAM-PIE/PAMcompiled. Sample data is provided under http://www.gitlab.com/PAM-PIE/PAM-sampledata. A detailed manual is found under http://pam.readthedocs.io. The workflow of the software as applied in this chapter is described in Supplemental Figure S5. Simulated photon data was generated by a subsection of PAM. This module is illustrated in Supplemental Figure S6. Simulation input parameters included: TCSPC range (50 ns), pixel intensity (defined by the number of frames pixel dwell time and the particle brightness ε), fluorescence lifetime, background intensity (0 kHz), diffusion coefficient D, number of species and their concentration, simulation box size, pixel size (50 nm) and image size, and (Gaussian) IRF width (250 ps). For the single-particle simulations, a single species of D = 0 µm²/s was used. For the concentration fraction line simulations, D = 100 µm²/s for both species and the fluorescence lifetime and brightness of one species was four times larger than that of the other species (resp. 4 ns and 1 ns), mimicking a species and its 75% quenched form. Particle detection was performed using the *Particle Detection* functionality within PAM, which localizes particles in the fluorescence intensity images using eccentricity (0.5), counts (>300), size in pixels (min:15, max 100) and a wavelet depth of 3, using the simple wavelet method (40). Colocalization of dsDNA particles was performed using the centroid positions of particles in the FRET donor and directly excited FRET acceptor images as input via a nearest neighbor search with a maximum distance tolerance of 5 pixels for successful colocalization. Statistical analysis was performed using GraphPad Software version 9.4.1. For particle intensity tests and comparison of photobleaching, a Shapiro-Wilk tests was first used to check normality of data. When no normality was found, a non-parametric (one-way ANOVA, Kruskal-Wallis) test was used to compare datasets of each IN-FP.

3.4.2 Phasor cloud center positions

The shape of a given phasor 'cloud' at low signal intensities is determined by inherent shot noise on the one hand, and the spectroscopic contribution of the different emissive species, i.e., the background and the different lifetime species in the observed spectral window. To determine the center position, we calculated a 'center of mass', where the average phasor location of all pixels within the phasor cloud is determined, with each pixel weighed for the photon content of that point.

3.4.3 Background and passive donor fraction

Background samples are measured specifically per experimental case and aim to determine the contributing component of background, stray light, dark counts and autofluorescence. The phasor analysis is performed identical to a normal sample analysis to determine the resulting background phasor location (BG). From all resulting phasor positions the photon weighted average position is determined and used as general background phasor. For DNA measurements the prepared non-labeled surface functionalized with PEG is imaged. In case of virus measurements, the viral particle itself is the main source of background and autofluorescence. Therefore, a photobleached region is imaged where viral particles are present in the scanned frame. The passive donor contribution in a FRET experiment skews the phasor to the pure donor phasor position, it is the fraction of donors that does not participate in FRET and has the same phasor location as a sample with only donors (DO).

3.4.4 FRET Histograms

Using the phasor analysis tools of PAM, a FRET trajectory was drawn with the respective passive donor (DO) and (BG) contributions starting from the center-of-mass of a measurement only containing donor labels at the DO location. Using a MATLAB routine we determined the nearest point of the FRET trajectory to every particle phasor location. From these FRET trajectory points a FRET histogram was made.

3.4.5 DNA strand hybridization

All DNA strands were purchased from IBA LifeSciences (Göttingen, Germany). For the single-color dsDNA experiments the sense strand that was used is 5'-GGCTC GCCTG TGTXG TGTTG TATGA TGTAT TCGGC AGTGC GGG-Biotin in which the X marks the 14th position that is labeled with ATTO 488 and biotin-labeled at its 3'-end. A compatible unlabeled antisense strand was used (5'-

CCCGC ACTGC CGAAT ACATC ATACA ACACA GGCGA GCC) for annealing into a single labeled dsDNA. For our double labeled dsDNA, the antisense strand (5'-Biotin-TTTTT AAGTT TGTGA TAGTT TGGAC TGGTT YGTGA AGAAA AZCGC CGAAA A, with Y and Z an Alexa Fluor 488 and ATTO 647N label respectively) is used covalently labeled with Alexa Fluor 488 on position 31 followed by an ATTO647N label 11 nucleotides further. In addition, the antisense strands are labeled with biotin on the 5' end. The complementary sense strand (5'-TTTTC GGCGA TTTTC TTCAC AAACC AGTCC AAACT ATCAC AAACT TAAAA A) is unlabeled. Sense and antisense DNA strands were hybridized by centrifuging the lyophilized strands for 1 min at 1000 g. Next, phosphate buffered saline (PBS, Merck, 806552, Sigma-Aldrich, Darmstadt, Germany) was used to dilute to a final concentration of 100 µM. The solution was homogenized by resuspension and vortexing. Afterwards, the top and bottom strand were annealed using a PCR machine (Doppio, VWR®-thermocyclerseries, VWR, part of Avantor, Radnor, US) increasing the temperature to 95 °C (3 min) and cooling down from 85 to 4 °C at a 1 min per degree to allow specific hybridization towards a final concentration of 10µM. Finally, the PCR product was transferred to a -80°C Eppendorf (Catalog Nr. 0030125215, Eppendorf Belgium) and directly flash-frozen in liquid nitrogen. Afterwards, the product was stored at -80°C. In order to remove the excess free dye as revealed by fluorescence correlation spectroscopy, a PD-10 desalting column was used.

3.4.6 DNA experiments

The glass surface immobilization protocol involved surface cleaning and surface functionalization. Firstly, the chamber glass coverslips (#1.0 chambered coverglass, Lab-Tek Cat. No. 155411) was cleaned by an incubation with 10 mM SDS for 1 hour at room temperature. Next, the surface was washed several times with *Milli-Q* followed by surface activation with UV-Ozone for 15 minutes. Functionalization was performed by adding 10 µg/mL of the passivation agent (PLL-PEG, SuSoS, Dübendorf Switzerland) together with PLL-biotin-PEG in a 1:1 ratio and left to incubate at room temperature for 30 minutes. After this, the surface was rinsed three times with DNA resuspension buffer (150 mM STE-buffer, BP2478-1, ThermoFisher scientific, Geel, Belgium) without letting the surface dry out. This was applied after each incubation step of the functionalization. Once the surface contained biotin, 10 µg/mL Neutravidin (ThermoFisher scientific) was added and incubated for 30 minutes followed by another three wash steps with 150 mM STE-buffer. Finally, DNA was diluted to the picomolar range using 150 mM STE-buffer and incubated for 30 minutes after which excess DNA was washed away. Colocalization of DNA particles was done using a MATLAB routine in which particle centers are determined in both donor and acceptor channel. Particles are

considered colocalized when a donor center position is equal or less than 5 pixels of the nearest acceptor center position.

3.4.7 Microscope

The microscope presented in this work is a custom-built confocal microscope. Its schematic is shown in Supplemental Figure S7. The base microscope is an Olympus IX70 modified with external pulsed excitation lasers, a scan unit and multichannel single photon detection. Five laser lines are available of which 4 are diode pulsed lasers (LDH series, PicoQuant GmbH, Berlin, Germany) and one supercontinuum laser (Solea, PicoQuant GmbH, Berlin, Germany). Laser pulsing and synchronization was set in the acquisitioning software SymphoTime 64 '1+2' (PicoQuant GmbH, Berlin, Germany). A multichannel diode laser driver (PDL 828 Sepia2, Picoquant) controls the laser frequency at 20 MHz to ensure full fluorescence decay when measuring donor and acceptor fluorophores with pulsed interleaved excitation. (Dichroic) Mirrors guide the laser lines into a polarization-maintaining single mode optical fiber (PMC-400Si-2.6- NA012-3-APB-150-P, Schäfter+Kirchhoff GmbH, Hamburg, Germany) via a lens-based coupler (60FC-4-RGBV11-47, SuK). Light is collimated again via a lens-based collimator (60FC-L-4-RGBV11-47, SuK). Excitation light is directed at a dichroic quadband mirror (zt405/488/561/640rpc or zt440/510/561/640rpc depending on needed excitation line, AHF, Tübingen-Pfrondorf, Germany) held in place by a kinematic fluorescence filter cube (DFM1/M, 30 mm cage compatible, Thorlabs, Munich, Germany) for easy optics switching, and reflecting the excitation beam to the scanhead (TILL Yanus IV digital scanner, FEI Munich, Gräfelfing, Germany) mounted straight onto the backport of the IX70. Scan motion is controlled with in-house software in C# Microsoft Visual Studio in combination with a National Instruments box (USB-6361 Multifunction I/O Device, NI, Austin, USA) that steers the xy galvo axis via a TILL photonics Scan Control Unit (SCU, FEI Munich, Gräfelfing, Germany). Pixel dimensions, number and dwell time are controlled by this software. Upon transmission of emission light through the quadband dichroic, the light is focused (150 mm AC254-15-A-ML, Thorlabs) onto a 50-µm pinhole (PS50S, Thorlabs), after being collimated again by (50 mm AC254-050-A-ML, Thorlabs). Detection is arranged over 3 detection channels, splitting the bundle with dichroic mirrors. For DNA experiments, both the 485-nm and 640-nm laser diodes (LDH-D-C-485 and LDH-D-C-640, Picoquant, Berlin, Germany) were used in pulsed interleaved excitation mode using the zt405/488/561/640rpc quadband. Emission light is split on a 560-nm-longpass (H560LPXR, AHF). Reflected light is cleaned up by a 530/50m (HQ, AHF) and recorded on an avalanche photo diode (APD, τ-SPAD, PicoQuant). Passing light is cleaned up by a 705/100 (ET bandpass, AHF analysentechnik, Tübingen-Pfrondorf, Germany). For mNeongreen, mClover3 and eGFP the 485-nm excitation source was used (LDH-D-C-485, Picoquant, Berlin,

Germany) and emission detected identically to the ATTO 488 labeled DNA. mTFP1 and mTurquoise2 were excited using a 440-nm diode (LDH-D-C-440, Picoquant, Berlin, Germany) in combination with the zt440/510/561/640rpc quandband BS. Emission light was reflected on the 560 nm longpass and detected by an APD (τ-SPAD, PicoQuant) after passing a cleanup filter (480/40, Brightline HC, AHF analysentechnik, Tübingen-Pfrondorf, Germany). mVenus was excited using a 510nm diode (LDH-D-C-510, Picoquant, Berlin, Germany) in combination with the zt440/510/561/640rpc quandband BS. Emission light was reflected on the 560-nm longpass and detected by an APD (τ-SPAD, PicoQuant) after passing a cleanup filter (540/15, Brightline HC, AHF analysentechnik, Tübingen-Pfrondorf, Germany). mCherry and mScarlet2 were excited using a 560-nm supercontinuum laser (Solea, Picoquant, Berlin, Germany) in combination with the zt440/510/561/640rpc quandband BS. Emission light was passed through the 560-nm longpass and detected by an APD (τ-SPAD, PicoQuant) after passing a cleanup filter (600/37, Brightline HC, AHF analysentechnik, Tübingen-Pfrondorf, Germany). For FRET experiments with mTurquoise2-mVenus all mission light of donor and acceptor is reflected on the 560-nm longpass and split on a 507-nm-longpass dichroic (H507LPXR, AHF analysentechnik, Tübingen-Pfrondorf, Germany) after which a 480/40 and 540/15 cleanup filter is used for mTurquoise2 and mVenus respectively before detection. In case of eGFP-mScarlet the eGFP emission is reflected on the 560-nm longpass is detected, after cleanup with a 530/50m filter. For mScarlet the emission passes the 560-nm longpass and is cleaned up with a 600/37 filter.

APD detectors were powered by a dedicated power supply (DSN-102, PicoQuant). APD NIM signals are directed towards the HydraHarp 400 (Picoquant) to supply it with photon timing information. For all data acquired on the microscope a 60x water objective (Olympus UPlanSApo 60x/1.20 W ∞/0.13-0.21/FN26.5) was used. The microscope was positioned on a vibration free isolated optical table (S-2000 series Stabilizer™, Newport Spectra-Physics BV, Utrecht, Netherlands).

Frequent system checks, setup alignment and quantifying confocal volume parameters were performed with fluorescence correlation spectroscopy (FCS) using ATTO425-COOH, ATTO488-COOH, Alexa Fluor 546 or ATTO655-COOH (ATTO-TEC GmbH, Siegen, Germany) (Alexa Fluor™, Thermofisher Scientific). Data was analyzed using PAM-*FCSfit* (Supplemental Figure S8). As references for phasor-FLIM, organic dyes were measured using the same optical setup for the assigned detection channel. Reference lifetimes were experimentally determined via PAM-*Taufit* (Supplemental Figure S8) where the decay was fit using a reconvolution fit for a mono-exponential with loaded IRF. Dyes used were ATTO488-COOH, ATTO425-COOH, Alexa Fluor 546 and ATTO 647N-maleimide.

3.4.8 Fluorescent HIV-1 particles

HIV-1-derived viral particles (Vesicular stomatitis virus glycoprotein (VSV-G)-pseudotyped) with fluorescent protein labeled integrase were synthesized using Vpr-mediated trans-incorporation (49, 50). HEK293T cells ($6.5x10^6$) were seeded in 10 cm petri dishes with DMEM supplemented at 2% FBS and 50 µg/mL gentamicin (Invitrogen). For transfection medium was replaced with Opti-MEM® (Life Technologies, ThermoFisher Scientific) supplemented with gentamicin (Invitrogen). Cells were transfected with branched polyethylenimine (bPEI, 10 µM stock solution, Merck, Sigma-Aldrich, Darmstadt, Germany) when 90% confluency was reached. A three-plasmid system, consisting of 5 µg pVSV-G, 15 µg pNL4–3. Luc.R−.E− and Vpr-IN-FP-encoding plasmid (5 µg for single FP viruses, twice 2.5 µg for viruses containing two fluorescent proteins) was used in transfection. pVpr-IN-FP constructs with mTFP1, mTurquoise2, mNeongreen, mClover3, mScarlet, mRuby3, eGFP and mCherry were used. pVpr-IN-FP constructs for mTFP1 and mVenus were made according to Borrenberghs et al. (50). Other pVpr-IN-FP constructs were made by starting from the original pVpr-IN-eGFP plasmid (49). Transfection lasted for 6 hours at 37°C and was terminated by replacing the medium with fresh 37°C Opti-MEM® (Life Technologies, ThermoFisher Scientific) supplemented with 50 µg/mL Gentamycin (Invitrogen). Virus supernatant was collected 48 h after initiating transfection, filtered through a 0.45-µm filter (Minisart® Syringe Filter, Sartorius, Göttingen, Germany), and concentrated by several washing steps in FBS-free Opti-MEM® and virus particles were concentrated by ultracentrifugation on a 60% (w/V) iodixanol cushion at 21°C (131,500 x g, 90 min, SW28 rotor, Beckman Coulter, Ireland) to a final volume of 1 mL. Iodixanol was removed by ultrafiltration (Vivaspin, MWCO 50K, Merck, Overijse, Belgium). All generated viral particles were kept up to 2 months at -80°C, without thaw-freeze cycles.

3.4.9 Glass coating and viral particle plating

Glass coverslips used for viral particle imaging were coated with Poly-D-lysine. This was done by incubating the wells for 20 minutes at 37°C in a 0.4 mg/ml solution (4X) of poly-D-lysine (Merck, P7280-5MG, Sigma-Aldrich, Darmstadt, Germany), made from a 1 mg/ml stock, and followed by washing three times with PBS. Coverslip coating was finished by removing all PBS, and coverslips were air dried in a sterile flow for 30 min. For imaging purposes, concentrated virus particles were freshly thawed and diluted in phosphate-buffered saline (PBS, Merck, 806552, Sigma-Aldrich, Darmstadt, Germany) based on the p24 antigen concentration in the supernatant, as determined by the p24-specific enzyme-linked immunosorbent assay (ELISA). Then, 200 µL of the virus dilution containing 1µg-3µg p24 antigen was transferred to a poly-D-lysine coated glass coverslip (#1 chambered

coverglass, Nunc™ Lab-Tek™, Cat. No. 155411, Thermo Scientific) and incubated at 37 °C for 3-5 hours. The virus particles were gently washed twice with PBS, after which 200 µL PBS was added to each well and the wells were sealed with parafilm to avoid evaporation.

3.4.10 Photobleaching of viral particles

Plated viral particles were imaged until photobleached. Particle tracking was performed across all image frames following total particle counts per frame using the *Particle Detection* module of PAM. Using a separate MATLAB routine, an exponential was fitted onto the decaying fluorescence intensity. All photobleaching rates are the determined b-coefficient of $a.e^{-bt}$ (see also Fig. S9).

3.5 Results

3.5.1 Particle-detection-based pixel binning improves phasor-FLIM of dim particles

As the quality of a phasor-FLIM experiment depends on the photon content of the fluorescence data, we first quantified the effect of pixel binning on phasor-FLIM data. Specifically, we examined the effect of grouping pixels from the same sub-resolution object on the accuracy of the estimated lifetimes. Practically, we simulated confocal FLIM data of non-diffusing fluorophores exhibiting a 4-ns fluorescence lifetime. Because of their random axial location in the simulation box, the resulting image displayed particles with varying intensity in the image plane (Fig. 3.1 *A*).

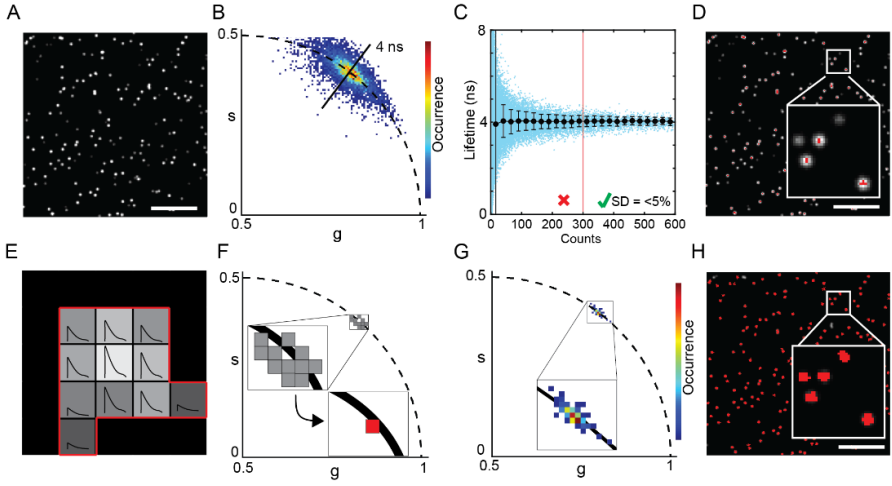


Figure 3.1: Pixel binning for particle phasor-FLIM. (A) Intensity image of simulated sub-resolution single particles with variety of intensities but a constant lifetime of 4 ns. (B) Phasor analysis of the simulated photon data results in a wide spread on the phasor plot where every pixel (threshold for pixels with more than 5 counts) is assigned one phasor. (C) In blue: scatterplot of the pixel counts against the phase lifetime determined from the phasor plot. In black: standard deviation and mean lifetime per bin. Bins are defined as 25 counts wide, mean and standard deviation are plotted in the center coordinate of each bin. (D) Intensity image color coded in red if the pixel counts >300, inset is a 2.5x2.5 µm box. (E) Schematic of a single particle consisting of pixels from the same sub-resolution origin and showing identical decay lifetime composition but different amplitudes. (F) Pixel binning improves the particle phasor. (G) Simulated data from (A-D) analyzed in phasor with particle-based pixel binning shows a compact phasor distribution. (H) Particles color coded if the particle counts are >300 counts. All scalebars are 5 µm.

Due to the overall low intensity per pixel, the resulting phasor plot exhibited a relatively large data spread (Fig. 3.1 *B*). When plotting the phasor determined lifetime (average of phase and modulation lifetime, Eq. 1-2) for every pixel, we observed an increase in lifetime precision for increased photon counts of the pixel (Fig. 3.1 *C*). We determined that a count of 300 photons was ideally needed to obtain lifetime values within a 5% deviation range of the true value. This value can therefore be considered a lower limit, acknowledging that a higher photon count is advised for more complex phasor component deconvolutions. Using this 300-photon count threshold, we false-color-coded the intensity image for the pixels that met this threshold and observed that relatively few pixels from the imaged particles were, in fact, colored (Fig. 3.1 *D*). Of note, multiple pixels share the signal originating from the same sub-resolution emitter with varying amplitudes but identical lifetime signature. Grouping of pixels originating from the same particle therefore should enhance the phasor coordinate calculation (Fig. 3.1 *E-F*). When we applied this pixel binning strategy to the simulated data, we noticed a greatly reduced spread and a highly concentrated particle datapoint population in the phasor plot, now clearly centered on the 4 ns semicircle location. (Fig. 3.1 *G*). Subsequent color-coding of the simulated image for the particles that are detected with a sum of ≥300 photons showed that almost all particles were included into the analysis (Fig. 3.1 *H*). In summary, grouped single-particle phasor analysis helps robustly and accurately determine phasors from dim emitters, such as sub-resolution particles. Additionally, 300 photons per pixel binned particle is a recommended minimum total pixel count target for reliable phasor lifetime determination.

3.5.2 Particle-based Phasor-FLIM resolves individual DNA molecule lifetimes

Next, we investigated whether particle-based phasor-FLIM could successfully allow determining the fluorescence lifetime of single molecules. Therefore, we imaged a model system containing PEG-Biotin immobilized DNA molecules labeled either with only a FRET donor (Fig. 3.2 *A-D*) or with both a FRET donor and acceptor spaced at a distance of 11 nucleotides as reported before (51, 52) (Fig. 3.2 *E-I*). All particles were identified, and particle phasor positions were analyzed in the phasor plot for the average lifetime. A donor only lifetime (τ_D) of 3.92 ns was found with a background (BG) contribution of 1.2% resulting in the measured phasor position (DO). Autofluorescence of the particles itself, here called BG, dragged an otherwise perfect monoexponential measurement inward of the semi-circle due to the complex lifetime signature of the background. The BG position was determined (see Materials and Methods) and was used to Measure the pure lifetime of the donor on the semi-circle using fractionality (Fig. 3.2 *C-D*). With this no-FRET control measured we continued with a double labeled (donor-acceptor) dsDNA system, in

which donor and acceptor labels are separated by 11 nucleotides (Fig. 3.2 *E*). These double-labeled single molecules were imaged using pulsed interleaved excitation (PIE), whereby the donor laser was pulsed at the beginning and our acceptor in the middle of our detection window in between pulses (53, 54). This way quasi synchronously measured both the donor and acceptor without suffering from spectral crosstalk (Fig. 3.2 *F*). Colocalization was confirmed in a subset of single molecules using both donor and acceptor channel information. Using a maximum distance of 5 pixels between colocalization candidate centers, 133 single molecule dsDNA particles were found. From the colocalized particles (Fig. 3.2 *G*), the donor signal upon donor excitation was used to calculate all phasor positions per particle using particle pixel binning. From the average position of the single (donor) labeled single dsDNA molecules (DO) and the previously measured *BG* coordinates (Fig. 3.2 *B*), a FRET trajectory was formed describing all possible FRET states ranging from 0% (phasor position equals the DO position) to 100% FRET (phasor position equals the only remaining signal of BG; all donor signal is quenched) (Fig. 3.2 *G*). Finally, the FRET histogram resulting from projection of phasor positions onto the FRET trajectory showed an average value of 56% FRET (Fig. 3.2 *H, I* and Fig. S1 *G*). Taking into account a Förster radius of 50.3 Å for Alexa 488 and ATTO 647N, the estimated donor-acceptor distance from our FRET measurement was determined to be 39 Å.

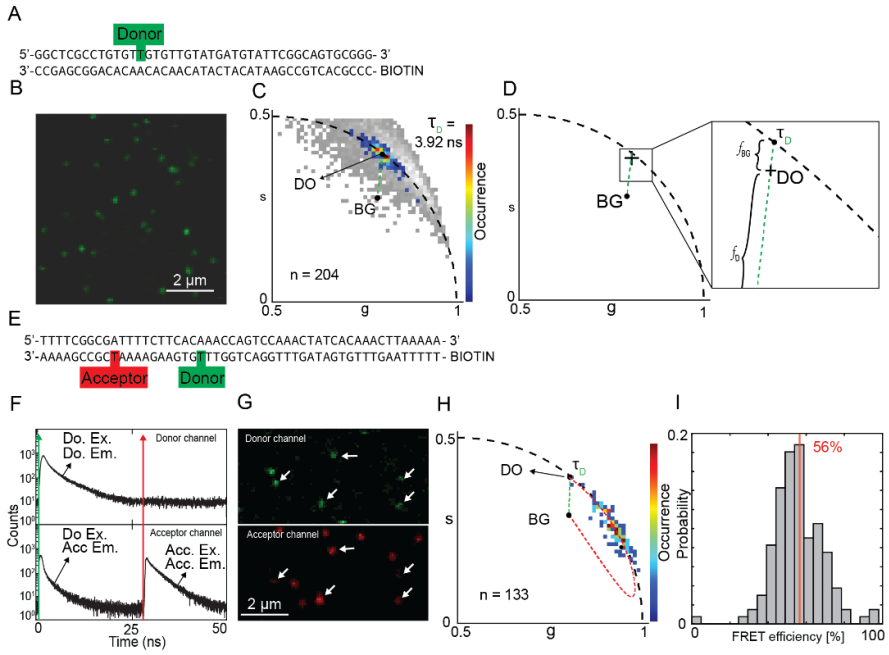


Figure 3.2: Determination of FRET labeled dsDNA FRET efficiency. (A) dsDNA strand with a single donor label on the sense strand. (B) microscopy image using 485

nm excitation revealing single particles. (C) Pixel-binned particle phasor analysis on the donor-labeled dsDNA reveals its photon weighted center of mass (DO) revealing the donor lifetime of 3.92 ns (τ_D) upon extension of the $BG - DO$ fraction line to reveal its pure contributing species. Pixel based phasor with a 10 photon/pixel threshold shown in gray. (D) Illustration of the contributing species to the phasor (DO) location (BG and τ_D) of the donor only labeled dsDNA. (E) dsDNA with on the antisense strand both donor and acceptor present and a biotin tag on the 5' end used for immobilization on the glass. (F) Pulsed Interleaved Excitation (PIE) measurement of FRET labeled dsDNA used for colocalization. (G) Intensity image of double labeled dsDNA showing a single region of interest for both donor and acceptor channel as determined by colocalization of both donor and acceptor channels for donor and acceptor excitation respectively. White arrows indicate colocalized particles. (H) Phasor plot of imaged FRET labeled dsDNA strands showing the autofluorescence phasor (BG), the donor only phasor DO, The quenching trajectory (red dashes) connecting the BG phasor with the DO phasor (see Eq. 22 & 23). The fraction line between BG en DO (green dashes). (I) FRET efficiency histogram derived from the FRET trajectory. Vertical red line visualizes the average value.

3.5.3 Performance comparison of single FP labeled integrase

With our positive FRET control in place, we connect to the open research field of HIV-1 integrase (IN) multimerization, previously conducted in our lab. Earlier, the FRET readout of recombinant HIV-1 particles containing fluorescent protein (FP) labelled IN (mTFP1-mVenus FRET pair) was investigated with intensity based acceptor photobleaching FRET methods throughout the replication cycle (41–43). To extend this study using our particle-based phasor-FLIM approach we explored which FP labels for IN performed superior for further application in FRET measurements involving donor FP and acceptor FP labeled IN monomers. Moreover, since an HIV-1 particle is a highly condensed environment and this might affect the fluorescence lifetime and overall FP performances, we furthermore decided to determine the optimal FRET pair directly in a HIV-1 particle context (55).

Practically we generated HIV-1 particles incorporating a single type of FP-labeled IN, allowing us to quantitatively compare several FRET donor and acceptor labels. First, we analyzed the HIV-1 particles for their brightness. We observed that especially particles containing IN-mTurquoise2 easily yielded more than 300 photons as the frequency distribution peaks less in the low photon range (<100 counts). Conversely, mNeongreen-particle preparations did not result in many high photon count particles as the frequency distribution peaked at 30-40 photons (Fig. 3.3 *A*). For acceptor candidates the photon distribution were rather similar (Fig. 3.3 *E*).

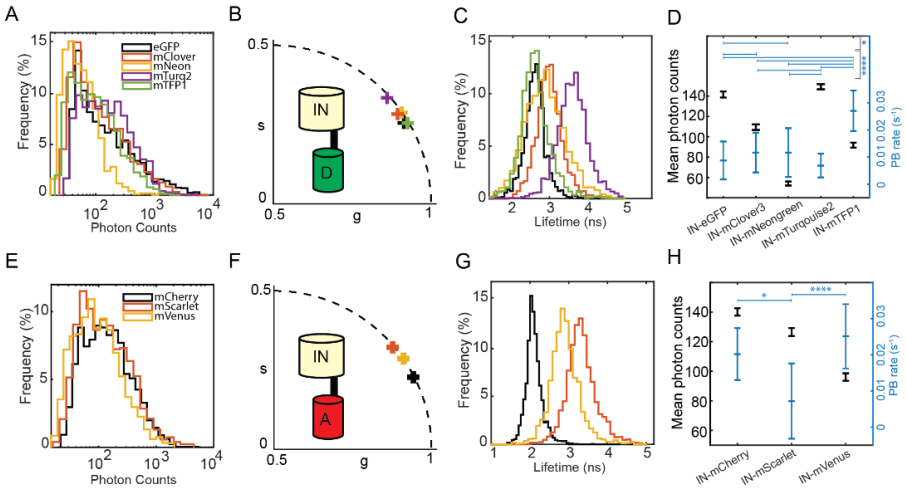


Figure 3.3: Lifetime, photon count and photobleaching study of single-FP HIV-IN labeled virions on glass. (A,E) Count distributions of donor (A) and acceptor (E) labeled HIV-IN-FP virions. (B,F) Photon weighted centroid position of the phasor clouds of all respective donor and acceptor HIV-IN-FP virions. (C,G) Mono-exponential phase lifetime distribution of the donor and acceptor HIV-IN-FP virions using a particle threshold of 10 counts to evaluate broadness of lifetime distribution. (D,H) Geometric mean photon counts normalized for excitation efficiency and the associated mean photobleaching rate of all donor and acceptor HIV-IN-FP particles. All geometric mean photon counts are significantly different from each other ($p<0.05$), significance levels for photobleaching rates are determined by a one-way ANOVA non-paired non-parametric Kruskal-Wallis test with multiple comparison (* = $p<0.05$, **** = $p<0.001$).

Next, we verified whether all IN-FP candidates, especially the donors, exhibited a mono exponential lifetime, which would enable us to use semi-circle derived lifetime values (phase or modulation lifetime would work) for evaluation. The plotted centroid positions of all measured particles in the phasor plot indicate that there is indeed a dominant mono exponential behavior (Fig. 3.3 *B,F*). Plotting all semi-circle derived phase lifetimes and their respective lifetime spread in a lifetime histogram shows their peak values and variability, introduced by the FP itself, the photon statistics per particle or shot noise. Histogram means for each fluorophore were: eGFP 2.66±0.31 ns (n = 2675), mTFP1 2.62±0.41 ns (n= 1769), mNeongreen 2.90±0.60 ns (n= 1972), mClover3 3.01±0.39 ns (n= 2219), mTurquoise2 3.68±0.45 ns (n= 2375), mCherry 2.10±0.22 ns (n= 2164), mScarlet 3.34±0.4 ns (n = 2309) and mVenus 2.71±0.39 ns (n = 2125). With a variability of more than 0.5 ns, IN-mNeongreen particles are most unfavorable (Fig. 3.3 *C,G*). Measured photobleaching rates of the fluorescent proteins indicated a high rate for mTFP1 (0.0280 ± 0.0075, n = 29) while other donor candidates have a more favorable

photobleaching rate: eGFP (0.0097 ± 0.0072, n = 143), mTurquoise2 (0.0078 ± 0.0044, n = 265), mClover3 (0.0127 ± 0.0073, n = 638), mNeongreen (0.0126 ± 0.0090, n = 112)(Fig. 3.3 *D*). When comparing the geometric mean photon counts all particles were significantly different from each other ($p<0.001$) and again eGFP (144.7, n = 2675) and mTurquoise2 (148.1, n = 2375) were best performing while mNeongreen (56.5, n = 1972), mClover3 (111.5, n = 2219) and mTFP1 (94.2, n = 1769) were significantly lower (all $p<0.001$)(Fig. 3.3 *D*). Regarding the measured acceptor photobleaching rates, mCherry (0.0202±0.0072, n = 15) and mVenus (0.0251 ± 0.0089, n = 17) exhibited a significantly larger photobleaching rate compared to mScarlet (0.0072 ± 0.0104, n = 14) ($p<0.05$ and $p<0.001$ respectively) (Fig. 3.3 *H*). Mean photon counts were again all significantly different ($p<0.001$) and mCherry (118.7, n = 2164) and mScarlet (110.5, n = 2309) outperformed mVenus (90.1, n = 2125) (Fig. 3.3 *H*). Based on these results, we selected eGFP and mTurquoise2 as they appear to be favorable donor candidates that can be paired with acceptors from our assay that also scored adequately. Due to its favorable photostability, mScarlet was shown to be the most promising acceptor compared to mCherry and mVenus. In summary, we have identified suitable FRET donors and acceptors attached to integrase in the HIV-1 viral particles. The mTurquoise2-mVenus and eGFP-mScarlet pairs were selected for further single-particle FRET experiments.

3.5.4 Graphical phasor analysis reveals integrase multimers in HIV-1 viral particles

IN is known to adopt different oligomeric states depending on the step in the replication cycle. Methods to quantify this oligomeric state of IN at the level of single viral particles and viral complexes are highly desired by virologists. In earlier work, the oligomeric state of IN was quantified with acceptor photobleaching intensity-based FRET. There, the dynamic range of the FRET quantifications was unavoidably lowered by the presence of (variable amounts of) FRET donor-only labeled complexes. Using phasor-FLIM in the present work, we sought to further disentangle the actual FRET species from any non-FRET species and background.

Now, we employ the particle-based phasor-FLIM methodology on the FRET measurements for our previously selected fluorescent FRET pairs. Each pair covers other sections of the visible spectrum, exhibits a slightly different Förster distance (58.3 Å for mTurquoise2-mVenus and 56.7 Å for eGFP-mScarlet from calculations assuming κ^2 to be 2/3 and refractive index n of 1.33 with the donor quantum yields being 0.93 and 0.60 respectively) and encompass a FRET donor with substantially different lifetimes. Ultimately, regardless of the fluorescent labels on IN, we wanted to evaluate the FRET state of IN complexes in the assembled

virus particles to gain further insight into IN multimerization. Assuming a system where only monomeric IN and dimeric IN is present, in any combination possible (A, D, D:D, D:A, A:D, A:A), in a matured HIV-1 particle, there will be a passive donor intensity fraction between 50% (all IN complexes are dimers, the donor-only signal intensity fraction constitutes 50% of the total donor signal intensity) and 100% (all IN complexes are monomers, no FRET occurs). It is only when higher order multimers such as tetramers are formed, leading to a range of different combination between D and A (e.g., DDDA, DDAD, DADD, ADDD, ADAD, DADA), that the fraction of passive donors in IN complexes is further lowered, simultaneously increasing the overall FRET signal of a single HIV-1 particle. Since at the particle level both FRET and the passive donor fraction are unknown, no direct FRET readout can be provided. However, matching the particle phasor data with the possible FRET trajectories constructed by a range of passive donor contributions, should still give insights into the multimer composition. Practically, as shown in Fig. 3.4 *A* and *B,* we recorded FLIM data of FRET donor/acceptor double labeled immobilized viral particles at photon counts compatible with single-particle phasor-FLIM and performed particle detection on the resulting FRET donor images. FRET trajectories are constructed using a background reference (see Materials and Methods) and the HIV-1 particle measurements with only the donor label (HIV-1 containing only IN-mTurquoise2 or IN-eGFP, see Fig. S10). Again, the signal intensity contribution of BG in the measured donor signal draws the phasor position away from the semi-circle and serves as starting position for the FRET quenching line (as is previously illustrated in Fig. 3.2 *D*). For particles with IN-mTurquoise2 and IN-mVenus BG had a 7.5% contribution and for IN-eGFP/IN-mScarlet particles 10.5%, as determined graphically from the phasor plot. Subsequently, HIV-1 particles containing both donor and acceptor labeled IN were measured and the particle-based phasor distribution was calculated. On top, we plotted all possible FRET trajectories for passive donor contributions between 0% and 50% and found that for IN-eGFP+IN-mScarlet particles, a 0-20% passive donor contribution resulted in FRET trajectories that described the data well (see also Fig. S12). The smaller phasor shift for FRET particles containing IN-mTurquoise+IN-mVenus relative to the D-only population, on the other hand, did not allow us to pinpoint a reasonable range of passive donor contribution. Critically, pixel-based phasors of the for IN-eGFP+IN-mScarlet particles also did not enable narrowing down the passive donor-contribution (Fig. S11). Finally, by projecting the phasor data of IN-eGFP+IN-mScarlet particles onto the FRET trajectory we determined average FRET efficiency distributions between 26% and 39% (in Fig. 3.4 *C* the FRET efficiency distribution for the 10% passive donors is shown) with an average FRET of 32%.

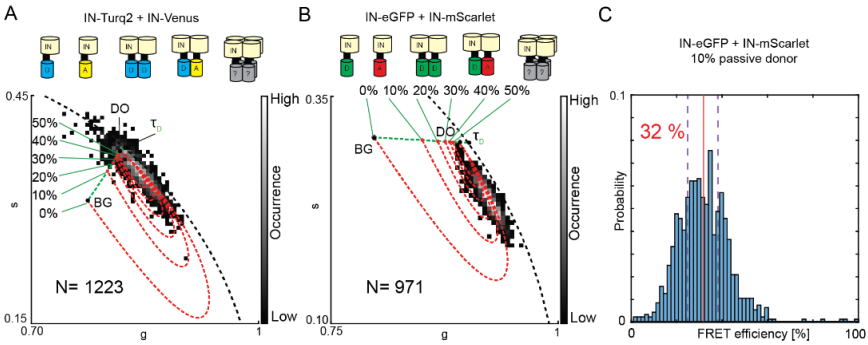


Figure 3.4: FRET trajectory analysis of HIV-1 particles containing donor labeled IN and acceptor labeled IN using particle-based pixel binning. (A) Phasor analysis of viral HIV-1 particles containing both donor and acceptor labeled IN (IN-Turquoise2+IN-mVenus) forming an unknown mix of multimers including monomers and dimers and potentially higher order multimers. The donor only phasor (DO) (g = 0.82, s:0.37 and background phasor (BG) (g = 0.78, s:0.31) determine the starting point and end of the FRET trajectory. Variations of the donor only signal contribution in the analyzed particles result in a variety of FRET trajectories and FRET trajectory end points (red dotted line). (B) Phasor analysis of viral HIV-1 particles containing both donor and acceptor labeled IN (IN-eGFP+IN-mScarlet) forming an unknown mix of multimers including monomers and dimers and potentially higher order multimers. The donor only phasor (DO) (g = 0.90, s:0.29) and background phasor (BG) (g = 0.79, s:0.31) determine the starting point and end of the FRET trajectory. Variations of the donor only signal contribution in the analyzed particles result in a variety of FRET trajectories and FRET trajectory end points (red dotted line). In both (A) and (B) the pure mono-exponential lifetime of the donor (τ_D) and BG determine by intensity fraction the position of DO on their connecting fraction line (green dotted line). (C) FRET histogram for (B) extracted from the 0%,10% and 20% passive donor contribution FRET trajectories of which the 0% and 20% histogram averages are indicated by purple dashed lines and the 10% passive donor histogram (shown) average is depicted as a vertical full red line with its value.

3.6 Discussion

In this chapter, we demonstrated the usage of time domain phasor-FLIM in combination with grouped pixel analysis for sub-resolution single particles. We applied this method on FRET labelled DNAs and on viral HIV-1 particles that contain single (donor) or double (donor and acceptor) labelled IN (intermolecular FRET), the latter exhibiting FRET upon multimerization as demonstrated before using intensity-based approaches (43, 50).

First, we studied the effect of grouping pixels to obtain a higher quality phasor determination, optimizing the analysis to utilize all available photons of a particle. In a perfect setting (no background) our simulations showed that 300 photons is the lower limit for proper particle photon statistics leading to a phasor determination within a 5% error range of the true lifetime of a single component. Therefore, when measuring with considerable background or working with complex multi-component samples, effects which can quantitatively be studied via similar simulations, it is advised to maximize the number of successfully detected and timed photons per object. The 4 ns reference used in the simulation was chosen to accommodate all lower fluorescence lifetime components, given a shorter fluorescence lifetime requires, in theory, fewer photons to be accurately determined. The needed photon budget for FRET analysis is the weak point of every FRET. On the other hand, the photon detection and timing efficiency is continuously improved with newer FLIM methodologies (e.g. digital frequency domain (10), Leica Falcon (56), Picoquant rapidFLIM (57), ...) with ultra-low detection dead times or allowing to detect more than one photon per excitation pulse. At the same time, using FLIM with PIE would additionally allow the simultaneous readout of intensity-based and FLIM-FRET, as is routinely done in smFRET burst measurements using multiparameter fluorescence detection with PIE (52, 58). Additionally, PIE would allow multiplexing of (FRET) probes, as in three or even four color immobilized FRET (59) or using dark acceptor probes (60). Single object FLIM analysis was first used by Qian et al. (40) for viral particle FLIM analysis and now further explored here with complex FRET behavior. We envision that this technique could be further applied in small organelles, protein complexes, immobilized single molecules or any system where signals originate from a sub-resolution entity (and are therefore measured as average, potentially spread over multiple pixels). Using object pixel binning allows for more precise analysis as one can oversample the image and later bin the pixels of desired structures. In this chapter we have shown the importance of our particle-based analysis given the increased resolution to utilize phasor in a graphical manner. As a remark, we measured our FLIM data using a 20 MHz pulse rate, combining both acceptor and donor pulsing in a 50-ns pulse window, to ensure full decays were considered in phasor analyses. For an illustration of the effects of decay truncation, larger lifetimes and used TAC range on the resulting phasor cloud

shape, the reader is referred to Supplemental Figure S13. When PIE is not required, the used pulsing frequency can be changed to optimize the usage of the phasor space for graphical purposes. A formula was provided by Clegg et al in 2005 for frequency-domain phasor analysis (9):

$$\omega_{optimal} = \frac{1+\sqrt{3}}{2\tau^2} = f_{optimal} 2\pi \ , \qquad \text{Eq. 24}$$

which would result in an optical frequency of ~46-50 MHz for a 4-ns lifetime. However, for time domain phasor applications the main improvement on the resolution of calculated *s* and *g* values will arise from a lowered TCSPC bin size.

Next, we tested the effect of pixel-grouping on labeled DNA structures, with two fluorescent dyes set 11 nucleotides apart, to evaluate the detection and quantification of FRET by using the graphical phasor approach to FLIM. The obtained value of 39 Å is in close agreement with the literature, which described a value of 40 Å, determined by FRET restrained positioning and screening (FPS) simulations (52). Since a broad cross-lab study on dye-labeled DNAs pointed out their robustness, we deem our measurements as a validation of the analysis performance (51). We confirmed that the object binning strategy together with the phasor plot analysis allowed for determination of single molecule FRET via their lifetime signatures. This DNA sample provided a double labeled single molecule structure exhibiting a FRET signal from a known donor-acceptor stoichiometry, not complicating the measurement with a donor only fraction.

Thirdly, we analyzed the performance of several fluorescent proteins as fusion proteins to IN inside viral particles, as it is difficult to predict the effect of IN coupling and the dense viral particle environment on the fluorescence brightness, lifetime and fluorescent protein maturation.

Table 3.1: Overview of measured single label IN in HIV-1 viral particles.

FP	Literature Lifetime (ns)	Measured lifetime (ns)	Measured photobleaching rate	Maturation (min)	Literature brightness	Measured geomean photon count	References
EGFP	2.6	2.61 ± 0.31	0.0097± 0.0073	25	33.54	144.7	(61)(62)
mClover3	3.2	3.01 ± 0.39	0.0127 ±0.0073	43.5	85.02	111.5	(62)(63)
mNeongreen	3.1	2.90 ± 0.60	0.0126 ± 0.0090	10	92.8	56.5	(63)
mTurquoise2	4.0	3.68 ± 0.45	0.0078 ± 0.0044	33.5	27.9	148.1	(64)
mTFP1	3.2	2.62 ± 0.41	0.0280 ± 0.0075	76.5	54.4	94.2	(65)
Cherry	1.49*	2.10 ± 0.22	0.0202 ± 0.0072	15	15.6	118.7	(66)(67)
Scarlet	3.86	3.34 ± 0.41	0.0072 ± 0.0104	174	71	110.5	(63)(68)
Venus	3.1	2.71 ± 0.39	0.0251 ± 0.0089	17.6	66.56	90.1	(69)

*Averaged 2 component lifetime

The donor fluorescence lifetimes were comparable to the known mono-exponential lifetimes found in literature for these FPs except mTFP1 which was 0.6 ns lower compared to the literature value of 3.2 ns (Table 3.1). The mCherry lifetime was also found to be inconsistent with literature, which could not be explained by the shifted ratios of the two exponential factors normally involved in a mCherry decay. Wu et al. described a two component lifetime for mCherry of 0.9 ns and 1.9 ns which are both lower than the measured 2.1 ns (70). mVenus and mScarlet on the other hand both measured 0.4 ns and 0.5 ns, which was above the normal literature values. In general, longer lifetimes are preferred for FRET because of higher dynamic range given a limited time resolution on the hardware side (62). Indeed, it is more straightforward to measure a 2 ns difference compared to a 0.5 ns difference to determine a 50% FRET efficiency in a donor with a respective lifetime of 4 and 1 ns. Further, we expected a photostability double as good for mNeongreen compared to mClover3 (71). However, we recorded a similar photostability, which could be hinting to a photophysical problem for mClover3 or a gained benefit for mNeongreen in the HIV-1 particle environment. Evaluating the particle photon counts, mClover3 and mNeongreen both underperformed while having the highest literature described brightness, further strengthening our belief that the emission of mClover3 is hampered in the viral particles. mTurquoise2 and mCherry performed well considering a generally low brightness. These findings lead us to conclude that fluorescent behaviors of IN-labeled proteins in HIV-1 are difficult to predict. We note that for some FPs of similar spectra identical filters were used and that the slightly different treatment of the filter of the emission spectrum could have introduced a small bias into our data.

Lastly, we studied viral particles using FRET. For both viral particles types used in our final FRET experiment with HIV-1 particles, the phasor was calculated. Based on the position of the phasor clouds on the plotted array of FRET trajectories, it can

be safely concluded that for IN-eGFP+IN-mScarlet particles only 0-20% passive donors are present in the particles. With that, a scenario in which only monomers are present (in equal numbers D and A) is already excluded. Even a combination of only monomers or dimers in the particles cannot result in our experimentally observed FRET readout, as this would still require the D-only fraction to be close to 50% passive donor signal (D, A, DA, AD, DD and AA results in ~50% signal D-only). Furthermore, owing to the quantification of the FRET trajectory incorporating the range of acceptable D-only fractions, we narrowed down the possible FRET values down to 26-39%. In samples with roughly equal numbers of IN-donor and IN-acceptor molecules this can only be explained by the presence of higher order multimers which reduce the overall pure donor species since more are involved in FRET-active oligomers. For particles containing IN-mTurquoise+IN-mVenus, narrowing down the FRET values by FRET trajectory analysis proved more challenging. It is anticipated that the particles contain too large amounts of passive donors as a result of more donor than acceptor labeled IN in the particles. Even though, at least for IN-eGFP/IN-mScarlet, phasor-FLIM did provide novel insights into the oligomeric state of IN inside viral particles, this graphical analysis of phasor plots remains challenging for a variety of reasons. Firstly, there remains a large error on the precise fraction of passive donors present in the particles, together with between-particle variation of that number. Additionally, every multimer formed in the imaged particles has its own FRET efficiency since it consists of a variable content of unlabeled and labeled (donor or acceptor) resulting in an extra variability in FRET readouts. Furthermore, the composition of unlabeled, donor labeled and acceptor labeled cannot be verified, adding to difficulty of data interpretation. Overall, we can assume that measuring close to or more than 1000 particles provides a strong averaged readout with valuable information on the FRET state and therefore insight in the multimeric state of HIV-IN in assembled virus particles. One possible avenue of further investigation is redesigning particles with variable D-A ratios, variable total amounts of labels per particle, or non-FP labeling strategies altogether. Additionally, because the number of fluorescent proteins per particle is limited, the photon output is low and contributions of background and shot noise are considerable. We clearly show that taking the fraction of passive donors into account is essential. This factor is often overlooked because estimating the donor only fraction is difficult. Using the phasor analysis, we acknowledged the presence of passive donors in our viral particles, which will in any case, lower the apparent FRET signal measured. Given a more precise technique to determine the number of passive donors, researchers would be able to pinpoint which FRET trajectory is suitable and derive more absolute FRET efficiency values. At the same time, determining the number of passive donors present in a mixture of FRET displaying IN multimers remains a variable that can change particle to particle and can therefore not be fully generalized. Although we cannot pinpoint the exact oligomerization state of every IN complex per particle, we can give a founded ensemble evaluation of the in vitro oligomeric state and expect to improve further

when photon yield of such experiments becomes more efficient, increasing our phasor data quality. By trying to deconvolve the passive donor contribution we increase out analysis sensitivity to FRET changes, since the significant contribution can overshadow it otherwise. Optimization of the viral particle production to eliminate passive donor molecules as much as possible is a future research target.

Several additional tools can be used when working with phasor representations of FLIM. In our work we chose to work with unfiltered phasor data, but a median or wavelet filter can concentrate the phasor cloud even more, although caution is advised in using these tools (see also Fig. S14). In addition, to disentangle contributions from shot noise and FRET heterogeneity, phasor analysis could be combined with photon distribution analysis (PDA) (72).

3.7 Conclusion

Having presented our work on phasor-FLIM using our particle-based analysis on FRET in viral particles, we aim to contribute in future research lines further enhancing the phasor methodology. The fit-free character of phasor should not pose a restraint for analyzing data in-depth and with great care. Used correctly, the phasor approach allows for very streamlined analysis and benefits from a highly interesting pixel-phasor reciprocity allowing to select parts of the image based on phasor locations (or clusters) or vice versa. Qualitatively, a phasor is a superior tool to dissect FRET-FLIM data. Quantitatively, it requires thought and challenging parameters such as the contribution of passive donors. Combined with the graphical nature of phasor analysis, the number of photons per analyzed pixel is crucial to establish solid photon arrival statistics and/or estimate FRET values or lifetime values. In this regard, the proposed particle-based phasor can strongly improve analysis in comparison with pixel-based when the sample allows for it. Using FRET labeled dsDNA we have shown the potential of quantitative FRET analysis extracting a FRET histogram from the phasor plot and in doing so match previous experiments determining the FRET in these single molecules. Particle-based FRET analysis on labeled IN in HIV-1 viral particles proved challenging. However, we provided a particle FRET range which would not be feasible in a straightforward manner using intensity-based FRET, as passive donors would obscure the value since they are unaccounted for.

3.8 Supporting material

Three supplemental notes and fourteen supplemental figures are available in **Addendum 1** of this thesis.

3.9 Acknowledgments

Jens de Wachter is thanked for assistance with the DNA experiments. Dr. Waldemar Schrimpf is thanked for implementing phasor analysis in PAM and evaluating the manuscript. Namjoo Vanderveken is acknowledged for assistance in producing the viral particle preparations. Rik Nuyts, Carine Jackers and Débora Linares are gratefully acknowledged for assistance in the lab and essential logistics. Dr. Kris Janssen is thanked for writing the software for galvanometric mirror scanning. Dr. Irena Zurnic Bönisch is acknowledged for critically reading the manuscript. J.Hofkens acknowledges financial support from the Research Foundation - Flanders (FWO Grant Numbers G0F2322N and ZW15_09-GOH6316), the Flemish government through long-term structural funding Methusalem (CASAS2, Meth/15/04) and the MPI as MPI fellow. J.Hendrix acknowledges Research Foundation Flanders (FWO, projects G0B4915, G0B9922N and G0H3716N) and KU Leuven Special Research Fund (C14/16/053).

3.10 References

1. T.M. Heaster, J.T. Sharick, A.A. Gillette, and M.C. Skala. 2020. Fluorescence lifetime imaging microscopy: fundamentals and advances in instrumentation , analysis , and applications. 25.
2. Chen, Y.C., B.Q. Spring, and R.M. Clegg. 2012. Fluorescence lifetime imaging comes of age how to do it and how to interpret it. *Methods Mol. Biol.* 875:1–22.
3. Berezin, M.M.Y., and S. Achilefu. 2010. Fluorescence Lifetime Measurements and Biological Imaging. *Chem. Rev.* 110:2641–2684.
4. Verveer, P.J., A. Squire, and P.I.H. Bastiaens. 2000. Global analysis of fluorescence lifetime imaging microscopy data. *Biophys. J.* 78:2127–2137.
5. Verveer, P.J., and P.I.H. Bastiaens. 2003. Evaluation of global analysis algorithms for single frequency fluorescence lifetime imaging microscopy data. *J. Microsc.* 209:1–7.
6. Digman, M.A., V.R. Caiolfa, M. Zamai, and E. Gratton. 2008. The phasor approach to fluorescence lifetime imaging analysis. *Biophys. J.* 94:L14–L16.
7. Weber, G. 1981. Resolution of the fluorescence lifetimes in a heterogeneous system by phase and modulation measurements. *J. Phys. Chem.* 85:949–953.
8. Jameson, D.M., E. Gratton, and R.D. Hall. 2007. The Measurement and Analysis of Heterogeneous Emissions by Multifrequency Phase and Modulation Fluorometry. *https://doi.org/10.1080/05704928408081716*. 20:55–106.
9. Redford, G.I., and R.M. Clegg. 2005. Polar plot representation for frequency-domain analysis of fluorescence lifetimes. *J. Fluoresc.* 15:805–815.
10. Colyer, R.A., C. Lee, and E. Gratton. 2008. A novel fluorescence lifetime imaging system that optimizes photon efficiency. *Microsc. Res. Tech.* 71:201–213.
11. Hinde, E., M.A. Digman, C. Welch, K.M. Hahn, and E. Gratton. 2012. Biosensor Förster resonance energy transfer detection by the phasor approach to fluorescence lifetime imaging microscopy. *Microsc. Res. Tech.* 75:271–281.
12. Lou, J., A. Solano, Z. Liang, and E. Hinde. 2021. Phasor Histone FLIM-FRET Microscopy Maps Nuclear-Wide Nanoscale Chromatin Architecture With Respect to Genetically Induced DNA Double-Strand Breaks. *Front. Genet.* 12:1–9.
13. Celli, A., S. Sanchez, M. Behne, T. Hazlett, E. Gratton, and T. Mauro. 2010. The epidermal Ca2+ gradient: Measurement using the phasor representation of fluorescent lifetime imaging. *Biophys. J.* 98:911–921.
14. Levitt, J.A., S.P. Poland, N. Krstajic, K. Pfisterer, A. Erdogan, P.R. Barber, M. Parsons, R.K. Henderson, and S.M. Ameer-Beg. 2020. Quantitative real-time imaging of intracellular FRET biosensor dynamics using rapid multi-beam confocal FLIM. *Sci. Rep.* 10:1–9.
15. Liu, Z., D. Pouli, C.A. Alonzo, A. Varone, S. Karaliota, K.P. Quinn, K. Mönger, K.P. Karalis, and I. Georgakoudi. 2018. Mapping metabolic changes by noninvasive, multiparametric, high-resolution imaging using endogenous contrast. *Sci. Adv.* 4.
16. Davis, R.T., K. Blake, D. Ma, M.B.I. Gabra, G.A. Hernandez, A.T. Phung, Y. Yang, D. Maurer, A.E.Y.T. Lefebvre, H. Alshetaiwi, Z. Xiao, J. Liu, J.W. Locasale, M.A. Digman, E. Mjolsness, M. Kong, Z. Werb, and D.A. Lawson. 2020. Transcriptional diversity and bioenergetic shift in human breast cancer metastasis revealed by single-cell RNA

sequencing. *Nat. Cell Biol.* 22:310–320.
17. Datta, R., A. Alfonso-Garciá, R. Cinco, and E. Gratton. 2015. Fluorescence lifetime imaging of endogenous biomarker of oxidative stress. *Sci. Rep.* 5:1–10.
18. Stringari, C., H. Wang, M. Geyfman, V. Crosignani, V. Kumar, J.S. Takahashi, B. Andersen, and E. Gratton. 2015. In Vivo Single-Cell Detection of Metabolic Oscillations in Stem Cells. *Cell Rep.* 10:1–7.
19. Wright, B.K., L.M. Andrews, M.R. Jones, C. Stringari, M.A. Digman, and E. Gratton. 2012. Phasor-flim analysis of NADH distribution and localization in the nucleus of live progenitor myoblast cells. *Microsc. Res. Tech.* 75:1717–1722.
20. Stringari, C., R.A. Edwards, K.T. Pate, M.L. Waterman, P.J. Donovan, and E. Gratton. 2012. Metabolic trajectory of cellular differentiation in small intestine by Phasor Fluorescence Lifetime Microscopy of NADH. *Sci. Rep.* 2.
21. Schrimpf, W., J. Jiang, Z. Ji, P. Hirschle, D.C. Lamb, O.M. Yaghi, and S. Wuttke. 2018. Chemical diversity in a metal-organic framework revealed by fluorescence lifetime imaging. *Nat. Commun.* 9.
22. Fereidouni, F., A.N. Bader, and H.C. Gerritsen. 2012. Spectral phasor analysis allows rapid and reliable unmixing of fluorescence microscopy spectral images. *Opt. Express*. 20:12729.
23. Scipioni, L., A. Rossetta, G. Tedeschi, and E. Gratton. 2021. Phasor S-FLIM: a new paradigm for fast and robust spectral fluorescence lifetime imaging. *Nat. Methods*. 18:542–550.
24. Ranjit, S., L. Lanzano, and E. Gratton. 2014. Mapping diffusion in a living cell via the phasor approach. *Biophys. J.* 107:2775–2785.
25. Scipioni, L., E. Gratton, A. Diaspro, and L. Lanzanò. 2016. Phasor Analysis of Local ICS Detects Heterogeneity in Size and Number of Intracellular Vesicles. *Biophys. J.* 111:619–629.
26. Chiu, C.L., and E. Gratton. 2013. Axial super resolution topography of focal adhesion by confocal microscopy. *Microsc. Res. Tech.* 76:1070–1078.
27. Verveer, P.J., A. Squire, and P.I.H. Bastiaens. 2000. Global Analysis of Fluorescence Lifetime Imaging Microscopy Data. 78:2127–2137.
28. Pelet, S., M.J.R. Previte, L.H. Laiho, and P.T.C. So. 2004. A Fast Global Fitting Algorithm for Fluorescence Lifetime Imaging Microscopy Based on Image Segmentation. *Biophys. J.* 87:2807–2817.
29. Ranjit, S., L. Malacrida, D.M. Jameson, and E. Gratton. 2018. Fit-free analysis of fluorescence lifetime imaging data using the phasor approach. *Nat. Protoc.* 13:1979–2004.
30. Rahim, M.K., J. Zhao, H. V. Patel, H.A. Lagouros, R. Kota, I. Fernandez, E. Gratton, and J.B. Haun. 2022. Phasor Analysis of Fluorescence Lifetime Enables Quantitative Multiplexed Molecular Imaging of Three Probes. *Anal. Chem.* 94:14185–14194.
31. Albertazzi, L., D. Arosio, L. Marchetti, F. Ricci, and F. Beltram. 2009. Quantitative FRET analysis with the E0GFP-mCherry fluorescent protein pair. *Photochem. Photobiol.* 85:287–297.
32. De Los Santos, C., C.W. Chang, M.A. Mycek, and R.A. Cardullo. 2015. FRAP, FLIM, and FRET: Detection and analysis of cellular dynamics on a molecular scale using

fluorescence microscopy. *Mol. Reprod. Dev.* 82:587–604.
33. Maus, M., M. Cotlet, J. Hofkens, T. Gensch, F.C. De Schryver, J. Schaffer, and C.A.M. Seidel. 2001. An experimental comparison of the maximum likelihood estimation and nonlinear least-squares fluorescence lifetime analysis of single molecules. *Anal. Chem.* 73:2078–2086.
34. Cotlet, M., S. Masuo, G. Luo, J. Hofkens, M. Van Der Auweraer, J. Verhoeven, K. Müllen, S.X. Xiaoliang, and F. De Schryver. 2004. Probing conformational dynamics in single donor-acceptor synthetic molecules by means of photoinduced reversible electron transfer. *Proc. Natl. Acad. Sci. U. S. A.* 101:14343–14348.
35. Kuimova, M.K., S.W. Botchway, A.W. Parker, M. Balaz, H.A. Collins, H.L. Anderson, K. Suhling, and P.R. Ogilby. 2009. Imaging intracellular viscosity of a single cell during photoinduced cell death. *Nat. Chem.* 1:69–73.
36. Okabe, K., N. Inada, C. Gota, Y. Harada, T. Funatsu, and S. Uchiyama. 2012. Intracellular temperature mapping with a fluorescent polymeric thermometer and fluorescence lifetime imaging microscopy. *Nat. Commun.*
37. Agronskaia, A. V, L. Tertoolen, and H.C. Gerritsen. 2004. Fast fluorescence lifetime imaging of calcium in living cells. .
38. Goryashchenko, A.S., A.A. Pakhomov, A. V. Ryabova, I.D. Romanishkin, E.G. Maksimov, A.N. Orsa, O. V. Serova, A.A. Mozhaev, M.A. Maksimova, V.I. Martynov, A.G. Petrenko, and I.E. Deyev. 2021. FLIM-Based Intracellular and Extracellular pH Measurements Using Genetically Encoded pH Sensor. *Biosensors*. 11.
39. Lin, H.J., P. Herman, and J.R. Lakowicz. 2003. Fluorescence Lifetime-Resolved pH Imaging of Living Cells. *Cytometry. A.* 52:77.
40. Qian, C., A. Flemming, B. Müller, and D.C. Lamb. 2022. Dynamics of HIV-1 Gag Processing as Revealed by Fluorescence Lifetime Imaging Microscopy and Single Virus Tracking. *Viruses*. 14.
41. Desimmie, B.A., R. Schrijvers, J. Demeulemeester, D. Borrenberghs, C. Weydert, W. Thys, S. Vets, B. Van Remoortel, J. Hofkens, J. De Rijck, J. Hendrix, N. Bannert, R. Gijsbers, F. Christ, and Z. Debyser. 2013. LEDGINs inhibit late stage HIV-1 replication by modulating integrase multimerization in the virions. *Retrovirology*. 10:1–16.
42. Borrenberghs, D., W. Thys, S. Rocha, J. Demeulemeester, C. Weydert, P. Dedecker, J. Hofkens, Z. Debyser, and J. Hendrix. 2014. HIV Virions as Nanoscopic Test Tubes for Probing Oligomerization of the Integrase Enzyme. .
43. Borrenberghs, D., L. Dirix, F. De Wit, S. Rocha, J. Blokken, S. De Houwer, R. Gijsbers, F. Christ, J. Hofkens, J. Hendrix, and Z. Debyser. 2016. Dynamic Oligomerization of Integrase Orchestrates HIV Nuclear Entry. *Sci. Rep.* 6:1–14.
44. J.R., L. 2006. Fluorescence-Lifetime Imaging Microscopy. In: Lakowicz JR, editor. Principles of Fluorescence Spectroscopy. Springer US. pp. 741–755.
45. Gadella, T.W.J., T.M. Jovin, and R.M. Clegg. 1993. Fluorescence lifetime imaging microscopy (FLIM): Spatial resolution of microstructures on the nanosecond time scale. *Biophys. Chem.* 48:221–239.
46. Ranjit, S., L. Malacrida, and E. Gratton. 2018. Differences between FLIM phasor analyses for data collected with the Becker and Hickl SPC830 card and with the FLIMbox card. *Microsc. Res. Tech.* 81:980–989.

47. Michalet, X. 2021. Continuous and discrete phasor analysis of binned or time-gated periodic decays. *AIP Adv.* 11.
48. Schrimpf, W., A. Barth, J. Hendrix, and D.C. Lamb. 2018. PAM: A Framework for Integrated Analysis of Imaging, Single-Molecule, and Ensemble Fluorescence Data. *Biophys. J.* 114:1518–1528.
49. Albanese, A., D. Arosio, M. Terreni, and A. Cereseto. 2008. HIV-1 Pre-Integration Complexes Selectively Target Decondensed Chromatin in the Nuclear Periphery. *PLoS One*. 3:2413.
50. Borrenberghs, D., W. Thys, S. Rocha, J. Demeulemeester, C. Weydert, P. Dedecker, J. Hofkens, Z. Debyser, and J. Hendrix. 2014. HIV virions as nanoscopic test tubes for probing oligomerization of the integrase enzyme. *ACS Nano*. 8:3531–3545.
51. Hellenkamp, B., S. Schmid, O. Doroshenko, O. Opanasyuk, R. Kühnemuth, S. Rezaei Adariani, B. Ambrose, M. Aznauryan, A. Barth, V. Birkedal, M.E. Bowen, H. Chen, T. Cordes, T. Eilert, C. Fijen, C. Gebhardt, M. Götz, G. Gouridis, E. Gratton, T. Ha, P. Hao, C.A. Hanke, A. Hartmann, J. Hendrix, L.L. Hildebrandt, V. Hirschfeld, J. Hohlbein, B. Hua, C.G. Hübner, E. Kallis, A.N. Kapanidis, J.Y. Kim, G. Krainer, D.C. Lamb, N.K. Lee, E.A. Lemke, B. Levesque, M. Levitus, J.J. McCann, N. Naredi-Rainer, D. Nettels, T. Ngo, R. Qiu, N.C. Robb, C. Röcker, H. Sanabria, M. Schlierf, T. Schröder, B. Schuler, H. Seidel, L. Streit, J. Thurn, P. Tinnefeld, S. Tyagi, N. Vandenberk, A.M. Vera, K.R. Weninger, B. Wünsch, I.S. Yanez-Orozco, J. Michaelis, C.A.M. Seidel, T.D. Craggs, and T. Hugel. 2018. Precision and accuracy of single-molecule FRET measurements—a multi-laboratory benchmark study. *Nat. Methods*. 15:669–676.
52. Vandenberk, N., A. Barth, D. Borrenberghs, J. Hofkens, and J. Hendrix. 2018. Evaluation of Blue and Far-Red Dye Pairs in Single-Molecule Förster Resonance Energy Transfer Experiments. *J. Phys. Chem. B*. 122:4249–4266.
53. Hendrix, J., W. Schrimpf, M. Höller, and D.C. Lamb. 2013. Pulsed interleaved excitation fluctuation imaging. *Biophys. J.* 105:848–861.
54. Müller, B.K., E. Zaychikov, C. Bräuchle, and D.C. Lamb. 2005. Pulsed interleaved excitation. *Biophys. J.* 89:3508–3522.
55. Toseland, C.P. 2013. Fluorescent labeling and modification of proteins. *J. Chem. Biol.* 6:85–95.
56. Alvarez, L.A.J., B. Widzgowski[1], G. Ossato, B. Van Den Broek, K. Jalink, L. Kuschel, M.J. Roberti, and F. Hecht. 2019. SP8 FALCON: a novel concept in fluorescence lifetime imaging enabling video-rate confocal FLIM. *Nat. Methods*. 20:2–4.
57. Orthaus-Müller, S., B. Krämer, R. Dowler, A. Devaux, A. Tannert, T. Roehlicke, M. Wahl, H.-J. Rahn, and R. Erdmann. 2016. rapidFLIM : The New and Innovative Method for Ultra fast FLIM Imaging. *PicoQuant Appl. Note*. 1–8.
58. Hendrix, J., and D.C. Lamb. 2013. Pulsed interleaved excitation: Principles and applications. 1st ed. Elsevier Inc.
59. Ratzke, C., B. Hellenkamp, and T. Hugel. 2014. Four-colour FRET reveals directionality in the Hsp90 multicomponent machinery. *Nat. Commun. 2014 51*. 5:1–9.
60. Laskaratou, D., G.S. Fernández, Q. Coucke, E. Fron, S. Rocha, J. Hofkens, J. Hendrix, and H. Mizuno. 2021. Quantification of FRET-induced angular displacement by monitoring sensitized acceptor anisotropy using a dim fluorescent donor. *Nat.*

Commun. 12:1–12.
61. Cormack, B.P., R.H. Valdivia, and S. Falkow. 1996. FACS-optimized mutants of the green fluorescent protein (GFP). *Gene*. 173:33–38.
62. Martin, K.J., E.J. McGhee, J.P. Schwarz, M. Drysdale, S.M. Brachmann, V. Stucke, O.J. Sansom, and K.I. Anderson. 2018. Accepting from the best donor; analysis of long-lifetime donor fluorescent protein pairings to optimise dynamic FLIM-based FRET experiments. *PLoS One*. 13:1–25.
63. McCullock, T.W., D.M. MacLean, and P.J. Kammermeier. 2020. Comparing the performance of mScarlet-I, mRuby3, and mCherry as FRET acceptors for mNeonGreen. *PLoS One*. 15:1–22.
64. Goedhart, J., D. Von Stetten, M. Noirclerc-Savoye, M. Lelimousin, L. Joosen, M.A. Hink, L. Van Weeren, T.W.J. Gadella, and A. Royant. 2012. Structure-guided evolution of cyan fluorescent proteins towards a quantum yield of 93%. *Nat. Commun.* 3.
65. Guerra, P., L.A. Vuillemenot, B. Rae, V. Ladyhina, and A. Milias-Argeitis. 2022. Systematic in Vivo Characterization of Fluorescent Protein Maturation in Budding Yeast. *ACS Synth. Biol.* 11:1129–1141.
66. Mukherjee, S., P. Manna, S.T. Hung, F. Vietmeyer, P. Friis, A.E. Palmer, and R. Jimenez. 2022. Directed Evolution of a Bright Variant of mCherry: Suppression of Nonradiative Decay by Fluorescence Lifetime Selections. *J. Phys. Chem. B*. 126:4659–4668.
67. Shaner, N.C., R.E. Campbell, P.A. Steinbach, B.N.G. Giepmans, A.E. Palmer, and R.Y. Tsien. 2004. Improved monomeric red, orange and yellow fluorescent proteins derived from Discosoma sp. red fluorescent protein. *Nat. Biotechnol.* 22:1567–1572.
68. Bindels, D.S., L. Haarbosch, L. Van Weeren, M. Postma, K.E. Wiese, M. Mastop, S. Aumonier, G. Gotthard, A. Royant, M.A. Hink, and T.W.J. Gadella. 2016. MScarlet: A bright monomeric red fluorescent protein for cellular imaging. *Nat. Methods*. 14:53–56.
69. Kremers, G.J., J. Goedhart, E.B. Van Munster, and T.W.J. Gadella. 2006. Cyan and yellow super fluorescent proteins with improved brightness, protein folding, and FRET förster radius. *Biochemistry*. 45:6570–6580.
70. Wu, B., Y. Chen, and J.D. Müller. 2009. Fluorescence fluctuation spectroscopy of mCherry in living cells. *Biophys. J.* 96:2391–2404.
71. Shaner, N.C., G.G. Lambert, A. Chammas, Y. Ni, P.J. Cranfill, M.A. Baird, B.R. Sell, J.R. Allen, R.N. Day, M. Israelsson, M.W. Davidson, and J. Wang. 2013. A bright monomeric green fluorescent protein derived from Branchiostoma lanceolatum. *Nat. Methods*. 10:407–409.
72. Antonik, M., S. Felekyan, A. Gaiduk, and C.A.M. Seidel. 2006. Separating structural heterogeneities from stochastic variations in fluorescence resonance energy transfer distributions via photon distribution analysis. *J. Phys. Chem. B*. 110:6970–6978.

Chapter 4

FRET tension sensing in vinculin using the phasor approach to time domain FLIM

Quinten Coucke, Samet Aytekin, Sarah Vorsselmans, Steven Huysecom, Kaizheng Liu, Johan Hofkens, Mar Condor, Susana Rocha

The work presented in this chapter was initiated by Prof. S. Rocha, Q. Coucke, Dr. K. Liu and Dr. M. Condor. The imaging experiments were performed by Q. Coucke, S. Aytekin and S. Huysecom. S. Aytekin and S. Vorsselmans were responsible for the molecular cloning of some DNA constructs. The data acquisition was performed on the home-built Pulsed Interleaved Excitation Fluorescence Lifetime Imaging Microscope (PIE-FLIM), initially built by G. Solis Fernandez and managed and updated by Q. Coucke and G. Solis Fernandez. Q. Coucke wrote this chapter and made the illustrations. Prof. Rocha and Prof. Hofkens supervised the work and provided scientific and editorial support where needed. This Chapter consists of unpublished results in preparation of a research paper.

4.1 Abstract

When we observe a cell, or any cellular process, it is crucial to understand and remember the mechanical cellular environment. Cells are always exposed to intra- and intercellular mechanical cues and respond to them. To investigate links between the behaviour of cells and the mechanical environment (surrounding stiffness, cell-cell connections, tensions in a tissue, …) it is important to visualize the forces at play inside the cell. The use of genetically encodable molecular tension sensors based on FRET has facilitated tension mapping inside cells. However, current published work heavily relies on intensity based or crude lifetime determination. Fluorescence lifetime imaging microscopy (FLIM) provides an intensity independent and direct probing of FRET through the donor lifetime.

In this work we aim at investigating vinculin tension sensors for FLIM imaging using the phasor approach. Such analysis will require some parameters to be measured beforehand but provide fast and smooth analysis of the whole dataset. We evaluate the efficacy of the FLIM-phasor approach and in doing so demonstrate the straightforward phasor approach to FRET imaging in the context of intramolecular FRET tension sensors. We compare the results for tension sensors with two different lengths of flexible linkers to determine their dynamic range and apply them to a tension inhibition experiment using ROCK inhibitor and blebbistatin.

4.2 Introduction

4.2.1 ECM-cell interactions

All cells in a living environment are subjected to mechanical stimuli. These forces are passed cell to cell in a tissue or through the extra cellular matrix (ECM) (1). Not only do these cells exert forces on their environment, but they can also sense them and even more importantly, act based on what is sensed. Per illustration, in 2013 Jansen et al. found that cells can stiffen the fibrin network (2). Mechanotransduction is the collective name for physical cues that are translated into biological responses inside the cell, changing the cellular behaviour. To translate physical cues into a response, the sensing of the cell ultimately needs to affect signalling molecules or mechanisms in the nucleus where transcription can be altered. Understanding the interplay between a cell and its environment plays a crucial role in tissue development research and advanced comprehension of certain pathologies. The link between ECM stiffness and cell fate has been extensively studied. While it was already suggested that stem cell differentiation was controlled by the unique local microenvironment (3, 4), the focus lied heavily on soluble ECM molecules to regulate differentiation. However, by changing the elasticity and stiffness of the matrix microenvironment Engler et al. could steer a mesenchymal stem cell population towards specific differentiated cell lineages (5).

Furthermore, it is not only differentiation that is influenced by physical properties of the cellular environment, proliferation and migration are also affected. The effect of stiffness on proliferation has been studied in a wide variety of cells confirming the ability of mechanotransduction to alter cell behaviour (6–8). Equally important, the migration traits of cells exposed to a wide array of mechanical stimuli are reported to change based on substrate stiffness. Per illustration, in 2013 the group of prof. A. J. Engler reported on the directed migration of mesenchymal stem cells based on stiffness gradients in a substrate (9).

The mechanical environment has been proven a determinant factor for cancer progression. Mechanotransduction of the stiff cancer tissue (in e.g. mammary or pancreatic cancer) results in a changed cellular phenotype (10). The YAP/TAZ (Yes-associated protein (YAP) and transcriptional coactivator with PDZ-binding motif (TAZ)) transcription factors are well studied and regulated by matrix stiffness (11) and are continuously studied for their link to cancer progression. Interestingly, the link with the epithelial-mesenchymal transition (EMT) of breast cancer cells experiencing a stiff tumour is reported, underlining the connection of matrix stiffness and cancer cell migration (12). An elaborate review was published by Chin et al. on the mechanotransduction processes in cancer which offers excellent extra reading and insights in the complex relation of cancer tumour stiffness and the associated downstream signalling effects (13).

4.2.2 Transduction towards the nucleus

To establish a cellular force acting on or sensing the environment, cells form multiprotein complexes at the cell membrane. Cell-ECM contacts are mediated through focal adhesions (FAs) while cell-cell contacts are made possible by adherens junctions (along with desmosomes and tight junctions) (14, 15). Both multiprotein structures connect the outside of the cell with the cytoskeleton and ultimately the nucleus, see Fig. 4.1.

FAs contain integrin alpha-beta heterodimers which span across the membrane and connect the ECM molecules with the scaffold proteins inside the cell. It is reported that nascent focal adhesions form based on the clustering of the beta-integrin subunit (16). Even more, the integrin patches recruit cytoskeleton connecting proteins such as talin, vinculin and tensin which are referred to as mechanosensing proteins or 'structural module' proteins, connecting integrins to the cytoskeleton. These proteins display turnover rates depending on substrate stiffness. Talin interacts directly with the actin filaments and beta-integrin, buffering tension by unfolding rod domains which in turn open up binding sites for vinculin linking talin to actin and stabilizing the integrin-actin connection, enabling force transduction towards the nucleus (17). Tensin is a phosphoprotein also binding the cytoplasmatic tail of beta-integrin and actin offering binding regions for focal adhesion kinase (FAK) once engaged. Additionally, Src, alpha-actinin, FAK and paxillin are mechanosignaling proteins that are recruited to a FA (18, 19). These proteins display high turnover rates, unaffected by ECM properties, and regulate the actin dynamics and mediate intracellular pathways in FAs. FAK and Src play their part in mediating FA turnover by facilitating phosphorylation of the myosin light chain kinase stimulating actomyosin contractility. This extra contractility might create more dense integrin spots which become destabilized. Paxillin is a FA associated adaptor protein responsible for recruiting signalling molecules ultimately facilitating cell spreading and motility (20). Src, activated by FAK, is directly related to p130cas/Rac pathways involved in actin polymerization (21, 22). Through formation of FAs, Rho/ROCK pathways are activated via GTPase leading to promoted myosin contractility and activation of the downstream YAP/TAZ nuclear translocation affecting gene transcription (23).

Cell-cell interactions in adherens junctions are driven by the homophylic velcro-like interactions between E-cadherins from two proximate epithelial cells. The single-pass transmembrane E-cadherin molecules, link the cytoskeleton of two adjacent cells using catenins. Alpha-catenins bind to beta-catenins and actin filaments of the cytoskeleton and the beta-catenins in turn bind to the cadherin proteins. Researchers investigating cancer cell metastasis are recently focusing on understanding the dysregulation of cell-cell interactions, since weakened cell adhesion and interactions is a first crucial step in elevated cell mobility (24). In

addition, a loss of E-cadherin expression drives cell detachment and improves motility (21). These mesenchymal characteristics are strongly linked to EMT in several cancer cell lineages (22, 25).

While not in the scope of this chapter, signals do not stop at the actin network. Once forces are transduced towards the cytoskeleton, several mechanisms are involved to directly affect the nucleus and regulate transcription factors. The family of nesprin proteins is crucial in connecting cytoskeletal components with the SUN protein (SUN-1/2). Nesprin-1/2, the most abundant form of nesprin, specifically attaches to the actin filaments and connects to the SUN domain. The protein complex containing SUN and nesprin spans the inner and outer nuclear membrane (INM and ONM) and is called Linker of Nucleoskeleton and Cytoskeleton (LINC) (1). While nesprin proteins span the ONM, the SUN protein traverses the INM. The C-terminal side of SUN proteins in the nucleoplasma link strongly with nuclear lamina through lamin A, principle protein component of the nuclear lamin that can assemble into filaments (26). Together with Src mediated phosphorylation of emerin, lamin A can regulate nuclear stiffening (27, 28) and is reported to influence transcription factors, RNA processing and chromatin organization. Heessen et al. reported already in 2007 on the sequestering of transcription factors due to binding of lamin A to transcription-silent heterochromatin near the INM (29).

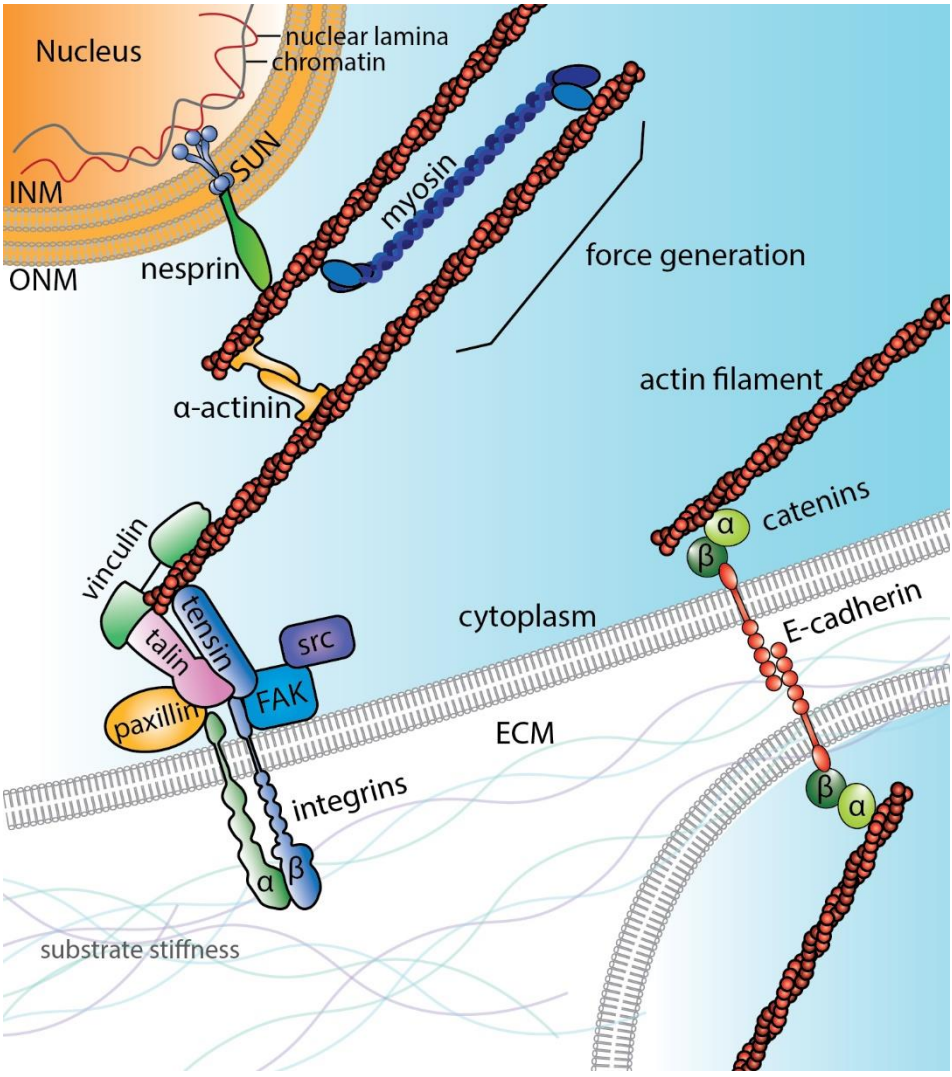


Figure 4.1: Schematic of the multiprotein structures involved in force transduction, simplified for key proteins. Stimuli from ECM-cell or cell-cell interactions are perceived through focal adhesions (FA) or adherens junctions (and others), respectively. Signals cascade towards the nucleus and activate several pathways through the FA assembly. In the nucleus mechanosensitive genes are regulated. FAK, Focal Adhesion Kinase; ECM, Extra Cellular Matrix; INM, inner nuclear membrane; ONM, outer nuclear membrane.

4.2.3 The toolbox for investigating cellular forces

The first report on measuring cellular traction dates from 1980 when Harris et al. observed cellular shearing forces on a thin layer of gelatine. Later, the same research group further investigated this by placing cells on top of a carefully produced an well-characterized thin layer of silicone to observe traction forces of the cell via the distortion and wrinkling of the substrate (30, 31). Silicone is well characterized, and therefore these deformations could be linked to certain mechanical properties and required forces exerted by the cells can/could be estimated. Methods derived from these early findings have become considerably more advanced, reaching the incorporation of machine learning to decipher cellular forces (32, 33). Fundamentally, these techniques are part of traction force microscopy (TFM). TFM aims at calculating the cellular forces based on the deformations induced in a material with well-known mechanical properties. Measuring wrinkles, is one (2D) way of assessing the cellular traction. However, many more advanced TFM methodologies have emerged.

TFM methods in 2D can be divided in two classes: the ones using discrete arrays of micropilllars or micro-posts and the ones using a continuous sheet of polymers. In the first class, researchers introduced microfabricated post-array detectors using micropillars or microposts to allow and quantify deformation by a cell placed on top (34, 35). The cell-induced deformations are converted to forces using Hooke's law and the spring constant of the pillars. Importantly, such setup allowed researchers to tune the array to the desired stiffness for a given experiment by changing micropost material, height, and density.

The second class of TFM methods overcomes the limitations of non-continuous substrates. Not limiting the anchoring points for cells, other 2D TFM approaches use highly deformable and tuneable continuous sheets of polymers. A well characterized substrate for this application is polyethylene glycol (PEG), polydimethylsiloxane (PDMS) and polyacrylamide (PAA). Dembo et al. introduced the use of PAA and it has since become most prevalent in TFM research (36, 37). To keep track of deformations within the substrate induced by the cell on top, fluorescent or reflective beads are embedded in the gel during polymerization (36, 38). Imaging the polymer before and after the cell applies traction reveals a displacement map of the embedded beads. From the bead displacements and a priori knowledge on the mechanical properties of the polymer, a traction force heatmap is generated using extensive computational methods such as Fast Fourier Transform (FFT) (39) and finite element method (FEM) (40). Improvements of the pioneering 2D work include 3D-TFM and super-resolved traction force microscopy (41–44).

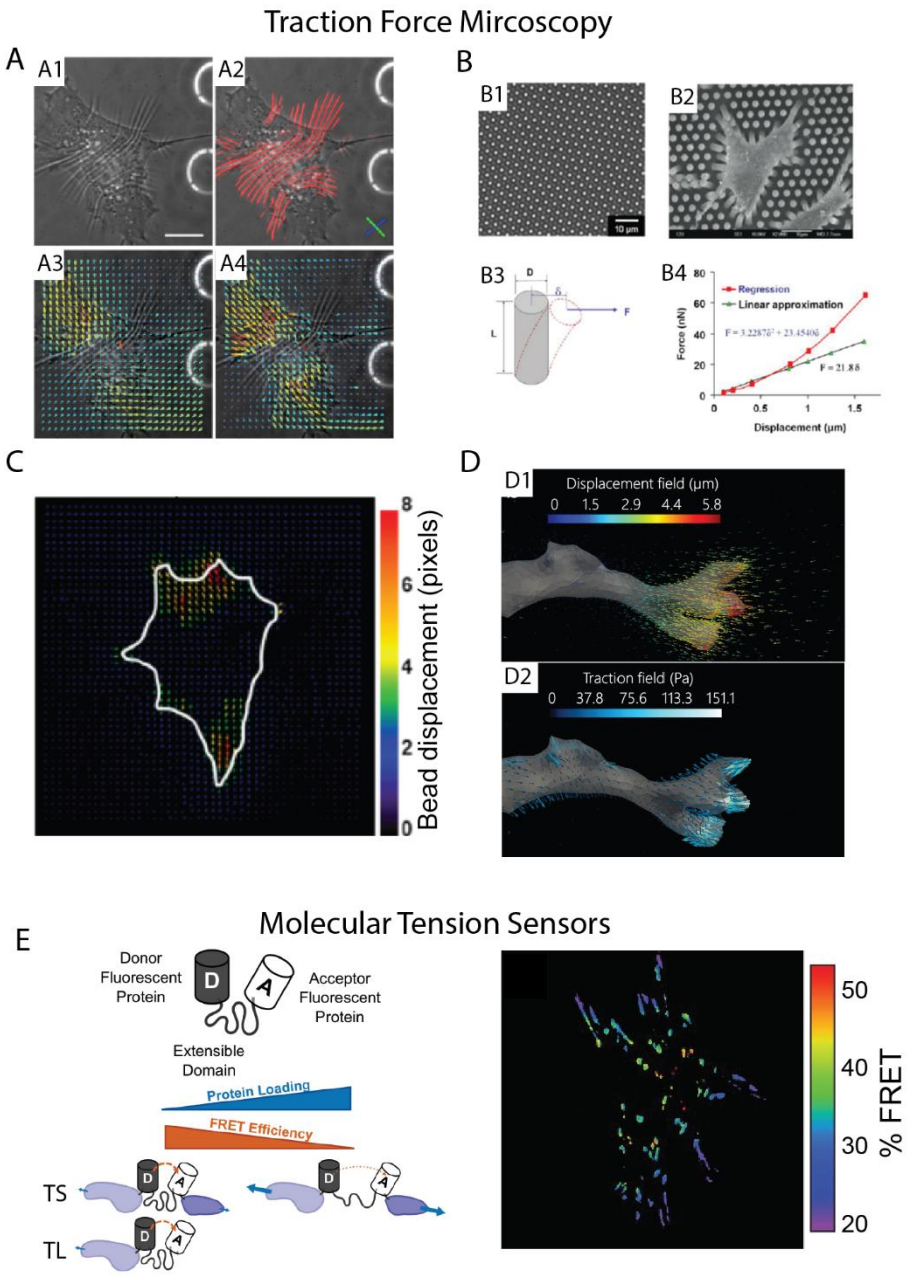


Figure 4.2: Overview of techniques used to map cellular tractions and forces. (A1-2) Traction force study on silicone substrate wrinkles. (A3) displacement field calculated from wrinkles. (A4) Traction force field derived from substrate properties and displacements. Adapted from Li et al. (32). (B1-2) Micropost array with and without a cell. (B3) cantilever

bending of a micropost under force. (B4) Force calibration of micropost top displacement. Panel adapted from Wang et al. (45) (C) Bead displacement of a vascular smooth muscle cell after chemical relaxation measured with 2D TFM. Panel adapted from Adhekari et al. (46)(D) 3D/4D TFM using TFMLAB, displaying tractions around a 3D cellular protrusion. Panel adapted from Barraso-Fano et al. (42). (E) (left) Mechanism of the molecular FRET tension sensor illustrating the relation between FRET and protein loading. Tension Sensitive (TS) and Tensionless (TL) variant of the tension sensor is depicted. (right) Calculated FRET efficiency differences report on molecular tensions in the imaged cell. Image of MEF double knockout vinculin cells transfected with VinTS-9. Panel adapted from (47).

Additionally, more molecular techniques exist to measure forces. Tension sensitive DNA hairpins which contain a fluorophore and quencher attached to a the hairpin ends will have a quenched donor signal in relaxed state but can be extended, unquenching the fluorophore. The tension needed for unzipping the hairpin can be tuned using the G/C content of the DNA. In general, tension sensitive DNAs are attached to a rigid substrate using streptavidin/biotin linkage providing a 2D tension map (48). This DNA module was also used in combination with FLIM and named molecular tension fluorescence lifetime imaging microscopy (MT-FLIM). Interestingly, both utilize Cy3B-BHQ1 (Black Hole Quencher 1) as fluorophore-quencher pair, highlighting the interest in dark FRET acceptors (49). Even atomic force microscopy (AFM) can be used to image cellular indentations in 'formvar' sheets (50) or to measure cell/substrate stiffness with its cantilever, often in combination with TFM (51).

However, this level of tension probing remains at the cell-matrix interaction level and is therefore blind to the molecular forces that act inside the cell which give rise to mechanotransduction. Inserting a tension probe inside a cell comes with many challenges such as fluorescent protein selection, molecular design, mode of application, … . In 2010, Grashoff et al. introduced a genetically encoded CFP-YFP FRET tension sensor in the force transducing protein vinculin (52). To construct such tension reporting protein the native linker part of vinculin is replaced with a FRET cassette. This cassette consists of a flexible elastic domain that is flanked with the FRET donor and acceptor. Each side of the cassette, i.e. the N-terminus of the donor fluorescent protein and the C-terminus of the acceptor protein is attached with a spacer to both functional ends of the tension bearing protein, in this case vinculin. When under tension, the adapted vinculin (VinTS, tension sensitive) will elongate resulting in unquenching of the donor. Controls are made by providing a vinculin protein without tail domain, which means the cassette cannot be put under tension (VinTL, tail less or tension less), or by eliminating the acceptor. On the individual module level, forces were calibrated using optical tweezers. In this work we use a more recent version of this sensor which was presented by Lacroix et al. (47). As one of the major changes, the folding/unfolding dynamics of the linker were optimized by abandoning the flagelliform spider silk flexible linker and opting for a $(GGSGGS)_n$ repeat. Additionally, the used FRET pair is updated to mClover-

mRuby3. These changed sensor characteristics led to improved dynamic range and brightness.

A visual overview of the discussed techniques is presented in Fig. 4.2.

4.2.4 FLIM for tension measuring

Given the complexity of the force transduction apparatus, a wide array of tension sensor proteins such as nesprin, cadherin and talin were created, all reporting on the molecular tension using FRET (53–55). In this work we focus on vinculin, situated in the focal adhesions (FAs). Previously the groups of Grashoff (2014) and Lacroix (2018) used intensity-based imaging of the FRET tension sensor. Such imaging requires trustworthy donor and acceptor signals, which have to be obtained in an accurate and pure manner or corrected for bleedthrough and crossover in the detection channels. Added to this, as cells live, focal adhesions become larger or smaller as they regulate tension, affecting the intensity signal and possibly the FRET analysis when imaging over time. Fluorescence lifetime imaging microscopy (FLIM) offers the possibility of FRET imaging in a largely concentration independent manner, with the added benefit that only the donor fluorescence is recorded to evaluate FRET, opening up possibilities for future multiplexing of said sensors. Analysis of FLIM data is traditionally performed with a frequency domain setup or fitting based algorithms using time correlated single photon counting (TCSPC) or gated FLIM. Recently, a technique from frequency domain FLIM has been adopted for use on TCSPC data which has become increasingly popular in many research labs. The so called phasor approach offers a visual representation of FLIM data (56–58), with a graphical fast analysis of lifetime information. Using the phasor approach for FRET, a FRET map can be readily obtained from the spatial sorting of pixels in the phasor plot, simplifying the process. In this chapter we will evaluate the performance of the phasor approach to FRET tension sensors in vinculin and discuss their future potential.

4.3 Materials and methods

4.3.1 Cell culture

For the imaging of focal adhesions (FAs) mouse embryonic fibroblasts were used. A wildtype and double vinculin knockout cell line of these MEF cells were available. Both lines were threated identically for cell seeding and sample preparation. These cells were donated by the lab of Prof. Dr. Wolfgang Goldman (Biophysics group Erlangen, Friedrich-Alexander University, Germany). MEF cells were maintained using Dulbecco's Modified Eagle Medium with 4.5 g/L D-glucose (Gibco™ DMEM 1X, Thermo Fisher Scientific, Geel, Belgium) supplemented with 10% fetal bovine serum (Gibco™ FBS), and 1%v/v non-essential amino acids (Sigma-Aldrich, 100X, Darmstadt, Germany). Protected incubation was performed in a Heracell™ VIOS 160i CO_2 Incubator (Thermo Fisher Scientific, Geel, Belgium) at 37 °C, 20% CO_2 and 5% oxygen. Cells were maintained in the flat growing bed within T25-flasks (Avantor, VWR, city) with a 25 cm^2 surface. Cells were incubated at a healthy confluency by performing passage once the flask reaches 80-90% confluency, making sure to reseed no more than 100 000 cells in order to keep at least two days in between passages. Passage protocol commenced with a double wash each using 3 mL of phosphaste buffered solution (PBS 1x, Thermo Fisher Scientific) without detaching any cells. Immediately after, cells were treated with 500 mL of TrypLE Express Dissociation Reagent (Gibco™) and incubated for 2 minutes in the incubator. TrypLE inactivated was done by adding 3mL of PBS to the detached cell mixture in the T25-flask. A small volume (30 µL) of this cell suspension was mixed with an equal volume of Tryphan Blue (Sigma-Aldrich) for visualization and counting under the CYTOSMART cell counter (Corning, New York, USA). After counting the correct concentration of the cell suspension was calculated to reseed (50.000) in a T-25 flask or seed on a 29 mm glass bottom dish #1.5 spec. with a 14 mm centred glass well for imaging (D29-14-1.5-N, Cellvis (formerly In Vitro Scientific), California, USA).

4.3.2 Transient transfection of MEF cells

FRET tension sensors were obtained from addgene.com (Plasmid numbers #111765; VinTS-tCRMod-GGSGGS9 and #111764; VinTS-tCRMod-GGSGGS9, both deposited by Prof. Dr. Brenton Hoffman (47)). These plasmids are the improved vinculin tension probes originally published by Grashoff et al. containing the GGSGGS elastic linker in the tension module flanked by mClover and mRuby3 as FRET pair (52).

As a control, we developed a tail-less (or tension-less, TL) variant of the Tension sensitive probe, with the 7 and 9 repeat GGSGGS-linker, aspiring the best dynamic range of the sensor. To create the TL versions, the original plasmid for TS was fully amplified with polymerase chain reaction (PCR) using the forward primer *ggtatcagtaagaattctgcagat* and reverse primer *gattcgaattcttacttgtacagctcgtccatccc*. These primers amplify the full plasmid with exception of the actin binding domain on the vinculin tail, creating a truncated tension probe protein. Since the used PCR primers introduced an EcoRI cutting site, the amplified fragment was self-ligated.

Cellular expression was achieved in the MEF cells using transient expression via TransIT-X2 Dynamic Delivery System (Mirus Bio, Madison, USA), a non-liposomal polymeric system. Approximately 24 hours after cell seeding TransIT-X2:DNA complexes were made. First, Opti-MEM I (Gibco™ Opti-MEM Media, Thermo Fisher Scientific, Geel, Belgium) and the vial of TransIT-X2 were brought to room temperature and vortexed briefly before use. For each transfected dish two sterile Eppendorf tubes (Eppendorf, Hamburg, Germany) were used. In one 50µL of the Opti-MEM media was combines with 1 µL of transfection reagent and in the second 250 ng of plasmid was added to another 50 µL Opti-MEM (Gibco™ Opti-MEM Media, Thermo Fisher Scientific, Geel, Belgium). Both tubes are combined to reach a final volume of 100 µL. After mixing both Eppendorf tubes, the mixture is left undisturbed for 15 minutes at room temperature allowing the complexes to form. Finally, and immediately after the incubation of 15 minutes the solution is pipetted with care (no pipetting up and down to mix) and added dropwise into the dish with seeded cells. Imaging preparation is concluded 24 hours post transfection with the fixation of the wells using 4% PFA as was proven to not affect FRET tension imaging (59). Imaging glass is always incubated for 2 hours with a 5µg/mL fibronectin solution (SKU: 11080938001, Sigma-Aldrich).

4.3.3 Fluorescence lifetime imaging microscopy in time-domain

In this chapter a home-built confocal time resolved fluorescence microscope was used to measure all fluorescence data. For general details on the TCSPC setup, microscope core, objectives the author kindly forwards to Chapter 3 of this thesis. For the experiments on the aforementioned mClover-mRuby3 FRET pair, a 485 nm laser was used (LDH series, PicoQuant GmbH, Berlin, Germany) in combination with a quadband filter discriminating excitation and emission fluorescence (zt405/488/561/640rpc, Chroma, Vermont, USA)). Emission was first split on a 560 nm long pass filter (H560LPXR, AHF analysentechnik AG, Tübingen, Germany) directing acceptor emission to a hybrid photomultiplier tube (PMA hybrid series, PicoQuant, Berlin, Germany). A 570 long pass filter could be used in case of direct acceptor excitation, where it served as clean-up filter. Donor emission was

directed towards a 530/50 band pass clean-up filter (AHF analysentechnik AG, Tübingen, Germany). The microscope is presented in Fig. 4.3. All TCSPC data is acquired using a 32 MHz laser pulse frequency, which is optimized for the target lifetime range (2-4 ns). An excitation power of 3 µW was set before entry of the light path in the microscope body for every measurement on cells.

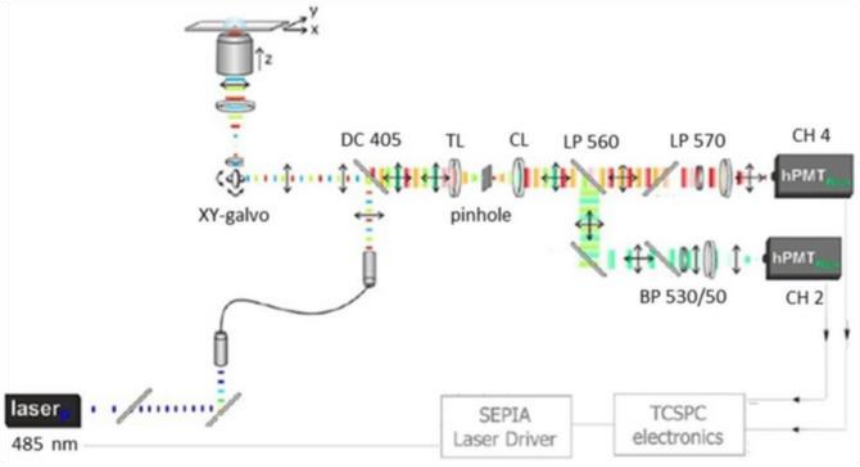


Figure 4.3: Schematic of the home-built confocal time resolved fluorescence microscope. DC; dichroic, TL; tube lens, CL; collimating lens, LP; long pass, BP; band pass, CH; channel, hPMT; hybrid photomultiplier tube.

4.3.4 FRET analysis with the phasor approach

Symphotime 64 (PicoQuant, Berlin, Germany) software is used to initially obtain our fluorescence data and store the timed photon information in a .PTU file. Analysis of the donor fluorescence is performed in matlab software: *Pulsed Interleaved Excitation (PIE) analysis with Matlab - PAM* (60). *PAM* is available as a matlab source code from gitlab (http:// www.gitlab.com/PAM-PIE/PAM), requiring MATLAB to run (or as standalone compiled version at http://www.cup.uni-muenchen.de/pc/lamb/software/pam.html) or hosted in Git repositories under http://www.gitlab.com/PAM-PIE/PAM and http://www.gitlab.com/PAM-PIE/PAMcompiled. A manual is found at: http://pam.readthedocs.io. Here, TCSPC data is referenced to a known lifetime standard (always ATTO488 for mClover) and transformed to a .phr file which stores all phasor information (G & S coordinates and pixel intensity per image pixel). The resulting phasor cloud of mapped image pixels in the phasor plot is analysed in the subtab of *PAM* (*phasor.m*). A FRET trajectory was drawn using additional information: the autofluorescence contribution (BG) and the pure donor phasor (DO, donor-only measurement). The g/s coordinates of the measurement using

only donor fluorophores and the g/s coordinates of the cellular autofluorescence determine the FRET trajectory end and starting point. Additional analysis such as line profiles, segmentation of focal adhesions and creation of histogram plots was performed in MATLAB using exported FRET index data (obtained by right clicking the left image in *phasor.m)*. Every image is segmented using a threshold suitable to isolate FAs which was individually determined for every cell. This allows the *bwconcomp* function in MATLAB 2020b to identify separate FAs and calculate the average FA FRET efficiency. Line profiles were drawn through FAs and only the pixels included in the segmentation were taken into account. The variable line profile lengths were normalized by extrapolating every line segment to 400 points, which is the maximal length of a line within the 400x400 pixel image. Statistical tests were conducted in MATLAB. For more information on using *PAM* for FRET analysis using a FRET trajectory, the authors refer to our previously published work (61).

4.3.5 ROCK-inhibitor and blebbistatin

FRET tension verification experiments were designed using inhibitors of cell contractility aiming at establishing a tension free measurement of vinculin equipped with the FRET module. To perform these experiments, cells were released from the imaging dish 8 hours post transfection by an incubation in 300 µL 1x TrypLE solution at 37°C at 5% CO2 for 5 minutes. Following the incubation, cells were resuspended in 1.7 mL of normal culturing medium and seeded in an 8-well Nunc Lab-Tek II Chamber slide (ThermoFisher Scientific) at a density of 7,500 cells per well. Cells are now further stored in the incubator until imaging. When imaging, the medium was replaced by 250 µL HBSS to maintain the cells at a low CO_2 environment, i.e. the microscope. Two different inhibitors that act on the FA-cytoskeletal contractility were used, namely rho-associated protein kinase inhibitor (ROCK-inhibitor or Y-27632, inhibitor of myosin light chain) and blebbistatin (myosin II inhibitor). For each well, only one cell could be imaged before adding 250 µL of the inhibitor solution. The cell was imaged again 10, 20 and 30 minutes after adding the inhibitor. The inhibitor solutions contained either 40 µM ROCK-inhibitor in HBSS or 100 µM blebbistatin in HBSS. The microscope objective was permanently equipped with a heating element keeping sample temperature around 35-37°C.

4.4 Results

4.4.1 FRET trajectory

In order to successfully analyse the lifetime information of the FRET-based tension sensors, the FRET trajectory needs to be calculated. This trajectory spans from 0 % to 100 % FRET efficiency. The starting point (0% FRET) consists of the pure donor lifetime, without any form of a nearby quencher. This measurement is ideally conducted in a sample similar to the subsequent measurements with a fully operational FRET sensor, given the influence of the direct environment to the fluorescence lifetime. In the case of the experiments performed here, this implies measuring the fluorescence signal of the donor expressed in wild type MEF cells. At 100% FRET efficiency all the emission from the donor is quenched and therefore the only remaining signal is the cellular autofluorescence and background. While background contributions (stray light or dark counts) can be assumed constant, the cellular fluorescence lifetime signature (phasor location) needs to be determined.

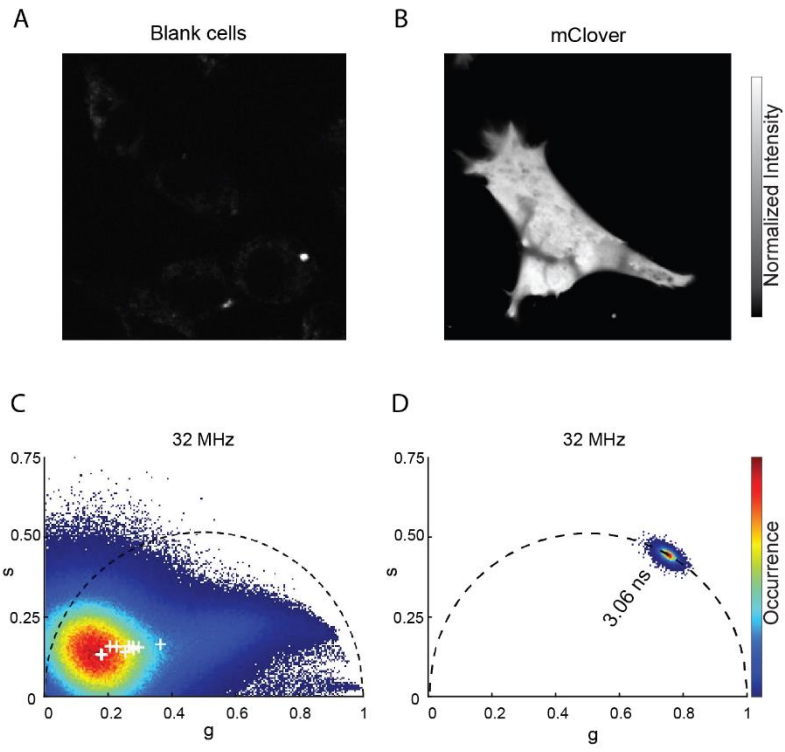


Figure 4.4: Reference measurements for phasor analysis of an mClover-mRuby3 FRET module. (A) Normalized intensity image of a non-transfected MEF-vinKO cell used to record the autofluorescence (B) Normalized intensity image of a MEF-vinKO cell transiently

expressing mClover (C) Phasor plot resulting from the analysis of panel A, white marks indicate the photon weighted centre of mass for every measured blank cell (n = 12) (D) Phasor plot of a cell expressing cytosolic mClover. Since the fluorescence decay is monoexponential, it is possible to retrieve the fluorescence lifetime (3.06 ns). Images- (A) and (B) have a size of 95 µm.

To calculate the phasor point corresponding to autofluorescence, unmodified cells were measured using the same laser power as the functional FRET samples. The phasor plot of those images, without thresholding, was then calculated (Fig. 4.4 *A, C*). The photon weighted average coordinates of the cellular background, as observed in MEF vinculin double knockout cells (n=12), are [g: 0.2552, s: 0.1427] and this point is referred to as BG (Background). This reference point will serve as endpoint of any FRET trajectory. To determine the trajectory starting point (0% FRET efficiency), we measured several cells only expressing cytosolic mClover. The total fluorescence signal from the cell was analysed (n=12) and the photon weighted average of the phasor plot was determined (Fig. 4.4 *B, D)*. The pure unquenched mClover coordinates were found to be [g: 0.7248, s: 0.4463] and this point is referred to as DO (Donor only). This point in the phasor plot will serve as starting point of the trajectory, but can be adjusted along the BG-DO line to accommodate cells with more autofluorescence. Given that the DO coordinate lies approximately on the semicircle, the lifetime of this measurement can be represented by a single exponential lifetime, which was determined to be 3.06 ns (see equations 9 and 10 in Chapter 3 for the according formula (61)). Using the reference points BG and DO, the FRET trajectory is calculated and plotted, enabling the direct retrieval of FRET efficiency.

4.4.2 Measuring molecular tension across vinculin molecules

To evaluate the molecular tension across the focal adhesion, a FRET-based sensor with a 7 repeat of the GGSGGS linker was used. In the tension-sensitive version (VinTS), the sensor was placed withing the vinculin molecule. As a control, a self-made tensionless vinculin sensor was also imaged (VinTL). In this case, the tail of the vinculin, responsible for binding to actin, was removed. Consequently, no tension can be applied. As depicted in Fig. 4.5 *A, B,* upon imaging of double vinculin knockout MEF cells (MEF-vinKO) transiently expressing either one of the sensors, separate phenotypes can be discriminated.

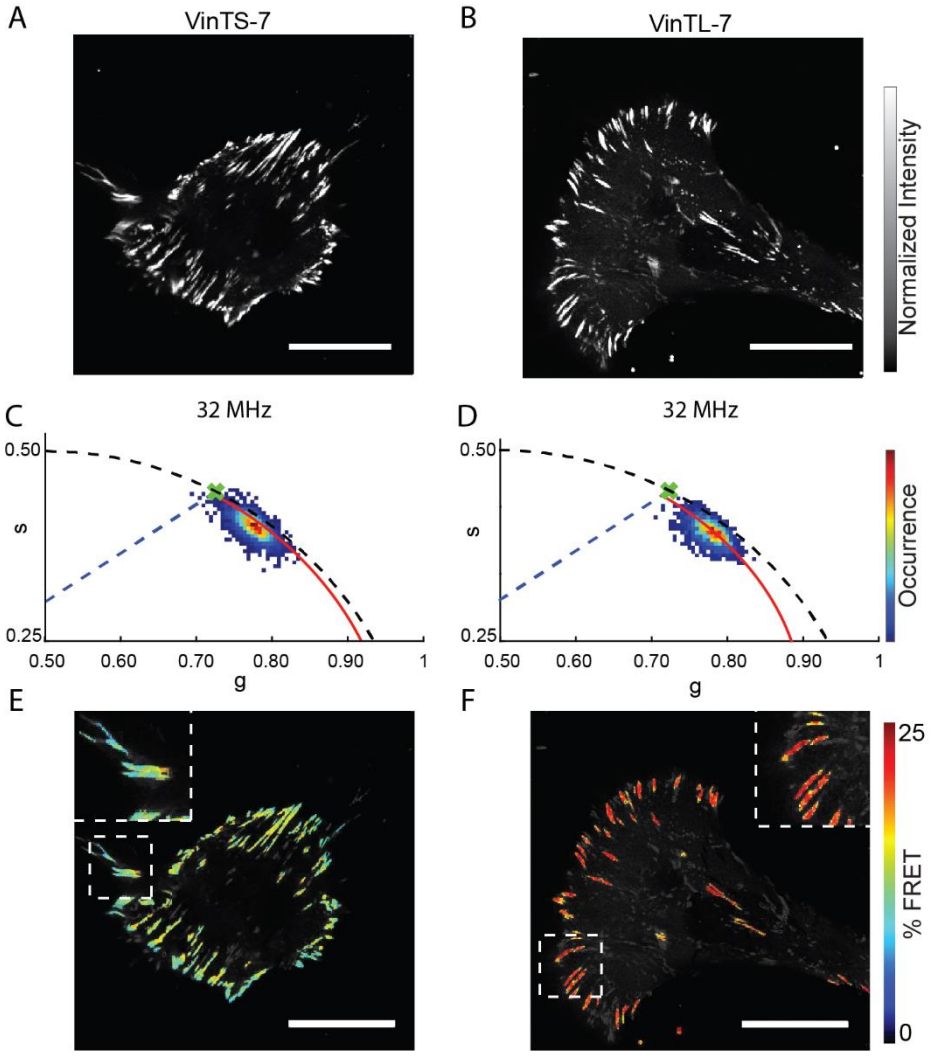


Figure 4.5: Phasor-FRET imaging of MEF-vinKO cells transiently transfected with a tension sensitive (VinTS-7) and tension less (VinTL-7) construct. (A, B) Representative intensity images of MEF-vinKO cell transiently transfected with VinTS-7 and self-cloned VinTL-7. (C, D) Phasor plot of cells in panel A and B with the constructed FRET trajectory. Red line: FRET trajectory; green mark: DO coordinate; blue dashed line: fraction line of all possible DO and BG combinations which will always cover start and end point of any trajectory. (E, F) FRET image generated from the phasor plot FRET trajectory of VinTS-7 and VinTL-7 cells where each pixel is coloured according to the corresponding FRET efficiency. Scale bars: 25 µm.

The fluorescence intensity images of cells transiently transfected with the vinculin TS constructs carrying 7 repeats (VinTS-7) show a broad distribution of FA sizes and heterogeneous distribution of focal adhesions (FAs) along the cell edge. In the VinTL-7 transfected cells, the formation of FAs appeared largely unaffected, yet some cells displayed inconsistencies in FA sizes. After the conversion of photo arrival times into phasor coordinates, we construct the FRET trajectory using the previously measured DO and BG coordinates. In the depicted VinTL-7 cell, the contribution of BG of 3% was necessary whereas in the VinTS-7 0.5% was sufficient to position the trajectory through the phasor cloud (Fig. 4.5 *C, D*). As shown in Fig. 4.5 *E, F*, the FRET efficiencies calculated from the FRET trajectory can be used to plot an 'FRET efficiency' image. Here the calculated values are plotted on top of the fluorescence intensity image to have cellular context. In the two depicted cells, a clear difference between the values of FRET efficiency is visible, a phenomenon not consistently observed due to cell-to-cell variability. Notably, VinTS-7 FAs display a gradient of FRET efficiencies: low FRET on the periphery of the cell, indicating high tension, and high FRET towards the centre of the cell, indicating low tension. This was not systematically observed in the VinTL-7.

To quantify these observations, line profiles were drawn on FAs of cells expressing both sensors, always directed outside-inside and normalized by the length of the focal adhesion. The resulting graphs are depicted in Fig. 4.6 *A, B*. For the VinTS-7, the average FRET efficiency value rises ~5% across the length of the FA. In contrast, for the VinTL-7 samples, no significant trend was observed as was also noted upon visual inspection of the FRET images. To ensure that the fluorescence intensity was not affecting these results, the intensity line profiles were also calculated (Fig. 4.6 *C*). The average of the profiles shows a bump, but shows no clear link with the FRET efficiency profiles.

In addition to the FRET efficiency across individual FA, we analysed and compared the FRET efficiency averaged per cell and per focal adhesion over multiple cells (Fig. 4.6 *D*). The analysis on both the single cell and single FA level presented different distributions. For instance, the 95% confidence intervals were notably wider for VinTL-7. The medians of both datasets showed a slight shift: from 12.3% to 17.0% for focal adhesion-wise analysis and from 12.4% to 17.8% for cell-wise analysis. This does indicate the presence of more tension in the TS cases compared to TL.

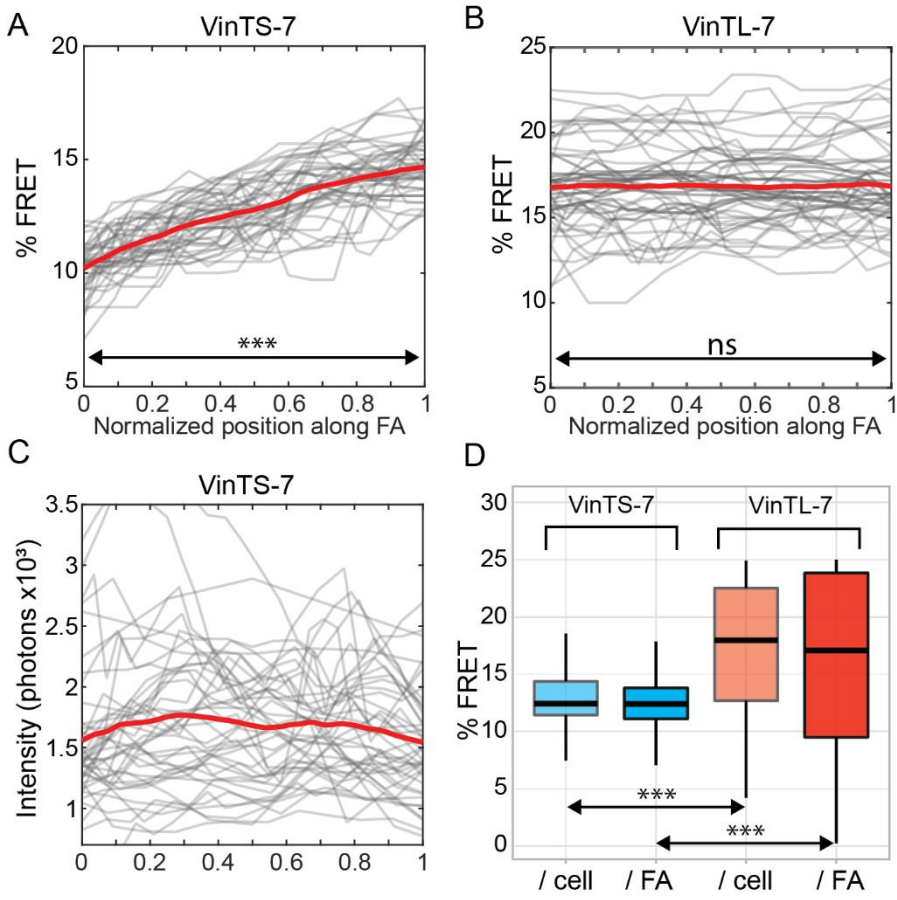


Figure 4.6: Focal adhesion FRET analysis of VinTS-7 and VinTL-7 in MEF-vinKO. (A, B) line profiles drawn on focal adhesions of VinTS-7 (FA: n = 44, cells: n = 4) and VinTL-7 (FA: n = 61, cells: n = 4) cells, respectively. (A) Significant trend of increased FRET (****, p<0.001, paired t-test at significance level of 0.05). (B) No significant trend of increased FRET (ns, p>0.05, paired t-test at significance level of 0.05). (C) Intensity line profiles of focal adhesions FA: n = 44, cells: n = 4) of a VinTS-7 transfected cell. (D) Boxplot overview comparing VinTS-7 and VinTL-7 per cell (VinTS-7, n = 65; VinTL-7, n = 49) and per FA (VinTS-7, n = 4204; VinTL-7, n = 6236). Statistics calculated with a non-parametric two-tailed Wilcoxon-Mann-Whitney U-test assuming no normal distribution with significance level of 0.05. *** equals a test with p<0.001, ns = not significant.

To evaluate whether the sensor with 9 repeats of the GGSGGS linker (VinTS-9) displays a higher dynamic FRET range, similar experiments and analyses were perform for the VinTS-9 and VinTL-9 sensors (Fig. 4.7 and 4.8). As shown in Fig. 4.7 *A, B,* the visual appearance of the FAs containing VinTS-9 or VinTL-9 is similar to the intensity images of the 7 repeat versions. The TS variant shows strong

focused protrusions with dense but fewer FAs while the TL expressing cells have wider protrusions with more distributed focal adhesions. For the depicted cells, the phasor

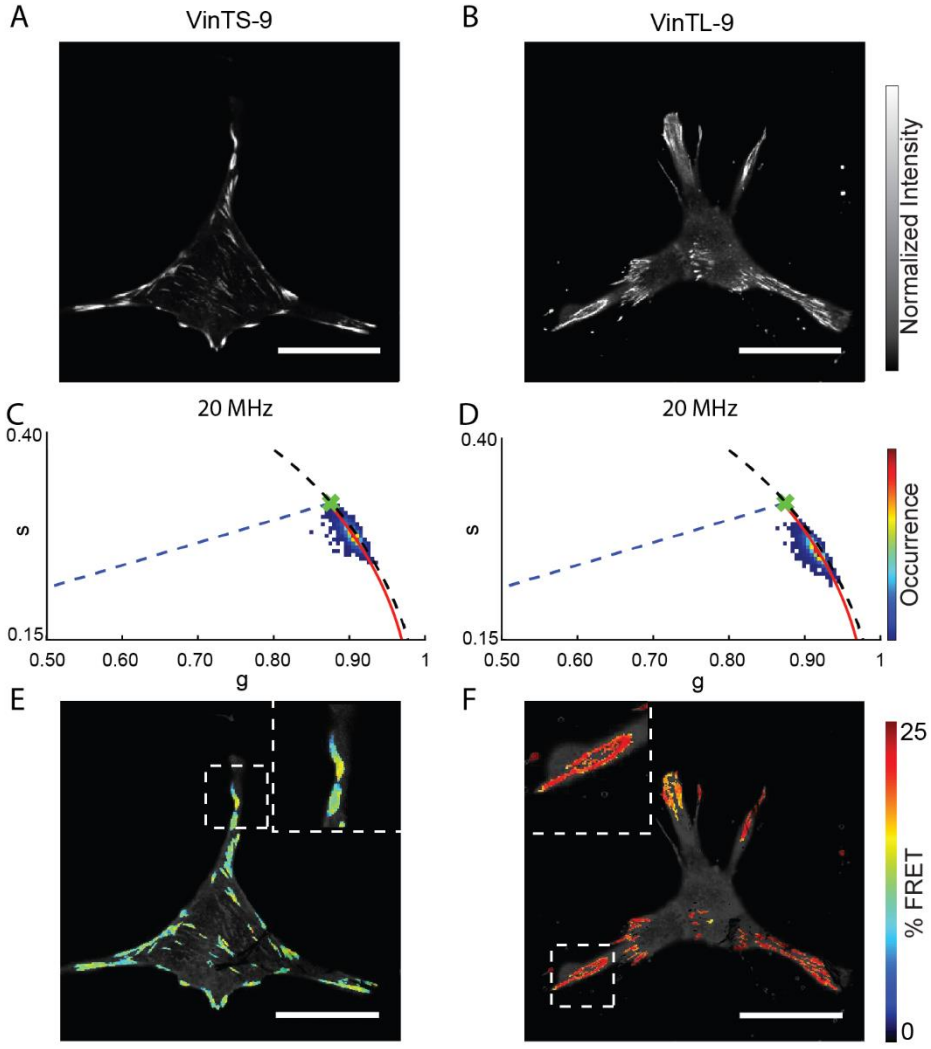


Figure 4.7: Phasor-FRET imaging of MEF-vinKO cells transiently transfected with a tension sensitive (VinTS-9) and tension less (VinTL-9) construct. (A, B) Representative intensity images of MEF-vinKO cell transiently transfected with VinTS-9 and self-cloned VinTL-9. (C, D) Phasor plot of cells in panel A and B with the constructed FRET trajectory. red line: FRET trajectory, green mark: DO coordinate, blue dotted line: fraction line of all possible DO and BG combinations which will always cover start and end point of any trajectory. (E, F) FRET image generated from the phasor plot FRET trajectory of VinTS-9 and VinTL-9 cells. All scale bars 25 µm.

plots with the corresponding FRET trajectory are shown (Figure 4.7 *C, D*). Both cells exhibited low autofluorescence, resulting in a trajectory that has a starting point close to the semicircle. The images containing the FRET efficiency are presented in Fig. 4.7 *E* and *F*. As was observed in VinTS-7 samples, FAs of the VinTS-9 cell display a FRET gradient along the length of the FA. However, this gradient was not observed in all focal adhesions throughout the cell. For VinTL-9, a generally higher FRET efficiency was recorded. However, large cell-to-cell differences in the FRET images for VinTL-9 were found.

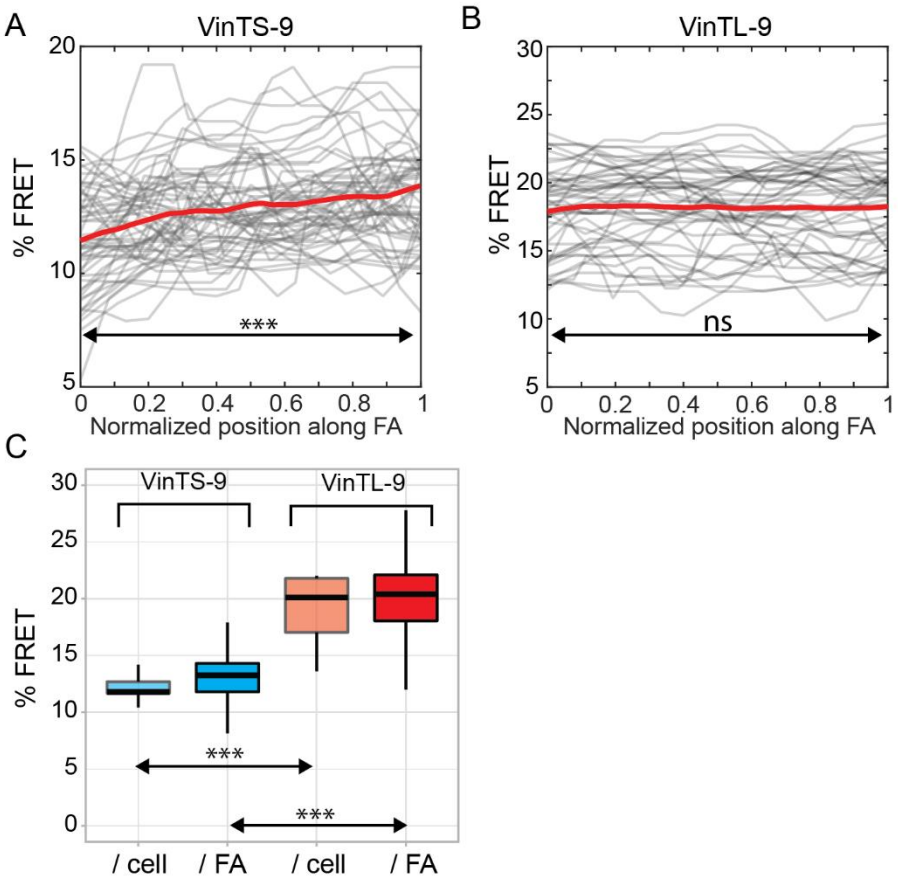


Figure 4.8: Focal adhesion FRET analysis of VinTS-9 and VinTL-9 in MEF-vinKO. (A, B) line profiles drawn on focal adhesions of VinTS-9 (FA: n = 58, cells: n = 4) and VinTL-9 (FA: n = 50, cells: n = 4) cells, respectively. (A) Significant trend of increased FRET (***, p<0.001, paired t-test at significance level of 0.05). (B) No significant trend of increased FRET (ns, p>0.05, paired t-test at significance level of 0.05). (C) Boxplot overview comparing VinTS-9

and VinTL-9 FRET efficiency using cell (VinTS-9, n = 15; VinTL-9, n = 10) and FA (VinTS-9, n = 1136; VinTL-9, n = 666) averages. Statistics calculated with a non-parametric two-tailed Wilcoxon-Mann-Whitney U-test assuming no normal distribution with significance level of 0.05. *** equals a test with $p<0.001$, ns = not significant

In analogy to Fig. 4.6, the dynamic range of FRET values across the focal adhesions of VinTS-9 transfected cells was evaluated using line profiles in several cells (Fig. 4.8 *A*, *B*).In For the VinTS-9 sensor, an upward trend is observed in the average of the line profiles. However, the separate profiles for the individual FAs, shown in gray, display a non-uniform trend. Additionally, the range of calculated FRET values is narrow (between 11.3 % FRET efficiency to 14.2 %). VinTL-9 did not show any trend in the FRET efficiency across the FAs (Fig. 4.8 *B*). When evaluating the average FRET efficiency per FA and per cell for both TS and TL samples, again a clear difference is found where TL samples present higher in FRET efficiencies (Fig. 4.8 *C*). The median FRET efficiency for VinTL-9 in FAs was found to be 20.3 %, smaller than the 13.8 % obtained for VinTS-9. While the cell-wise data spread for VinTS-9 was found to be smaller compared to FA-wise analysis, a larger spread was found for VinTL-9 data. This indicates a large cell-to-cell heterogeneity in measured FRET efficiency.

4.4.3 Evaluating the effect of tension inhibitors

Having observed the highest dynamic range for VinTS-7, we decided to continue with this construct to evaluate the effect of chemical inhibitors on the tension across vinculin molecules. More specifically, we used the molecular sensors to monitor the changes in tension in live cells upon the addition of a tension inhibitor drug. In this chapter, we used two different compounds: Y-27632, a ROCK-inhibitor that disturbs the rho-mediated phosphorylation of myosin light chain20 (MLC20); and blebbistatin, which disables the myosin-II specific ATPase required for acto-myosin mobility (Fig. 4.9). While both compounds reduce the capability of exerting tension on the mechanotransduction chain, it is not clear what the tension implications are on the single protein level.

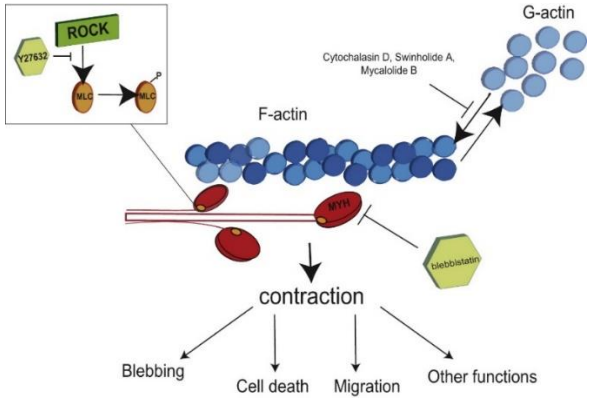


Figure 4.9: Schematic showing the inhibitory effects of blebbistatin and Y-27632/ROCK-inhibitor. Figure adapted from Chen et al. (62).

Fig. 4.10 *A* and *B* show cells imaged for 30 minutes after the addition of ROCK inhibitor.

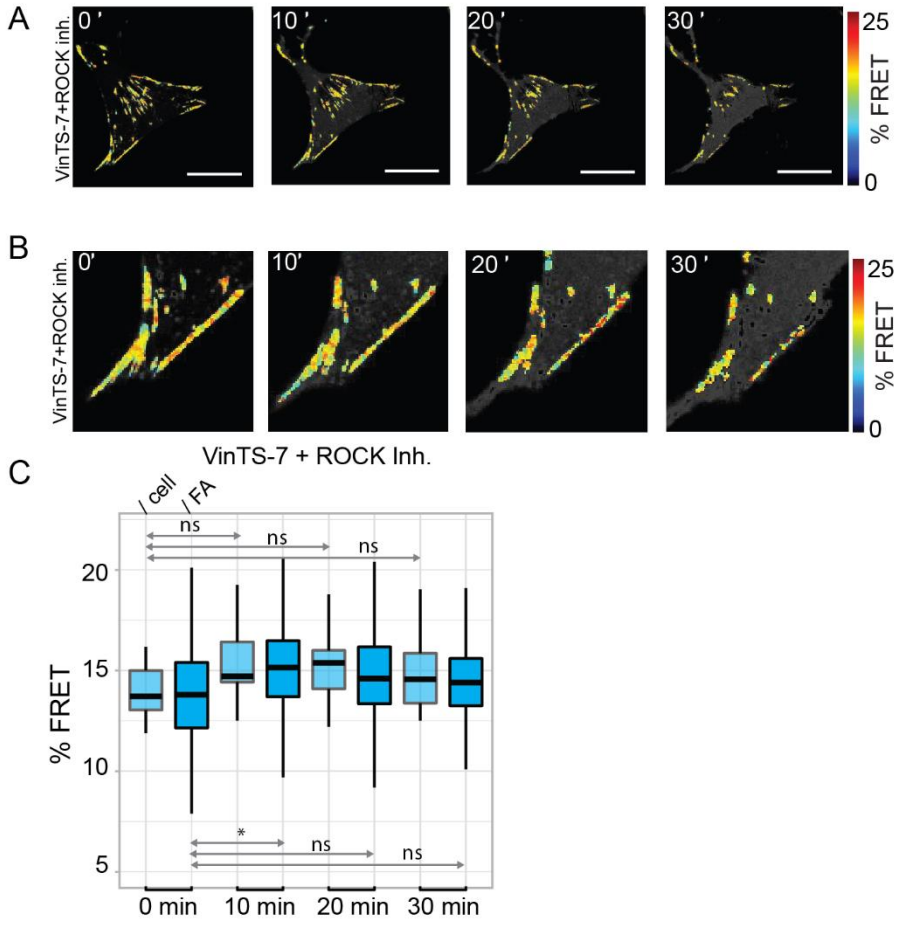


Figure 4.10: MEF-vinKO cells transiently transfected with VinTS-7 treated with ROCK inhibitor (Y-27632). (A) FRET efficiency image derived from the phasor FRET trajectory displayed over time after admission of ROCK inhibitor. (B) 25 µm wide zoom in on a FA feature over the measured timepoints. (C) Quantification of the cell-wise and FA-wise FRET efficiency measured over multiple cells (n = 9). Focal adhesions analysed over every timepoint respectively: 539, 475, 443 and 406. Statistics calculated with a non-parametric two-tailed Wilcoxon-Mann-Whitney U-test assuming no normal distribution with significance level of 0.05. *** equals p<0.001, * equals p<0.05, ns = not significant.

The acquisition time for each image was approximately 5 minutes and images were taken before admission (t = 0 min) and at the 10, 20 and 30 min intervals. Over time, a clear decrease of focal adhesion size was observed. A reduced fluorescence intensity across the whole cell is confirmed by the apparent increase of the cell background in the normalized image. FRET efficiency images do not display a clear shift in tension. Analysing the FRET efficiency per FA and per cell

indicates a general rise in FRET efficiency but does not result in a significant change when looking at cellular average values of FRET. The only difference was found between 0 min and 10 min when looking at the FA FRET datapoints. At 20 minutes, the initial difference with the starting point has reduced to a non-significant change. In other words, looking at the subsequent timepoints, both focal adhesion and cell-based values seem to regress toward their initial measurements.

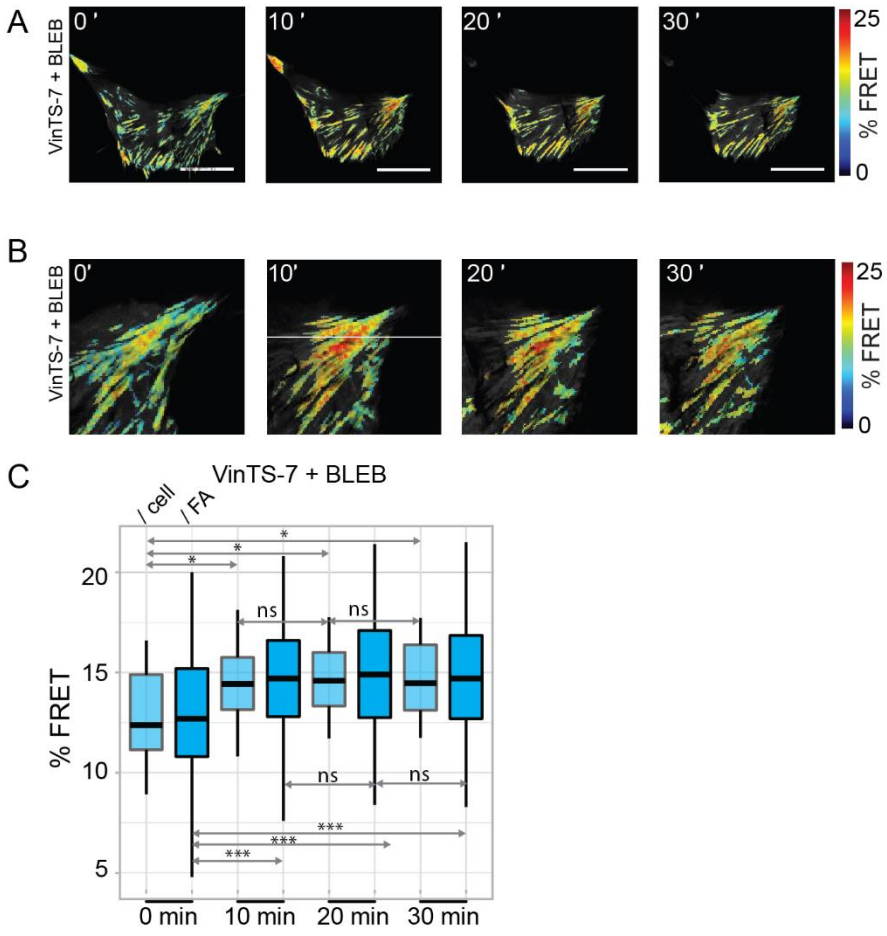


Figure 4.11: MEF-vinKO cells transiently transfected with VinTS-7 treated with blebbistatin (myosin inhibitor). (A) FRET efficiency image derived from the phasor FRET trajectory displayed over time after admission of blebbistatin. (B) 25 µm wide zoom in on a FA feature over the measured timepoints. (C) Quantification of the cell-wise and FA-wise FRET efficiency measured over multiple cells (n = 18). Focal adhesions analysed over every timepoint respectively: 1569, 1243, 1051 and 913.

To provide additional insights in the tension biosensors response to disturbances in the mechanotransduction pathway, the MEF-vinKO cells were also examined using blebbistatin (Fig. 4.11). The change in cellular morphology indicates the fast release of the previously stretched protrusions (Fig. 4.11 *A).* The magnified images shown in Fig. 4.11 *B* reveal a visual increase of FRET efficiency after 10 minutes, gradually declining as FA further degrade towards the 30-minute mark. However, the observed extend of FA disassembly was not as pronounced as with the ROCK inhibitor treatment. When quantifying the FRET efficiency per cell and per FA, the 10, 20 and 30 min timepoints differ significantly (***) from the initial image. While less significant (*), this is also the case for the analysis using cellular average.

4.5 Discussion and conclusion

In this chapter we explored the potential of phasor analysis to visualize FRET using time domain fluorescence lifetime imaging microscopy. We applied the developed methodology to investigate how cellular traction forces are distributed across vinculin molecules, abundantly present in focal adhesions. While the results obtained with different elastic linkers were not always consistent, we were able to detect and quantify the gradients of tension within focal adhesions. The gradient found in both VinTS-7 and VinTS-9 shows an increase in FRET towards the centre of the cell, indicating a higher force on the cell periphery. This observation is in line with earlier reports where FRET efficiencies were calculated using intensity-based approaches and in agreement with the current operational models of FAs (47, 52, 63). Importantly, we also showed that the measured FRET gradients were independent on the intensity signal, further validating the results obtained.

While we anticipated a higher dynamic range when using the VinTS-9 module, this sensor underperformed, showing a 2.7% FRET variation on average, whereas VinTS-7 exhibit a more substantial 5% leap across the gradient. This result, coupled with the high cell-to-cell variability, prompted us to consider potential issues with the 9-repeat plasmids. In our current hypothesis the 9-repeat spring module recombined during the plasmid amplification, leading to a plethora of alterations that might induce frame shifts and absence of the acceptor protein. Subsequently, during transfection, both the correct and truncated versions of the sensor are expressed in the cells. To address this recombination problem, we should consider creating a new linker which carries less/no repeats in the nucleic acid sequence of the plasmid but maintains the GGSGGS amino acid structured repeat (scrambled DNA sequence).

Interestingly, the observed dynamic range described by the gradient in FAs of ~5 % FRET efficiency in VINTS-7 with our phasor approach is substantially lower than the reported 16 % (a change from 24 to 40 %) measured by the group of Lacroix et al. in 2018 (47) using the 3-cube method to sensitized emission. In addition, the minimum and maximum FRET efficiency values reported are higher than the ones obtained using our approach. The large observed difference in FRET efficiencies obtained for vinculin in MEF cells remains a topic of debate. However, using our phasor approach, we were able to detect changes in the FRET efficiency within a focal adhesion, mirroring earlier reported patterns by Lacroix et al.

While we are the first to use phasor analysis to analyse FRET-based sensors, in 2019, the group of Hiroki Yokato and Jing Liu presented FLIM measurements of vinculin tension sensors in Nature's Scientific Reports (using the original CFP-YFP sensor with a 40 amino acid long peptide linker sensing region) (64). Their FRET measurements were, identically to ours, always scaled from 0 to 25%. In comparing

the VinTS and VinTL (with mTFP1-mVenus), they found a difference of only 6% FRET efficiency, but struggled at visualizing gradients in single FAs. However, these measurements were performed in osteocytes, what could affect the VinTS (FRET efficiency distribution peak at 21 %), but not the VinTL (FRET efficiency distribution peak at 27 %). These TCSPC-FLIM measurements were done using a single exponential decay curve fitting approach to find the donor lifetime (in presence of an acceptor), with the pure donor lifetime separately calculated. In any case, our method delivers much crisper FRET imaging of the FAs and improves heavily on reproducibility.

In this work, we used a sensor lacking the C-terminus of vinculin as a control. In this case, we expect the sensor to be insensitive to forces applied by the actin and therefore remain in a high FRET conformation. While the distribution of the FRET efficiencies reflect trends in our data, these results required some considerations. It was expected to have a narrow distribution in TL data since all the sensors were expected to adopt the same conformation. However, in our measurements, the spread was frequently larger for TL than TS. For VinTS, cellular heterogeneity was expected due to variations in high and low force areas, as averaged FA data might overlook differences within each FA. Nevertheless, the observed spread for TS was relatively small, indicating a similar average FRET per FA. The larger heterogeneity within the TL sensor might be caused by the incorrect cellular localization or different interactions with other molecules, as a large fragment of the vinculin is absent. A better control would therefore be to have a tension sensor where only those amino acids responsible for binding to the actin are mutated. Compared to the TL version used here, it would maintain the possible effect of the vinculin tail on the acceptor to which it is attached. Such strategy has been reported for vinculin where directed mutations caused loss of talin or actin binding (65). Further improving the phasor analysis, imaging another variant of the vinculin sensor with only donor label would be an improvement over our cytosolic reference measurement, but require more cloning. To investigate the cellular effect of a cell transfected with the TL sensor variant, monitoring stress fibres are a direct cue for places of tension in the cell and would be a good next step in investigating the tension dissipation in the cell. It is a future outlook to investigate the stress fibres with all of the different sensor types (TS7, TS9, TL7 and TL9) and treatments (ROCK-inhibitor and blebbistatin) used.

The potential of the molecular tension sensors used was illustrated by monitoring changes after exposing the cells to drugs that reduce cellular traction forces. Experiments with a ROCK inhibitor and blebbistatin revealed a small, yet noticeable increase in the obtained FRET efficiency 10 minutes after the addition of the chemical compound looking at FA data. This is in agreement with observations made in previous work (47), where a loss of tension (increase of FRET) was seen upon adding Y-276632 (ROCK inhibitor). We hypothesize that this initial loss of tension results from FA disassembly coupled with a decrease in myosin motility

induced by the added drug. However, as the focal adhesion continues to disassemble, the residual tension is transferred to the remaining mechanotransduction chains, potentially increasing the load on mechanosensitive proteins such as vinculin, thereby increasing the tension once more. It should also be acknowledged that any photobleaching effect within the image series will decrease the signal intensity, which will resemble the degradation of FAs. Nevertheless, it is important to note that photobleaching should not impact the measured FRET efficiency since FLIM data is concentration independent.

Regarding the measured FRET values, it is important to stress that our FRET efficiency values cannot be linked to actual forces within the measured cells. However, tension sensors provide a reliable relative indication of the spatial distribution of molecular tension within the cell. The extraction of quantitative information is challenging due to several factors. Tension, for instance, is spread over a focal adhesion area and the exact number of tension sensitive modules carrying the load is unknown. Consequently, a larger focal adhesion subject to the same pulling load might show a relatively high FRET values (low tension per molecule). Additionally, the conformation of the fluorescent proteins that are directly in line with the loaded tension might be affected, potentially leading to a loss of fluorescence and thereby influence the FRET readout (66–68). Furthermore, the effects of the dense packing of the tension sensitive modules within a FA are not known, implying that the observed changes can partially result from energy transfer or reduced donor fluorescence lifetime due to packing of the module and not due to decreased tension. Lastly, the twisting of the FRET tension module under load presents and unknown variable, as this could potentially influence the energy transfer by altering the relative orientation of the donor and acceptor.

In this work we studied focal adhesions in a flat 2D surface using a confocal microscope. While the pinhole isn't creating an optical section thinner compared to the estimated height of a FA, it is difficult to guarantee an identical imaging plane throughout images. However, the FLIM recordings are insensitive to intensity variations making this issue less prominent. Additionally, Kanchanawong et al. demonstrated with interferometric photoactivated localization microscopy that the molecular architecture of a focal adhesion is predominantly flat when looking at labelled vinculin (69).

On the outlook and future applications of FRET sensing we propose the multiplexed use of these tension sensors to get a more insightful probing of the tensions that are transferred from the cell-edge to the nucleus. Several interesting combinations are possible with readily available sensors. The multiplexing of vinculin or talin (70) tension sensors with cadherin (cell-cell interactions, (71)) or nesprin (in the LINC complex, (53)) is a good example. Such research line has been explored by Grashoff et al. in a report where two versions of a talin tension sensor were combined: one with a dark acceptor (mTFP1-ShadowG), and one with a large stoke

shift FRET pair (LLSmOrgange-mKate2) (72). These type of experiments can be further extended and improved using the phasor approach, avoiding the often used decay fitting approach with only a single exponential, which simplifies the FRET data.

In conclusion, our evaluation of the phasor approach has yielded a positive assessment, as it enables near-direct FRET analysis consistently. This method allowed us to distinguish details in the FRET heterogeneity within single focal adhesions. However, assessing the resulting FRET information from tension-based sensors remains challenging due to the involvement of numerous influencing factors. While quantitative information seems far off, the relative measurement and comparative power remains valuable.

4.6 References

1. Martino, F., A.R. Perestrelo, V. Vinarský, S. Pagliari, and G. Forte. 2018. Cellular mechanotransduction: From tension to function. *Front. Physiol.* 9:378185.
2. Jansen, K.A., R.G. Bacabac, I.K. Piechocka, and G.H. Koenderink. 2013. Cells actively stiffen fibrin networks by generating contractile stress. *Biophys. J.* 105:2240–2251.
3. Fuchs, E., T. Tumbar, and G. Guasch. 2004. Socializing with the neighbors: Stem cells and their niche. *Cell.* 116:769–778.
4. Watt, F.M., and B.L.M. Hogan. 2000. Out of Eden: stem cells and their niches. *Science*. 287:1427–1430.
5. Even-Ram, S., V. Artym, and K.M. Yamada. 2006. Matrix Control of Stem Cell Fate. *Cell.* 126:645–647.
6. Shkumatov, A., M. Thompson, K.M. Choi, D. Sicard, K. Baek, D.H. Kim, D.J. Tschumperlin, Y.S. Prakash, and H. Kong. 2015. Matrix stiffness-modulated proliferation and secretory function of the airway smooth muscle cells. *Am. J. Physiol. Lung Cell. Mol. Physiol.* 308:L1125–L1135.
7. Razinia, Z., P. Castagnino, T. Xu, A. Vázquez-Salgado, E. Puré, and R.K. Assoian. 2017. Stiffness-dependent motility and proliferation uncoupled by deletion of CD44. *Sci. Rep.* 7.
8. Yeh, Y.T., S.S. Hur, J. Chang, K.C. Wang, J.J. Chiu, Y.S. Li, and S. Chien. 2012. Matrix Stiffness Regulates Endothelial Cell Proliferation through Septin 9. *PLoS One*. 7:e46889.
9. Vincent, L.G., Y.S. Choi, B. Alonso-Latorre, J.C. Del Álamo, and A.J. Engler. 2013. Mesenchymal stem cell durotaxis depends on substrate stiffness gradient strength. *Biotechnol. J.* 8:472–484.
10. Ishihara, S., and H. Haga. 2022. Matrix Stiffness Contributes to Cancer Progression by Regulating Transcription Factors. *Cancers (Basel).* 14.
11. Scott, K.E., S.I. Fraley, and P. Rangamani. 2021. A spatial model of YAP/TAZ signaling reveals how stiffness, dimensionality, and shape contribute to emergent outcomes. *Proc. Natl. Acad. Sci. U. S. A.* 118:e2021571118.
12. Wei, S.C., L. Fattet, J.H. Tsai, Y. Guo, V.H. Pai, H.E. Majeski, A.C. Chen, R.L. Sah, S.S. Taylor, A.J. Engler, and J. Yang. 2015. Matrix stiffness drives epithelial–mesenchymal transition and tumour metastasis through a TWIST1–G3BP2 mechanotransduction pathway. *Nat. Cell Biol. 2014 175*. 17:678–688.
13. Chin, L.K., Y. Xia, D.E. Discher, and P.A. Janmey. 2016. Mechanotransduction in cancer. *Curr. Opin. Chem. Eng.* 11:77–84.
14. Zancla, A., P. Mozetic, M. Orsini, G. Forte, and A. Rainer. 2022. A primer to traction force microscopy. *J. Biol. Chem.* 298:101867.
15. Knights, A.J., A.P.W. Funnell, M. Crossley, and R.C.M. Pearson. 2012. Holding Tight: Cell Junctions and Cancer Spread. *Trends Cancer Res.* 8:61.
16. Baade, T., C. Paone, A. Baldrich, and C.R. Hauck. 2019. Clustering of integrin β cytoplasmic domains triggers nascent adhesion formation and reveals a protozoan origin of the integrin-talin interaction. *Sci. Rep.* 9.
17. Del Rio, A., R. Perez-Jimenez, R. Liu, P. Roca-Cusachs, J.M. Fernandez, and M.P.

Sheetz. 2009. Stretching single talin rod molecules activates vinculin binding. *Science (80-.).* 323:638–641.
18. Iskratsch, T., H. Wolfenson, and M.P. Sheetz. 2014. Appreciating force and shape — the rise of mechanotransduction in cell biology. *Nat. Rev. Mol. Cell Biol. 2014 1512*. 15:825–833.
19. Wehrle-Haller, B. 2012. Structure and function of focal adhesions. *Curr. Opin. Cell Biol.* 24:116–124.
20. Schaller, M.D. 2001. Paxillin: a focal adhesion-associated adaptor protein. *Oncogene 2001 2044*. 20:6459–6472.
21. Matsui, H., I. Harada, and Y. Sawada. 2012. Src, p130Cas, and Mechanotransduction in Cancer Cells. *Genes Cancer*. 3:394.
22. Parsons, J.T. 2003. Focal adhesion kinase: the first ten years. *J. Cell Sci.* 116:1409–1416.
23. Tortorella, I., C. Argentati, C. Emiliani, F. Morena, and S. Martino. 2022. Biochemical Pathways of Cellular Mechanosensing/Mechanotransduction and Their Role in Neurodegenerative Diseases Pathogenesis. *Cells 2022, Vol. 11, Page 3093*. 11:3093.
24. Beavon, I.R.G. 2000. The E-cadherin–catenin complex in tumour metastasis: structure, function and regulation. *Eur. J. Cancer*. 36:1607–1620.
25. Rice, A.J., E. Cortes, D. Lachowski, B.C.H. Cheung, S.A. Karim, J.P. Morton, and A. Del Río Hernández. 2017. Matrix stiffness induces epithelial–mesenchymal transition and promotes chemoresistance in pancreatic cancer cells. *Oncog. 2017 67*. 6:e352–e352.
26. Haque, F., D.J. Lloyd, D.T. Smallwood, C.L. Dent, C.M. Shanahan, A.M. Fry, R.C. Trembath, and S. Shackleton. 2006. SUN1 Interacts with Nuclear Lamin A and Cytoplasmic Nesprins To Provide a Physical Connection between the Nuclear Lamina and the Cytoskeleton. *Mol. Cell. Biol.* 26:3738–3751.
27. Osmanagic-Myers, S., T. Dechat, and R. Foisner. 2015. Lamins at the crossroads of mechanosignaling. *Genes Dev.* 29:225–237.
28. Guilluy, C., L.D. Osborne, L. Van Landeghem, L. Sharek, R. Superfine, R. Garcia-Mata, and K. Burridge. 2014. Isolated nuclei adapt to force and reveal a mechanotransduction pathway in the nucleus. *Nat. Cell Biol. 2014 164*. 16:376–381.
29. Heessen, S., and M. Fornerod. 2007. The inner nuclear envelope as a transcription factor resting place. *EMBO Rep.* 8:914–919.
30. Harris, A.K., P. Wild, and D. Stopak. 1980. Silicone Rubber Substrata: A New Wrinkle in the Study of Cell Locomotion. *Science (80-.).* 208:177–179.
31. Harris, A.K. 1978. JOURNAL OF MICROSCOPY. *J. Microsc.* 114.
32. Li, H., D. Matsunaga, T.S. Matsui, H. Aosaki, G. Kinoshita, K. Inoue, A. Doostmohammadi, and S. Deguchi. 2022. Wrinkle force microscopy: a machine learning based approach to predict cell mechanics from images. *Commun. Biol. 2022 51*. 5:1–9.
33. Harris, A.K., D. Stopak, and P. Wild. 1981. Fibroblast traction as a mechanism for collagen morphogenesis. *Nat. 1981 2905803*. 290:249–251.
34. Desai, R., M. Yang, N. Sniadecki, W. Legant, and C. Chen. 2007. Microfabricated post-array-detectors (mPADs): an approach to isolate mechanical forces. *J. Vis. Exp.* 311.
35. Tan, J.L., J. Tien, D.M. Pirone, D.S. Gray, K. Bhadriraju, and C.S. Chen. 2003. Cells lying

on a bed of microneedles: an approach to isolate mechanical force. *Proc. Natl. Acad. Sci. U. S. A.* 100:1484–1489.
36. Dembo, M., T. Oliver, A. Ishihara, and K. Jacobson. 1996. Imaging the traction stresses exerted by locomoting cells with the elastic substratum method. *Biophys. J.* 70:2008–2022.
37. Dembo, M., and Y.L. Wang. 1999. Stresses at the cell-to-substrate interface during locomotion of fibroblasts. *Biophys. J.* 76:2307.
38. Oliver, T., K. Jacobson, and M. Dembo. 1995. Traction forces in locomoting cells. *Cell Motil. Cytoskeleton*. 31:225–240.
39. Del Álamo, J.C., R. Meili, B. Alonso-Latorre, J. Rodríguez-Rodríguez, A. Aliseda, R.A. Firtel, and J.C. Lasheras. 2007. Spatio-temporal analysis of eukaryotic cell motility by improved force cytometry. *Proc. Natl. Acad. Sci. U. S. A.* 104:13343–13348.
40. Hur, S.S., Y. Zhao, Y.S. Li, E. Botvinick, and S. Chien. 2009. Live Cells Exert 3-Dimensional Traction Forces on Their Substrata. *Cell. Mol. Bioeng.* 2:425–436.
41. Colin-York, H., D. Shrestha, J.H. Felce, D. Waithe, E. Moeendarbary, S.J. Davis, C. Eggeling, and M. Fritzsche. 2016. Super-Resolved Traction Force Microscopy (STFM). *Nano Lett.* 16:2633–2638.
42. Barrasa-Fano, J., A. Shapeti, Á. Jorge-Peñas, M. Barzegari, J.A. Sanz-Herrera, and H. Van Oosterwyck. 2021. TFMLAB: A MATLAB toolbox for 4D traction force microscopy. *SoftwareX*. 15:100723.
43. Franck, C., S.A. Maskarinec, D.A. Tirrell, and G. Ravichandran. 2011. Three-Dimensional Traction Force Microscopy: A New Tool for Quantifying Cell-Matrix Interactions. *PLoS One*. 6:1–15.
44. Steinwachs, J., C. Metzner, K. Skodzek, N. Lang, I. Thievessen, C. Mark, S. Münster, K.E. Aifantis, and B. Fabry. 2016. Three-dimensional force microscopy of cells in biopolymer networks. *Nat. Methods*. 13:171–176.
45. Wang, J.H.C., and B. Li. 2009. Application of cell traction force microscopy for cell biology research. *Methods Mol. Biol.* 586:301–313.
46. Adhikari, N., K.C. Shekar, R. Staggs, Z. Win, K. Steucke, Y.W. Lin, L.N. Wei, P. Alford, and J.L. Hall. 2015. Guidelines for the Isolation and Characterization of Murine Vascular Smooth Muscle Cells. A Report from the International Society of Cardiovascular Translational Research. *J. Cardiovasc. Transl. Res.* 8:158–163.
47. Lacroix, A.S., A.D. Lynch, M.E. Berginski, and B.D. Hoffman. 2018. Tunable molecular tension sensors reveal extension-based control of vinculin loading. 1–36.
48. Zhang, Y., C. Ge, C. Zhu, and K. Salaita. 2014. DNA-based digital tension probes reveal integrin forces during early cell adhesion. *Nat. Commun.* 5:5167.
49. Glazier, R., J.M. Brockman, E. Bartle, A.L. Mattheyses, O. Destaing, and K. Salaita. 2019. DNA mechanotechnology reveals that integrin receptors apply pN forces in podosomes on fluid substrates. *Nat. Commun.* 10:4507.
50. Labernadie, A., A. Bouissou, P. Delobelle, S. Balor, R. Voituriez, A. Proag, I. Fourquaux, C. Thibault, C. Vieu, R. Poincloux, G.M. Charrière, and I. Maridonneau-Parini. 2014. Protrusion force microscopy reveals oscillatory force generation and mechanosensing activity of human macrophage podosomes. *Nat. Commun.* 5.
51. Lu, L., S.J. Oswald, H. Ngu, and F.C.P. Yin. 2008. Mechanical Properties of Actin Stress

Fibers in Living Cells. *Biophys. J.* 95:6060.
52. Grashoff, C., B.D. Hoffman, M.D. Brenner, R. Zhou, M. Parsons, M.T. Yang, M.A. McLean, S.G. Sligar, C.S. Chen, T. Ha, and M.A. Schwartz. 2010. Measuring mechanical tension across vinculin reveals regulation of focal adhesion dynamics. *Nature*. 466:263–266.
53. Arsenovic, P.T., and D.E. Conway. 2018. Using Nesprin Tension Sensors to Measure Force on the LINC Complex. *Methods Mol. Biol.* 1840:59.
54. Borghi, N., M. Sorokina, O.G. Shcherbakova, W.I. Weis, B.L. Pruitt, W.J. Nelson, and A.R. Dunn. 2012. E-cadherin is under constitutive actomyosin-generated tension that is increased at cell-cell contacts upon externally applied stretch. *Proc. Natl. Acad. Sci. U. S. A.* 109:12568–12573.
55. Kumar, A., K.L. Anderson, M.F. Swift, D. Hanein, N. Volkmann, and M.A. Schwartz. 2018. Local Tension on Talin in Focal Adhesions Correlates with F-Actin Alignment at the Nanometer Scale. *Biophysj*. 115:1569–1579.
56. Hinde, E., M.A. Digman, C. Welch, and K.M. Hahn. 2012. Biosensor FRET detection by the phasor approach to fluorescence lifetime imaging microscopy (FLIM). *Microsc. Res. Tech. Author Manuscr.* 75:271–281.
57. Digman, M.A., V.R. Caiolfa, M. Zamai, and E. Gratton. 2008. The phasor approach to fluorescence lifetime imaging analysis. *Biophys. J.* 94:L14–L16.
58. Redford, G.I., and R.M. Clegg. 2005. Polar plot representation for frequency-domain analysis of fluorescence lifetimes. *J. Fluoresc.* 15:805–815.
59. Gates, E.M., A.S. LaCroix, K.E. Rothenberg, and B.D. Hoffman. 2019. Improving Quality, Reproducibility, and Usability of FRET-Based Tension Sensors. *Cytom. Part A*. 95:201–213.
60. Schrimpf, W., A. Barth, J. Hendrix, and D.C. Lamb. 2018. PAM: A Framework for Integrated Analysis of Imaging, Single-Molecule, and Ensemble Fluorescence Data. *Biophys. J.* 114:1518–1528.
61. Coucke, Q., N. Parveen, G.S. Fernández, C. Qian, J. Hofkens, Z. Debyser, and J. Hendrix. 2023. Particle-based phasor-FLIM-FRET resolves protein-protein interactions inside single viral particles. *Biophys. Reports*. 3.
62. Chen, G., Z. Hou, D.R. Gulbranson, and J.A. Thomson. 2010. Actin-Myosin Contractility Is Responsible for the Reduced Viability of Dissociated Human Embryonic Stem Cells. *Cell Stem Cell*. 7:240–248.
63. Rothenberg, K.E., D.W. Scott, N. Christoforou, and B.D. Hoffman. 2018. Vinculin Force-Sensitive Dynamics at Focal Adhesions Enable Effective Directed Cell Migration. *Biophys. J.* 114:1680–1694.
64. Li, F., A. Chen, A. Reeser, Y. Wang, Y. Fan, S. Liu, and X. Zhao. 2019. Vinculin Force Sensor Detects Tumor-Osteocyte Interactions. *Sci. Rep.* 1–11.
65. Rothenberg, K.E., D.W. Scott, N. Christoforou, and B.D. Hoffman. 2018. Vinculin Force-Sensitive Dynamics at Focal Adhesions Enable Effective Directed Cell Migration. *Biophys. J.* 114:1680–1694.
66. Ganim, Z., and M. Rief. 2017. Mechanically switching single-molecule fluorescence of GFP by unfolding and refolding. *Proc. Natl. Acad. Sci. U. S. A.* 114:11052–11056.
67. Dietz, H., and M. Rief. 2004. Exploring the energy landscape of GFP by single-

molecule mechanical experiments. *Proc. Natl. Acad. Sci. U. S. A.* 101:16192–16197.
68. Perez-Jimenez, R., S. Garcia-Manyes, S.R.K. Ainavarapu, and J.M. Fernandez. 2006. Mechanical unfolding pathways of the enhanced yellow fluorescent protein revealed by single molecule force spectroscopy. *J. Biol. Chem.* 281:40010–40014.
69. Kanchanawong, P., G. Shtengel, A.M. Pasapera, E.B. Ramko, M.W. Davidson, H.F. Hess, and C.M. Waterman. 2010. Nanoscale architecture of integrin-based cell adhesions. *Nat. 2010 4687323*. 468:580–584.
70. Kumar, A., K.L. Anderson, M.F. Swift, D. Hanein, N. Volkmann, and M.A. Schwartz. 2018. Local Tension on Talin in Focal Adhesions Correlates with F-Actin Alignment at the Nanometer Scale. *Biophys. J.* 115:1569–1579.
71. Eder, D., K. Basler, and C.M. Aegerter. 2017. Challenging FRET-based E-Cadherin force measurements in Drosophila. *Sci. Rep.* 1–12.
72. Ringer, P., A. Weißl, A.L. Cost, A. Freikamp, B. Sabass, A. Mehlich, M. Tramier, M. Rief, and C. Grashoff. 2017. Multiplexing molecular tension sensors reveals piconewton force gradient across talin-1. *Nat. Methods 2017 1411*. 14:1090–1096.

Chapter 5

Discussion and future outlook

5.1 Phasor for intermolecular FRET

In this dissertation, we used the phasor approach to explore two distinct FRET sensing modes: intermolecular and intramolecular. Given their extensive application in modern biochemistry research, it was important to highlight the seamless applicability of the phasor approach to FLIM imaging for both types. This, however, required a thorough understanding of its graphical analysis methodology.

The work presented in **Chapter 3** illustrated the investigation of intermolecular FRET focusing on the HIV-1 integrase protein. We showed that there is a minimum photon budget needed to perform reliable phasor analysis (for a pixel or a pixel group). Additionally, we demonstrated that we could accurately determine the FRET efficiency of dual-labelled DNA strands using the FRET trajectory generated using the phasor plot. After the phasor-derived lifetime evaluation of various donor- or acceptor labelled integrases in HIV-1 virions using the phasor approach, we investigated the oligomerization of this enzyme in FRET-labelled viral particles. Our results underlined the importance of the donor-engagement ratio when determining the oligomerization state in our measurements. In our experiments, when donor--labelled integrases would interact with other donor-labelled integrases, there is no measurable FRET signal. Added to the complexity, multimers with more donors than acceptors, multimers with more acceptors or donors and monomeric donor and acceptor labelled integrase can be present in the particle. Taken together, measurements of the donor signal cannot unveil the precise multimeric state(s) of integrase. Importantly, our measurements collected donor signal over the whole particle and not single-molecule wise. Because of this, there is a considerable number of passive donors within each particle. Our phasor-based analysis allowed to plot several FRET trajectories for several possible percentages of passive donor contributions. Using this, the estimated particle average FRET, which is expected to increase upon multimerization was reported. From the presented FRET data, it was concluded that tetramers or higher order multimers must be present pre-infection. As such, the importance of the often-overlooked factor of passive donors in a measurement was illustrated. In providing a complete description of the graphical analysis presented and the involved factors, an honest and accessible overview of phasor analysis was provided for other researchers.

Chapter 3 focussed on the oligomerization of integrase in viral particles, pre-infection. In the past, the oligomerization of this enzyme was studied by during and hours after infection (1). In that study, in both cases FRET provided evidence of increased multimerization but the results were difficult compare with other external studies since the AP-FRET method leads to lab dependant FRET values. They remain valuable within the study, but difficult to compare outside. As such a FLIM based analysis provide a more lab-comparable approach. Added with the important

unknown of the number of exponentials are required for a fit of this data, phasor analysis can step in. Looking to the future, we can extend on the established work by combining single particle tracking and particle-based FRET using the phasor analysis to monitor the formation or dissociation of multimers during the several stages of the infection cycle, in live cells. Such feat would require a single-frame FLIM timelapse or samples fixated at several timepoints during the infection process.

In 2015, an innovative paper was published to quantify the bound and unbound fractions of a FRET experiment using the donor and acceptor lifetime information (2). While not directly applicable for our study, analysis of the acceptor lifetime in-growth might be a useful added parameter in FRET analysis of complex problems to consider in the future for intermolecular FRET studies.

5.2 Phasor for FRET-based molecular tension sensors

The increasing popularity of tension-based sensors underscores the need for additional methodologies to fully unlock their potential. As highlighted in the discussion of **Chapter 4**, to understand mechanotransduction, researchers would benefit from multiplexed imaging of FRET (tension) sensors targeting different tension-sensitive proteins at the same time. To achieve this, optimization of the available light spectrum is necessary. In the original work of Hofmann and Grashoff on vinculin tension sensors, the intensity-based FRET method of sensitized (acceptor) emission was used (3, 4). This approach requires both donor and acceptor emission for its calculation, consequently occupying a significant portion of the useable spectrum for imaging. A combination of more than one type of FRET pair, as would be required for spatially overlapping sensors, soon becomes problematic in terms of detecting pure signal. As FLIM imaging only probes the donor signal, allowing the use of dark acceptors to calculate FRET efficiencies (5, 6) and thereby freeing part of the spectrum for another FRET sensor.

In the presented work, experiments showed successful measurements of the relative tension heterogeneities within single focal adhesions. Importantly, this isn't a fully conclusive observation. FA tension and (vinculin) molecular tension are not equal and the obtained values should be regard within the context of an averaged view over many tension loaded molecules. In our case, a combination with super resolution techniques to investigate the number of molecules in the focal adhesion could result in interesting observations, since it will provide context to the obtained FRET tension maps.

The measurements of genetically encoded FRET tension sensors in cells remains sensitive to autofluorescence/background, which is, importantly, straightforward to correct in the phasor approach. In contrast, for fitting based algorithms it is not easy to pinpoint the lifetime signature of autofluorescence. Describing autofluorescence with a single additional component in a fit scheme (monoexponential) would heavily oversimplify, while describing autofluorescence with a highly multiexponential component might be near impossible to determine in itself. With the phasor technique, only the coordinates of the autofluorescence are required. Fortunately, in these sensors, the challenges associated with unknown donor-acceptor stoichiometry (as discussed in **Chapter 3)** are not at play. For these and other unimolecular biosensors, a 1:1 ratio is expected, as both the donor and acceptor are expressed together in a single protein FRET module. Which makes the FRET analysis more straight forward and more accurate. However, it is important to keep the maturation time of the used fluorescent proteins in mind, as this can affect the donor-acceptor ratio.

In this work, I presented fluorescence data acquired from transiently transfected cells, which, inevitably, results in both overexpression and a variable expression level among individual cells. In order to perform experiments that accurately reflect the true biological/mechanical state of an imaged cell, the generation of a stable cell line that follows natural expression is desired. This implies the insertion of the FRET sensing module within the gene encoding the target proteins. Alternatively, sticking to transfection methodologies, designing the plasmid with the original vinculin promotor instead of CMV (as used in this dissertation) might be an intermediate solution to achieve normal expression levels. This raises the question: what are the optimal expression levels? While no clear answer is readily available, one could imagine that a cell where all vinculins are the modified versions, is not fully representative of its true function. On the other hand, reducing the amount of expressed sensor will further reduce the measurable signal.

In the work of Lacroix, where VinTS-7 was first measured using sensitized emission FRET, a gradient within focal adhesions was observed, spanning a 16 % increase (with the maximum FRET efficiency at 40 %). Our methodology displayed similar relative shifts, albeit with lower FRET efficiency values overall (10 to 15 %). The exact reason for this difference is unknown. Contributing to the relative nature of tension measurements using FRET sensors are two additional factors. Firstly, the unknown number of molecules that are load bearing inside a focal adhesion (FA) and effectively share the load. Secondly, the assumption that forces are transduced across a protein along a single N-terminal to C-terminal axis. The first constraint could be partially resolved with the application of MINFLUX (minimal photon fluxes). This super-resolution method can achieve a spatial resolution of <10 nm and has therefore the potential to resolve single molecule tension modules. While still challenging, the number of molecules present in the focal adhesion would no longer affect the FRET efficiencies measured.

The possibility to measure the molecular tension associated with different proteins within cells enables the investigation of the mechanotransduction pathways. An approach commonly used to do this is to study the effects of certain inhibitory molecules. Commonly used inhibitors of mechanotransduction in research include cytochalasin-D, ROCK-inhibitor (Y-27632) or blebbistatin (7, 8). Despite their wide application aimed at disturbing the tensions across the cytoskeleton, the exact operating mechanisms of these drugs are still under investigation. The duration and concentration for exposure of these inhibitors to cells varies from one study to another, which presents challenges for standardization. Importantly, prolonged exposure to these drugs can ultimately result in cell death and therefore creating an experiment in which cells remain physiologically healthy but, for example, without tension onto FAs is extremely challenging. At the same time, the ideal control experiment should be performed in the same cell, where the 'pre' imaged situation can be compared with a second image in which the tensions are perturbed, eliminating cell-to-cell differences. Although creating such experiment is no straightforward task, an innovative approach can be drawn from the work of the French research group of G. Renauld. They presented a paper on nano surgery of the cytoskeleton using a picosecond pulsed laser (>500 ps pulse duration at 355 nm) in live cells (9), as shown in Fig. 1. These short, high-energy bursts from a frequency tripled Nd:YAG-pulsed laser, perform plasma-induced ablation of biological structures. It has been shown that this technique can break apart microtubules, centrioles and actin filaments (10, 11). Combining laser mediated ablation of actin filaments with FRET imaging of vinculin tension sensors might provide a direct readout of the unloaded focal adhesion, allowing the investigation of the link between cytoskeletal stress and tension in the focal adhesions (or other mechanosensitive structure).

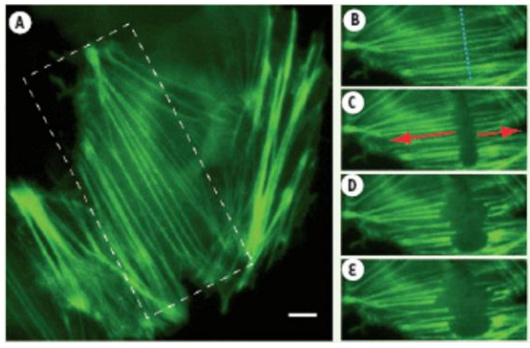


Figure 1: Illustration of actin nano surgery through ablation in mammalian Ptk-2 cells transfected with actin-eGFP. (A) Overview of an actin stress fibre bundle. (B-E) Retraction of actin fibres after ablation at 0, 10, 20 and 30 seconds after ablation. Image adapted from (9).

In the wake of the research presented in **Chapter 4**, our research group is now actively exploring the possibilities of combining traction force microscopy (TFM) and FRET-based tension sensing in one sample. While TFM yields the ability to report on the forces a cell applies to certain regions, FRET-based tension sensors can supply information on the molecular tension. A larger focal adhesion will engage more force, but how this relates to molecular forces is not known. In practice, this combination of technologies could connect the force field outside the cell with mechanotransduction inside the cell and open a new dimension in evaluating cellular forces and interpretation of cellular tractions.

While Chapter 4 was focussed on the molecular based FRET tension sensors, in the last years DNA-based molecular tension sensors have also been used to probe cellular forces. For these sensors, the force-sensing component is a DNA-hairpin which unzips when force is applied. The sensing range is tuned by adjusting the number of complementary bases and the GC content of the hairpin region. To monitor the opening and closing of the hairpin, a donor/acceptor pair is place at the end of the hairpin. While the protein-based sensors used in this dissertation show a broad FRET-range, linked to the array of possible 'stretched' conformations, DNA-based sensors display an on/off behaviour on the molecular level. These limited FRET sensor conformations (open and close), greatly reduce the analysis complexity.

These sensors can be multiplexed together with genetically encoded tension sensors or serve as standalone measurements. This type of tension sensors cannot be genetically encoded are therefore mainly used on the outside of the cell. There they measure forces in between the cellular membrane proteins (such as integrin) and the ECM (12–14). In recent years, successful efforts were made utilizing DNA based hairpin sensors inside cells, for example to measure forces in the actin network (15). DNA-based tension sensors can be easily measured using FLIM-FRET or intensity-based FRET, using two fluorescent probes or a fluorescent probe and a non-emitting quencher. Alternatively, DNA-based sensors can be monitored using the binding of small DNA strands complementary to the hairpin region. This enable combining tension-sensing with super-resolution imaging using DNA-PAINT. Using this approach it was possible to resolve piconewton mechanical loads with a ~25 nm resolution for single probe evaluation (16).

5.3 The future of phasor application in FLIM microscopy

The central aspect of this thesis has been to explore the application of phasor-FLIM methodology to FRET inter- and intramolecular biosensors while making such approach accessible to unexperienced microscopists. Therefore, it is important to state that phasor analysis of FLIM data is not limited to FRET or biosensors, and it

has been applied in many fields of bio-imaging: label free imaging of NADH lifetimes to image metabolic states in cells (17) or the material characterization/identification of micro- and nano carbonaceous particles (18). Regardless of the research question, phasor analysis can be applied to a wide range of fluorescence lifetimes, from monoexponential to more complex decays. Phasor analysis has the added value of providing graphical representations of lifetime clustering of the acquired image pixels. Importantly, the representation of FLIM data in a phasor plot does not require any a priori knowledge on the exact lifetime heterogeneity in the sample.

Phasor imaging is a computational fast approach to FLIM and FRET imaging. In the commercial systems developed in the last 5 years, phasor analysis of FLIM has been broadly introduced. Illustrating this is the newest Leica SP8 FALCON software which offers a live constructed phasor plot is, during image acquisition. Additionally, the FALCON system uses a hybrid TCPSC system that digitizes pulse and photon signal and feeds it into a fast 10 GHz sampler which replaces the TCSPC 'clock' with a permanent bitstream. This allows for nearly 50 times as many recorded photons per excitation pulse compared to conventional TCSPC, largely due to the ultra-short detector dead time and advanced signal algorithms (19).

An exciting emerging field in FLIM imaging is the combined use of the phasor approach for lifetime studies and the analogous phasor plot representation of spectral data in hyperspectral imaging (20, 21). Such method can effectively map an imaged pixel using several useful parameters: two separate phasor plots (spectral-phasor and lifetime-phasor, each containing S&G coordinates), intensity information (number of photons per pixel), and the conventional spatiotemporal dimensions (x-y-z-t). This treasure of information can provide information past intensity and lifetime to segment an image. Additionally, I anticipate that machine learning will be further introduced in the analysis of phasor plots, as illustrated already for imaging-based transcriptomics and image segmentation (20, 22). Added, I expect a fast further development of methodologies that fully use the phasor plot representation. For instance, phasor has recently been used to analyse intensity variations of fluorescence emission caused by a modulated STED intensity leading to improved spatial resolution (23).

Regarding possible future applications of phasor, I would like to highlight the work of Joron et al. on liquid-liquid phase separated (LLPS) condensates (25). In this novel paper, local density heterogeneities in the LLPS nuclear condensates were studied using the fluorescence lifetime of mCherry. More crowded environments will affect the photophysics of the fluorescence protein, reducing its lifetime. The authors fitted the recorded fluorescence decay using a single exponential, which will inevitably lower the lifetime-based study of local heterogeneities. Phasor-based sorting and colour coding of the image pixels might be more insightful.

To showcase the wide application range of use of phasor-FLIM, phasor analysis and its intrinsic segmentation capabilities have been used in the investigation of varnish layers in art conservation and restoration (27). Removing varnish is a crucial step in painting conservation. Thanks to the fluorescent properties of two common varnish types (dammar and mastic), FLIM can be used to investigate their presence. Here, the authors used a lightweight (4.8 kg) FLIM setup to probe a painting surface for the types of varnish, and its age using the phasor analysis to colour code the image based on predefined phasor-regions. This example highlights the potential of the method to non-expert users.

The biggest achievement of the presented work is the detailed, but honest description of the method. In many papers, FRET results are overinterpreted and claims are made without full understanding of the data that was obtained. I will be the first to acknowledge that the phasor approach to FLIM, or by extension FRET, is not easy to fully understand. However, once the principles are known, the way FLIM data is presented in a 2D plot opens op an extra connection with the acquired data. A visual method, with readily interpretable locations (monoexponentials and multiexponentials), visually fraction lines, … seem like a highly transparent analysis process compared to the optimal solution found by a fitting algorithm. The visual connection with your analysis, the maintained phasor-pixel reciprocity and limited set of 'phasor rules' create an environment in which many researchers can learn how to interpret their data. Added to this potential the usage of the higher harmonics of the phasor analysis were not discussed in this work. Using a higher harmonic analysis, not one but two periods of the sine and cosine are used to describe one period of the periodic signal. In many cases this can further improve the spatial separation of clusters in the phasor plot since it redefines where a lifetime is plotted (for time-domain FLIM, second harmonic will spread the TCSPC bins on two full circumferences of the universal circle instead of one). The potential of using higher harmonics in biological image analysis with phasor is not yet fully developed since higher photon counts are required, which is the main difficulty in biological experiments using fluorescent proteins. However, with the arrival of more sensitive measuring techniques and better performing fluorescent labels, this could become possible in the future.

On a critical note, in most FRET literature covering FLIM-FRET, a fluorescence lifetime image is shown and from this a FRET image is calculated. Especially for FLIM-FRET, researcher try hard to calculate a single lifetime for a pixel that contains a whole heterogeneity of components. As seen in this dissertation, a FRET pixel in a biological context is an averaged view on the pixel content (autofluorescence, several FRET sensor stages, unbound donors, …) which will always create a multiexponential lifetime signature. Needless to say, this information can't be poured into a single 'lifetime' image where every pixel just gets one value assigned. Therefore, the phasor analysis provides a more honest approach, in which the heterogeneity of a sample can be assessed in the phasor

plot. While the FRET image obtained from the phasor-derived FRET trajectory is also an approximation, it does not hide as bluntly the complexity of the sample by allowing a more layered analysis approach (accounting DO, BG, …). As such, phasor analysis contains much more nuances on the sample lifetime heterogeneity which is a major aspect in fully understanding your sample and noticing abnormalities.

5.4 Popularizing home-built microscopes for biology research labs

The research presented in this thesis was measured using a home-built microscope and analysed using open-source software and custom MATLAB scripts. This choice results from my belief that a home-built microscope stands as an incredibly valuable research and learning tool. Of course, MATLAB licenses are not free and require research laboratories to make a considerable yearly investment. Therefore, a valuable future goal should be the transfer of the MATLAB code to a true open-source software like python. While this would also require a considerable investment in software finetuning and programming, only by transferring our software to a fully open-access and free platform the phasor analysis with PAM can be fully accessible to all.

A homebuilt microscope is more affordable than commercially available alternatives and offers unparallel flexibility for researchers to explore a wide array of experimental possibilities. A commercial confocal, for instance Leica SP8 (costing around €400k), offers numerous advantages over the PIE-FLIM setup used here. It provides novel features, such as counts per pulse, fully customizable excitation wavelength and detection ranges, easy adjustment of the pixel size and 3D imaging, among others. However, as it remains a closed system (black box) and a rigid tool for method development. With this thesis I would like to advocate for the widespread adoption of home-built microscopes and encourage labs to consider this option. With this perspective in mind, I propose some modifications to the current hardware of the PIE-FLIM microscope, as discussed in **Addendum II**. Firstly, the installation of a motorized stage would allow saving of sample positions which facilitates sample manipulations (e.g., adding a substance) in between imaging rounds. Adding a z-axis to such stage would open the 3D volume for confocal scanning. For example, when imaging a cell with a vinculin tension sensor on top of a gel, the imaging plane for focal adhesions at the cell-gel interface is often not perfectly flat. This could then be mediated by acquiring a few planes on the z-axis. Additionally, such stage would be used in future measurements of cells in a 3D environment (a biomimetic gel such as PIC hydrogel (28)) to further investigate the effect of the mechanical properties of the ECM on cellular mechanotransduction. Added, autofocus control would assure proper focus during,

for example, addition of an inhibitor or to eliminate drift when imaging for a longer time period. As discussed in Chapter 3, to retrieve accurate FLIM measurements (and therefore FLIM-FRET) using the phasor approach, enough photons need to be collected. To maximise photon detection and reduce the acquisition time, I propose to do a low-tech adaptation to the microscope by combining multiple hybrid PMT detectors to jointly measure the emission signal. While this would also reduce the count rate in each detector, this is an advantage to avoid pile-up of emission photons and thus allow higher excitation powers.

5.5 References

1. Borrenberghs, D., L. Dirix, F. De Wit, S. Rocha, J. Blokken, S. De Houwer, R. Gijsbers, F. Christ, J. Hofkens, J. Hendrix, and Z. Debyser. 2016. Dynamic Oligomerization of Integrase Orchestrates HIV Nuclear Entry. *Sci. Rep.* 6:1–14.
2. Chen, W.Y., E. Avezov, S.C. Schlachter, F. Gielen, R.F. Laine, H.P. Harding, F. Hollfelder, D. Ron, and C.F. Kaminski. 2015. A Method to Quantify FRET Stoichiometry with Phasor Plot Analysis and Acceptor Lifetime Ingrowth. *Biophys. J.* 108:999.
3. Grashoff, C., B.D. Hoffman, M.D. Brenner, R. Zhou, M. Parsons, M.T. Yang, M.A. McLean, S.G. Sligar, C.S. Chen, T. Ha, and M.A. Schwartz. 2010. Measuring mechanical tension across vinculin reveals regulation of focal adhesion dynamics. *Nature*. 466:263–266.
4. Lacroix, A.S., A.D. Lynch, M.E. Berginski, and B.D. Hoffman. 2018. Tunable molecular tension sensors reveal extension-based control of vinculin loading. 1–36.
5. Ringer, P., A. Weißl, A.L. Cost, A. Freikamp, B. Sabass, A. Mehlich, M. Tramier, M. Rief, and C. Grashoff. 2017. Multiplexing molecular tension sensors reveals piconewton force gradient across talin-1. *Nat. Methods 2017 1411*. 14:1090–1096.
6. Demeautis, C., F. Sipieter, J. Roul, C. Chapuis, S. Padilla-Parra, F.B. Riquet, and M. Tramier. 2017. Multiplexing PKA and ERK1&2 kinases FRET biosensors in living cells using single excitation wavelength dual colour FLIM. *Sci. Reports 2017 71*. 7:1–14.
7. Bhadriraju, K., M. Yang, S. Alom Ruiz, D. Pirone, J. Tan, and C.S. Chen. 2007. Activation of ROCK by RhoA is regulated by cell adhesion, shape, and cytoskeletal tension. *Exp. Cell Res.* 313:3616–3623.
8. Shi, J., X. Wu, M. Surma, S. Vemula, L. Zhang, Y. Yang, R. Kapur, and L. Wei. 2013. Distinct roles for ROCK1 and ROCK2 in the regulation of cell detachment. *Cell Death Dis.* 4.
9. Colombelli, J., R. Pepperkok, E.H.K. Stelzer, and E.G. Reynaud. 2006. La nanochirurgie laser en biologie cellulaire. *médecine/sciences*. 22:651–658.
10. Botvinick, E.L., V. Venugopalan, J. V. Shah, L.H. Liaw, and M.W. Berns. 2004. Controlled ablation of microtubules using a picosecond laser. *Biophys. J.* 87:4203–4212.
11. Colombelli, J., E.G. Reynaud, J. Rietdorf, R. Pepperkok, and E.H.K. Stelzer. 2005. In vivo Selective Cytoskeleton Dynamics Quantification in Interphase Cells Induced by Pulsed Ultraviolet Laser Nanosurgery. *Traffic*. 6:1093–1102.
12. Dutta, P.K., Y. Zhang, A.T. Blanchard, C. Ge, M. Rushdi, K. Weiss, C. Zhu, Y. Ke, and K. Salaita. 2018. Programmable Multivalent DNA-Origami Tension Probes for Reporting Cellular Traction Forces. *Nano Lett.* 18:4803–4811.
13. Zhang, Y., C. Ge, C. Zhu, and K. Salaita. 2014. DNA-based digital tension probes reveal integrin forces during early cell adhesion. *Nat. Commun.* 5:5167.
14. Blakely, B.L., C.E. Dumelin, B. Trappmann, L.M. McGregor, C.K. Choi, P.C. Anthony, V.K. Duesterberg, B.M. Baker, S.M. Block, D.R. Liu, and C.S. Chen. 2014. A DNA-based molecular probe for optically reporting cellular traction forces. *Nat. Methods 2014 1112*. 11:1229–1232.
15. Jayachandran, C., A. Ghosh, M. Prabhune, J. Bath, A.J. Turberfield, L. Hauke, J. Enderlein, F. Rehfeldt, and C.F. Schmidt. 2021. A DNA-based optical force sensor for

live-cell applications. *bioRxiv*. 2021.12.21.473677.
16. Brockman, J.M., H. Su, A.T. Blanchard, Y. Duan, T. Meyer, M.E. Quach, R. Glazier, A. Bazrafshan, R.L. Bender, A. V. Kellner, H. Ogasawara, R. Ma, F. Schueder, B.G. Petrich, R. Jungmann, R. Li, A.L. Mattheyses, Y. Ke, and K. Salaita. 2020. Live-cell super-resolved PAINT imaging of piconewton cellular traction forces. *Nat. Methods 2020 1710*. 17:1018–1024.
17. Stringari, C., R.A. Edwards, K.T. Pate, M.L. Waterman, P.J. Donovan, and E. Gratton. 2012. Metabolic trajectory of cellular differentiation in small intestine by Phasor Fluorescence Lifetime Microscopy of NADH. *Sci. Rep.* 2.
18. Aslam, I., M. Bravo, I. Van Zundert, S. Rocha, and M.B.J. Roeffaers. 2023. Label-Free Identification of Carbonaceous Particles Using Nonlinear Optical Microscopy. *Anal. Chem.* 95:8045–8053.
19. Alvarez, L.A.J., B. Widzgowski[1], G. Ossato, B. Van Den Broek, K. Jalink, L. Kuschel, M.J. Roberti, and F. Hecht. 2019. SP8 FALCON: a novel concept in fluorescence lifetime imaging enabling video-rate confocal FLIM. .
20. Vu, T., A. Vallmitjana, J. Gu, K. La, Q. Xu, J. Flores, J. Zimak, J. Shiu, L. Hosohama, J. Wu, C. Douglas, M.L. Waterman, A. Ganesan, P.N. Hedde, E. Gratton, and W. Zhao. 2022. Spatial transcriptomics using combinatorial fluorescence spectral and lifetime encoding, imaging and analysis. *Nat. Commun. 2022 131*. 13:1–14.
21. Scipioni, L., A. Rossetta, G. Tedeschi, and E. Gratton. 2021. Phasor S-FLIM: a new paradigm for fast and robust spectral fluorescence lifetime imaging. *Nat. Methods 2021 185*. 18:542–550.
22. Gratton, E., A. Vallmitjana, and B. Torrado. 2021. Phasor-based image segmentation: machine learning clustering techniques. *Biomed. Opt. Express, Vol. 12, Issue 6, pp. 3410-3422*. 12:3410–3422.
23. Sarmento, M.J., M. Oneto, S. Pelicci, L. Pesce, L. Scipioni, M. Faretta, L. Furia, G.I. Dellino, P.G. Pelicci, P. Bianchini, A. Diaspro, and L. Lanzanò. 2018. Exploiting the tunability of stimulated emission depletion microscopy for super-resolution imaging of nuclear structures. *Nat. Commun. 2018 91*. 9:1–11.
24. Castello, M., G. Tortarolo, M. Buttafava, T. Deguchi, F. Villa, S. Koho, L. Pesce, M. Oneto, S. Pelicci, L. Lanzanó, P. Bianchini, C.J.R. Sheppard, A. Diaspro, A. Tosi, and G. Vicidomini. 2019. A robust and versatile platform for image scanning microscopy enabling super-resolution FLIM. *Nat. Methods 2019 162*. 16:175–178.
25. Joron, K., J.O. Viegas, L. Haas-Neill, S. Bier, P. Drori, S. Dvir, P.S.L. Lim, S. Rauscher, E. Meshorer, and E. Lerner. 2023. Fluorescent protein lifetimes report densities and phases of nuclear condensates during embryonic stem-cell differentiation. *Nat. Commun. 2023 141*. 14:1–18.
26. Kim, D., W. Hwang, and D.Y. Kim. 2021. Phasor approach for Fluorescence Anisotropy. *SPIE Proc.* 11650:6.
27. Wilda, C.B., A. Burnstock, K. Suhling, F. Mattioli Della Rocca, R.K. Henderson, and J. Nedbal. 2023. Visualising varnish removal for conservation of paintings by fluorescence lifetime imaging (FLIM). *Herit. Sci.* 11:1–21.
28. Liu, K., M. Wiendels, H. Yuan, C. Ruan, and P.H.J. Kouwer. 2022. Cell-matrix reciprocity in 3D culture models with nonlinear elasticity. *Bioact. Mater.* 9:316–331.

Addendum I

Supplemental Information Chapter 3

Note S1

In the case an unquenched species with a mono-exponential decay co-exists in the same pixel with a quenched form, the fluorescence fraction of one species f is not equal to the concentration fraction f_C when looking at the fraction line connecting both phasors. The formula used to determine the concentration fraction in this case can be derived as following. A pure fluorescence species with mono-exponential decay can be approximated by the following equation, omitting a possible effect of the instrument response function (IRF).

$$I(t) = A.exp[-t/\tau]. \qquad \text{Eq. S1}$$

Here the time-dependent intensity, $I(t)$, follows from an exponential with amplitude A (proportional to the measurement duration), lifetime τ and time t. For a mixture of two species with different lifetimes, this gives:

$$I(t) = A_1.exp[-t/\tau_1] + A_2.exp[-t/\tau_2] \qquad \text{Eq. S2}$$

The concentration fraction of species 1 is simply given by:

$$f_{C,1} = \frac{A_1}{A_1 + A_2} \qquad \text{Eq. S3}$$

The fraction of photons radiating from species 1, i.e., the intensity fraction of species 1, on the other hand, is given by [J.R. Lakowicz, Springer US, 2006]:

$$f_{int,1} = \frac{A_1\tau_1}{A_1\tau_1 + A_2\tau_2}, \qquad \text{Eq. S4}$$

We now rearrange this equation as follows:

$$\frac{1}{f_{int,1}} - 1 = \frac{A_2\tau_2}{A_1\tau_1} \qquad \text{Eq. S5}$$

Since the ratio of amplitudes is the same as the ratio of concentrations, the following is true:

$$\frac{\tau_1}{\tau_2}\left(\frac{1}{f_{int,1}} - 1\right) = \frac{A_2}{A_1} = \frac{f_{C,2}}{f_{C,1}} = \frac{1 - f_{C,1}}{f_{C,1}} = \frac{1}{f_{C,1}} - 1 \qquad \text{Eq. S6}$$

Hence, the concentration fraction of species 1 in the mixture can be calculated from the different lifetimes and their corresponding intensity fractions:

$$f_{C,1} = \left(\frac{\tau_1}{\tau_2}\left(\frac{1}{f_{int,1}} - 1\right) + 1\right)^{-1}. \qquad \text{Eq. S7}$$

Implementations of concentration fractions in the phasor plot are illustrated in supplemental figure S11.

Note S2

The FRET trajectory or FRET quenching line is constructed using Equations 22 and 23. In practice, it describes a series of points determined by the FRET efficiency (E). For every value of *E* between 0 and 1 a $g_{quenchline}$ and $s_{quenchline}$ coordinate can be found for the mixture of three components (passive donors 'pD', background 'BG' and quenched donors '$D_{quenched}$'). Consequently, a mixture of three components is found in the triangle connecting each (blue lines in the figure below). When we combine the BG and fraction of passive donors into one point ($g_{BG\&pD}$, $s_{BG\&pD}$), the previous mixture of three can now be described by a line connecting $D_{quenched}$ at ($g_{quenched\ D}$, $s_{quenched\ D}$) and ($g_{BG\&pD}$, $s_{BG\&pD}$)(black line in the figure below). ($g_{BG\&pD}$, $s_{BG\&pD}$) is also the end point of the FRET trajectory. When the FRET efficiency E approaches 0% ($E \to 0$), the fractional contribution of the FRET-active donor $(1 - f_{BG\&pD})$ maximizes. Conversely, when E approaches 100% ($E \to 1$) the fractional contribution of the FRET-active donor $(1 - f_{BG\&pD})$ approaches 0% since its fluorescence quantum yield approaches 0% rendering the fractional intensity of the other signals $f_{BG\&pD} = 1$. The quantum yield of BG and pD remain unchanged at 100% FRET and, as can be seen, in the equations, $g_{quenchline} = g_{BG\ \&\ pD}$ and $s_{quenchline} = s_{BG\ \&\ pD}$, which indeed marks the endpoint of the FRET trajectory.

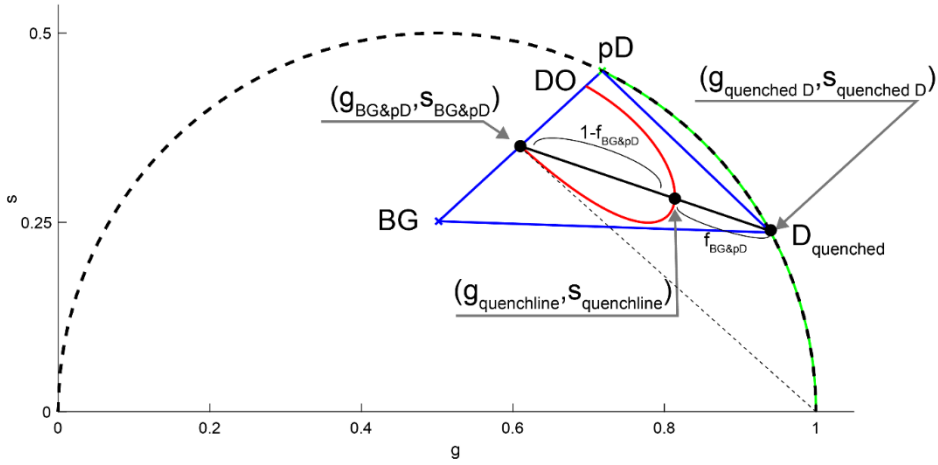


Figure: Illustration of Equations 22-23, describing a FRET trajectory with an autofluorescence background contribution of 10% BG ($f_{BG} = 0.10$) and passive donor contribution of 10% pD ($f_{pD} = 0.10$). Blue lines connect the three 3 pure species. The phasor signature of their mixture is always found inside the blue triangle. The red line is the FRET trajectory from *E*=0 to *E*=1. The black line is the fraction line of $(g_{BG\&pD}, s_{BG\&pD})$ and $(g_{quenched\ D}, s_{quenched\ D})$. As the FRET efficiency increases, the quantum yield of $D_{quenched}$ decreases, leading to a reduced photon intensity fraction $(1 - f_{BG\&pD})$. The straight dashed line represents the theoretical fraction line for *E* = 1, for which the contribution of $D_{quenched}$ is 0 since the quantum yield of $D_{quenched}$ is also 0. For completeness, the green dashed line is the FRET trajectory for a sample in absence of passive donors (pD) or background (BG). The curved dashed black line describes the phasor semi-circle.

Note S3

The Förster distance can be calculated using the following formula:

$$R_0 = 0.211 \cdot \sqrt[6]{\kappa^2 n^{-4} Q_D J(\lambda)} \qquad \text{Eq. S8}$$

Here, R_0 is the Förster radius, κ^2 is the orientation factor kappa squared, n is the refractive index of the medium, Q_D is the donor quantum yield and $J(\lambda)$ is the overlap integral of the donor emission and acceptor absorption spectrum. For the FRET pairs used in Fig. 4 the following parameters were used:

FP-pair	κ^2	Q_D	J(λ) (*10^{-15} $M^{-1}cm^{-1}nm^4$)	n	R_0[Å]
mTurquoise2-mVenus	2/3	0.93	2.30	1.33	58.3 Å*
eGFP-mScarlet	2/3	0.60	2.97	1.33	56.75 Å

Values are obtained from the online fluorescent protein database FPbase (fpbase.org/fret/). For mTurquoise-mVenus the found Förster radius is confirmed by Goedhart et al.. No literature value has been found for eGFP-Scarlet.

*Goedhart, J., von Stetten, D., Noirclerc-Savoye, M. *et al.* Structure-guided evolution of cyan fluorescent proteins towards a quantum yield of 93%. *Nat Commun* **3**, 751 (2012). https://doi.org/10.1038/ncomms1738

Figure S1

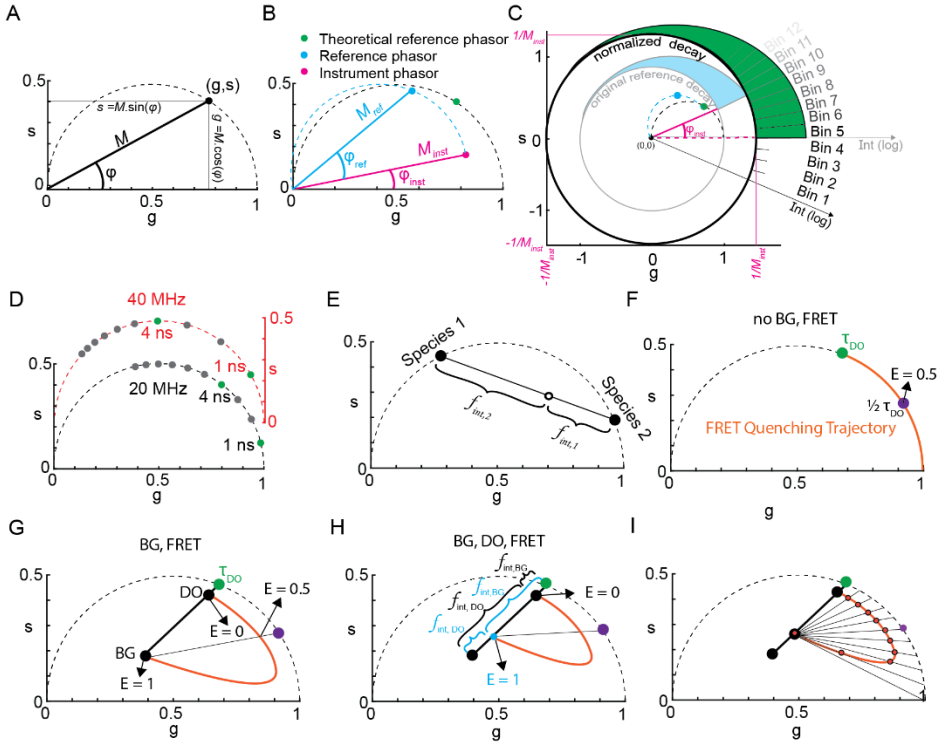


Figure S1: Overview figure of phasor theory for time-domain FLIM. (A) Every phasor, or phase vector, in the phasor space has two ways to be described. First, the phase and modulation of the signal can be determined and used to plot a vector with a length M and angle φ. Second, phasors can be described using cartesian coordinates g and s which represent the sine and cosine Fourier transform of the signal. Phasors 'on' the semicircle represent mono-exponential lifetimes and phasors 'within' the semicircle multi-exponential lifetimes. A phasor which falls outside of the semicircle is the result of a non-exponential process added to the transformed signal or erroneous referencing (B) Direct phasor calculation of an experimental fluorescence decay results in a misplaced phasor. A phasor of a single exponential will not be found on the semicircle since the microscope is not a perfect machine. IRF and decay start vary in placement within the used TAC-range. When a reference sample with known mono-exponentiality and a known lifetime is measured we can calculate its expected position (green dot, see also Theory section Eq. 9-10). In reality the measured phasor is misplaced (blue dot). A new coordinate system can be found in which the measured phasor is on the expected semi-circle position (blue dotted line). To get from the old coordinate system to the new, a rotation and resizing is required. To determine the exact values of these

operations we look at the changes of the basis in both semicircles which are attributed to the instrument: M_{inst} and φ_{inst}. In the depicted example, the coordinate system that is measured needs to be rotated φ_{inst} degrees clockwise and stretched with a factor $1/M_{inst}$ in order to reobtain a normalized coordinate system in which the base of the semicircle has a length of 1. (C) Another way to visualize the referencing and normalization used in time-domain phasor-FLIM is by displaying the decay onto a 'universal circle'. The universal circle carries all TCSPC bins in the TAC range, which are spread over the circle's circumference starting at $(1,0)$. Every position on the universal circle, representing a TAC-bin, is weighted by the photons that arrived in that bin. The average position of all photon-weighted universal circle positions determines the phasor position. When we normalize the measured phasor, the universal circle is again rotated by φ_{inst} and its radius is resized using $1/M_{inst}$. This leads to a correct representation of lifetimes in and on the semicircle starting in $(1,0)$ at zero lifetime and nearing infinite lifetime at $(0,0)$. The infinity lifetime at $(0,0)$ is achieved when a time domain measurement has no decay. This equal contribution of all bin-positions on the universal circle will average out at $(0,0)$. (D) Depending on the used TAC range, lifetimes are distributed accordingly for 20 MHz (black) and 40 MHz (red). (E) A combination of fluorescent species, a biexponential in the case of two species, will be located within the semi-circle and on the line connecting both species. Its position is the result of fractional contribution of photons from both species. (F) A FRET quenching line is used to represent all positions for *E* = 0-1 of a donor quenched by an acceptor. In case of no background (BG) and donor molecules not taking part in the FRET process (DO) the possible phasors follow the semicircle towards $(0,1)$. (G) When BG is convoluted within the measured decay, there is an increasing contribution of BG as the quenched donor reduces its intensity fraction. At the point of fully quenched donor, the quenching line ends at the only contributing species, BG. (H) In case there are donor molecules not taking part in FRET (passive donors whose phasor location is DO) and there is BG (as mentioned in panel G, the trajectory is additionally influenced with the endpoint closer to DO on the $BG - DO$ fraction line. As such, the quenching line is adjusted forming a more compact trajectory for increasing DO. Fractional contributions of the situation at *E*=0 and *E*=1 are shown in black and blue respectively. (I) Every point on the quenching line is determined from the fractionality between the phasor determined by $BG + DO$ and the quenched species phasor on the semicircle leading to rapidly increasing FRET efficiencies towards the end of the quenching line. Note that the FRET trajectory always converges to the line connecting the trajectory endpoint and the 0 ns lifetime at $(1,0)$.

Figure S2

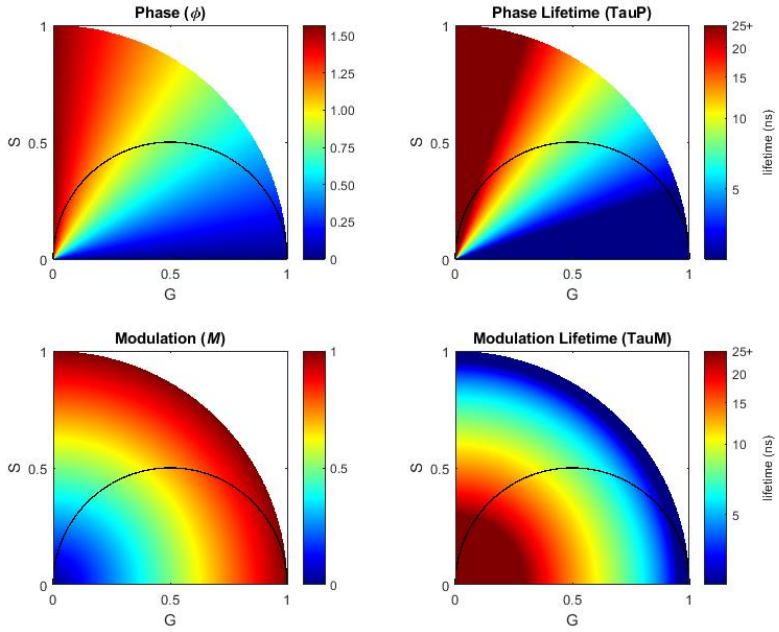


Figure S2: Color-coding of phase and modulation values in the first quadrant of the universal circle, containing the semi-circle. While the phase and modulation are clearly different, the therefrom calculated phase lifetimes and modulation lifetimes display equal values along the semicircle. This demonstrates the phasor property that mono-exponential lifetimes situated on the semicircle (and only there) have an identical phase and modulation lifetime.

Figure S3

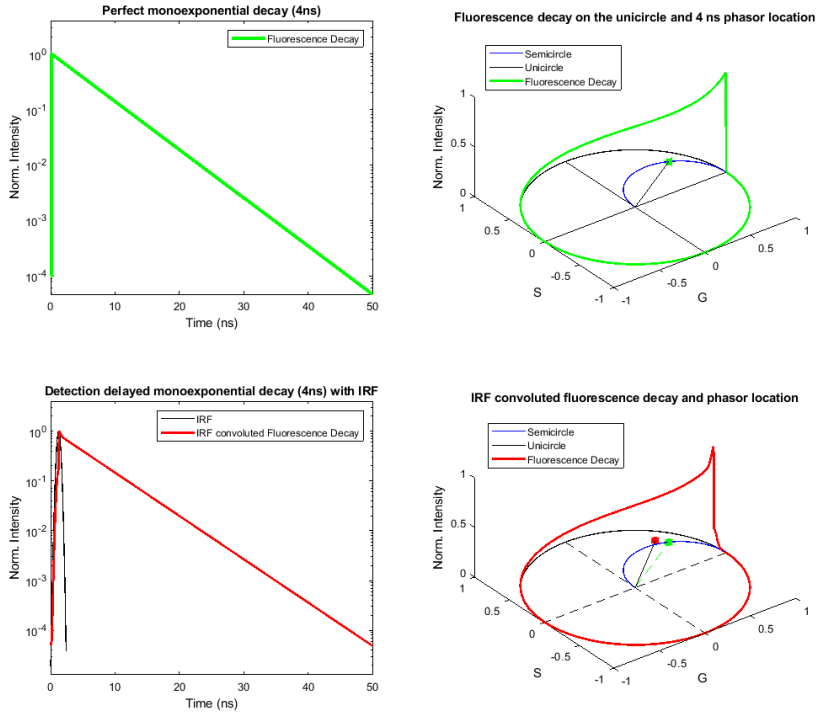


Figure S3: Graphical representation of the effect of IRF convolution on the phasor analysis of a perfect 4-ns decay. The green data represents a prefect decay and a visual representation on the universal circle (unicircle) of that decay, leading to a phasor spot perfectly on the expected location on the semi-circle. (B) When an IRF is convoluted with the decay, and there is a delay of detection on the TCSPC, the resulting phasor location is no longer on the semi-circle due to the added non-exponential component. This effect is corrected by applying a phase and modulation change extracted from a reference sample.

Figure S4

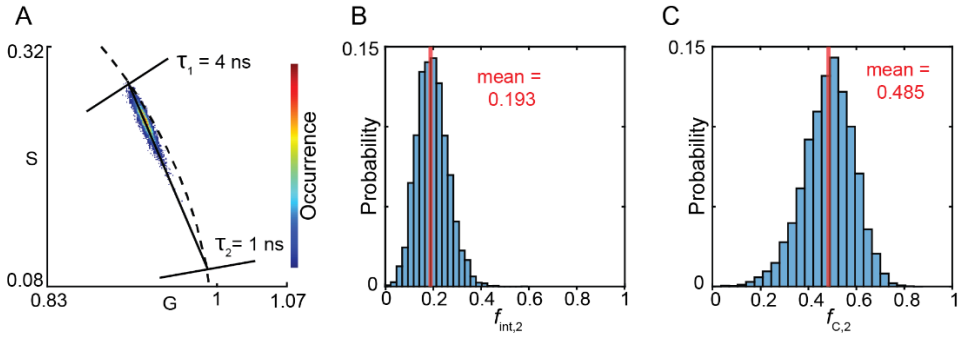


Figure S4: Simulation data illustrating the determination of concentration fraction. (A) Phasor plot resulting of a mixture of two fluorescent species with lifetimes of 4 ns and 1 ns for which the latter has an intensity of 1/4th of the 4 ns component. Species are simulated to have free yet identical diffusion to obtain an image of simulated photon data containing pixels with a distribution near 50/50 concentration. Similarly, FRET experiments often contain pixels with unquenched and quenched forms of the donor. A fraction line (black line) can be drawn in between. (B) All phasor positions are projected onto the fraction line leading to a distribution of intensity fractions. (C) Using Eq. 20 (see also Supplemental Note 1), the intensity fractions can be converted to concentration fractions resolving back into the simulated 1:1 concentration ratio of species.

Figure S5

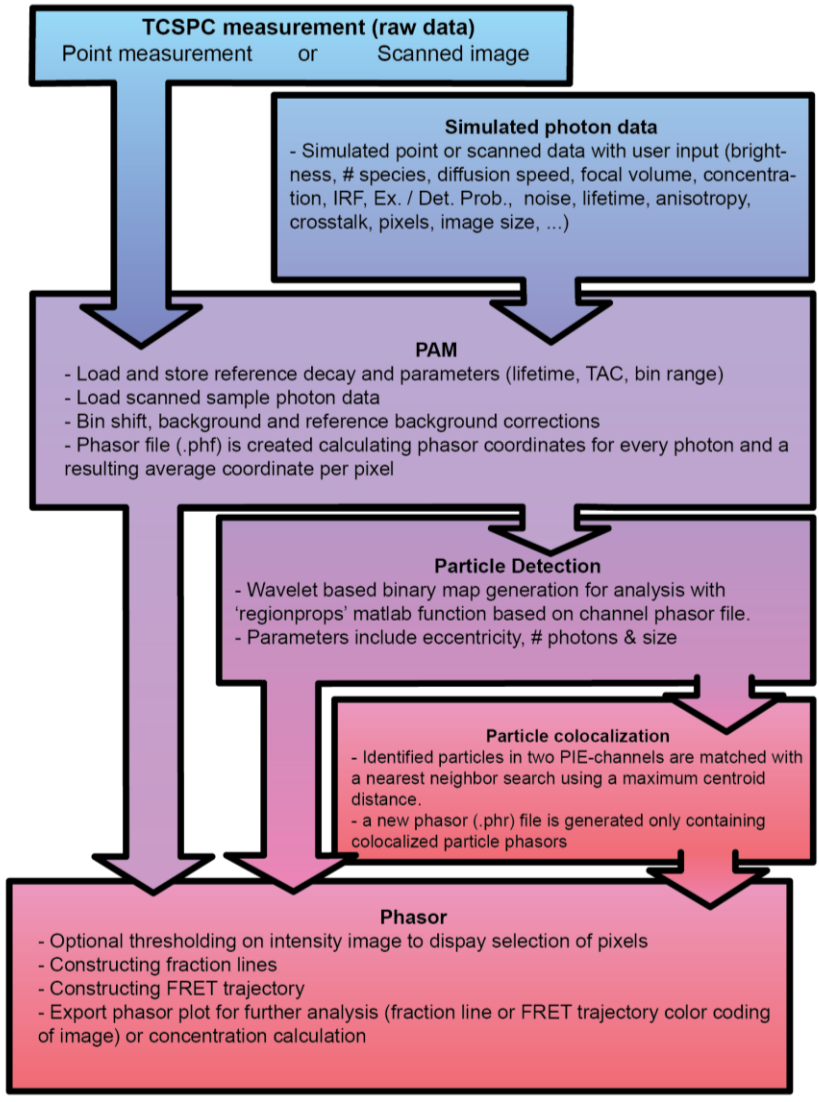


Figure S5: Flow-chart of the PAM software package showing the modules used in their respective order.

Figure S6

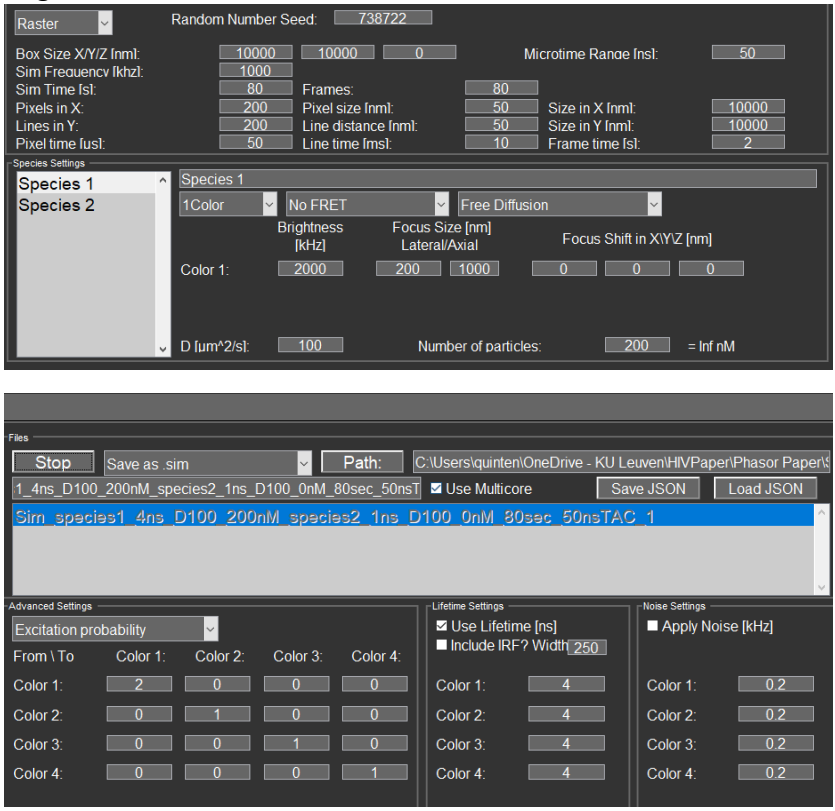


Figure S6: UI of the PAM simulation module. In the General setting, a simulation box can be chosen in XYZ and the scan settings, imaging duration and pulse frequency is set. In the species settings tab multiple species can be added, each with a desired brightness, diffusion speed and focus size. Additionally, the user chooses to include a one- or multicolor species, a static or dynamic FRET model and chooses from a list of diffusion types. Advanced settings allow to set the excitation probability, crosstalk and detection and bleaching probabilities. Finally, color-bound anisotropy lifetime and noise info can be given as input and an IRF can be convoluted with the simulated photon data.

Figure S7

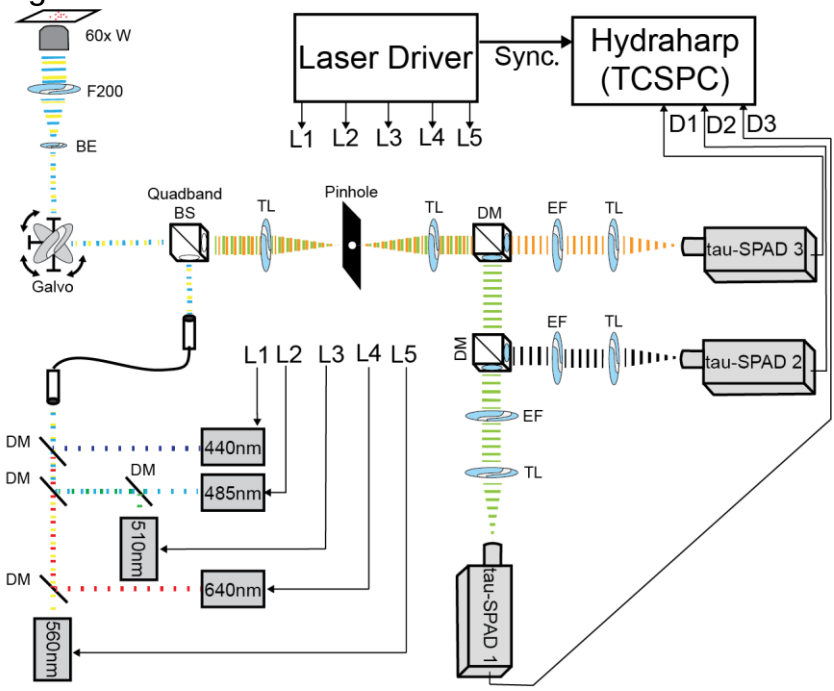


Figure S7: Schematic of a custom-built time resolved confocal setup. Abbreviations used: (W) water, (F200) lens with focus distance of 200mm, (BE) beam expander, (DM) dichroic mirror, (TL) tube lens, (EF) emission filter, (L) laser line, (D) detection line, (BS) beam splitter. All lasers are shown before entering the optical fiber. Afterwards the 485 nm and 560 nm combination is illustrated, as used for an eGFP/mScarlet FRET experiment. In this case the second magnetic DM holder is empty, allowing all fluorescence to pass to tau-SPAD1.

Figure S8

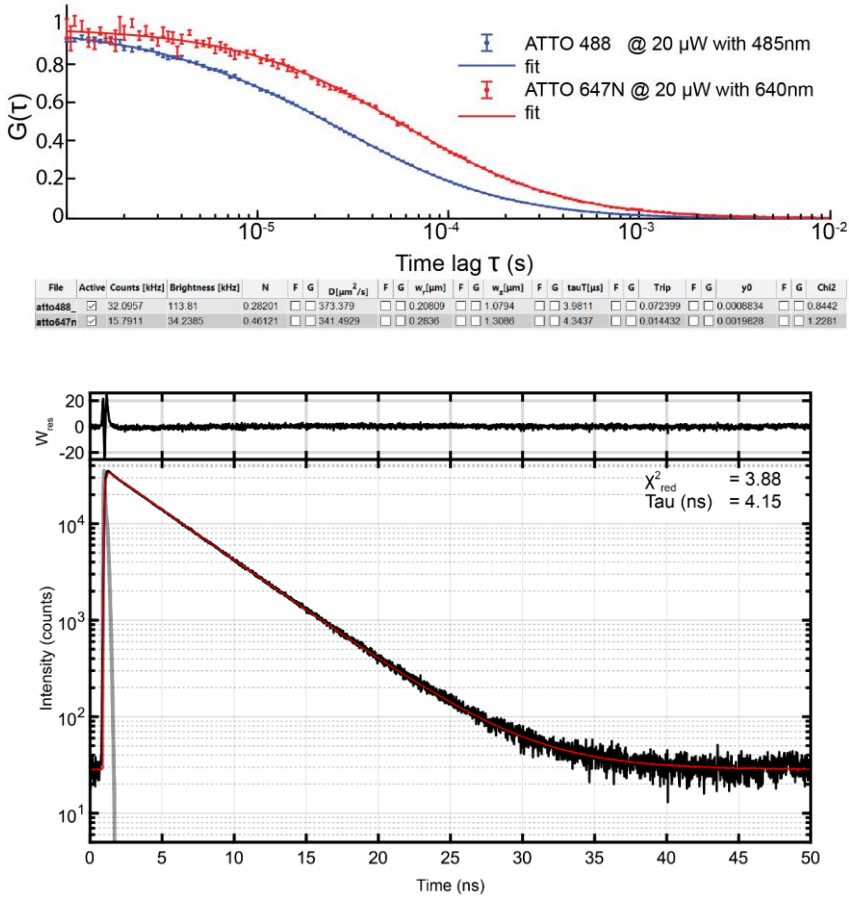


Figure S8: Illustration of PAM-*FCSfit* and PAM-*Taufit* data from PAM to verify microscope alignment and to characterize the reference lifetime for phasor referencing. (top) Fluorescence correlation spectroscopy (FCS) analysis with ATTO-488and ATTO-647N on our homebuilt confocal results in excellent focal parameters and photon sensitivity and is performed every measuring session. (bottom) Convolution data fitting with the experimentally determined IRF to identify the lifetime of the measured reference sample used in phasor calculation.

Figure S9

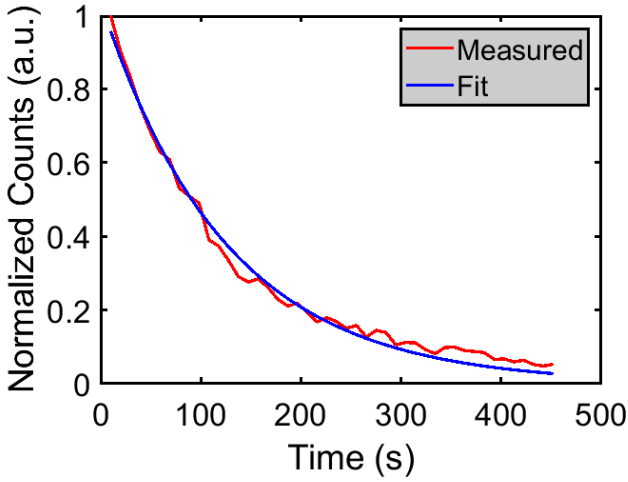


Figure S9: Exemplary plot demonstrating the exponential fit of the photobleaching time trace of a single HIV-1 particle containing IN-eGFP. Bleaching rates are derived from the exponential fit.

Figure S10

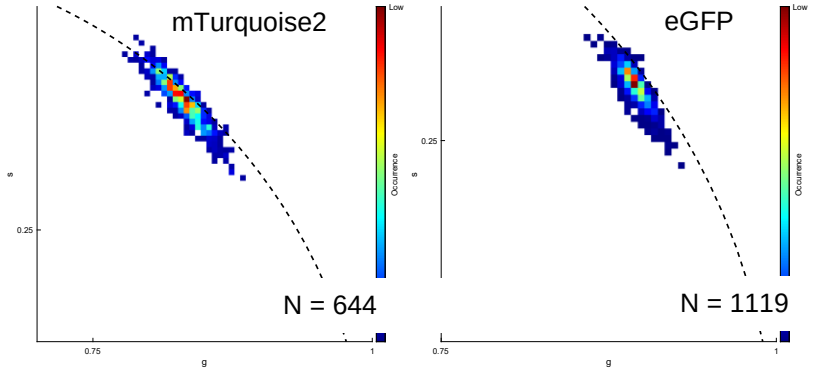


Figure S10: Donor-only phasors of HIV-1 IN FRET particles (particle-based) used to determine the FRET trajectory starting point (*DO*) in Fig. 4.

Figure S11

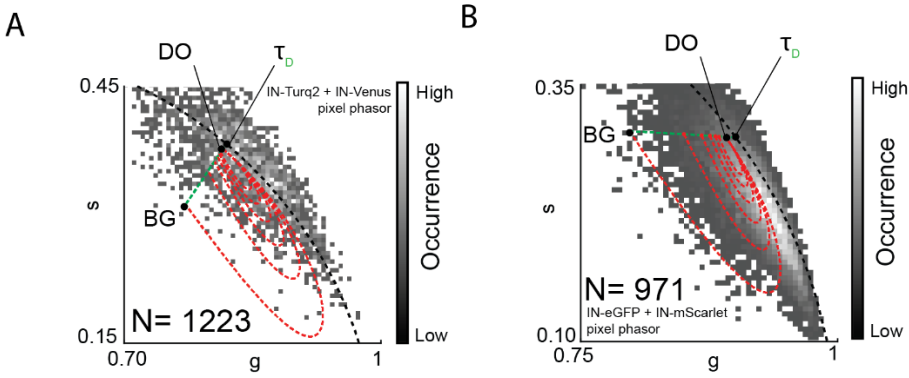


Figure S11: Pixel-based phasor of the measured HIV-1 IN FRET particles with IN-mTurquoise2 and IN-mVenus (A) or IN-eGFP and IN-Scarlet (B). It is clear that it is impossible to match the trajectories for 0-50% passive donor fractions (dashed red lines, longest trajectory is 0% passive donors, shortest is 50%) with the measured data. A pixel selection threshold of 20 photons/pixel was used to exclude non-particle pixels.

Figure S12

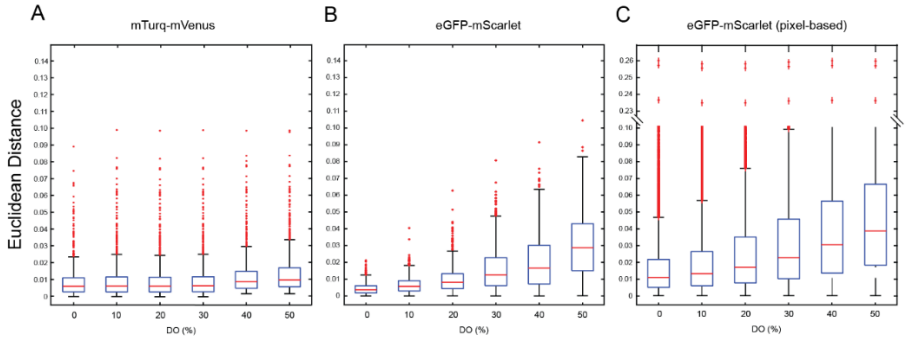


Figure S12: Quantification of Euclidean distances for all phasor points to the closest point on the FRET trajectory described for a range of 0% to 50% passive donor. (A) HIV-1 particles with IN-mTurquoise2 and IN-mVenus (B) HIV-1 particles with IN-eGFP and IN-mScarlet.(C) Comparative pixel-based distance quantification (threshold of 20 photons to select pixels), see also Fig. S11B.

Figure S13

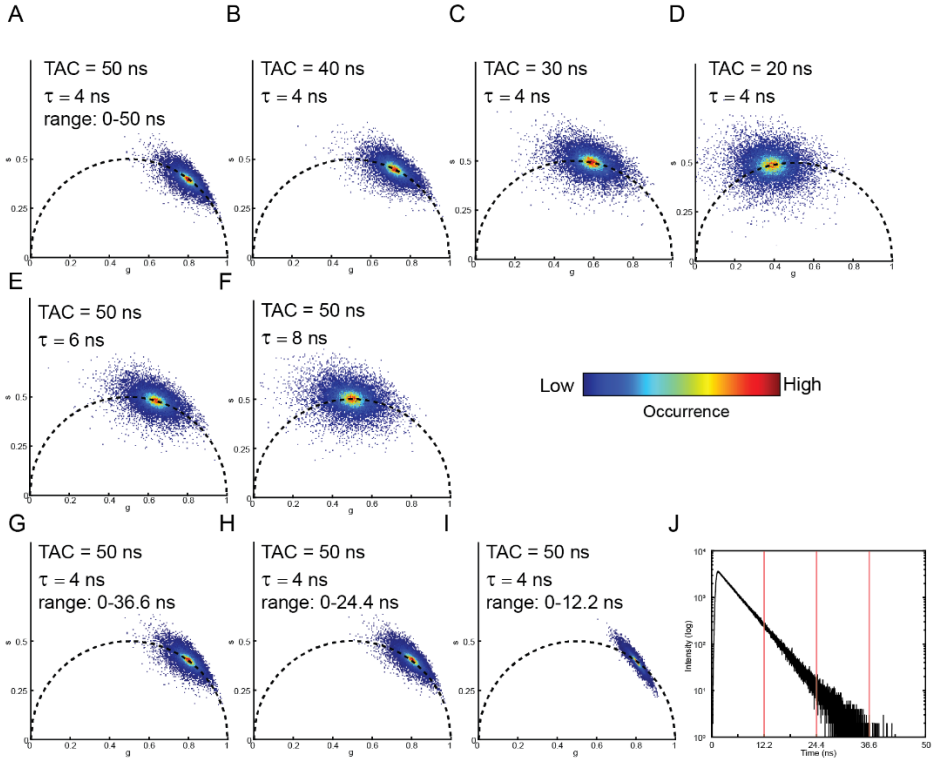


Figure S13: Effect of TAC width, fluorescence lifetime and used TAC range on resulting phasor data. (A)-(D) Simulated photon data for a 4-ns fluorescence lifetime measured in a TAC range of 50 ns, 40 ns, 30 ns and 20 ns, respectively. Not only does the phasor location on the semicircle change, also the shape of the phasor cloud is influenced. (E)-(F) Simulated photon data identical to *(A)* for a lifetime of 6 ns and 8 ns, respectively. For an identical TAC range the phasor cloud becomes rounder for larger lifetimes. (G)-(I) Simulated photon data identical to *(A)* for a lifetime of 4 ns with a TAC range of 50 ns, but the portion of the TAC range used for phasor analyses is shortened to 36.6 ns, 24.4 ns and 12.2 ns, respectively, emulating imperfect signal periodicity. (J) Decay of *(A)* illustrating the truncated portions of panel (G)-(I).

Figure S14

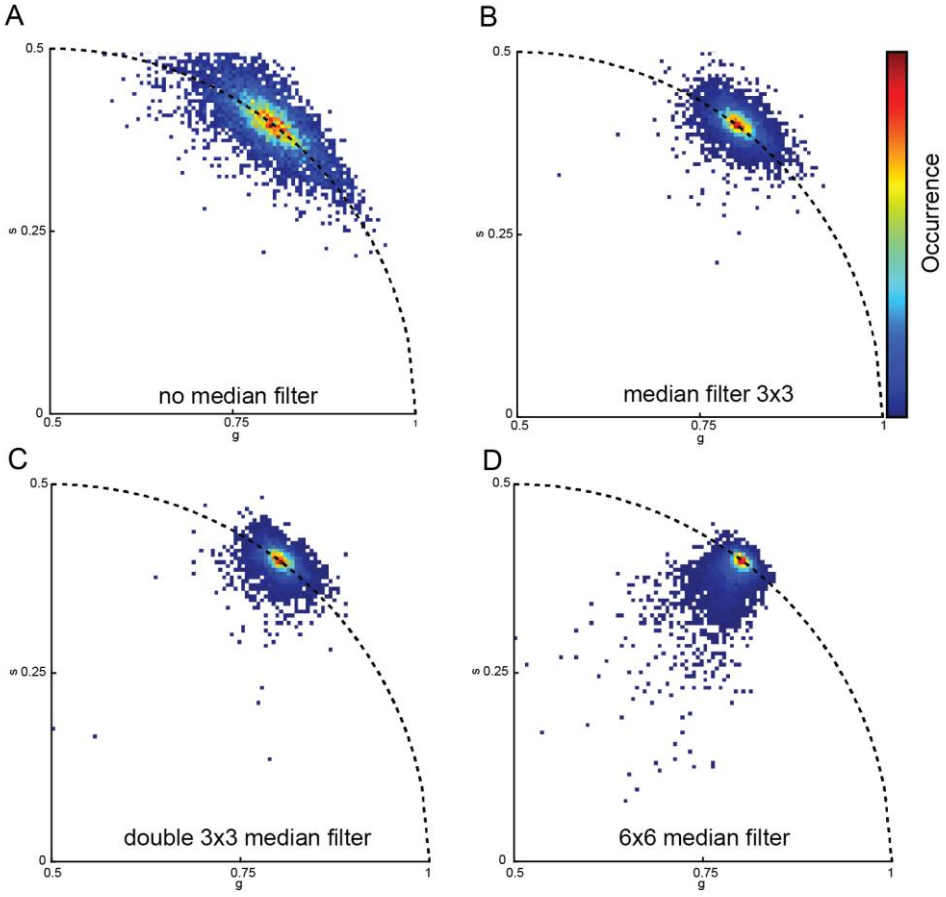


Figure S14: Effect of median filtering of g/s data for 4-ns-lifetime simulated photon data. (A) No median filter. The original image is identical to Figure 1A. (B) 'Normal' median filtering in 3-by-3 pixel regions. (C) Double application of a 3-by-3 median filtering (D) Excessive median filtering in 6-by-6 regions.

Addendum II

Protocols for a home-built confocal time-resolved fluorescence microscope

Quinten Coucke & Guillermo-Solís Fernández

1 Intro to Addendum

A commercial fluorescence (confocal) microscope is a workhorse in many labs. It allows for qualitative and potentially quantitative checks on biological and non-biological samples. Especially time resolved microscopes are able to unveil an extra layer of information from the image. However, the experimental setup of such experiments, the chosen analysis approach or the measurement procedure often requires from trial and error. Working with a home-built time-resolved confocal microscope is not only a deep dive into the essentials of microscopy and optics, it also allows the user to tinker with hardware and test several approaches for their intended experiments. Additionally, such microscopes provide the rawest form of data. While this may not by advantageous for the everyday biologist, it is the perfect environment to understand your experiment and learn. This, combined with the highest form of flexibility regarding possible changes in the light path, detectors, filters, … makes a home-built microscope a true asset. In this chapter we explain the microscope, the *PIE-FLIM*, which was built and used for all experiments showcased in this thesis. The microscope is explained in its current form and alongside a series of protocols used on the microscope is supplied for future use.

2 The PIE-FLIM microscope

The PIE-FLIM is a custom-built confocal microscope incorporating Pulsed Interleaved Excitation (PIE) and fluorescence lifetime imaging microscopy (FLIM). This microscope was built to perform high precision ns time resolved fluorescence imaging for a wide range of 2D samples. The home-built character of this setup is advantageous for exploring researchers and method developers. It is equipped with a range of excitation lines, detectors and light paths.

The microscope has been thoroughly described in its used configurations in chapter 3 and 4. However, Fig. 1 displays the full microscope hardware. This includes a polarizing beam splitter (PBS) which was integrated in this microscope to detect anisotropy in FRET measurement by Laskaratou et al. (1). Analysis of TCSPC-FLIM data and images was conducted in PAM (2), where FCS (*FCSfit.m*), decay fitting (*Taufit.m*), phasor analysis (*phasor.m*), Raster Image correlation spectroscopy (RICS) (Microtime Image Analysis, *MIA.m*) and more tools are readily available in a UI environment.

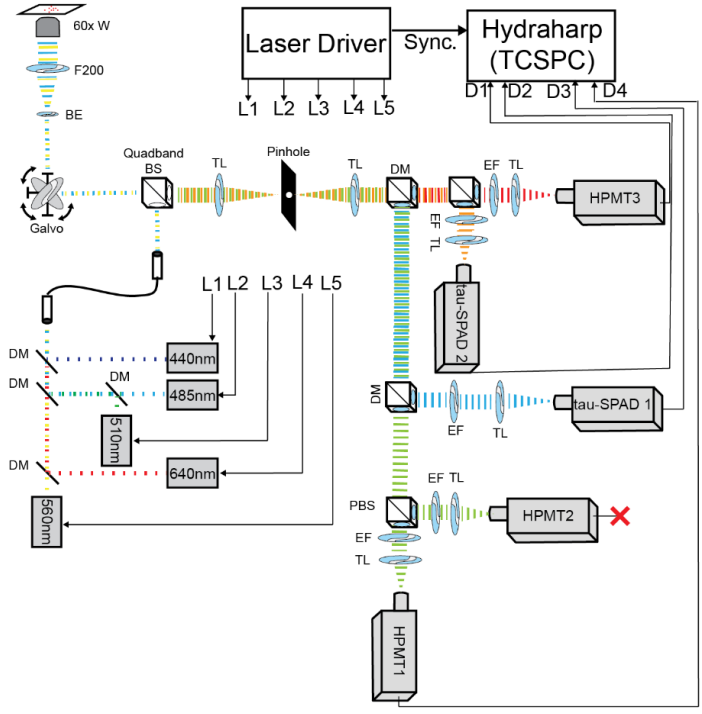


Figure 1: Schematic illustration of the PIE-FLIM home-built microscope. (EF) Emission Filter; (TL) Tube Lens; (PBS) Polarizing Beam Splitter ;(DM) Dichroic Mirror ;(BS) Beam splitter; (L#) Laser line nr.; (D#) detection line nr.

3 Alignment

A homebuilt microscope is notorious for small deviations in the optical hardware. These are caused by temperature fluctuations, user disturbances, vibrations, relaxation of tension in screws, … In general, alignment of the microscope is performed at several sections on the optical table. Firstly, the excitation lasers need to be directed into the optical fiber in such a way that the laser line remains parallel to the optical table and follows a path of right 90° angles. A standing target with height indications allows the user to check for consistent laser height. To aim a laser beam into the optical fiber, one always uses at least two separate kinematic mirror/dichroic holders which can adjust for up to 4 degrees of pitch or yaw. To start aligning a laser into the fiber, one starts with the kinematic holder furthest away from the optical fiber (closest to the laser source) adjusting only pitch, followed by the kinematic holder closer to the optical fiber. This process is repeated for the yaw. Both procedures are cycled until there is an optimal alignment and the laser power meter placed after the optical fiber displays a maximum value.

A Z-shape configuration of dichroic mirrors is not only used to combine lasers, it is a general alignment strategy more used in this microscope. Already in the section following the optical fiber, two alignment mirrors are in place between the quadband dichroic and the galvo.

3.1 Alignment of excitation light to the objective

One of the most crucial alignment sections of the microscope is situated just before the galvo scan unit. Here, light is reflected on a set of mirrors in between the galvo scan unit and the quadband excitation/emission filter. If a misalignment is situated here, light can often not reach the sample and emission will also not find its way to the pinhole. The principle behind the alignment is to make sure that the light arriving at the back of the objective is collimated and hitting perpendicular. Alignment of this sector is achieved by adjusting the angle of the two mirrors before the galvanometric scanner. In an ideally aligned scenario, if we checked the position of the collimated beam coming through an empty position of the objective revolver the beam should going straight up when the microscope stage is perfectly horizontal. To assess the collimation and angle of the beam, the laser light is sent through a long (1 m) rod that is attached in the objective revolver. The rod is carefully manufactured to be mounted perfectly straight in the objective threads. A longer rod would be even more beneficial, but practically not feasible. Adjustable irises are incorporated in both ends of the rod, and can be used to evaluate the position of the beam, relative to the center of the rod. When closing both irises, the intensity

of the spot that appears on the ceiling (which is laser light) will serve us to judge whether the beam is centered or not.

1. Close both the irises and evaluate whether there is already light visible on the ceiling at the beginning of the alignment process. Turn of ambient light in the room to judge this better.
2. Open the top iris and close the bottom one. Now use the adjustment screws from the mirror situated farthest from the galvo scanner to optimize intensity of the visible light. Iterate both screws until you reach a maximum of intensity at the ceiling spot.
3. Open the bottom iris and close the iris at the top of the rod. Now use the mirror closest to the galvo scanner. Use the adjustment screws again to find the maximal intensity of the spot at the ceiling.
4. Close both the irises and evaluate the intensity.
5. Iteratively repeat this process until you reach a point where any subtle changes to one of the mirrors results in a decreasing intensity or when you can't see an improvement with both irises closed after each iteration.
6. Remove the rod and re-insert the objective.
7. For final evaluation, place a sample with a water droplet on the stage and focus on the glass/water interface. When you move the focus back and forward over this focus point, the shape of the spot should stay centered and circular.

3.2 Collar ring adjustments

The objective is a key element in every microscope. For a confocal microscope especially, focusing light to the confocal volume and avoiding spherical aberrations is crucial. Spherical aberrations are most often introduced because of variations in the glass coverslip thickness (production tolerance or different coverslip types), a change of the temperature or measuring wavelength. In practice, spherical aberration results in a defocused image resulting from refractions in the light path. The objective collar ring is created to counter such distortion. However, this is only needed for non-oil immersion objectives, since there is no change in refractive index between the objective oil and the glass of a coverslip. In the PIE-FLIM setup, we used a water immersion objective. Fig. 2 illustrates how a coverslip can affect the focusing of the excitation light for a water immersion objective. Excitation light exiting the objective at different angles are refracted differently when a coverslip is introduced. To restore proper focus, the correction collar/ring can be turned, moving the central optics in the objective. Placement of the collar ring can be evaluated through FCS (reducing the confocal volume parameters and increased brightness).

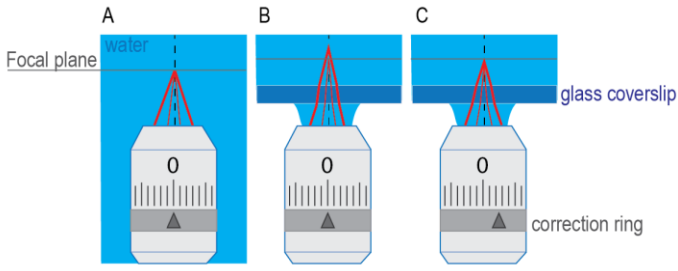


Figure 2: Exaggerated illustration of the collar ring adjustment, mending the effect of coverslip thickness. (A) The natural focus of an objective is found on its focal plane. (B) When a coverslip of a certain thickness is introduced, the refractions at the glass-water interfaces create a defocused image, depending on the angle of the light to the objective axis. (C) By adapting the correction ring, the focusing of all light rays into one focal spot can be restored.

3.3 Evaluation of alignment through FCS

Fluorescence correlation spectroscopy (FCS) is a technique where the signal of a detector is compared with itself after a given period of time via autocorrelation (3).

Naturally, the autocorrelation (G) of a dye diffusing through a confocal volume will sharply decrease as the time lag increases. For short time lag values, the molecule diffusing through the focus will most likely still remain in the focal volume and thus the fluorescence signal will not change, and result in a positive autocorrelation. As the lag time increases the probability for the molecule to diffuse out of the confocal volume increases and the autocorrelation value will subsequently decrease.

For optimal FCS measuring, the dye in solution should have a concentration that gives rise to N<1, with N being the average number of molecules in focus at a certain timepoint. This parameter is important since a N>1 would result in a lower correlation score since one molecule's signal will be correlated with a second molecule instead of resulting in successful autocorrelation.

Upon fitting (least squares curve fit with a $\chi 2_{red}$. score) of the autocorrelation curve, several parameters can be calculated from the fit curve. The most important are:

- W_r and W_z are the confocal volume parameters. They describe the measures of the prolate spheroid. With W_r being the lateral radius of the volume and W_z the axial measure
- When we divide the counts measured at the detector by the average amount of molecules (N) in the confocal volume, the brightness of the dye for the microscope is calculated. Improved alignment will contribute to more counts per molecule and therefore a higher brightness.

- When the confocal parameters are known, the time a single molecule spends in the confocal volume leads to the calculation of the molecule's diffusion speed.

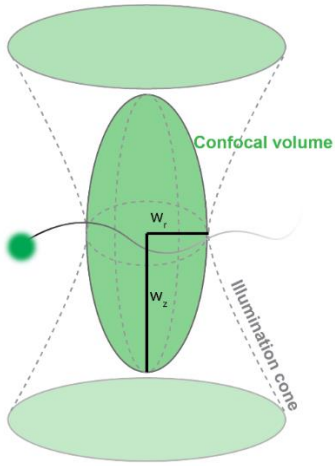


Figure 3: Illustration of the confocal volume within the illumination cone. During FCS the user aims at registering single events of diffusing molecules through the confocal volume. When the diffusion speed of a molecule at a certain temperature in the measuring liquid is well documented, accurate confocal volume measures can be retrieved, and vice versa.

Additionally, using the FCS autocorrelation score is a good approach to finetune the collar ring position since the improved confocal volume affects the FCS autocorrelation parameters.

3.4 Choice of single-photon detector

The PIE-FLIM is equipped with two type of single photon detectors: single photon avalanche diode photodetectors (SPAD) and hybrid photomultiplier detector assembly (PMA hybrid). When creating an experiment, it is valuable to consider the differences of these detectors. A SPAD provides a high sensitivity but produce a wider instrument response function (IRF) in the measured fluorescence decay. They are characterized by a small active area (150 µm diameter) which can be troublesome for alignment. On the opposite, PMA detectors have a large sensor surface (5 mm diameter) and produce a sharp IRF, which is preferable for TD-FLIM. Importantly, they each exhibit different photon detection efficiencies over the spectrum, as illustrated in Fig. 4. The APD-type SPAD detectors are also known to have a strong instrument response function (IRF) dependency based on the count

rate, mostly due to thermal effects or electric charges. This can lead to a time shift of the measured decay or FWHM broadening of the IRF.

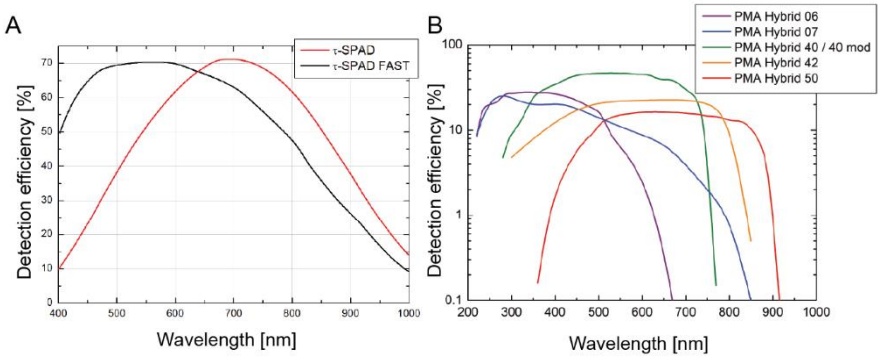


Figure 4: Photon detection efficiency of several single photon detectors. (A) PicoQuant Tau-SPADs (B) PicoQuant PMA detectors.

3.5 Pinhole alignment

Small pinhole alignments can be done by manually adjusting the x-y position of the pinhole holder. In general, the z axis parallel to the optical table is never altered.

1) Make sure a stable signal is present and that it is originating from the sample on the microscope.
2) Optimize one axis at a time until there is a stable improved signal for every axis optimization.
3) Stop when an iteration on both x and y axis didn't improve signal or FCS autocorrelation score.
4) Check the alignment of the detector equally optimizing the x-y axis for the best result.

Upon larger mishaps or total misalignment (i.e. no signal at detector), check whether the signal is fully absent:

1) Use bright dye solution and high laser power to check for a visible emission that is observable with a piece of paper
    a. When no signal is observed, perform the above x-y axis optimization steps for the pinhole with the bright dye providing visual feedback.
    b. If still no signal is visible after the pinhole, measure the distances of the tube lenses to the pinhole (based on their focal distance, and

adjust the pinhole z-axis until the pinhole is positioned at the correct focal distances from the tube lenses.

2) Once the pinhole lets focused light pass, optimize to get the brightest possible spot.
3) Now change the sample to a normal diluted reference sample and turn ON the detector.
4) Further finetune pinhole and detector position, occasionally performing FCS measurements to track and optimize brightness and focal parameters.

3.6 Pixel size determination

The image size is determined by the angles created in the scanning piezo. This results in an image size difference for different objectives. To determine the actual image size accurately, a target is imaged with a reflective size which displays a pattern of repeating lines with several line densities. Originally these targets were used for resolution determination, however, by calculating the number of pixels in between a line pair, the image size or pixel size can be retrieved as well. Here, the protocol for imaging the target and pixel size determination is supplied:

1) Place a larger reflective feature on the objective and block the laser excitation light. Laser cleanup filters and dichroic mirrors can stay in place in the microscope.
2) With the detector open, slowly unblock the excitation light gradually increasing the laser power at the reflective sample. Monitor the count rate measured at the detector. Be careful not to overflow/saturate the detector. Aim for 3000-5000 counts per second.
3) Place the USAF target with the reflective side down. Use the brightfield lamp op the microscope to navigate to the smallest features (group 7 element 6) using the view through the eyepiece.
4) Set the scan settings to the values for which you want to determine the image size (i.e. 20000 nm x 20000 nm).
5) Scan the image and save the intensity image.
6) Using a Matlab script or Fiji/ImageJ, measure the distances over multiple line pairs and calculate their spacing in pixel, as demonstrated in figure 5. Derive the true distance using the USAF supplied table (see Table 1). The smallest target on this resolution will suffice for most confocal microscopes at a line pair measurement of 4.386 µm for group 7, element 6.

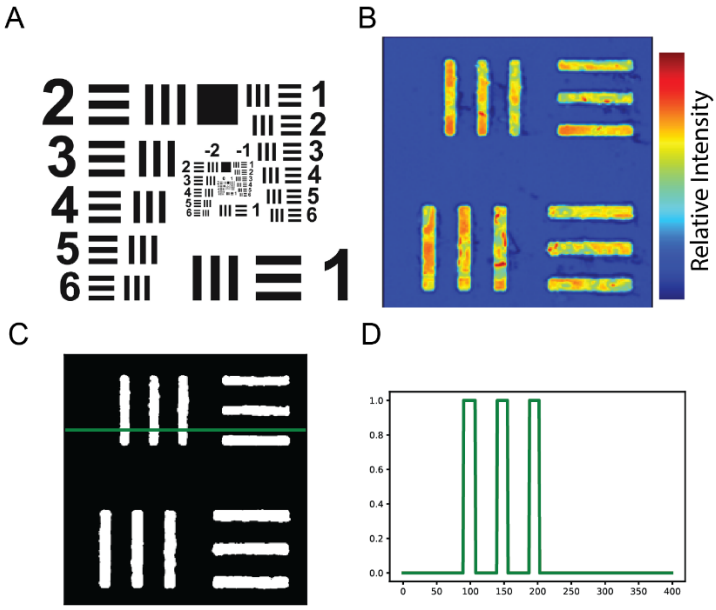


Figure 5: Illustration of pixel size determination using the USAF resolution test chart 1951. (A) 1951 U.S. Air Force resolution target schematic with line paurs in several groups, each containing 6 elements (B) Intensity image of the reflective lines as measured on the microscope (C) Generated binary image (D) The pixel distance of every line pair can be derived from the leading edge of every 'bump' in the line profile. This length is edge-to-edge and equals one line pair distance.

Table 1: Look up table for group 7 and 8 in the USAF target.

Number of line pairs per mm for USAF power test target 1951		
Element	Group Number	
	6	7
1	64.0	256.0
2	71.8	287.0
3	80.6	323.0
4	90.5	362.0
5	102.0	406.0
6	114.0	456.0

4 Instrument Response Function

The instrument response function (IRF) of a TD-FLIM system ideally contains the pulse shape of an infinitely short fluorescence lifetime. It collects all signal broadening factors of the system (laser, detector, optics and electronics) and is often used to correct measured FLIM signals, since this contribution is not sample-bound. To measure the IRF, several options exist, each mimicking this infinitely short lifetime. A 0 ns lifetime sample can't be made, as the fluorescence quantum yield would also be zero. The problem is circumvented using very short lifetime measurements, like measuring the laser pulse in reflection or measuring heavily quenched fluorescence, Which will approximate the true IRF.

4.1 Reflection measurements

By measuring the back scattering of laser light at the glass water interface of a drop of water (or a reflective surface) the imperfect functioning of the imaging dichroic mirrors is exploited to measure an IRF decay. The imaging dichroics allow a very small fraction of the laser light to be returned from the sample and pass the excitation dichroic towards the detection branch. Ideally all optics remain identical to the imaging conditions. However sometimes the laser cleanup filter before the detector is too efficient and needs to be removed for this type of IRF measurement.

4.2 Potassium Iodide (KI) quenching of a dye for IRF measurements

Potassium Iodide is a collisional quencher for most fluorescent dyes. Adding a small amount of ATTO 488 to a saturated solution of KI will quench the fluorescence (lower the fluorescence quantum yield) and thereby reduce the measured fluorescence lifetime. This measurement approximates the measurement instantaneous fluorescence or the pure IRF contribution. Such sample is made according to the following protocol:

1) In a falcon tube of 15 mL, combine 7 g of KI (CAS 7681-11-0) with 6 mL of pure MilliQ water at room temperature to achieve a saturated solution*.
2) Leave overnight strapped to a platform rocker and wrapped in aluminum foil (light protection) at room temperature, gently rocking.

   *note: not all KI will dissolve, this is aimed at ensuring a saturated solution

3) Before usage, centrifuge and directly pipet from the top of the solution to avoid pipetting crystals.

4) Pipet a drop of 50 µL KI on a flat imaging surface and cover with an extra water filled container under the cover to reduce evaporation.
5) Add 1/50th of volume concentrated dye, mix by pipetting up and down and leave the solution for 5 minutes to homogenize.
6) Verify the lack of crystals in the sample and a stable time-trace monitoring the count rate in the sample.
7) Measure the sample using a point measurement at a count rate of 10000-40000 counts per second. More (concentrated dye) or more laser light is needed to obtain more counts. Keep the laser power at the diode (controlled by PicoQuant software) constant as to remain identical to normal imaging settings. Removing OD filters in the excitation area of the microscope or physically adjusting laser light blockages is allowed as this maintains the same IRF profile.
8) Measure for maximum 60 seconds to avoid excessive sample evaporation introducing KI crystallization.
9) Load the PTU file in *PAM.m* and save the decay as IRF for a given detection channel. More info on how to do this can be found in the read-the-docs online manual of PAM: https://pam.readthedocs.io/ .

4.3 Relation IRF–Pulse power

It is important to remark that the power used by the laser driver will heavily affect the IRF width and shape. Therefore, it is advised to keep the laser power to a minimum for the desired power density in the sample. Especially in our homebuilt microscopy setup, power is fine-tuned by physical blockage of the laser beam prior to entering the optical fiber. This manual finetuning is heavily reduced when an adequate laser power is set at the laser driver.

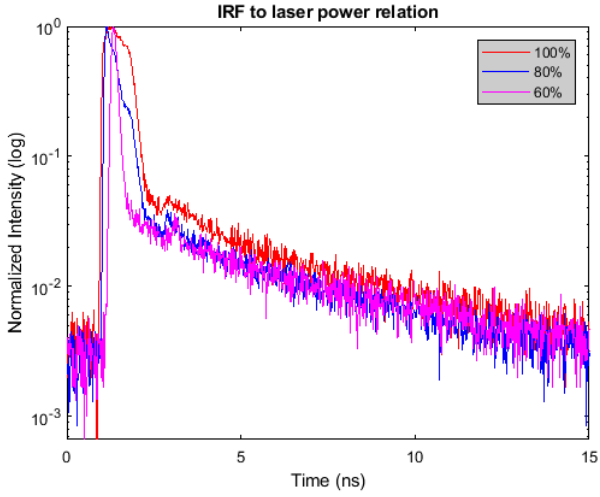


Figure 5: Reflection measurement in water without emission filter. A clear dependency of the laser power from the laser driver to the width of the IRF is found. Therefore, it is advised to keep the laser power at the laser driver as low as possible, instead of keeping a high laser power and reducing it on the microscopy table (e.g. with physical blocking, optical density filters, …).

4.4 IRF correction for Phasor analysis

When measuring a fluorescence decay in TD-FLIM, it is not a perfect fluorescence decay. Due to the IRF, there is not an instant rise time and a direct decay at the peak. Added, there is often the delay of several empty TCPSC bins between the start of the TCSPC period and the decay start. These two factors combined are the reason a direct phasor transformation of a monoexponential decay does not land on the expected position on the phasor semicircle. Therefore, the phasor plot needs to be referenced.

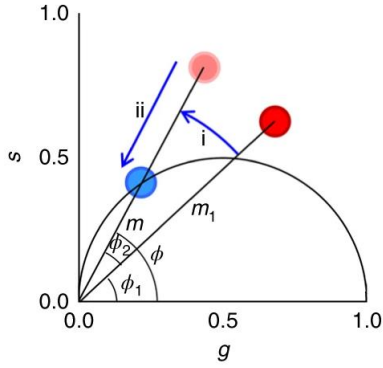


Figure 6: Illustration of the shift realized by a reference measurement. Upon measuring a sample of known lifetime, a theoretical phasor position can be calculated for it (light blue). The measured unreferenced phasor (red) can undergo a phase shift (change of the phase vector angle) and amplitude change (modulation) to land on the predicted phasor. Figure adapted from Ranjit et al. *Nature Protocols* (4).

Protocol:

1. Identify the normal measuring count rates of typical samples measured on the microscope. Ideally this is a photon count frequency that stays below 1-3% of the pulse rate to avoid photon pile-up effect (20 MHz results in a 200-600x10^3 photons per second). Generally, we aimed at 20-30x10^3 counts per second for our reference.
2. Identify a dye which has similar spectral properties to the fluorescent protein or dye used in the experiment. This way the recorded IRF in the measurement is highly similarly influenced by the optics as would be the case for the actual FRET sample.

- ATTO 488 for eGFP/mClover/mNeongreen
- ATTO 425 for mTurquoise/mTFP1

3. Make a dilution for the dye that, at the same laser power (at the diode) results in the targeted count rates.
4. Measure for 60 seconds
5. Use the *Taufit.m* application within PAM to load and tailfit the fluorescent decay of the measurement. A tailfit is accepted given the pure monoexponential properties of the reference dye.
6. Determine the reference background by selecting a range of 100 bins (i.e. 3001-3100) behind the full decay and note the photons in this range. Calculate the total background photons and derive the background count-rate as shown in the following example:

$$N = 3125 \qquad TAC = 50ns \qquad measurement\ time = 120s$$

$$sum\ bin3000 \rightarrow 3100 = 8000\ bins$$

$$800\ photons * \left(\frac{3125\ bins}{100\ bins}\right) = 25.10^3 photons$$

$$\frac{25.10^3\ photons}{120s} = 208{,}3\ hz$$

7. Load the reference .ptu file in *PAM.m* and navigate to the 'phasor' tab.
8. Enter the time-bins only containing the reference. Keep the start of the range at the first TCPSC time bin so it aligns with your future measurement.
9. Enter the value of the tailfit as reference lifetime.
10. Save the reference.

*note for phasor measurements system alignment checks and the phasor referencing measurement is performed in one go using the diluted dye (point measurement for 60 seconds while doing FCS with TCSPC)

5 References

1. Laskaratou, D., G.S. Fernández, Q. Coucke, E. Fron, S. Rocha, J. Hofkens, J. Hendrix, and H. Mizuno. 2021. Quantification of FRET-induced angular displacement by monitoring sensitized acceptor anisotropy using a dim fluorescent donor. *Nat. Commun.* 12:1–12.
2. Schrimpf, W., A. Barth, J. Hendrix, and D.C. Lamb. 2018. PAM: A Framework for Integrated Analysis of Imaging, Single-Molecule, and Ensemble Fluorescence Data. *Biophys. J.* 114:1518–1528.
3. Magde, D., E.L. Elson, and W.W. Webb. 1974. Fluorescence correlation spectroscopy. II. An experimental realization. *Biopolymers*. 13:29–61.
4. Ranjit, S., L. Malacrida, D.M. Jameson, and E. Gratton. 2018. Fit-free analysis of fluorescence lifetime imaging data using the phasor approach. *Nat. Protoc.* 13:1979–2004.

Addendum III

Curriculum Vitae

Education:

- B.S. in Biochemistry and Biotechnology, KU Leuven division Kortrijk (KULAK), 2012-2016
- M.S. in Biochemistry, KU Leuven, 2016-2018
  Master thesis: “Studying multimerization of Integrase during HIV infection using a FLIM-based FRET phasor analysis”
    - Supervisor: Prof. Dr. J. Hendrix
    - Co-supervisor: Prof. Dr. J. Hofkens
- Ph.D in Biochemistry, KU Leuven, 2018-2023
    - Supervisor: Prof. Dr. J. Hofkens
    - Co-supervisor: Prof. Dr. S. Rocha

Conference presentations

- Pacifichem 2021 conference (online-only conference due to COVID-19 regulations)
  https://pacifichem.org/
  “Phasor for FLIM-FRET analysis of intracellular vinculin tension sensors”
- Plenary session on FRET analysis for biosensors at the 2021 ‘Feel the Force summer school’ at KU Leuven
  (https://www.kuleuven.be/english/summer-schools/feeltheforce/home)
  “Analysis of FRET Data using Intensity and FLIM methods”
- Open presentation for the chemistry department
  "Phasor analysis for FLIM-FRET biosensor data:
  a case study of HIV-Integrase oligomerization and vinculin tension sensors"

Conference poster presentations

- Dutch Biophysics 2018 Veldhoven, The Netherlands
- Satellite Workshop of the DGfB biannual meeting "Advanced Fluorescence Spectroscopy and Imaging" 2018 Düsseldorf, Germany
- 25th PicoQuant ‘Single Molecule, Spectroscopy and Super-resolution Microscopy in the Life Sciences’ meeting 3-6 sept 2019 Berlin, Germany
- Let there Be …Light – Frans De Schryver Symposium – October 2019 Leuven
- EACR tumor microenvironment 2020 - March 2020, Lisbon, Portugal

Publications:

Particle-based phasor-FLIM-FRET resolves protein-protein interactions inside single viral HIV-1 particles

First-Author, Publishing date: 2023-08-08, Biophysical Reports
Quinten Coucke; Nagma Parveen; Guillermo Solís Fernández; Chen Qian; Johan Hofkens; Zeger Debyser; Jelle Hendrix
DOI: 10.1016/j.bpr.2023.100122

Sub-millisecond conformational dynamics of the A2A adenosine receptor revealed by single-molecule FRET

Co-Author, Publishing date: 2023-03-01, Communications Biology
Authors: 'Ivan Maslov, Oleksandr Volkov, Polina Khorn, Philipp Orekhov, Anastasiia Gusach, Pavel Kuzmichev, Andrey Gerasimov, Aleksandra Luginina, **Quinten Coucke**, Andrey Bogorodskiy, Valentin Gordeliy, Simon Wanninger, Anders Barth, Alexey Mishin, Johan Hofkens, Vadim Cherezov, Thomas Gensch, Jelle Hendrix, Valentin Borshchevskiy'
DOI: https://doi.org/10.1038/s42003-023-04727-z

Quantification of FRET-induced angular displacement by monitoring sensitized acceptor anisotropy using a dim fluorescent donor

Co-Author, Publishing date: 2021-05-05, Nature Communications
Authors: 'Danai Laskaratou, Guillermo Solís Fernández, **Quinten Coucke**, Eduard Fron, Susana Rocha, Johan Hofkens, Jelle Hendrix & Hideaki Mizuno'
DOI: https://doi.org/10.1038/s41467-021-22816-7

Synthetic fibrous hydrogels as a platform to decipher cell-matrix mechanical interactions

Co-Author, Publishing date: 2023-03-03, PNAS
Authors: Hongbo Yuan, Kaizheng Liu, Mar Cóndor, Jorge Barrasa-Fano, Boris Louis, Johannes Vandaele, Paula de Almeida, **Quinten Coucke**, Wen Chen, Egbert Oosterwijk, Chenfen Xing, Hans Van Oosterwyck, Paul H. J. Kouwer, Susana Rocha'
DOI: https://doi.org/10.1073/pnas.2216934120

Navigating FRET Techniques for Biosensor Applications: A Tutorial

First-Author, manuscript in preparation.

Presentations:

- Presentation 17 December 2021 at the Pacifichem conference (International Chemical Congress of Pacific Basin Societies) which was converted to an online-only conference due to COVID-19 regulations (https://pacifichem.org/).
    - Accepted abstract: “Phasor for FLIM-FRET analysis of intracellular vinculin tension sensors”

- Presenter of a plenary session on FRET analysis for biosensors at the 2021 ‘Feel the Force summer school’ (free entry for KU Leuven ADS students)
    - (https://www.kuleuven.be/english/summer-schools/feeltheforce/home)
    - “Analysis of FRET Data using Intensity and FLIM methods”

- Presenter of Interlaboratory meeting with Radboud University
    - “Measuring cellular forces with FLIM-FRET phasor”

- Presenter at the monthly departmental meeting 21 February 2023 of *Molecular Imaging and Photonics* open to the public and popular venue for students following *Capita Selecta* courses in the Master of Science.- (Accompanied with full departmental invite mailing)
    - “Phasor analysis for FLIM-FRET biosensor data:
      a case study of HIV-Integrase oligomerization and vinculin tension sensors”